CRYSTALLOGRAPHIC CHARACTERIZATION OF TRANSIENT C–H AMINATION INTERMEDIATES

A Dissertation

by

ANUVAB DAS

Submitted to the Office of Graduate and Professional Studies of
Texas A&M University
in partial fulfillment of the requirements for the degree of

DOCTOR OF PHILOSOPHY

Chair of Committee,	David C. Powers
Committee Members,	François P. Gabbaï
	Marcetta Y. Darensbourg
	Hae-Kwon Jeong
Head of Department,	Simon W. North

December 2020

Major Subject: Chemistry

ABSTRACT

Metal–ligand (M–L) multiply bonded complexes hold a central place in inorganic chemistry and catalysis: From fundamental and historical perspectives, these species have played a critical role in the articulation of important bonding principles (*i.e.,* the vanadyl ion in the development of molecular orbital theory); from a practical perspective, these species are critical intermediates in a variety of chemical reactions (*i.e.,* N_2 and O_2 reduction, H_2O oxidation, and C–H functionalization). The reactivity of these species simultaneously renders them attractive intermediates for catalysis but challenging synthetic targets to observe and characterize. Synthetic manipulation of the coordination geometry and ligand donicity, as well as introduction of sterically encumbering ligands, have emerged as powerful methods to tame the inherent reactivity of kinetically labile M–L multiple bonds. While these efforts have resulted in families of well-characterized complexes and provided critical insights regarding structure and bonding, the synthetic derivatization required to stabilize M–L fragments of interest often obviates the substrate functionalization activity relevant to catalysis. Photochemical synthesis of reactive species provides a conceptually attractive strategy to generate reactive M–L fragments under conditions compatible with time-resolved or cryogenic steady-state characterization, and photogeneration has enabled observation of a number of reactive M–L fragments. However, the suite of tools available to characterize photogenerated species is substantially more limited than is typically available for kinetically stabilized complexes and structural characterization is typically not possible. The chapters in this thesis discuss

our efforts to characterize transient species by coupling synthetic photochemical techniques with *in situ* crystallography. We first established photocrystallography as a tool to interrogate the structures of reactive intermediates in C–H functionalization, by photogenerating a Ru_2 nitride within a single-crystal matrix and characterizing it structurally. Next, we developed new photochemical strategies to generate Rh_2 nitrenoid intermediates which was then utilized to spectroscopically characterize them using time-resolved and cryogenic matrix isolation techniques. Finally, we have demonstrated that this strategy can be used to structurally characterize the reactive intermediates that are relevant to C–H amination catalysis, by structurally characterizing Rh_2 nitrenoid species.

DEDICATION

Dedicated to my loving parents and my teachers.

ACKNOWLEDGEMENTS

I would like to thank the chemistry department as a whole for giving me the opportunity to pursue a Ph.D. at Texas A&M University. When I first arrived here, everything was new to me, Sandy Horton and Valerie McLaughlin helped me figure out everything, and for that I am very grateful to them.

On the technical side, I would like to thank Dr. Joseph H. Reibenspies and Dr. Yu-Sheng Chen for teaching me everything about X-ray crystallography and Dr. Nattamai Bhuvanesh for teaching me the basics of Powder X-ray diffraction and SQUID. I'd also like to thank Dr. Gregory P. Wylie and Dr. Valdimir Bakhmoutov for training me on NMR and EPR instruments and also helping me with the *in situ* experiments. I am also very thankful to Yohannes H. Rezenom and Michael Raulerson for teaching me the basics of MALDI instrumentation and also helping me with specialized mass spectrometry experiments. I would also like to thank Dr. Sarbajit Banerjee and his group for training me and letting me use their IR instrument.

When I joined the graduate program at Texas A&M, I wanted to work for someone else. Before committing to a group, we had to talk with other PI's also, I decided to talk with Dr. David C. Powers, who was a budding new professor at that time. He got me excited about science and photocrystallography, which made me change my mind and I decided to join his group. Looking back, I'm glad that I made that choice and I am also grateful to Dave for mentoring me and helping me grow as a scientist. Being one of the first batch of students in the group, I got to learn everything first-hand from him. He also

gave me the freedom to design my own projects and experiments, and always supported me when I wanted to learn or try something new. Science is not only about obtaining results, but also about communicating it and Dave has helped me improve my science communication skills. Setting up a new lab is challenging, but he took out time to talk with each one of us, be it about science or life. The road to earning a Ph.D. degree is no doubt tough, but working with Dave has definitely made the journey enjoyable. Apart from being a great mentor, Dave has also been a great friend.

I'd like to thank my group members as a whole for being extremely supportive to me over the last five years and for being the best colleagues one could wish for. I would like to specially thank Dr. Wen-Yang Gao, Sung-Min Hyun, Asim Maity, Gerard 'Trip' Van Trieste, and Andrew 'Andy' Ezazi for tolerating my nuisances and also for making the lab exciting. I have also had the opportunity to mentor some very talented undergraduates, and would like to thank all of them – Madeline Hicks, Ryan Burk, Deene Wise, and Brianna Lilly – for helping me develop my mentoring and teaching skills.

I would also like to thank the family and friends I made in College Station. They made life fun outside lab and did not let me realize that I was far away from my home. I'd like to specifically thank Dr. Rajat Maji, Asim Maity, Anushree Mondal, and Nandini Kundu for being there for me and encouraging me to keep moving forward.

Lastly, I am forever grateful to my parents. It is because of their hard work and sacrifices that I am here now. Without their love and support, it would not have been possible.

CONTRIBUTORS AND FUNDING SOURCES

Contributors

This work was supervised by a dissertation committee consisting of Professors David C. Powers, François P. Gabbaï and Marcetta Y. Darensbourg of the Department of Chemistry and Professor Hae-Kwon Jeong of the Department of Chemical Engineering.

Gerard Pierre Van Trieste III contributed with the literature survey presented in Chapter I. Yu-Sheng Chen and Joseph H. Reibenspies helped in refining and analyzing the single-crystal X-ray diffraction described in Chapter II. Gregory P. Wylie and Vladimir Bakhmoutov helped with acquiring NMR and EPR measurements in Chapter II. Nattamai Bhuvanesh helped with acquiring SQUID measurement of dirhodium complex in Chapter III. Elemental analyses in Chapter III were performed by Atlantic Microlab (Norcross, GA). Andrew G. Maher carried out the transient absorption experiments on the dirhodium complex in Chapter III. Joshua Telser helped with simulating and analyzing the EPR measurements acquired in Chapter III. David C. Powers carried out the computational calculations on the dirhodium complexes in Chapter III. Michael R. Raulerson and Doyong Kim helped with acquiring variable laser MALDI-TOF and high resolution ESI-MS respectively, in Chapter III. Joseph H. Reibenspies and Yu-Sheng Chen helped in refining and analyzing the single-crystal X-ray diffraction described in Chapter IV. Yohannes H. Rezenom helped with acquiring variable laser MALDI-TOF and high resolution ESI-MS on the dirhodium complexes in Chapter IV. Ashley D. Cardenal helped with acquiring variable temperature NMR measurements in Chapter IV. David C.

Powers carried out the calculations on the dirhodium complexes in Chapter IV. Gerard Pierre Van Trieste III helped with collecting the X-ray diffraction data discussed in Chapter V, while Joseph H. Reibenspies and Yu-Sheng Chen helped in refining and analyzing the single-crystal X-ray diffraction described in Chapter V. Cheng-Jun Sun assisted with the EXAFS and XANES experiment, and Chen-Hao Wang analyzed and fitted the EXAFS data presented in Chapter V. Yohannes H. Rezenom helped with acquiring variable laser MALDI-TOF data. Computational portions of this research were conducted with the advanced computing resources provided by Texas A&M High Performance Research Computing.

Funding Sources

This work was funded by Texas A&M University, the Welch Foundation (A-1907), and the U.S. Department of Energy (DOE), Office of Science, Office of Basic Energy Sciences, Catalysis Program under Award Number DE-SC0018977. Portions of this research used resources of the Advanced Photon Source, a U.S. Department of Energy (DOE) Office of Science User Facility operated for the DOE Office of Science by Argonne National Laboratory under Contract No. DE-AC02-06CH11357. EXAFS and XANES data were collected at Sector 20-ID-C of APS/ANL. Single-crystal X-ray diffraction was collected at NSF's ChemMatCARS Sector 15 which is principally supported by the Divisions of Chemistry (CHE) and Materials Research (DMR), National Science Foundation (NSF), under grant numbers NSF/CHE-1346572, NSF/CHE-1834750, and NSF/DMR-1531283.

TABLE OF CONTENTS

Page

LIST OF FIGURES

LIST OF TABLES

Page

CHAPTER I

INTRODUCTION: CRYSTALLOGRAPHY OF REACTIVE INTERMEDIATES*

I.1. Introduction

Metal–ligand (M–L) multiply bonded species (L = CR^{3-}, CR_2^{2-}, O^{2-}, NR^{2-}, and N^{3-}) are ubiquitous intermediates in biological and heterogeneous catalysis, as well as important reactive intermediates in synthetic chemistry. Among other applications, M–L multiply bonded species have been invoked as intermediates in N_2 and O_2 reduction, NH_3 and H_2O oxidation, as well as various C–H functionalization schemes.[1-4] C–H hydroxylation chemistry in cytochrome P450 enzymes is effected by an active site-bound terminal Fe oxo species, generated by the combination of O_2 and NADH.[5-9] Similarly, a non-heme diiron site housed at the core of soluble methane monooxygenase (sMMO) catalyzes the hydroxylation of methane via the intermediacy of an aerobically generated Fe oxo intermediate (both terminal and bridging oxo intermediates have been proposed).[10] Surface-bound nitride and imido species are potential intermediates in the reduction of N_2 to NH_3 during Haber-Bosch chemistry.[11-12] Extensive efforts to develop heterogeneous electrocatalysts for water oxidation rely on surface-bound oxo species to mediate O–O bond-forming reactions,[13] and families of molecular catalysts for C–H hydroxylation have been developed as platforms to introduce complexity and functionality in organic

* Data, figures, and text in this chapter were adapted with permission from "Crystallography of Reactive Intermediates" by Das, A.; Van Trieste III, G. P.; Powers, D. C. *Comment. Inorg. Chem.* **2020**, *40*, 116–158. Copyright 2020 Taylor & Francis.

molecules.[14] Metal-catalyzed carbene transfer reactions have been developed that enable synthetically important elaboration of C–H bonds to C–C bonds.[15-24]

The reactivity of M–L multiply bonded species is intimately dependent on the electronic structure of the M–L fragment. For a transition metal ion supported by a tetragonal ligand field, the molecular orbital picture illustrated in **Figure I-1**, which is derived from Gray and Ballhausen's articulation of molecular orbital theory in the context of the vanadyl ion,[25] is often utilized as a basis to analyze M–L bonding. As can be seen, in addition to M–L σ-bonding, symmetry allowed overlap of filled ligand-based orbitals with vacant M-based π* orbitals can give rise to M–L multiple bonding. For low d-electron count metals, significant M–L multiple bonding is expected which typically manifests of kinetically stable structures. Addition of d-electrons (i.e., by moving to later metals or to lower oxidation states) results in population of antibonding orbitals and reduction of the extent of M–L π-bonding.[26-27] In the limit, a molecule with tetragonal symmetry is unable to form a M–L multiply bonded oxo if more than 6 d-electrons are present (i.e., the 'oxo wall').[28] While often proposed as intermediates in catalysis, a bona fide oxo wall violator has not been isolated.

This dissertation will focus on the structures and reactivity of M–L multiply bonded fragments relevant to C–H functionalization chemistry, with a specific focus on M–NR fragments that are relevant to C–H amination catalysis. In this context, the structure of the M–L fragment is a critical predictor of the detailed mechanism — for example on the mechanistic continuum between H-atom abstraction and radical rebound[29] or direct C–H insertion[30] — by which C–H functionalization is accomplished.

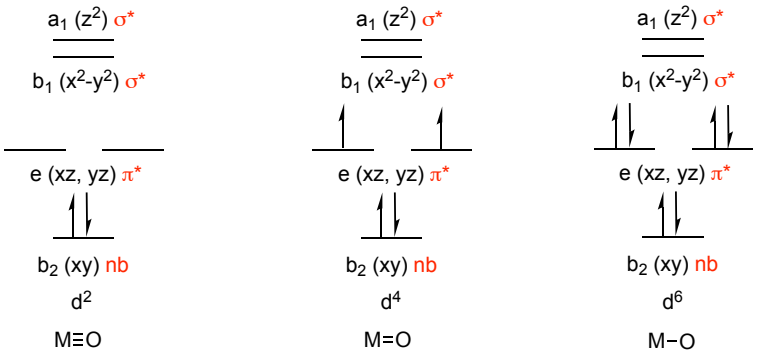

Figure I-1. d-Orbital splitting diagrams for C_{4v} oxo complexes highlight the extent of M–L multiple bonding that is available as a function of d-electron count. Population of π* orbitals (i.e., d_{yz} and d_{xz}) reduces M–L multiple bonding. Complexes that feature empty d_{yz} and d_{xz} orbitals display M–L triple bonds. Complexes with fully populated d_{yz} and d_{xz} orbitals would display a M–L single bond; nb = non-bonding.

I.2. Structure, Bonding, and Reactivity of Nitrenes

Organic nitrenes feature six valence electrons at nitrogen and are typically highly reactive species.[31] Elimination of N_2 from organic azide derivatives, which can be stimulated either thermally or photochemically, is a common strategy to access nitrenes.[32] Both singlet and triplet electronic configurations are accessible, and for unstabilized nitrenes the triplet configuration is preferred as predicted by Hund's rule (**Figure I-2a**). Similar to the stabilization of electronically unsaturated carbon centers in N-heterocyclic carbenes, π-donation from α-heteroatom substituents can stabilize the singlet electronic configuration. Application of this strategy has resulted in the isolation of a small family of singlet nitrenes (e.g. **I-1–I-3**, **Figure I-2b**).[33-36]

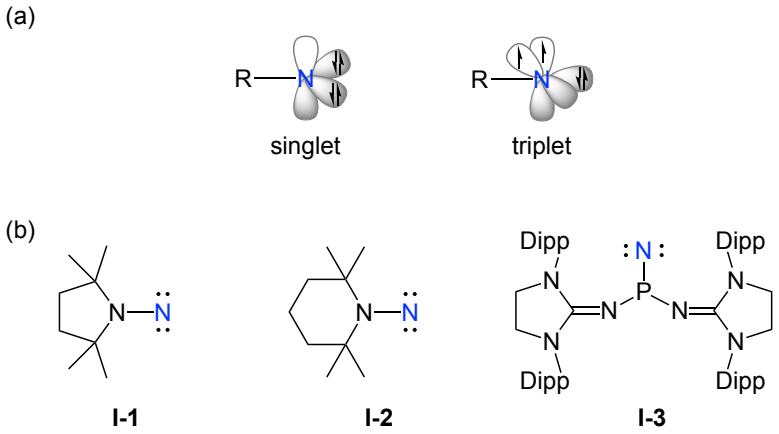

Figure I-2. Configuration and structures of stable nitrenes. (a) Singlet and triplet configurations are accessible to nitrenes. Consistent with Hund's rule, the triplet configuration is typically more stable. The singlet configuration can be stabilized by π-donation from α-heteroatom substituents. (b) Examples of isolated singlet nitrenes that have been stabilized by π-donation from α-heteroatoms.

While free nitrene (i.e., NH) has been observed in the low-density environment of interstellar space,[37] nitrenes are highly reactive in the condensed phase.[38-40] For example, Gudmundsdóttir and co-workers studied the photolysis of alkyl azides in the presence of triplet sensitizers.[38] **Figure I-3** summarizes the product distribution obtained, which included the products of nitrene dimerization (i.e., **I-6**), H-atom abstraction (i.e., **I-7**), C-to-N migration (i.e., **I-8**), and C–H insertion into solvent (i.e., **I-9**).[38] Similar photolysis reactions in the presence of olefinic substrates can give rise to aziridination products (i.e., **I-10**).[41] The observed product mixtures were rationalized as arising from a triplet nitrene intermediate. A similar product distribution was observed for the triplet-sensitized photolysis of benzyl azide.[38]

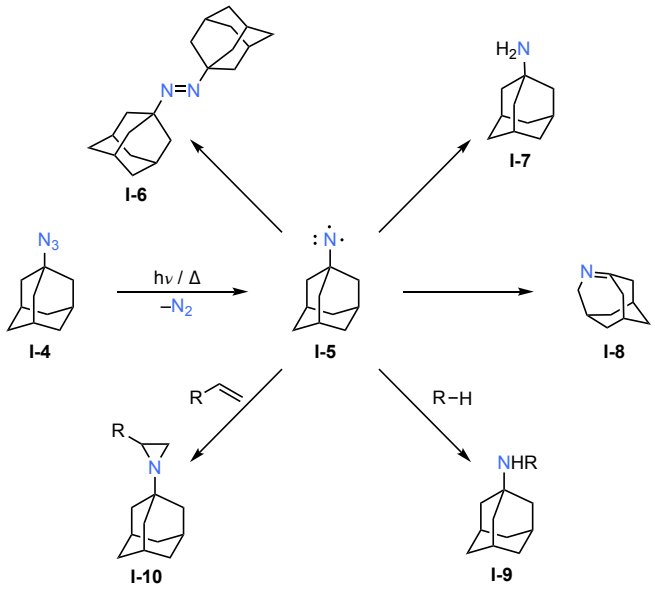

Figure I-3. Reaction chemistry of unstabilized nitrenes. Photoextrusion of N_2 from adamantyl azide (**I-4**) generates the corresponding nitrene **I-5**. Nitrene **I-5** can participate in dimerization to generate diazene **I-6**, H-atom abstraction to generate amine **I-7**, and C-to-N migration to generate imine **I-8**, as well as intermolecular C–H amination to afford amine **I-9** and olefin addition to afford aziridine **I-10**.

Extensive work has been carried out to develop selective nitrene transfer catalysis, which could significantly streamline the synthesis of nitrogen-containing compounds (**Figure I-4**).[42] Since the seminal work of Breslow in the early 1980s, which demonstrated that various transition metal catalysts, such as FeCl(tpp), MnCl(tpp), and $Rh_2(OAc)_4$, promote C–H amination with iminoiodinane reagents,[43-44] nitrene-transfer catalysis has become an important technology for the introduction of nitrogen-based functional groups in organic synthesis (tpp = tetraphenylporphyrin). Among the many catalyst systems that have been explored, Ti,[45-46] V,[47] Mn,[48] Fe,[49-50] Co,[51-52] Ni_2,[53] Cu,[54-56] Ru_2,[57] Rh_2,[58-60] and Ag[61-62] catalysts have been developed for nitrene transfer chemistry. More recently, the

power of metal nitrenoid intermediates for amination catalysis has been extended to enzymatic systems with the emergence of biocatalytic amination methodologies.[63]

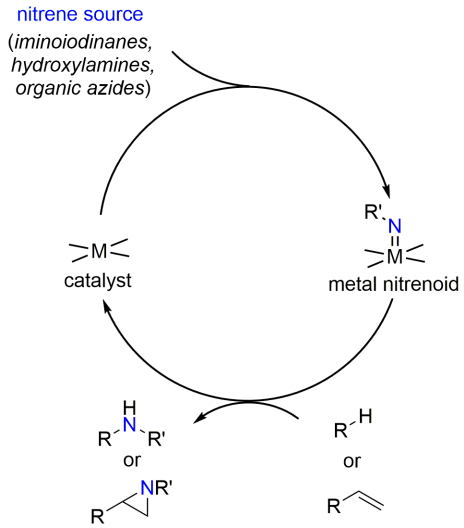

Figure I-4. Generic catalytic cycle for transition metal catalyzed nitrene transfer. Nitrene transfer reagents, including iminoiodinanes, organic azides, and hydroxylamine derivatives, have been developed as functional nitrene sources. Families of metal catalysts have been developed that enable rational control over the chemoselectivity of nitrene transfer reactions.

The bonding picture for a transition metal center with a nitrene fragment depends on the relative orbital energies of the two fragments (**Figure I-5**).[64-65] The relatively high d-orbital energies of early transition metals results in highly polarized M–N bonding, accounts for the observed nitrogen-centered nucleophilicity, and in which the nitrogen ligand can be considered as a –2 fragment (i.e., metal imido complexes). As the d-orbital energy of the metal fragment decreases (i.e., the nitrogen ligand acting as a –1 donor). Complexes that are described by this bonding picture are referred to as metal iminyl or metal nitrene radical complexes. This bonding picture is analogous to oxyl radical

complexes of the late metals.[66-70] For late-transition metals, the HOMO of the complex is predominantly metal-centered (i.e., the metal d-orbitals become lower in energy than the nitrogen p-orbital). This results in an inversion of the ligand field when compared to metal imido complexes and results in the observed electrophilicity of the nitrogen ligand (i.e., metal nitrene complexes). Similar to free nitrenes, the nitrene fragment can bind as either singlet or triplet configuration. Because intimate knowledge of the bonding picture of specific complexes is not always available, we will generically refer to M–NR complexes as metal nitrenoids.

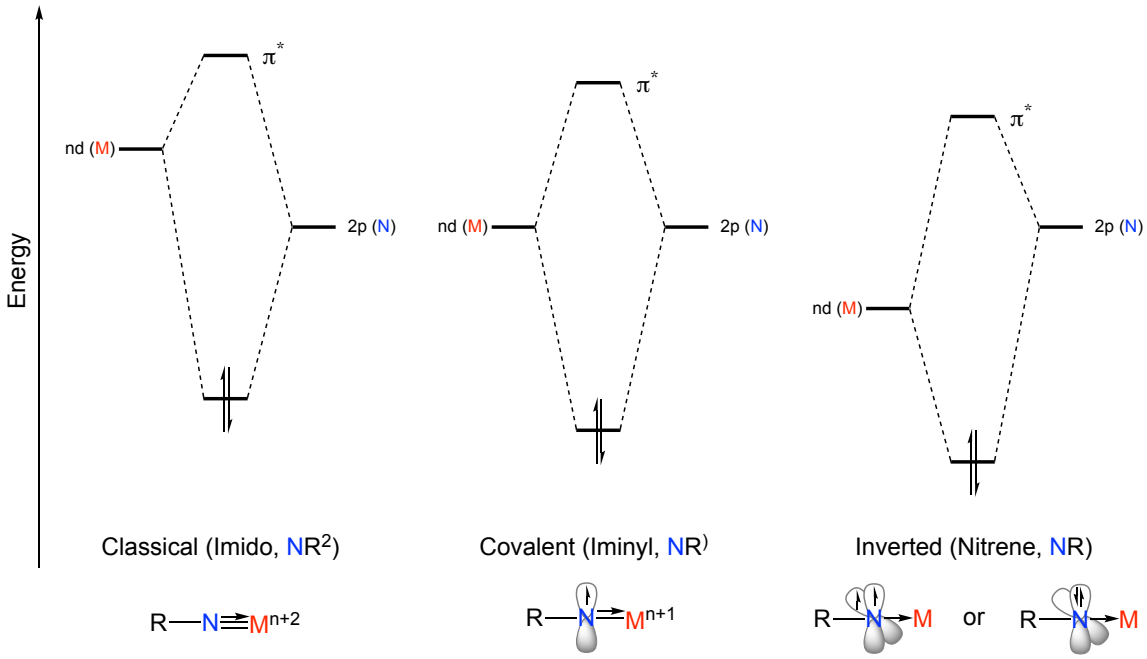

Figure I-5. Impact of frontier molecular orbital energies on the bonding between nitrene fragments and transition metal ions. For early transition metals, high d-orbital energies give rise to highly polarized M–N bonding that results in nucleophilic nitrogen ligand (i.e., imido complexes). As the metal d-orbital energy decreases across the periodic table, M–L covalency increases (i.e., iminyl radical complexes). For late metal complexes, the metal d-orbital energies become lower than that of the nitrogen fragment, which gives rise to electrophilic character at the nitrogen ligand (i.e., nitrene complexes). Adapted from reference 64.

I.3. Structural Characterization of Kinetically Stable M–NR Complexes

In large part motivated by the need to experimentally define structure-activity relationships, the synthesis and characterization of metal nitrenoid complexes has been the topic of sustained research effort. As described above, early metal nitride and metal imido complexes are often isolable and thus crystallographic characterization of chemical structure is straightforward. Structural characterization of reactive metal nitrides and nitrenoids that participate in C–H functionalization catalysis is intrinsically more challenging due to the experimental demands inherent to handling species that are

sufficiently reactive to functionalize C–H bonds. A number of strategies — including perturbation of the coordination geometry of the transition metal ion, modification of ligand donicity, and introduction of sterically encumbering ligands — have been pursued to enable stabilization and isolation of M–L fragments of interest. Below we highlight application of each of these strategies to the characterization of reactive M–L fragments.

I.3.1. Geometric Stabilization

Ligand-enforced deviation from tetragonal symmetry has emerged as a successful strategy to enable isolation of metal oxo complexes of late metals.[25, 27-28] In C_{4v} symmetry, one non-bonding orbital, d_{xy}, is below two π^*-symmetry orbitals, d_{xz} and d_{yz} (**Figure I-6**). A d^4 oxo complex in this geometry would be expected to display a M–O bond order of two and a d^6 oxo complex would be expected to display no multiple bonding character. In C_{3v} symmetry, a degenerate set of non-bonding orbitals, d_{xy} and $d_{x^2-y^2}$, is beneath the σ^* and π^* orbitals. Thus, a d^4 oxo in C_{3v} symmetry is expected to display a M–O bond order of three and a d^6 oxo would be expected to display a M–O double bond.

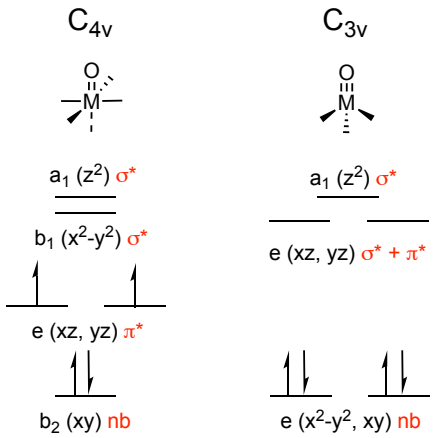

Figure I-6. Comparison of the M–O bonding in C_{4v} and C_{3v} complexes with four d-electrons. In C_{4v} symmetry, two electrons occupy π^* orbitals, while in C_{3v} symmetry, the π^* orbitals are unfilled.

In C_{4v} symmetry, metal nitride complexes exhibit qualitatively similar d-orbital splitting compared to metal oxo complexes (**Figure I-7a**).[71] In general, the energies of the d_{xz} and d_{yz} orbitals are raised and the energy of the $d_{x^2-y^2}$ orbital is lowered for the nitride complexes relative to the corresponding oxo complexes. The relative energies of the $d_{x^2-y^2}$ orbital and the d_{xz} and d_{yz} orbitals is sensitive to the ligand field strength of the ancillary donors. In C_{3v} symmetry, the qualitative d-orbital splitting diagrams for metal nitrido and imido complexes resemble that of the corresponding oxo complexes. For imido complexes, the d_{z^2} orbital energy is sensitive to the extent of σ-donation from the N-bound R group (**Figure I-7b**).[72]

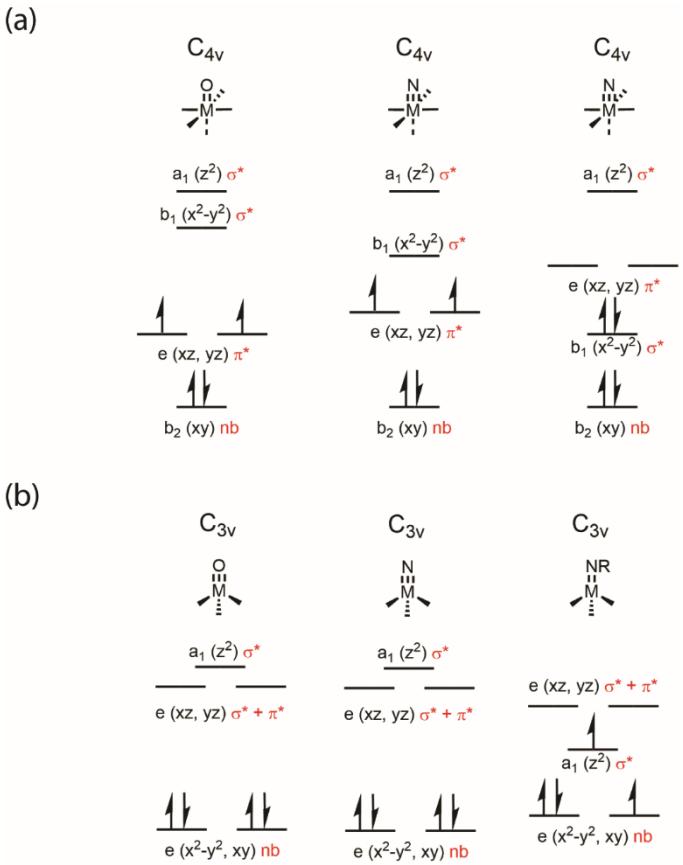

Figure I-7. Representative d-orbital splitting diagrams for d^4 M–L multiply bonded complexes. (a) Qualitative d-orbital splitting diagrams for metal oxo complexes (left) and metal nitride complexes with strong-field (center) and weak-field ligands (right) in C_{4v} symmetry. (b) Qualitative d-orbital splitting diagrams for metal oxo (left), metal nitride (center), and metal imide complexes (right) in C_{3v} symmetry. The relative energy of the d_{z^2} orbital is sensitive to the σ-donation of the –NR group. Adapted from references 71 and 72.

The increased M–O bond order observed in pseudotetrahedral geometries has been used to stabilize a number of reactive M–L fragments.[73-78] In 1993, Wilkinson reported the isolation and crystallographic characterization of $IrO(mes)_3$ (**I-11**), which displays C_{3v} symmetry at the Ir center (**Figure I-8a**).[79] Similar ligand-enforced trigonal symmetry enabled the isolation and crystallographic characterization of Fe(III) and Mn(III) oxo

complexes by Borovik and the recent isolation and crystallographic characterization of pseudotetrahedral Co(III) oxo complex **I-12** by Anderson (**Figure I-8b**).[80-82] In the context of nitride chemistry, Peters reported the synthesis and characterization (^{1}H NMR and Mössbauer spectroscopies) of a pseudotetrahedral Fe(IV) nitride, supported by a *tris*-phosphine ligand.[83-84] Structural characterization was precluded by dimerization upon concentration of solutions of the complex. Meyer and Smith separately isolated and structurally characterized Fe(IV) nitrides,[85-87] and together characterized a Fe(V) nitride **I-13** (**Figure I-8c**).[88] Moreover, Meyer isolated and structurally characterized a Mn(IV) nitride **I-14**, which could be oxidized or reduced by one electron facilitating access to Mn(III) and Mn(V) nitrides (**Figure I-8d**).[89] The Mn(IV) and Mn(V) species were structurally characterized, however the Mn(III) species was too reactive to be structurally characterized. Similarly, pseudotetrahedral Fe(III) imide **I-15** (**Figure I-8e**)[90] and Co(III) imide **I-16** have been isolated and crystallographically characterized by Peters and Smith, respectively (**Figure I-8f**).[91] Beyond psuedotetrahedral geometries, Milstein reported the observation and reactivity of a Pt(IV) oxo supported by a PCN pincer ligand, which was proposed to exhibit C_s symmetry (not crystallographically characterized),[92] and Fortier, Meyer, Mindiola, Caulton and co-workers reported the isolation of a *cis*-divacant octahedral Fe(IV) imido complex (crystallographically characterized).[93] Similarly, Schneider and Holthausen recently reported the photocrystallographic structure of a Pt(II) nitrene radical supported by a PNP pincer ligand.[94]

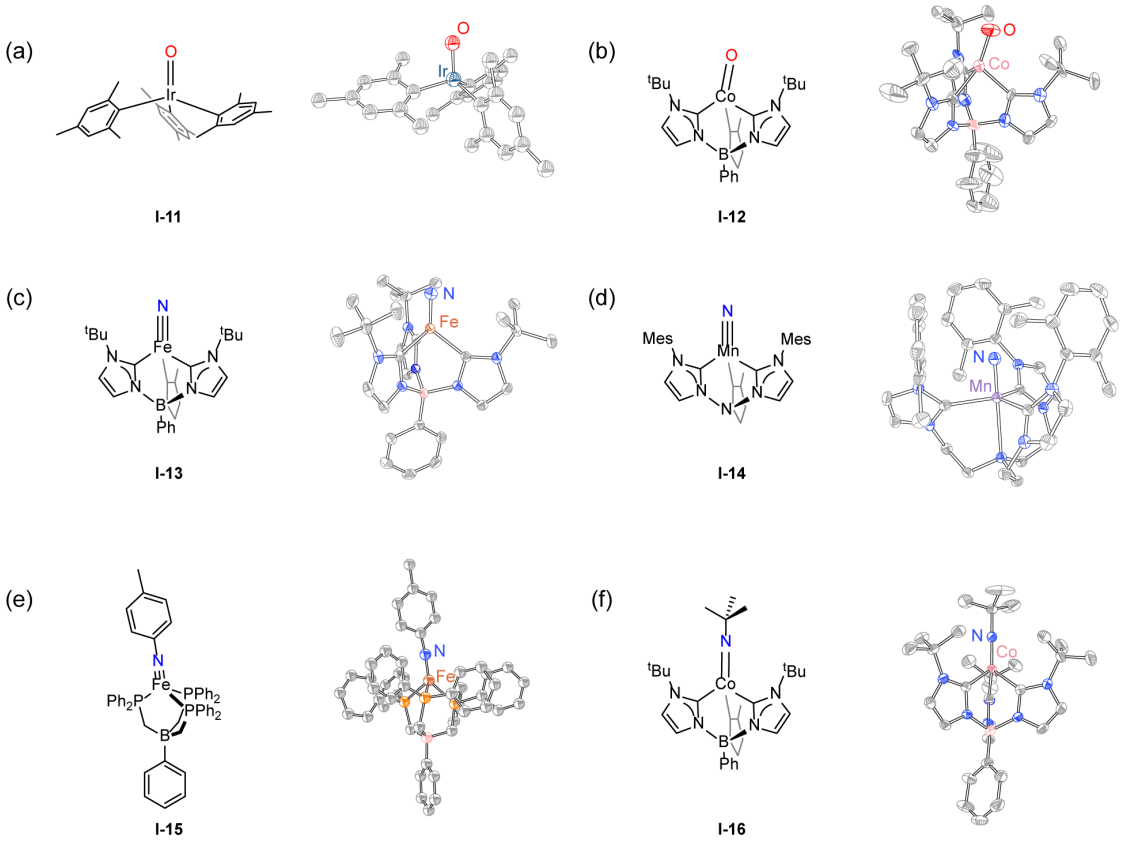

Figure I-8. Ligand-enforced pseudotetrahedral geometry has enabled the crystallographic characterization of M–L multiply bonded fragments. Structural characterization of (a) an Ir(V) oxo **I-11**, (b) a Co(III) oxo **I-12**, (c) an Fe(V) nitride **I-13**, (d) a Mn(V) nitride **I-14**, (e) an Fe(III) imide **I-15**, and (f) a Co(III) imide **I-16**.

I.3.2. Electronic Stabilization

Perturbation of the donicity of the ancillary ligand field has also been pursued as a strategy to stabilize reactive M–L multiply bonded fragments. For example, Mn(V) nitrenoids have been invoked as intermediates in Mn porphyrin catalyzed nitrene transfer catalysis (**Figure I-9a**).[43, 95-96] The inherent reactivity of the intermediate Mn(V) nitrenoid (i.e., **I-18**) has thus far prevented characterization of this synthetically important

intermediate. Towards the goal of stabilizing analogs to Mn nitrenoids relevant to amination catalysis, *tris*-anionic ligands, such as corroles and corrolazines, have been utilized in place of porphyrins.[97] For example, Abu-Omar and co-workers structurally characterized Mn(V) imido **I-20**, supported by a *tris*-pentafluorophenylcorrole ligand, by photolysis of the corresponding Mn(III) corrole in the presence of mesityl azide (**Figure I-9b**).[98] Similarly, Mn(V) imido **I-21**, supported by a perarylated corrolazine ligand was reported by Goldberg and co-workers (**Figure I-9c**).[99] In both corrole-supported complex **I-20** and corrolazine-supported complex **I-21**, the replacement of the *bis*-anionic ligand with *tris*-anionic ligands substantially suppressed the reactivity of the resulting Mn–NR fragment; neither **I-20** nor **I-21** react with olefinic substrates.

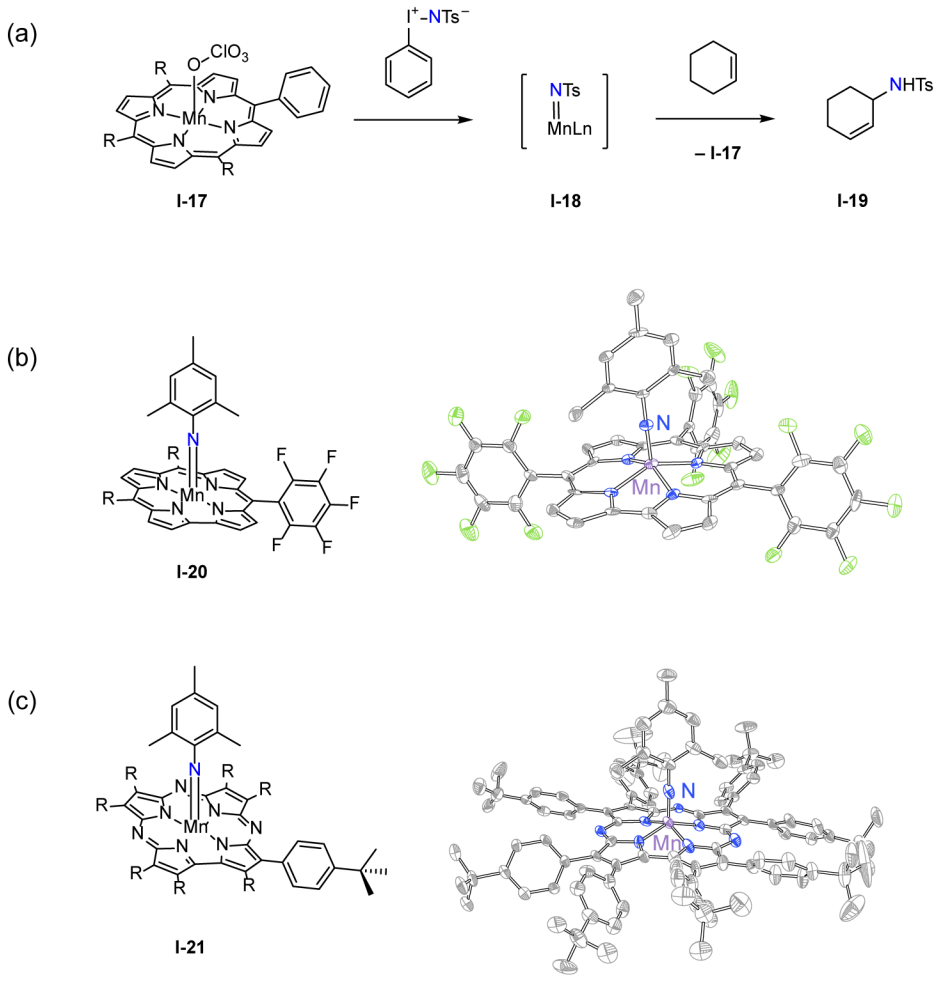

Figure I-9. Electronic stabilization has enabled the crystallographic characterization of M–L multiply bonded fragments. (a) Mn nitrenoids have been proposed as intermediates in Mn porphyrin-catalyzed nitrene transfer catalysis. (b) A *tris*-anionic corrole ligand has been utilized to stabilize Mn(V) imide **I-20**. (c) Isolation of Mn(V) imide **I-21** using *tris*-anionic corrolazine ligand scaffold.

I.3.3. Steric Stabilization

The aforementioned strategies — modification of ligand geometry and donicity — fundamentally perturb the electronic structure of the ligand-supported M–L fragment. Introduction of sterically demanding ligands, which can suppress bimolecular

decomposition reactions such as dimerization and solvent functionalization, provides a complementary approach to kinetic stabilization of reactive M–L bonds in which the M–L fragment is not directly manipulated.[100-104] As an example of this strategy, Lancaster, Betley, and co-workers recently isolated and characterized a Cu nitrene complex relevant to C–H amination and aziridination catalysis.[64] Exposure of Cu complex **I-22** to various organic azides resulted in the observation of amination and aziridination products (**Figure I-10a**); however, the putative nitrene intermediate in this chemistry was too reactive to be isolated. Introduction of sterically demanding 1,1,7,7-tetraethyl-1,2,3,5,6,7-hexahydro-3,3,5,5-tetramethyl-s-indacene groups retarded bimolecular reaction chemistry (both dimerization and solvent functionalization) and enabled the isolation and crystallization of nitrenoid **I-23** (**Figure I-10b**). The solid-state structure indicated a linear M–N–R vector and L-edge XAS studies were most consistent with formulation of **I-23** as a triplet nitrene adduct of Cu. This study highlights a common observation with steric protection of reactive sites: While this approach can provide new structural insights into specific M–L fragments, the steric encumbrance that is required to observe reactive species often precludes observation of the substrate functionalization chemistry of interest, and thus direct correlation of structure and reactivity is inhibited.

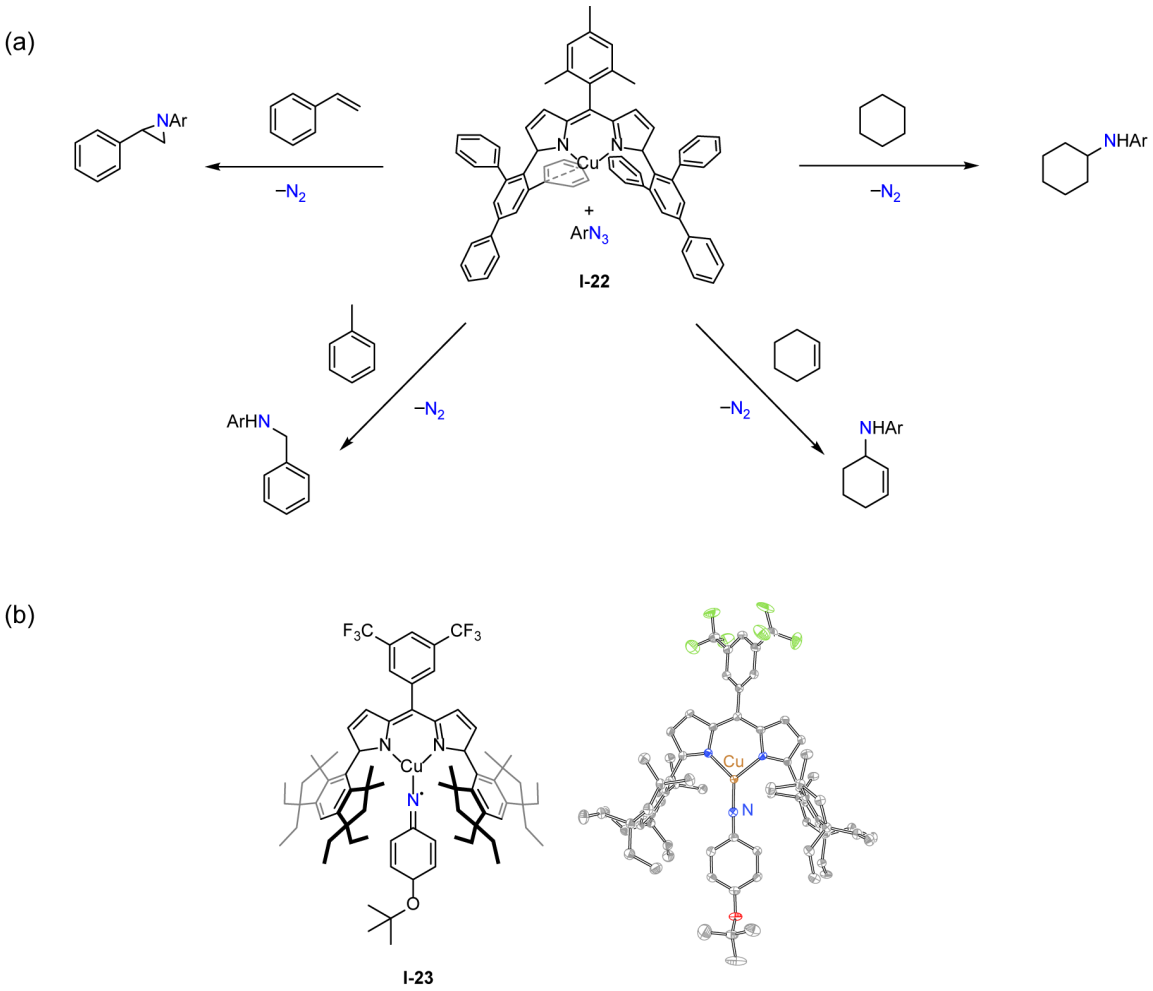

Figure I-10. Steric stabilization has enabled the crystallographic characterization of Cu(I) nitrene. (a) Dipyrrin supported Cu(I) complex **I-22** effects nitrene transfer chemistry to a variety of organic substrates. (b) Introduction of sterically demanding groups enabled isolation and characterization of nitrenoid **I-23** by inhibiting bimolecular reaction chemistry.

I.4. Spectroscopic Characterization of Transient M–NR Complexes

As described above, observation of thermally generated reactive species can be challenging due to competing reaction pathways that consume the species of interest. Numerous synthetic methods have been developed to generate M–L multiply bonded intermediates such as formation of metal nitrides from nitrosyl deoxygenation and N–N

bond cleavage from diazo complexes, generation of metal oxos by O–O bond cleavage from ozone adducts and N–O bond cleavage from nitrous oxide adducts, evolution of N_2 from diazo complexes to give metal carbenes.[51, 105-113] Coupling these synthetic approaches with either cryogenic- or stopped-flow characterization techniques can enable spectral characterization of reactive species. However, these methods are often incompatible with *in situ* crystallographic techniques, thus structural characterization is a challenge. Photochemistry represents a complementary synthetic strategy to generate reactive species and is conceptually attractive because of its feasibility to be coupled with *in situ* crystallography.

Building on the experiments described in **Figure I-3**, Gudmundsdóttir and co-workers demonstrated the utility of both cryogenic matrix isolation and time-resolved spectroscopy to directly characterize vinylnitrene **I-25** (**Figure I-11**).[114] Photolysis of **I-24** in argon (8 K) or 2-Me-THF (5 K) matrices enabled observation of a triplet nitrene (i.e., ^{3}**I-25**) by IR and EPR spectroscopies, respectively. Further irradiation of matrix-isolated samples of **I-25** led to the conversion to nitrile **I-26**. At ambient temperature, laser flash photolysis of a solution of azide **I-24** resulted in the appearance of absorption bands at 460 nm and 350 nm (τ = 22 μs), which were attributed to ^{3}**I-25** based on comparison with TD-DFT calculations, which predicted major electronic transitions at 311 nm, 364 nm and 484 nm.

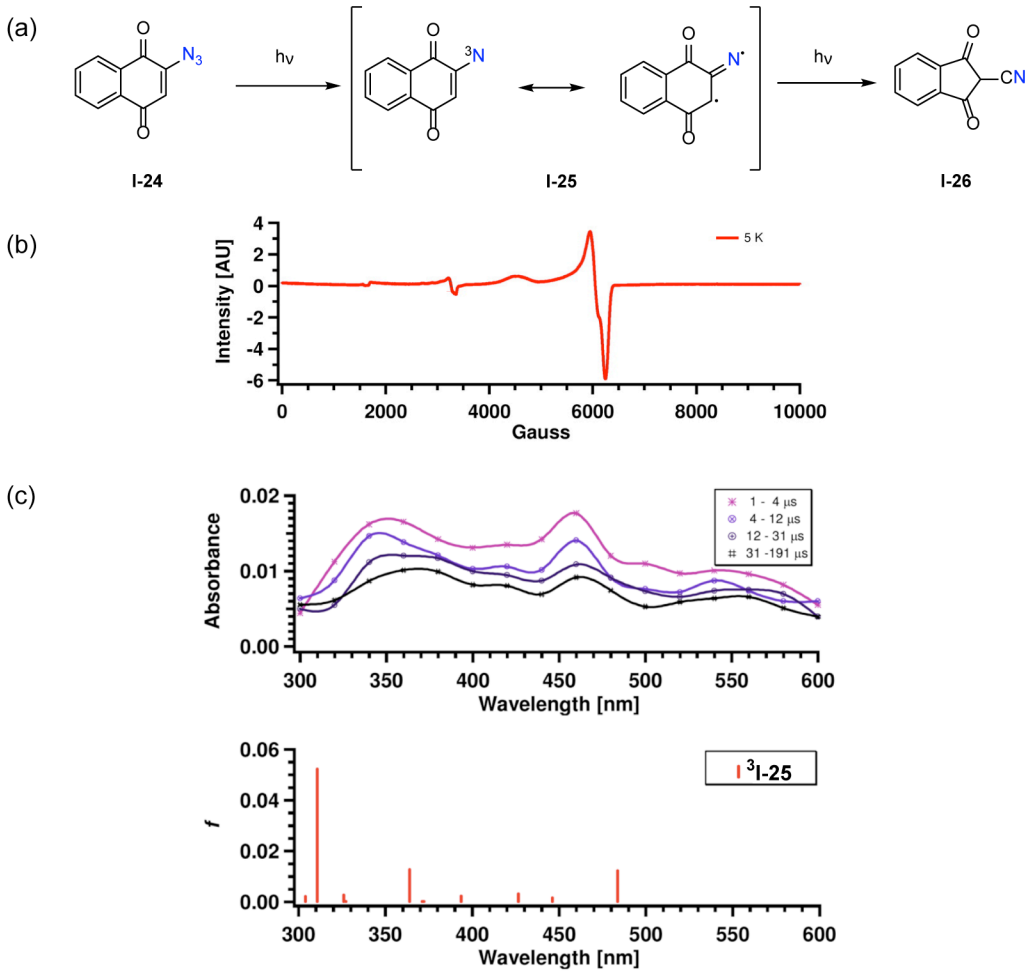

Figure I-11. Spectroscopic characterization of free nitrene using time-resolved techniques. (a) Photogeneration of vinylnitrene **I-25** from azide **I-24** facilitates characterization using a suite of time-resolved and cryogenic matrix isolation techniques. (b) Cryogenic EPR spectroscopy of ^{3}**I-25** is consistent with a triplet electronic structure. (c) Laser flash photolysis of azide **I-24** generated transient spectral features (top) that were assigned to the vinylnitrene **I-25** based on TD-DFT analysis (bottom). Figure I-11b and I-11c reprinted with permission from reference 114. Copyright 2015 American Chemical Society.

I.4.1. Time-Resolved Characterization of Transient M–L Multiply Bonded Species

Photochemical methods have also been leveraged to provide time-resolved spectral data of transient M–L multiply bonded species. Early work by Newcomb and co-

workers demonstrated application of time-resolved methods to the characterization of transient Fe- and Mn-porphyrin oxo complexes.[115-118] Laser flash photolysis of an acetonitrile solution of Mn(III) perchlorate **I-27** resulted in the appearance of a transient species that displayed an optical absorption at 432 nm (τ = 0.50 ms). The transient species was assigned as Mn(V) oxo **I-28**, which was generated by photochemical heterolysis of the O–Cl bond in Mn(III) perchlorate **I-27** (**Figure I-12a**). Similar laser flash photolysis of an acetonitrile solution of Mn(III) chlorate complex **I-29** resulted in a non-steady-state intermediate with an optical absorption at 422 nm (τ = 1.2 s), which was assigned to Mn(IV) oxo **I-30**, generated by O–Cl homolysis (**Figure I-12b**). The above structural assignments were made based on the following observations: (1) A stopped-flow UV-vis experiment in which a Mn(III) chloride complex was combined with m-chloroperbenzoic acid (m-CPBA) revealed a new feature at 430 nm; and (2) thermal decomposition of **I-30** is second order in **I-30**, which suggests that substrate functionalization proceeds via initial disproportionation of **I-30** to Mn(III) and Mn(V), with subsequent oxygen-atom transfer from Mn(V) oxo **I-28**.

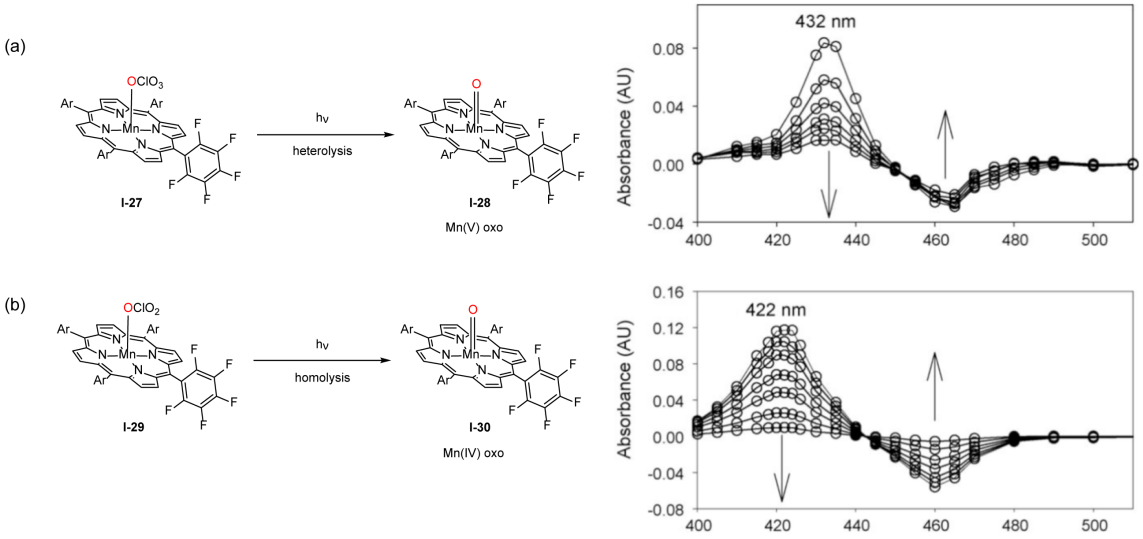

Figure I-12. Spectroscopic characterization of Mn oxo complexes using time-resolved UV-vis spectroscopy. (a) Photolysis of Mn(III) perchlorate **I-27** results in the heterolytic cleavage of O–Cl bond cleavage to generate Mn(V) oxo **I-28**, which displays λ_{max} = 432 nm. (b) Photolysis of Mn(III) chlorate **I-29** results in the homolytic cleavage of O–Cl bond cleavage to generate Mn(IV) oxo **I-30**, which displays λ_{max} = 422 nm. Reprinted with permission from reference 118. Copyright 2006 Elsevier B. V.

I.4.2. Cryogenic Matrix Isolation of Transient M–L Multiply Bonded Species

Cryogenic matrix isolation techniques, in which reactive species are trapped at low temperature in unreactive matrices, can also provide a platform to observe reactive M–L fragments. Early examples by Andrews and co-workers demonstrated that diatomic MN and triatomic $M(N)_2$ fragments, generated by laser ablation of Co, Ni, Fe, Ru and Os atoms over solid argon matrix containing N_2 at 10 K, could be observed by vibrational spectroscopy.[119-120] For example, CoN and $Co(N)_2$ were observed by IR spectroscopy following laser ablation of Co atoms over a $^{14}N_2$ matrix at 10 K.[104] The spectral assignments were aided by comparing spectral data obtained for a $^{14}N_2$ matrix with those obtained with a $^{15}N_2$ matrix.

Examples of cryogenic matrix isolation of photo-generated reactive organometallic intermediates relevant to C–H functionalization are abundant in the literature. For example, Berry and co-workers reported the synthesis and spectroscopic characterization of Ru_2 nitride **I-32** by photolysis of a frozen dichloromethane solution of Ru_2[II,III] azide **I-31** (**Figure I-13a**).[121-124] Conversion of azide **I-31** to nitride **I-32** was monitored by resonance Raman and revealed the disappearance of azide stretching band at 2058 cm^{-1} and formation of a new, isotopically sensitive band at 847 cm^{-1} that was assigned as the Ru≡N stretching mode (^{15}N substitution 822 cm^{-1}). An EPR spectrum of **I-32** displayed an axial signal ($g_\perp$ = 2.189 and g_{II} = 1.90) consistent with an S = ½, δ* ground state. Ru K-edge XAS measurement of the photolyzed sample was consistent with photooxidation from $[Ru_2]^{5+}$ to $[Ru_2]^{7+}$, and analysis of the EXAFS region indicated a Ru≡N bond length of 1.76 Å. The anomalously long Ru–N vector was interpreted as evidence for a strong structural trans effect for the distal Ru center. Consistent with labilization of the nitride by a strong kinetic trans effect, thawing of the frozen photolyzed sample afforded the Ru[II,III] amide **I-33**, the product of intramolecular C–H amination.

In the context of mononuclear systems, Meyer and co-workers reported that the photolysis of Co(II) azide complex **I-34** in a frozen 2-Me-THF matrix (77 K) resulted in the formation of Co(IV) nitride **I-35** (**Figure I-13b**).[125] The EPR spectrum of **I-35** displayed a signal at g = 2.01 with an eight-line hyperfine coupling, which is consistent with a low-spin, S = ½, d^5 Co(IV) nitride **I-35**. Thawing of the photolyzed sample led to the formation of Co(II) complex **I-36**, in which the nitride ligand inserted into the Co–carbene bond. Meyer and co-workers isolated a similar Co(III) imide supported by a *tris*-

carbene ligand scaffold and also observed insertion of the imide into a Co–C bond of the carbene ligand.[126] Relatedly, Schneider and co-workers reported the photochemical synthesis and spectroscopic characterization of Rh(IV) nitride **I-38** (**Figure I-13c**).[127] Monitoring the photolysis of a frozen toluene matrix (77 K) of Rh(II) azide **I-37** by EPR spectroscopy revealed the disappearance of **I-37** with concurrent development of a new EPR signal that was assigned as Rh(IV) nitride **I-38**. The EPR spectrum of **I-38** is similar to that previously observed for a related square planar Ir(IV) nitride.[128] Thawing the sample of **I-38** promoted nitride dimerization, which converts paramagnetic Rh(IV) nitride **I-38** to diamagnetic Rh(I) complex **I-39**.

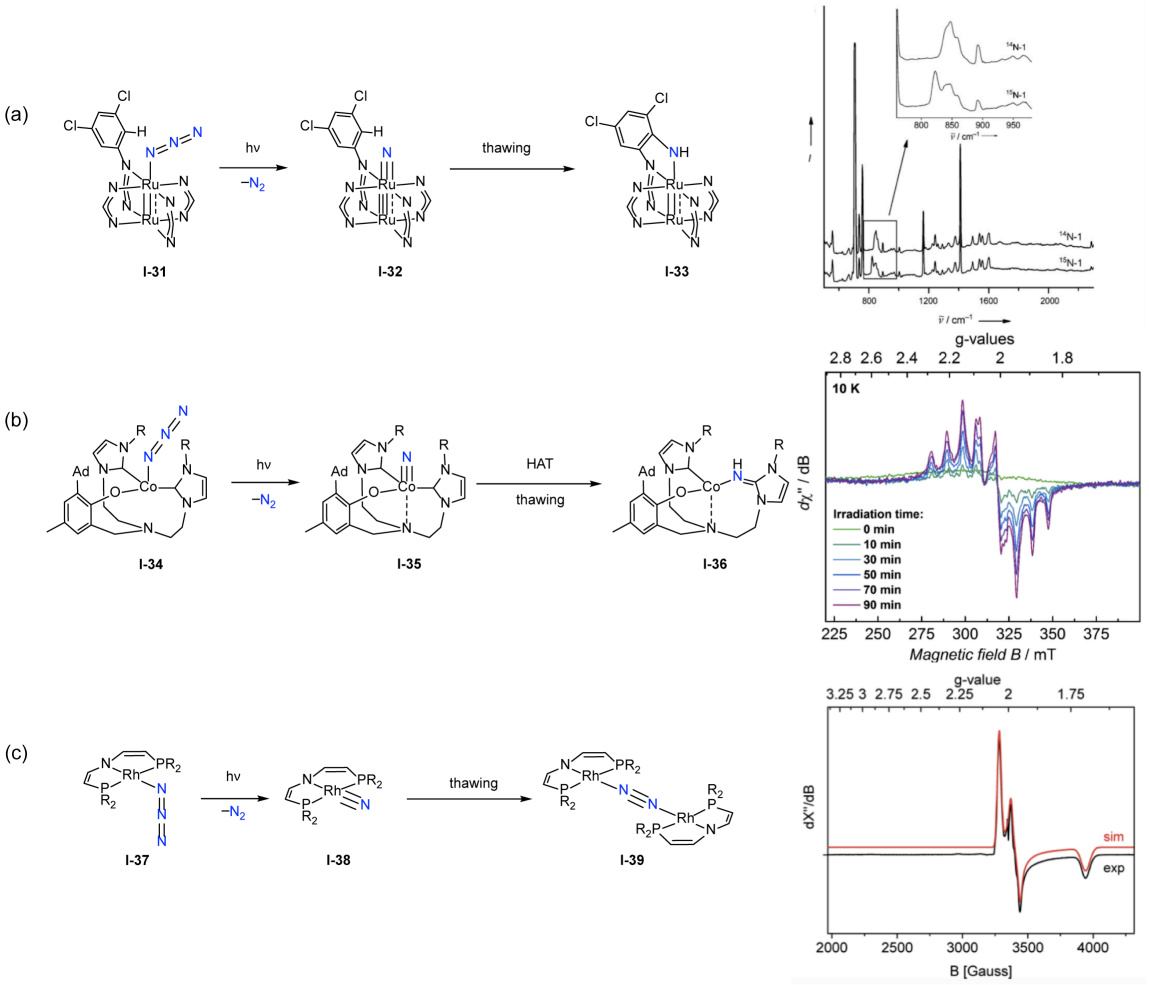

Figure I-13. Examples of cryogenic matrix isolation for the characterization of reactive metal nitrides. (a) Photolysis of Ru_2 azide **I-31** at 77 K generated Ru_2 nitride **I-32**, which was characterized by resonance Raman spectroscopy (ν(Ru≡N) at 847 cm^{-1}; Ru≡^{15}N at 822 cm^{-1}). (b) Photolysis of Co(II) azide **I-34** led to the formation of Co(IV) nitride **I-35** that was characterized by EPR spectroscopy. The EPR displayed an eight-line hyperfine coupling with g = 2.01, indicating a low-spin d^5 Co(IV) with S = ½ spin. (c) Photolysis of Rh(II) azide **I-37** generates a Rh(IV) nitride **I-38**, which was characterized by EPR spectroscopy. Figure I-13a reprinted with permission from reference 123. Copyright 2008 Wiley-VCH. Figure I-13b reprinted with permission from reference 125. Copyright 2014 American Chemical Society. Figure I-13c reprinted with permission from reference 127. Copyright 2013 American Chemical Society.

I.5. Structural Characterization via *In Crystallo* Matrix Isolation

Site isolation within a crystalline matrix provides the opportunity to simultaneously prevent many of the bimolecular pathways that can lead to decomposition of reactive species and apply diffraction-based methods for absolute structure determination. A number of examples have been disclosed in which the ordered environment of single crystalline samples has been leveraged to observe reactive coordination complexes. For example, Long and co-workers characterized an Fe–N_2O adduct relevant to the oxidation of ethane to ethanol, by powder neutron diffraction (**Figure I-14a**).[129] The powder neutron diffraction data revealed 3:2 ratio of O-bound to N-bound coordination, with Fe–N_2O distances of 2.42(3) Å (Fe–O) and 2.39(3) Å (Fe–N) respectively. Similarly, Harris and co-workers characterized O_2 adducts of Mn porphyrins, which are relevant to O_2 activation in cytochrome P450s, by confinement within the porous crystalline lattice of Mn(II) PCN-224 (**Figure I-14b**).[130] Exposure of single crystals of Mn(II) PCN-224 to O_2 resulted in the formation of a Mn–O_2 adduct. The O_2 molecule was bound side-on, in an η^2 fashion, resulting in the oxidation of the Mn center by two electrons and the formation of a Mn(IV) peroxo complex. O_2 binding was accompanied by elongation of the Mn–N bonds from 1.998(5) Å to 2.170(9) Å and the formation of a new Mn–O bond at 1.76(3) Å. Single-crystal-to-single-crystal transformations within molecular crystals have also been utilized to characterize transient coordination motifs. For example, Weller and co-workers hydrogenated a single crystal of a Rh(I) olefin complex **I-40** to generate a crystalline sample of a σ-alkane complex **I-41** (**Figure I-14c**).[131] Fujita and co-workers visualized transient hemiaminal intermediates

involved in imine condensation chemistry using *in situ* crystallography within a porous coordination network.[132] Diffusion of acetaldehyde into a network with free aromatic amines afforded the corresponding hemiaminal intermediate confined within a crystalline lattice. Thermolysis of these single crystals promoted conversion to the corresponding imine.

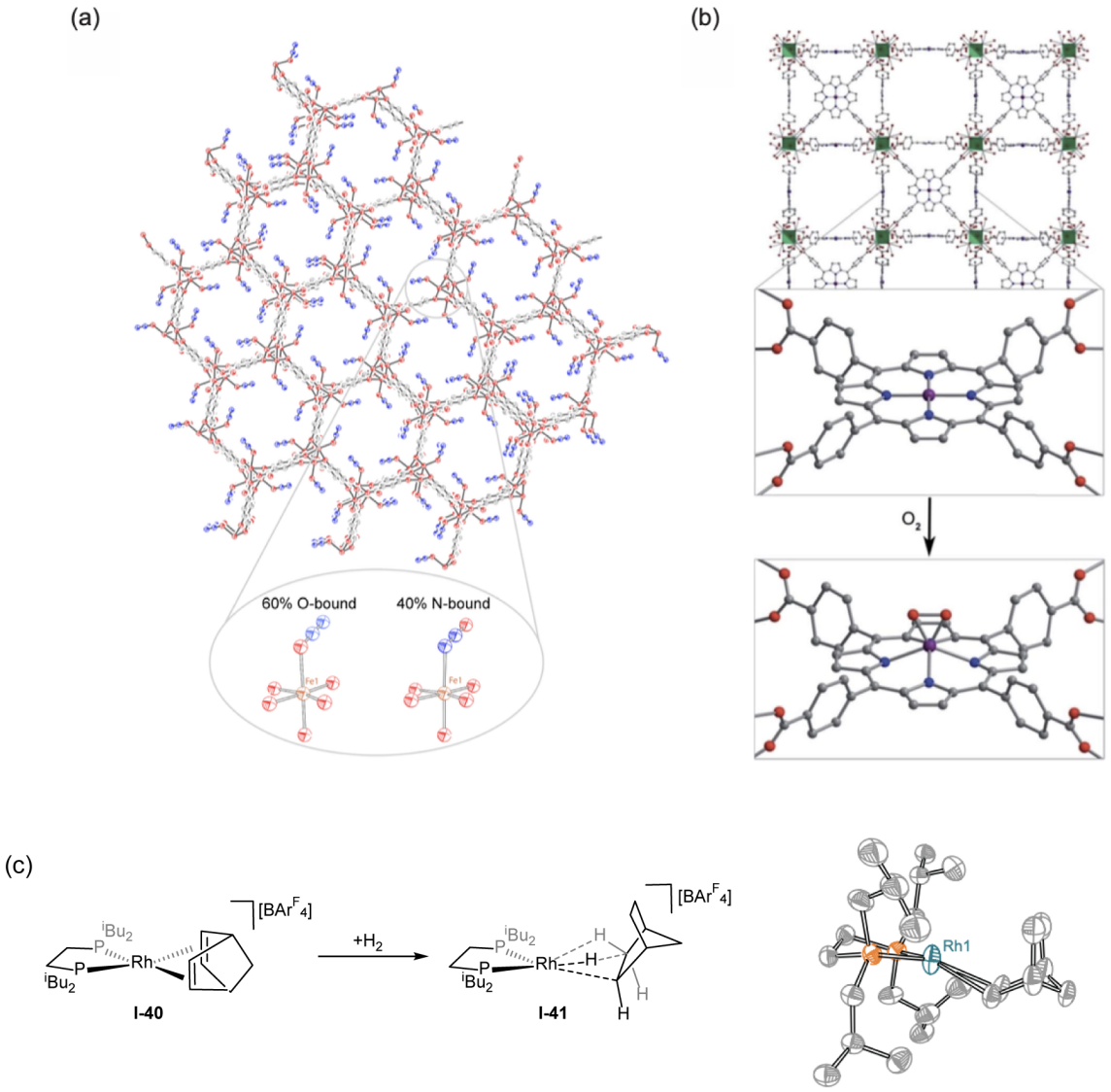

Figure I-14. Crystalline matrix isolation of metal adducts. (a) Reversible binding of N_2O with the Fe-center in Fe_2(dobdc) MOF. (b) Reversible binding of O_2 with Mn porphyrin within PCN-224 MOF. (c) *In situ* crystallography was utilized to structurally characterize a Rh(I) σ-complex **I-41** by hydrogenating a Rh(I) alkene complex **I-40** via single-crystal-to-single-crystal transformation by flowing H_2 gas. Figure I-14b reprinted with permission from reference 130. Copyright 2018 The Royal Society of Chemistry.

I.6. Photocrystallography

In previous sections, the potential for photochemistry to provide access to reactive species under conditions that were compatible with direct characterization were highlighted. Reliance on solution-phase photochemical methods to prepare reactive intermediates limits the array of tools that can be utilized to characterize the resulting compounds by preventing structural determination by crystallographic methods. Photocrystallography, which was pioneered by Coppens and Ohashi,[133-135] combines in crystallo photochemistry with X-ray diffraction experiments, to enable crystallographic characterization of photogenerated species. This experimental approach combines the attributes of cryogenic matrix isolation with solid state confinement within a regular crystal lattice to trap reactive species of interest, and enable observation by X-ray diffraction.[136-138]

Photocrystallography has been used to structurally characterize geometric and linkage isomers of coordination complexes in the solid state.[139-141] For example, Coppens utilized photocrystallography to characterize the light induced isomerism from a Ru–SO_2 **I-42** to a Ru–κ(SO)O isomer **I-43**, where both the sulfur and oxygen atom are bound to the ruthenium (**Figure I-15a**).[140] This change was marked by the elongation of the Ru–S bond length from 2.080(1) Å to 2.32(2) Å and a new Ru–O3 bond (2.19(3) Å). This isomerism was also marked by the expansion of the O3–S–O4 bond angle from 114.8(2)° to 138(3)°. Similarly, photolysis of a single crystal *cis*-Ru(NO)(NO_2) compound **I-44** resulted in isomerization of the NO binding mode to afford *cis*-Ru(ON)(ONO) **I-45** (**Figure I-15b**).[142] This change was marked by the Ru–N1 bond length of 1.769(1) Å

changing to Ru–O1 bond with a length of 1.59(2) Å. Similar changes were seen in the NO_2 moiety where the Ru–N2 bond length of 2.088(1) Å changing to a Ru–O2 bond with a length of 2.02(2) Å. Further computational and IR studies support the proposed mechanism of isomerization to go via oxygen atom transfer from the NO_2 moiety to insert into the Ru nitrosyl.

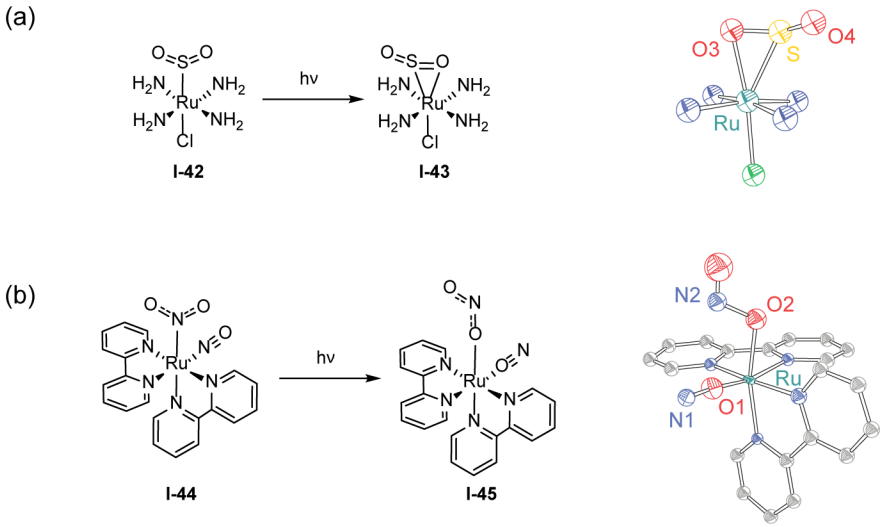

Figure I-15. Photocrystallographic characterization of linkage isomers. (a) Photolysis of a Ru–SO_2 adduct **I-42** in the crystalline state results in the formation of the Ru–κ(SO)O complex **I-43**. (b) Photolysis of the Ru(NO)(NO_2) compound **I-44** leads to formation of the linkage isomer **I-45** via oxygen atom insertion from the photo-excited η^2-(NO)O moiety into the Ru–NO bond, resulting in a Ru–ON and Ru–ONO bonds.

Photocrystallography has also been used to characterize organic radicals,[143-144] free carbenes,[145] free nitrenes,[146] and excited state species.[147-148] In 2001, Ohashi utilized photocrystallography to characterize free carbenes and nitrenes that were generated via single-crystal photoreactions.[145] Steady-state photolysis of a single crystal of diazo compound **I-46** afforded carbene **I-47** with concurrent expulsion of N_2 (**Figure I-16a**).[145]

Structure determination revealed that upon N_2 loss, the C–C–C bond angle at the carbene center (i.e., C21A–C1A–C11A) expanded from 127.1(1)° to 142(2)° and the C–C bond lengths from the carbene center (i.e., C21A–C1A and C1A–C11A) contracted from 1.477(1) Å and 1.480(1) Å to 1.437(1) Å and 1.423(2) Å, respectively. Similarly, photolysis of a single crystal of azide-containing ammonium carboxylate salt **I-48** resulted in the co-evolution of nitrene **I-49** and N_2 via a single-crystal-to-single-crystal transformation (**Figure I-16b**).[146] The resulting crystallographic data revealed that the nitrene linkage (i.e., C1R–N1R) contracted from 1.4296(1) Å to 1.34(4) Å upon N_2 extrusion. Coppens used photocrystallography to characterize nitrile imine **I-51** that was generated by photolysis of 2,5-diphenyltetrazole **I-50**. Structure determination revealed that upon N_2 loss N1–N2–C5 bond angle contracted from 122.74(2)° to 110(5)° (**Figure I-16c**).[134]

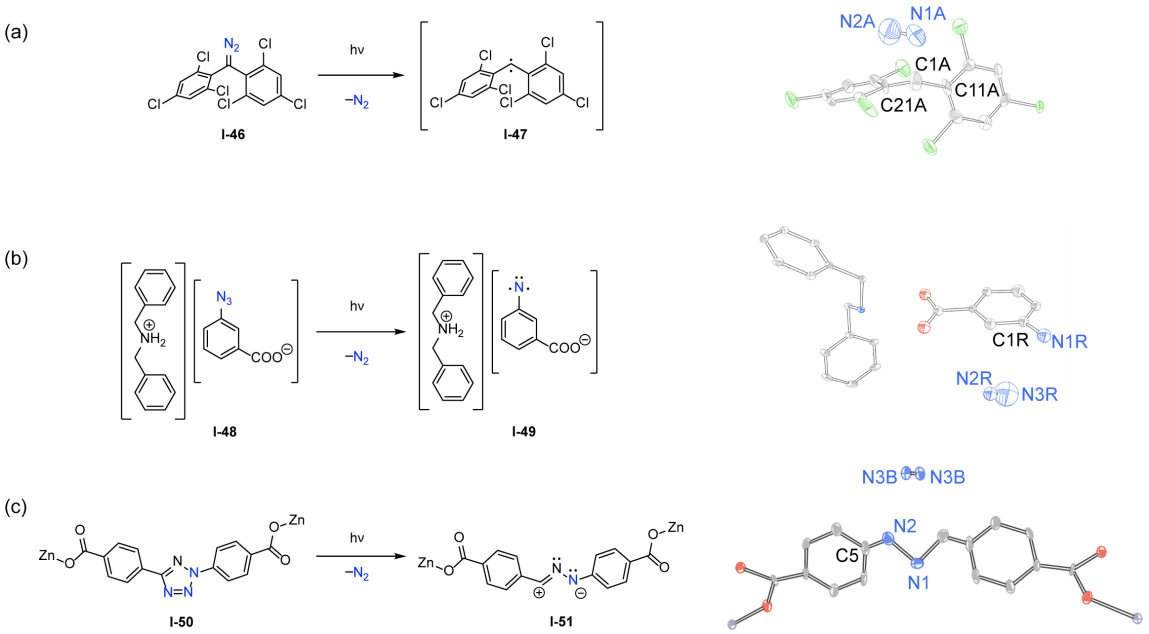

Figure I-16. Photocrystallographic characterization of unstabilized carbenes and nitrenes. (a) Photolysis of the diazo compound **I-46** in the crystalline state results in the formation of the carbene **I-47** with N_2 expulsion. (b) Photolysis of the organic azide salt **I-48** leads to formation of nitrene **I-49** along with N_2 extrusion via a single-crystal-to-single-crystal transformation. (c) Photolysis of tetrazole **I-50** within a crystalline matrix results in the formation of nitrile imine **I-51** via N_2 extrusion.

I.7. Outlook

While the innate reactivity of metal–ligand (M–L) multiply bonded complexes makes them attractive intermediates for catalysis, it also renders them as challenging synthetic targets to observe and characterize. Thus, obtaining information on these species has heavily relied on theory. This chapter reviewed strategies for the characterization of M–L multiply bonded species. A number of important strategies have been advanced to enable experimental characterization of mid- to late-metal–ligand multiply bonded species. Synthetic manipulation of the coordination geometry and ligand donicity, as well as introduction of sterically encumbering ligands, have each emerged as powerful methods

to tame the inherent reactivity of kinetically labile M–L multiple bonds. While these efforts have resulted in families of well-characterized complexes and provided critical insights regarding structure and bonding, the synthetic derivatization required to stabilize M–L fragments of interest often obviates the substrate functionalization activity relevant to catalysis. In the similar context, photochemical synthesis of reactive species provides a conceptually attractive strategy to generate reactive M–L fragments under conditions compatible with time-resolved or cryogenic steady-state characterization, and photogeneration has enabled observation of a number of reactive M–L fragments. However, the suite of tools available to characterize photogenerated reactive species is often more limited than typical for kinetically stabilized complexes and structural characterization is typically not possible.

The research in this thesis was predicated on the combination of photochemical strategies with crystallographic techniques to facilitate the structural characterization of reactive intermediates in C–H functionalization. Two outstanding challenges to this goal were: (1) the development of the necessary tool to structurally characterize transient intermediates, (2) the development of new photochemical strategy to photo-generate the reactive intermediates from stable photo-precursors under cryogenic conditions. The following chapters demonstrate photocrystallographic characterization of reactive M–L multiply bonded species and the development of new photosynthetic strategies, both of which facilitate in the characterization of reactive intermediates.

CHAPTER II

DIRECT CHARACTERIZATION OF A REACTIVE LATTICE-CONFINED DIRUTHENIUM NITRIDE BY PHOTOCRYSTALLOGRAPHY*

II.1. Introduction

Metal−oxygen (M–O) and metal−nitrogen (M–N) multiply bonded complexes are critical intermediates in synthetic and biological oxidation catalysis as well as O_2 and N_2 reduction schemes.[8, 149-153] As such, complexes featuring metal−ligand (M−L) multiple bonds are longstanding targets for chemical synthesis. High-valent early transition metals support strong M−L multiple bonds via efficient overlap of filled ligand-based π-symmetry orbitals with vacant metal-based π* orbitals. In contrast, M−L multiple bonds of mid-to-late transition metals, which feature higher d-electron counts and thus destabilizing filled π−π* interactions, tend to be reactive.[14, 28, 154] The relative reactivity of mid-to-late M−L multiply bonded complexes renders these structures attractive intermediates for catalysis but challenging species to isolate and structurally characterize. Synthetic tuning of the ancillary ligand field and metal coordination geometry has been pursued extensively to stabilize higher d-electron count M−L multiple bonds;[14, 28, 149, 154] however, the design considerations that allow isolation of these structures inevitably attenuate their reactivity.[155] We are interested in directly characterizing reactive M−L multiple bonds

* Data, figures, and text in this chapter were adapted with permission from "Direct Characterization of a Reactive Lattice-Confined Ru_2 Nitride by Photocrystallography" by Das, A.; Reibenspies, J. H.; Chen, Y.-S.; Powers, D. C. *J. Am. Chem. Soc.* **2017**, *139*, 2912–2915. Copyright 2017 American Chemical Society.

without synthetic derivatization. In this chapter, we report direct crystallographic characterization of a reactive Ru_2 nitride intermediate photogenerated within a crystalline matrix.

Reactive metal nitride complexes are potential intermediates in C−H amination and olefin aziridination reactions.[156-158] Similar to other reactive M−L multiply bonded complexes, metal nitrides that are sufficiently reactive to functionalize C−H bonds are challenging to structurally characterize because facile oxidative decomposition pathways preclude access to the requisite crystalline samples.[159-162] The challenges inherent in characterization of reactive metal nitrides are illustrated by the chemistry of Ru_2 nitride **II-3**, which was originally reported by Berry and co-workers (**Figure II-1a**).[124] Photolysis of Ru_2 azide complex **II-2**[163] at low temperature has been proposed to generate Ru_2 nitride **II-3**,[124] which upon warming functionalizes a proximal ligand-based C−H bond to generate Ru_2 amide **II-4**.[121-122] Other nitride decomposition pathways, such as insertion into ancillary M−L bonds[125, 164-165] (i.e., conversion of Co(IV) nitride **II-6** to Co(II) imine complex **II-7**,[125] (**Figure II-1b**) and bimolecular nitride coupling reactions[83, 127-128] to generate N_2 (i.e., conversion of Rh(IV) nitride **II-9** to N_2-bridged Rh_2 complex **II-10**,[127] **Figure II-1c**) are common decomposition pathways of reactive metal nitrides that can preclude crystallization. In the absence of crystallographic data, IR, EPR, electronic absorption spectroscopies and EXAFS spectral fitting have been used, in combination with high-level calculations, to assign structures for highly reactive M−L multiply bonded intermediates.[166]

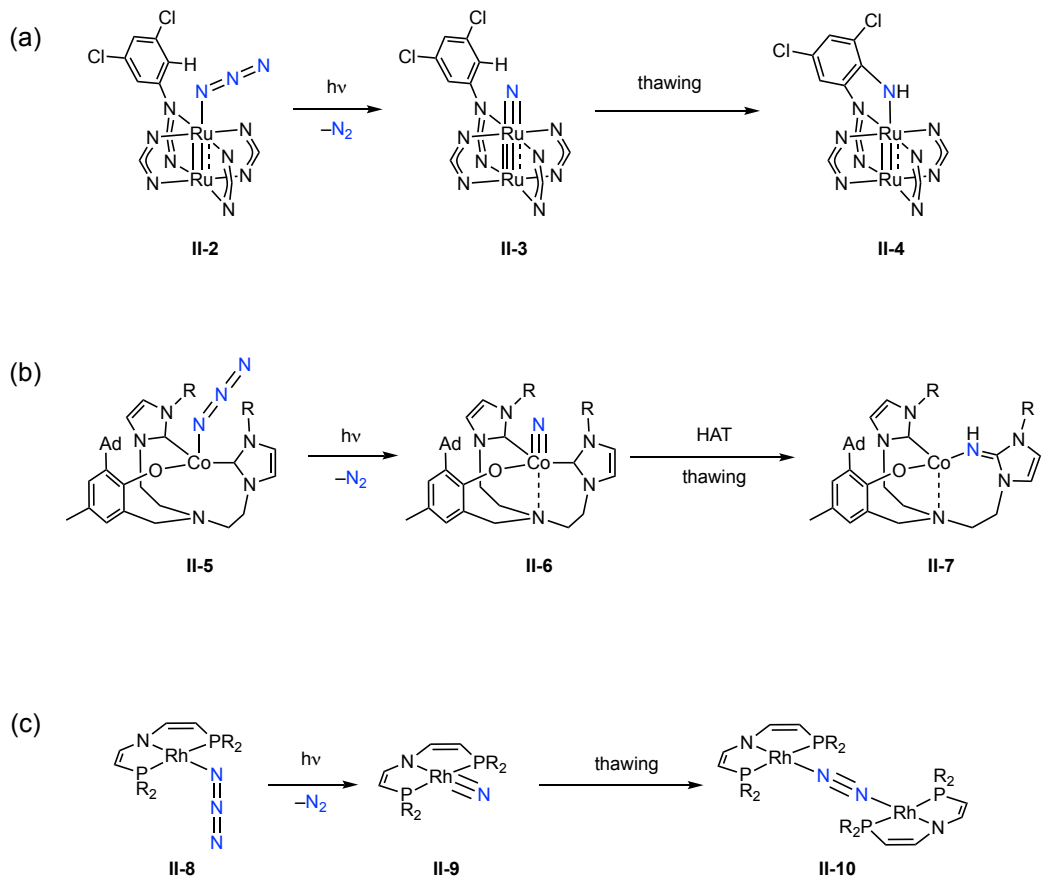

Figure II-1. Various reactivity pathways available for different metal nitrides. Reactive metal nitrides are challenging to structurally characterize because both intra- (i.e., via amination of pendant C–H bonds (**II-3** to **II-4**) or *N*-atom insertion into ancillary M–L bonds (**II-6** to **II-7**)) and intermolecular (i.e., nitride dimerization (**II-9** to **II-10**)) decomposition pathways can be facile.

We considered that direct structural characterization of highly reactive M−L multiply bonded intermediates could be achieved if the targeted structures could be generated within a crystalline matrix. For example, if a stable molecular precursor of the intermediate of interest could be converted to the reactive species without disrupting the ordered crystal lattice, X-ray diffraction techniques could be utilized to establish the structures of reactive intermediates. Such an experiment is akin to classical matrix isolation

experiments. For example, isolation of FeN,[119] RuN, and OsN[120] in both Ar and N_2 matrices has allowed characterization of these reactive fragments by vibrational spectroscopy, but traditional matrix isolation experiments do not allow the structural characterization available in crystalline samples. Coppens and Ohashi have pioneered photocrystallography, an approach for *in situ* crystallographic characterization of photochemically generated structures.[136, 138] Photocrystallography has been applied to the characterization of organic radicals,[143, 167] carbenes,[145, 168] unsaturated metal complexes,[137] metastable linkage isomers,[169-172] and molecular excited states.[139, 147, 173] Photocrystallographic experiments are challenging to apply to irreversible photoreactions and have not previously been applied to the characterization of reactive intermediates in C−H functionalization.

II.2. Results and Discussions

We targeted characterization of Ru_2 nitride **II-3** because (1) in comparison to isolable mononuclear Ru_2 nitride complexes,[174-175] it has been proposed to exhibit an anomalously long Ru−N bond due to the presence of M−M interactions,[124] (2) it is reactive toward C−H bonds at low temperature,[121-122] and (3) it has been characterized by EXAFS,[124] which allows benchmarking of our photocrystallographic results. Ru_2 azide **II-2** crystallizes in a $P2_1/c$ space group and the solid-state absorption spectrum of **II-2** is well-matched to the solution phase spectrum (**Figure II-2**). A goniometer-mounted crystal of **II-2** was irradiated with a 365 nm LED source and reaction progress was monitored in real-time by X-ray diffraction at the Advanced Photon Source (APS) housed at Argonne National Laboratory (ANL)

(**Figure II-3**). Irradiation of **II-2** leads initially to a phase transition from a $P2_1/c$ to a C2/c space group. The observed phase transition is accompanied by the linearization of the azide ligand binding mode: the Ru(1)−N(1)−N(2) bond angle expands from 152.9(5)° to 165.5(1)°. The photoinduced phase transition is not reversible if the light source is removed. Continued irradiation leads to evolution of nitride complex **II-3**, as evidenced by both the contraction of the Ru(1)−N(1) vector (2.047(6) Å to 1.72(2) Å) and the observation of a new electron density peak above the Ru_2 nitride. The electron density peak integrates as 12 e^- and was satisfactorily modeled as a molecule of N_2 (85% occupancy, see **Figure II-4** for refinement details). The N_2 molecule is located in a bowl-shaped void space that is defined by the aromatic substituents on the formamidinate ligands.

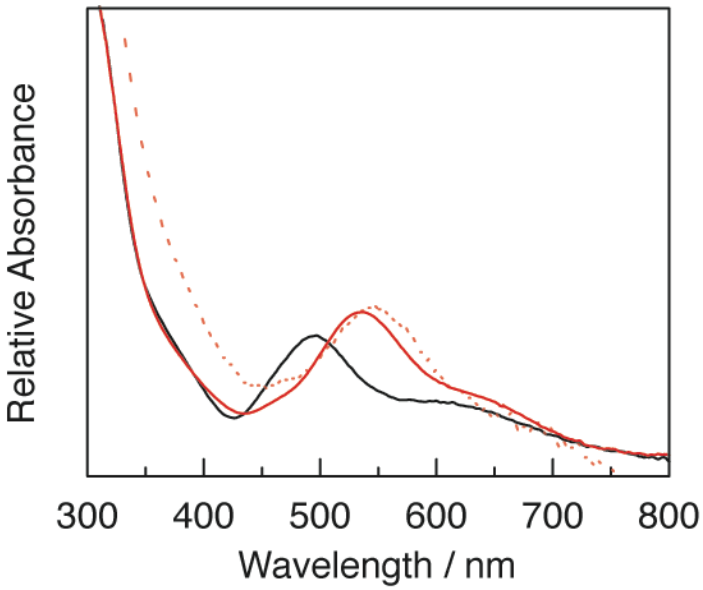

Figure II-2. Electronic absorption spectra of Ru_2 complexes II-1 and II-2. Ru_2 chloride **II-1** (—) and Ru_2 azide **II-2** (—) recorded as dilute CH_2Cl_2 solutions. Electronic absorption spectrum of Ru_2 azide **II-2** (---) recorded as a drop-cast thin film.

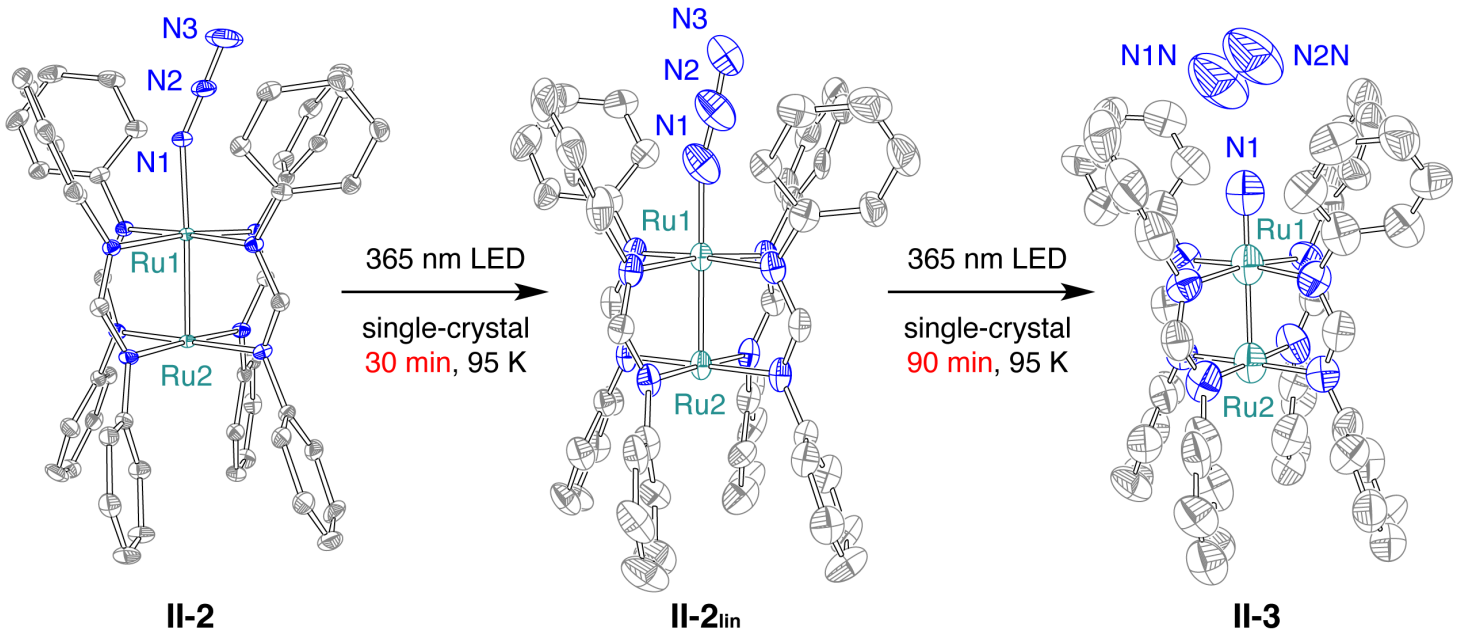

Figure II-3. Photocrystallographic characterization of reactive Ru_2 nitride II-3. Photolysis (λ = 365 nm) of a single crystal of Ru_2 azide **II-2** at 95 K results first in a phase transition ($P2_1/c$ to $C2/c$) to generate **II-2$_{lin}$**, which is promoted by photoinduced crystal heating, and subsequently in extrusion of N_2 to generate Ru_2 nitride complex **II-3**. Thermal ellipsoids are drawn at 50% probability. H- and Cl-atoms are omitted for clarity. Metrics: **II-2**, Ru(1)−Ru(2) = 2.3445(8) Å; Ru(1)−N(1) = 2.047(6) Å; Ru(1)−N(1)−N(2) = 152.9(5)°; **II-2$_{lin}$**, Ru(1)−Ru(2) = 2.373(2) Å; Ru(1)−N(1) = 2.01(1) Å; Ru(1)−N(1)−N(2) = 165.5(1)°; **II-3**, Ru(1)− Ru(2) = 2.408(3) Å; Ru(1)−N(1) = 1.72(2) Å.

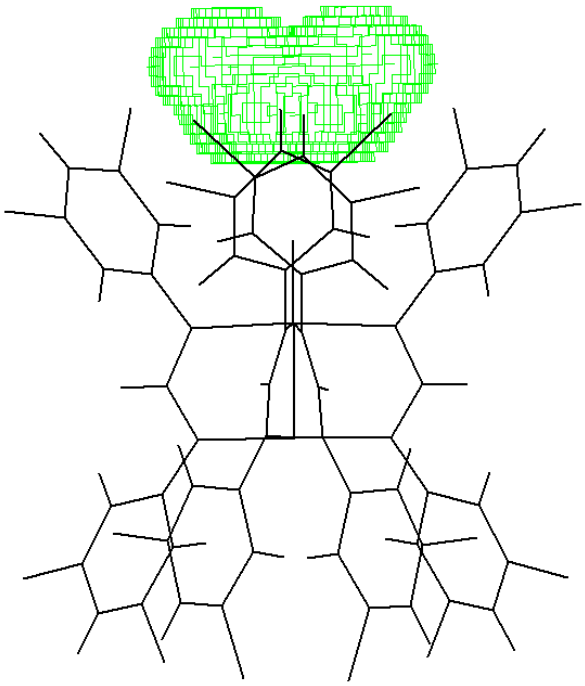

Figure II-4. SQUEEZE structure of Ru_2 nitride II-3. Application of a solvent mask to the photogenerated electron density peak above the nitride resulted in 12 e^- equivalents of unassigned density, which is approximately 85% of an N_2 molecule (SQUEEZE output above). The illustrated void generated by SQUEEZE is 45 $Å^3$, which is appropriately sized to fit a molecule of N_2 (kinetic diameter 3.7 Å;[176] volume ~27 $Å^3$). The density peak was refined as a disordered N_2 molecule. The image in Figure II-3 of the manuscript was generated by fixing the N–N distance to 1.1 Å and constraining the nitrogen ellipsoids using ISOR. The constraints were necessary to obtain a satisfactory model due to disorder of the N_2 position within the crystal cavity.

The metrical parameters of **II-3** determined by photocrystallography (Ru(1)−Ru(2) = 2.408(3) Å; Ru(1)−N(1) = 1.72(2) Å) are in good agreement with values extracted from EXAFS spectral fitting (Ru(1)−Ru(2) = 2.42 Å; Ru(1)−N(1) = 1.76 Å).[124] In addition to bond length information, photocrystallographic structure determination

provides direct measurement of bond angles, which are challenging to obtain by other experimental methods. Of note is the linearity of the Ru−Ru−N unit. Comparison of the structure of **II-3** with a refinement in a triclinic unit cell confirms that the metrical parameters are not symmetry enforced (**Table II-1**).

Table II-1. Comparison of metrical parameters for Ru_2 nitride II-3 refined with monoclinic (C2/c) and triclinic (P-1) symmetries.

	Monoclinic, C2/c	Triclinic, P-1
Ru(1)–Ru(2) / Å	2.408(3)	2.401(3)
Ru(1)–N(1) / Å	1.72(2)	1.71(2)
Ru(2)–Ru(1)–N(1) / °	180	179.7(5)

Ru_2 nitride **II-3** generated by photolysis of a solid-state powdered-crystalline sample of **II-2** is spectroscopically identical to **II-3** generated by photolysis of a frozen CH_2Cl_2 glass of **II-2**. As shown in **Figure II-5**, photolysis of **II-2**, as either a powder or as a frozen glass, results in the evolution of an axial EPR signal characteristic of the δ* ground state of nitride **II-3**.[124] Powder X-ray diffraction (PXRD) analysis of the solid-state sample confirmed that the powder used in the EPR experiment exhibits the same crystal phase as the sample utilized for photocrystallographic analysis (**Figure II-6**).

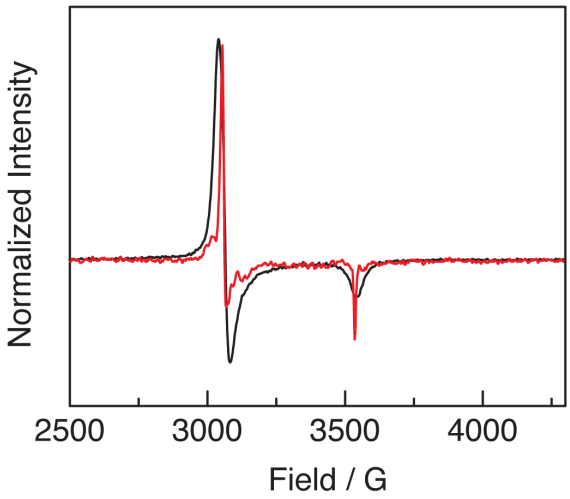

Figure II-5. X-band EPR spectra of Ru_2 nitride II-3 generated in solid and frozen solvent phase. Ru_2 nitride **II-3** generated in the solid state (powdered crystals, —) and a frozen CH_2Cl_2 glass (—) demonstrate that nitride **II-3** generated in the solid state is spectroscopically indistinguishable from that generated in a frozen glass.

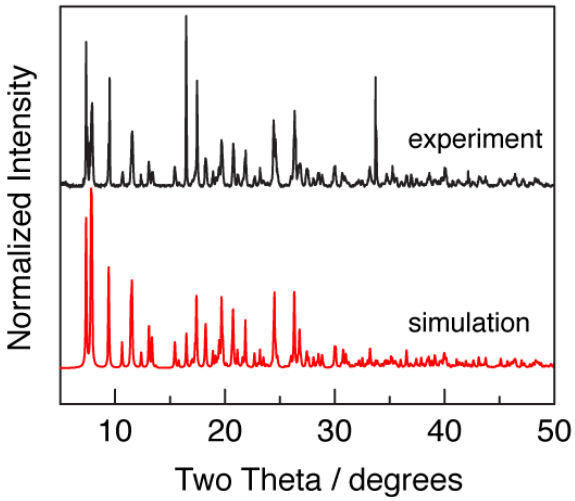

Figure II-6. Powder X-ray diffraction (PXRD) of the ground crystalline sample of Ru_2 azide II-2 used in the EPR experiment. Comparison of the predicted PXRD and the experimental pattern demonstrates that the powdered sample used for EPR measurements displays the same crystal phase as the single-crystal sample used for photocrystallographic measurements.

As described above, photolysis of Ru_2 azide **II-2** at 95 K leads first to a $P2_1/c$ to $C2/c$ phase transition that is characterized by linearization of the Ru(1)−N(1)−N(2) bond angle (**II-2$_{lin}$**), and subsequently to the evolution of nitride **II-3**. An identical phase transition is observed when photolysis is carried out at 15 K, but at this temperature we do not observe substantial formation of nitride **II-3**, even after extended photolysis. Because substantial conversion of **II-2** to **II-3** was not observed when photolysis was carried out at 15 K, examination of the structural changes associated with the observed phase transition was pursued with this lower-temperature data set. We considered two possibilities to account for the observed linearization of the azide ligand during photolysis. First, local photoinduced sample heating is common during condensed-phase photoreactions,[177] and thus the observed phase transition could be thermally promoted. Second, we considered that the phase transition may be due to evolution of a thermally trapped molecular excited state.[178] To explore the origin of the observed phase transition, variable-temperature (VT) X-ray diffraction data for Ru_2 azide **II-2** were collected between 15 and 250 K; metrical parameters and unit cell data as a function of temperature are presented in **Table II-2** and **Table II-3**. The same $P2_1/c$ to $C2/c$ phase transition that is observed at early irradiation times was observed between 150 and 200 K in the VT crystallography experiment. In addition, the Ru(1)−N(1)−N(2) bond angle is highly temperature dependent, displaying a 150.9(4)° bond angle at 15 K and 168.8(6)° bond angle at 250 K (**Figure II-7**). In contrast, the Ru−Ru distance, which is sensitive to changes in molecular spin state,[179] is invariant with temperature.

Table II-2. Evaluation of photo-induced crystal phase transfer using bond metrical parameters. Selected metrical parameters for Ru_2 azide **II-2** as a function of temperature. The Ru(1)–N(1)–N(2) angle observed during 15 K photolysis is consistent with photo-induced sample heating to ~225 K.

Temperature / K	Ru(1)–Ru(2) / Å	Ru(1)–N(1) / Å	Ru(1)–N_{eq} / Å	Ru(2)–N_{eq} / Å	Ru(1)–N(1)–N(2) / °
15	2.3429(6)	2.050(4)	2.112(4)	2.066(4)	150.9(4)
30	2.3471(5)	2.055(4)	2.114(4)	2.067(4)	151.1(3)
50	2.3465(5)	2.046(4)	2.114(4)	2.066(4)	152.1(4)
70	2.3464(4)	2.053(4)	2.115(3)	2.067(3)	152.1(3)
95	2.3445(8)	2.047(6)	2.112(5)	2.064(5)	152.9(5)
110	2.3394(2)	2.048(2)	2.107(2)	2.058(2)	153.3(2)
150	2.3397(3)	2.045(2)	2.108(2)	2.057(2)	156.9(2)
200	2.3384(3)	2.021(3)	2.107(2)	2.057(2)	168.7(5)
250	2.3400(6)	2.018(4)	2.104(3)	2.054(3)	168.8(6)
300[i]	2.3472(5)	2.042(4)	2.111(2)	2.059(2)	---
Photolysis of **II-2** at 15 K	2.373(2)	2.01(1)	2.120(8)	2.065(9)	165.5(1)

[i]In the original report, the azide was refined as a bent structure, and thus the Ru(1)–N(1)–N(2) angle cannot be compared to our refinement.[163]

Table II-3. Evaluation of photo-induced crystal phase transfer using unit cell parameters. Unit cell parameters of Ru_2 azide **II-2** as a function of temperature. The unit cell volume observed during 15 K photolysis is consistent with photo-induced sample heating to ~225 K.

Temperature / K	a / Å	b / Å	c / Å	α / °	β / °	γ / °	Volume / Å^3
15	27.202(2)	14.105(1)	18.651(1)	90	124.312(1)	90	5911.1(8)
30	27.233(2)	14.1493(9)	18.660(1)	90	124.281(1)	90	5941.0(6)
50	27.254(2)	14.1552(9)	18.673(1)	90	124.336(1)	90	5948.4(6)
70	27.278(1)	14.1598(6)	18.6973(7)	90	124.394(1)	90	5959.4(4)
95	27.278(2)	14.139(1)	18.703(1)	90	124.476(1)	90	5946.5(8)
110	27.264(1)	14.1358(8)	18.702(1)	90	124.585(1)	90	5934.2(6)
150	27.334(1)	14.163(7)	18.761(9)	90	124.773(1)	90	5966.1(5)
200	27.396(1)	14.1974(6)	18.854(2)	90	125.054(1)	90	6003.3(6)
250	27.512(5)	14.209(3)	18.943(4)	90	125.318(4)	90	6042.3(2)
300[ii]	27.676(3)	14.253(2)	19.044(2)	90	125.424(2)	90	6122(1)
Photolysis of **II-2** at 15 K	26.951(4)	14.350(2)	18.720(3)	90	124.381(3)	90	5975.1(2)

[ii]In the original report, the azide was refined as a bent structure.[163]

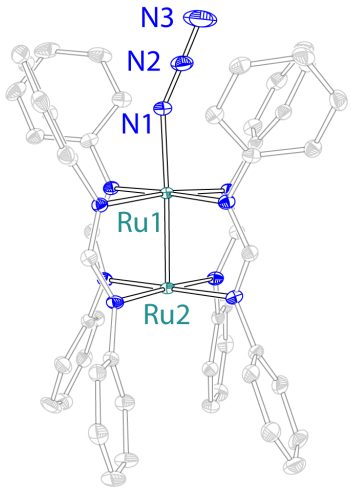

Temp / K	Ru1–N1–N2 / °
15	150.9 (4)
30	151.1 (3)
50	152.1 (4)
95	152.9 (5)
150	156.9 (2)
200	168.7 (5)
250	168.8 (6)
Irradiated at 15 K	165.5 (2)

Figure II-7. Temperature dependence of the Ru(1)−N(1)−N(2) bond angle in Ru_2 azide II-2. Linearization of this angle upon photolysis at 15 K is consistent with photo-induced heating of the sample.

The size of thermal ellipsoids of atoms that are not involved in the primary photoreaction can be used as an *in situ* probe of the effective temperature of crystalline samples.[177] Comparison with the thermal ellipsoids of a crystal photolyzed at 15 K with the thermal ellipsoid obtained from VT crystallography reveals that photoinduced heating renders the effective sample temperature closer to 200 K, which is in good agreement with the measured linearization of the azide ligand (data collected in **Figure II-8**). Together, these data suggest that the phase transition that precedes nitride evolution is driven by photoinduced crystal heating. Similar analysis indicates that the effective sample temperature during 95 K irradiation is approximately 350 K (**Figure II-9**).

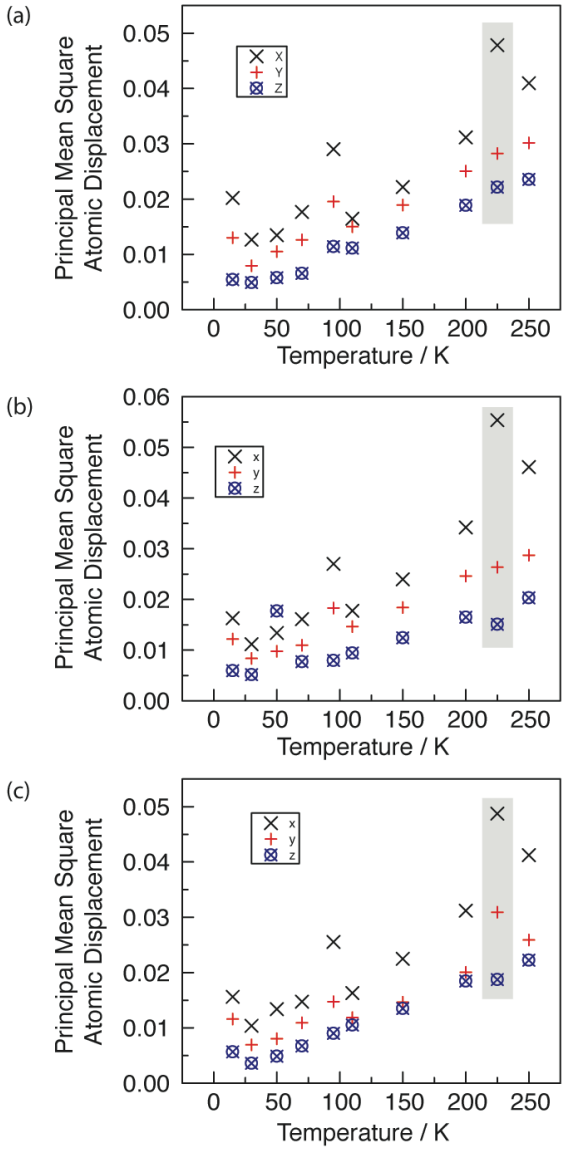

Figure II-8. Comparison of average principal mean square atomic displacements (U) for Ru_2 azide II-2 as a function of temperature with 15 K photolysis. Data plotted for (a) the central carbon atoms of the bridging formamidinate ligands, (b) the formamidinate nitrogen atoms bound to Ru(II), and (c) the formamidinate nitrogen atoms bound to Ru(III). Thermal parameters obtained during photocrystallography at 15 K are highlighted in the gray box for each plot. Apparent photo-induced crystal heating of a 15 K crystal to approximately 225 K is indicated from these data.[177]

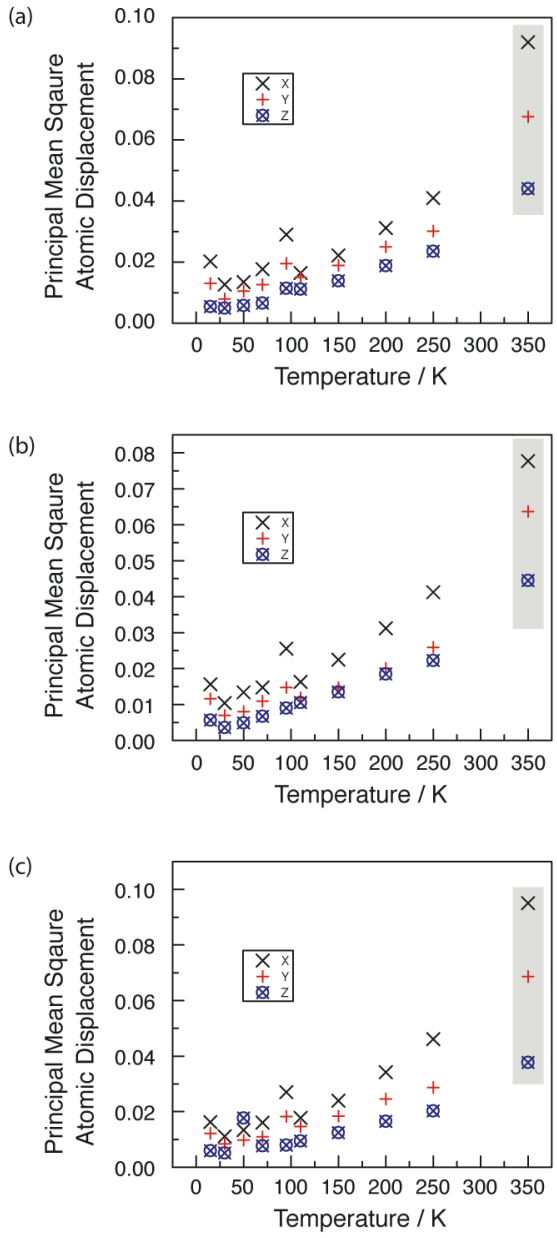

Figure II-9. Comparison of average principal mean square atomic displacements (U) for Ru_2 azide II-2 as a function of temperature with 95 K photolysis. Data plotted for (a) the central carbon atoms of the bridging formamidinate ligands, (b) the formamidinate nitrogen atoms bound to Ru(II), and (c) the formamidinate nitrogen atoms bound to Ru(III). Thermal parameters obtained from Ru_2 nitride **II-3** during photocrystallography at 95 K are highlighted in the gray box for each plot. Apparent photoinduced crystal heating of a 95 K crystal to approximately 350 K is indicated from these data.[177]

We further confirmed that the phase transition observed crystallographically is not due to a change in electronic structure by photolyzing both solution-phase and powdered samples of **II-2** in the cavity of an EPR spectrometer maintained at 15 K. No signals were observed other than those attributable to azide **II-2** and a minor amount of **II-3** (**Figure II-10**). After photolysis at 15 K, the sample was warmed to 95 K in the dark and no evolution of the EPR spectrum was observed. Taken with the VT X-ray diffraction data, these experiments suggest that photoinduced crystal heating is responsible for the linearization of the azide ligand prior to evolution of nitride **II-3**. Attempts to observe conversion of lattice-confined nitride **II-3** to amido complex **II-4** were unsuccessful. Consistent with experimentally determined activation parameters,[121-122] C−H insertion does not proceed at 95 K. Slow warming of crystalline samples of **II-3** to 200 K led to sample cracking, manifest as diminished diffraction intensity and quality, which precluded observation of C−H functionalization. We speculate that the observed sample cracking may be due to diffusion of lattice-bound N_2 at higher temperature.

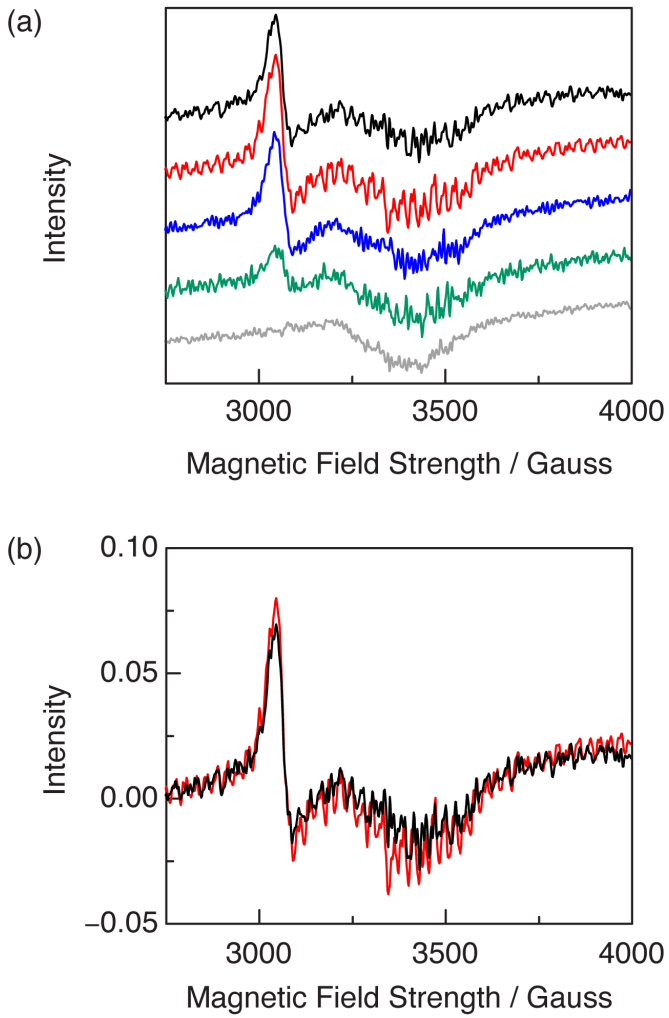

Figure II-10. *In situ* X-band EPR of Ru_2 nitride complex II-3. (a) EPR spectra obtained by photolysis of a powdered sample of **II-2** inside the EPR cavity. Spectra were obtained of Ru_2 azide **II-2** at 15 K (—), after 1.25 h photolysis at 15 K (—), after 4.25 h photolysis at 15 K (—), after 4.25 h photolysis at 15 K with the light source turned off (—), and after 4.25 h photolysis at 15 K and then warming to 95 K with the light source turned off (—). Spectra display signals attributable only to Ru_2 azide **II-2** and Ru_2 nitride **II-3**. (b) Overlay of the spectra obtained after 4.25 h photolysis at 15 K with the light source turned off (—), and after 4.25 h photolysis at 95 K with the light source turned off (—), which demonstrate that no spectral evolution is observed upon warming the low temperature photolysis reaction mixture.

II.3. Conclusion

The results reported in this chapter demonstrate photocrystallography to be a viable approach to investigating directly the structures of highly reactive M−L multiply bonded intermediates relevant to C−H amination. The success of these experiments, which do not require synthetic stabilization of the reactive fragment of interest, are likely due to a combination of low-temperature photogeneration of the targeted reactive intermediates and lattice confinement of those structures, which restricts motions of reactive intermediates. Experimental definition of metrical parameters is critical to rigorous correlation of structure, reactivity, and electronic structure. We anticipate that photocrystallography will contribute to these efforts and may find application as a tool for the direct structure elucidation of additional reactive intermediates.

II.4. Experimental Details

II.4.1. General Considerations

Materials All reactions were carried out under an ambient atmosphere unless otherwise noted. Anhydrous tetrahydrofuran (THF) was obtained from a drying column and stored over activated 4 Å molecular sieves.[180] All other solvents were ACS reagent grade and were used as received. Thin layer chromatography (TLC) was carried out with aluminum-backed silica gel plates coated with a fluorescent indicator (F_{254}) acquired from EMD Millipore. Triethyl amine (NEt_3) and glacial acetic acid (AcOH) were purchased from Fisher Scientific, lithium chloride (LiCl) and 3,5-dichloroaniline were purchased

from Alfa Aesar, triethyl orthoformate, acetic anhydride (Ac_2O), and silica gel (0.060–0.200 mm, 60 Å for column chromatography) were obtained from Acros Organics, and $RuCl_3 \cdot \times H_2O$ was purchased from Strem Chemicals. O_2 (99.6%) was purchased from Conroe Welding Supply. All reagents were used as received. NMR solvents were purchased from Cambridge Isotope Laboratories and were used as received.

Characterization Details NMR spectra were recorded on Inova 500 FT NMR operating at 499.53 MHz for ^1H acquisitions and 125.62 MHz for ^{13}C acquisitions and were referenced against solvent signals: $CDCl_3$ (7.26 ppm, ^1H; 77.16 ppm, ^{13}C) and D_2O (4.79 ppm, ^1H).[181] ^1H NMR data are reported as follows: chemical shift (δ, ppm), (multiplicity: s (singlet), d (doublet), t (triplet), m (multiplet), br (broad), integration). ^{13}C NMR data are reported as follows: chemical shift (δ, ppm). UV-vis spectra were recorded at 293 K in quartz cuvettes on an Ocean Optics Flame-S miniature spectrometer with DH-mini UV-vis NIR light source and were blanked against the appropriate solvent. Solid-state UV-vis spectra were recorded using drop-cast thin films on glass slides and were blanked against the glass slide. IR spectra were recorded on a Shimadzu FTIR/IRAffinity-1 spectrometer. Spectra were blanked against air and were determined as the average of 64 scans. IR data are reported as follows: wavenumber (cm-1), (peak intensity: s, strong; m, medium; w, weak). Powder X-ray diffraction (PXRD) measurements were carried out on a Bruker D8 Advance Eco X-ray diffractometer (Cu Kα, 1.5418 Å; 40 kV, 25 mA) fitted with LynxEye detector. The angular range was measured from 5.00 to 49.99º (2θ) with steps of 0.020º and a measurement time of 4.8 s per step. Simulated PXRD patterns were generated from the appropriate .cif using the Mercury 3.7 software package.

X-Ray Crystallography Details Variable-temperature (VT) X-ray diffraction data were collected using either 1) synchrotron radiation (0.41328 Å; ChemMatCARS located at the Advanced Photon Source (APS) housed at Argonne National Laboratory (ANL)) on a vertically mounted Bruker D8 three-circle platform goniometer equipped with an Apex II CCD and an Oxford Diffraction Helijet operating between 15–70 K, 2) synchrotron radiation (0.82656 Å; ChemMatCARS located at the APS housed at ANL) on a vertically mounted Bruker D8 three-circle platform goniometer equipped with an Apex II CCD and an Cryojet N_2 cold stream operating at 95 K, or 3) radiation from a graphite fine focus sealed tube Mo Kα (0.71073 Å) source on a Bruker three-circle platform goniometer equipped with an Apex II CCD and an Oxford cryostream cooling device operating between 110–250 K. For data collected between 15–95 K, crystals were mounted on a glass fiber pin using Paratone N oil and for data collected at or above 110 K, crystals were mounted on MiTeGen loops. Data were collected as a series of φ and/or ω scans, were integrated using SAINT, and were scaled with a multi-scan absorption correction using SADABS.[182] Structures were solved by intrinsic phasing using SHELXT (Apex2 program suite v2014.1) and refined against F^2 on all data by full matrix least squares with SHELXL-97.[183-184] All non-hydrogen atoms were refined anisotropically. H atoms were placed at idealized positions and refined using a riding model. VT X-ray data for Ru_2 azide **II-2** are summarized in **Tables II-2**, **Table II-3** and **Figure II-8**. Photocrystallographic data were collected using synchrotron radiation (0.41328 Å or 0.82656 Å) at ChemMatCARS located at the APS housed at ANL. Photocrystallographic data were collected at either 15 K (Oxford Diffraction Helijet) or 95 K (Cryojet N_2 cold

stream) using a vertically mounted Bruker D8 three-circle platform goniometer equipped with an Apex II CCD. Illumination was provided by a Thor Labs 365 nm LED (M365L2) and was delivered to the sample via a 100 μm ID fiber optic. Light intensity was measured with a power meter to be 2 mW at the crystal mount and the spot size of the fiber-delivered light was ~100 μm in diameter. Data were collected as a series of φ and/or ω scans. Data were integrated using SAINT and scaled with a multi-scan absorption correction using SADABS. Structures were solved by intrinsic phasing using SHELXT (Apex2 program suite v2014.1) and refined against F^2 on all data by full matrix least squares with SHELXL-97.[183-184] All non-hydrogen atoms were refined anisotropically. H atoms were placed at idealized positions and refined using a riding model.

***In Situ* EPR Details** EPR spectra were recorded at X-band on a Bruker ELEXSYS Spectrometer with a Cryogen-Free In-Cavity temperature control system. EPR spectra of photogenerated reactive intermediates were collected in two ways: 1) irradiation (75 W Xe lamp) of samples in an N_2-cooled (77 K) quartz finger dewar (Wilmad Glass, WG-819-B-Q) and subsequent transfer of the cold samples into a pre-cooled EPR cavity, and 2) irradiation of samples inside a precooled EPR cavity. *In situ* photolysis was accomplished using a 365 nm LED source (ThorLabs M365FP1, ThorLabs KPS101 (power supply), ThorLabs LEDD1B (power modulator)) delivered to the EPR cavity via fiber optic (ThorLabs M200L025-UV), a collimator (ThorLabs F671SMA-405), and a home-built window assembly to center the irradiation on the sample.

II.4.2. Synthesis and Characterization

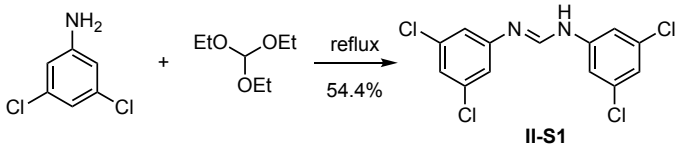

II-S1

Synthesis of N,N'-bis(3,5-dichlorophenyl)formamidine (II-S1) N,N'-bis(3,5-dichlorophenyl)formamidine (**II-S1**) was prepared according to literature methods.[185] A round-bottom flask was charged with 3,5-dichloroaniline (16.2 g, 100 mmol, 2.02 equiv.) and triethyl orthoformate (7.33 g, 49.5 mmol, 1.00 equiv.). The reaction mixture was heated at reflux (~140 °C) for 12 h. The reaction mixture was allowed to cool to 23 °C and was then filtered through a glass frit. The collected solid was washed thoroughly with hexanes and dried *in vacuo* to afford the title compound as a colorless powder (8.99 g, 54.4% yield). ^{1}H NMR (δ, 23 °C, $CDCl_3$): 8.06 (s, 1H), 7.11 (s, 2H), 6.96 (s, 4H), 1.69 (br s, 1H). ^{13}C NMR (δ, 23 °C, $CDCl_3$): 148.69, 135.89, 124.08, 117.89. The recorded ^{1}H and ^{13}C NMR spectra are shown in **Figure II-11** and **Figure II-12**, respectively.

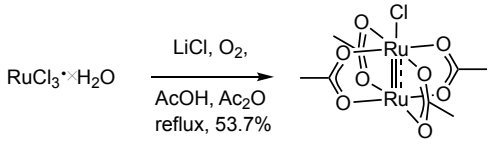

II-S2

Synthesis of $Ru_2(OAc)_4Cl$ (II-S2) $Ru_2(OAc)_4Cl$ (**II-S2**) was prepared according to literature methods.[186] A round-bottom flask was charged with $RuCl_3 \cdot \times H_2O$ (0.506 g, 2.44 mmol, 1.00 equiv.) and anhydrous LiCl (0.529 g, 12.5 mmol, 5.12 equiv.). A mixture of glacial acetic acid (18.0 mL) and acetic anhydride (4.0 mL) was added to the flask and the resulting solution was heated at reflux (~125 °C) for 5 h under a slow stream of O_2. The

reaction mixture was cooled to 10 °C for 12 h at which time a red-brown precipitate was observed. The precipitate was collected on frit and washed with MeOH and Et_2O and dried *in vacuo* to afford the title compound as a red-brown powder (0.310 g, 53.6% yield). ^{1}H NMR (δ, 23 °C, D_2O): – 45.98 (s, 12H). IR (cm^{-1}): 2933 (w), 1441 (s), 1394 (s), 1384 (m), 1042 (m), 1014 (w), 944 (w), 689 (s), 630 (m). The recorded ^{1}H NMR spectrum is shown in **Figure II-13**.

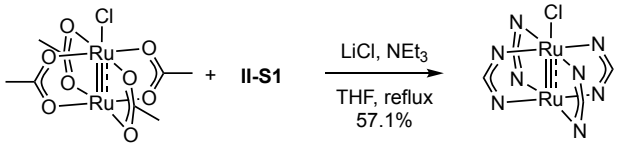

II-1

Synthesis of Ru_2(3,5-Cl_2form)$_4$Cl (II-1) Complex **II-1** was prepared according to literature methods.[187] A Schlenk flask was charged with **II-S2** (0.151 g, 0.318 mmol, 1.00 equiv.), **II-S1** (0.696 g, 2.08 mmol, 6.54 equiv.), LiCl (0.352 g, 8.30 mmol, 26.1 equiv.), NEt_3 (~1 mL), and THF (25.0 mL). The headspace was briefly evacuated and the flask was refilled with an atmosphere of N_2. The reaction mixture was heated to 90 °C for 48 h under an N_2-atmosphere. The reaction mixture was cooled to 23 °C. Open to ambient atmosphere, the reaction mixture was filtered through a glass frit to remove excess LiCl. Solvent was removed *in vacuo* and the residue was purified on a silica gel column with hexanes/EtOAc as a linear gradient eluent system (v/v: 98/2 to 95/5). The solvent was removed to afford the title complex as a dark purple powder (0.285 g, 57.1% yield). R_f = 0.55 (95/5 hexanes/EtOAc). ^{1}H NMR (δ, 23 °C, $CDCl_3$) 6.47 (br s, 2H), 0.85 (s, 1H), – 11.74 (s, 1H), –21.38 (br s, 2H), –36.56 (br s, 1H). UV-vis (CH_2Cl_2), λ_{max} (nm, ε (M^{-1} cm^{-}

^{1})): 496 (7.7 × 10^{3}), 599 (4.2 × 10^{3}). IR (cm^{-1}): 2979 (w), 1582 (m), 1563 (s), 1524 (s), 1426 (s), 1327 (m), 1214 (m), 1108 (m), 995 (s), 933 (s), 848 (s), 800 (s), 727 (m), 677 (m). The recorded ^{1}H NMR spectrum is shown in **Figure II-14**.

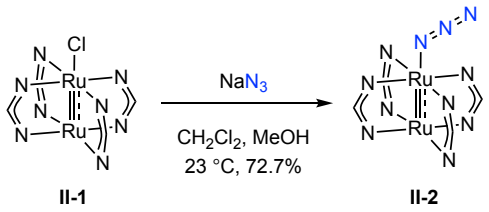

II-1 **II-2**

Synthesis of Ru_2(3,5-Cl_2form)$_4N_3$ (II-2) Complex **II-2** was prepared according to literature methods.[163] A round-bottom flask was charged with complex **II-1** (0.100 g, 0.064 mmol, 1.00 equiv.) and NaN_3 (2.13 g, 32.8 mmol, 512 equiv.). The reaction vessel was wrapped in aluminum foil to exclude ambient light. CH_2Cl_2 (25.0 mL) and MeOH (2.0 mL) were added to the flask and the reaction mixture was allowed to stir in dark for 72 h. The mixture was then filtered to remove excess NaN_3. The filtrate was concentrated *in vacuo*. The residue was purified on a silica gel column with hexanes/CH_2Cl_2 as a linear gradient eluent system (v/v: 98/2 to 60/40) to afford the title complex as a purple powder (0.0730 g, 72.4% yield). Single crystals were obtained by layering a CH_2Cl_2 solution with equal volume of ethanol. ^{1}H NMR (δ, 23 °C, $CDCl_3$): 1.26 (s, 2H), 0.89 (s, 1H), –1.16 (s, 1H), –11.59 (s, 1H), –20.84 (br s, 1H), –34.86 (br s, 1H). UV-vis (CH_2Cl_2), λ_{max} (nm, ε (M^{-1} cm^{-1})): 536 (8.9 × 10^{3}), 641 (3.9 × 10^{3}). IR (cm^{-1}): 2923 (m), 2981 (m), 2034 (m), 1582 (m), 1563 (s), 1524 (s), 1416 (m), 1330 (m), 1214 (m), 1094 (m), 994 (m), 932 (m), 848 (m), 799 (m), 726 (m), 675 (m). The recorded ^{1}H NMR spectrum is shown in Figure **II-15**.

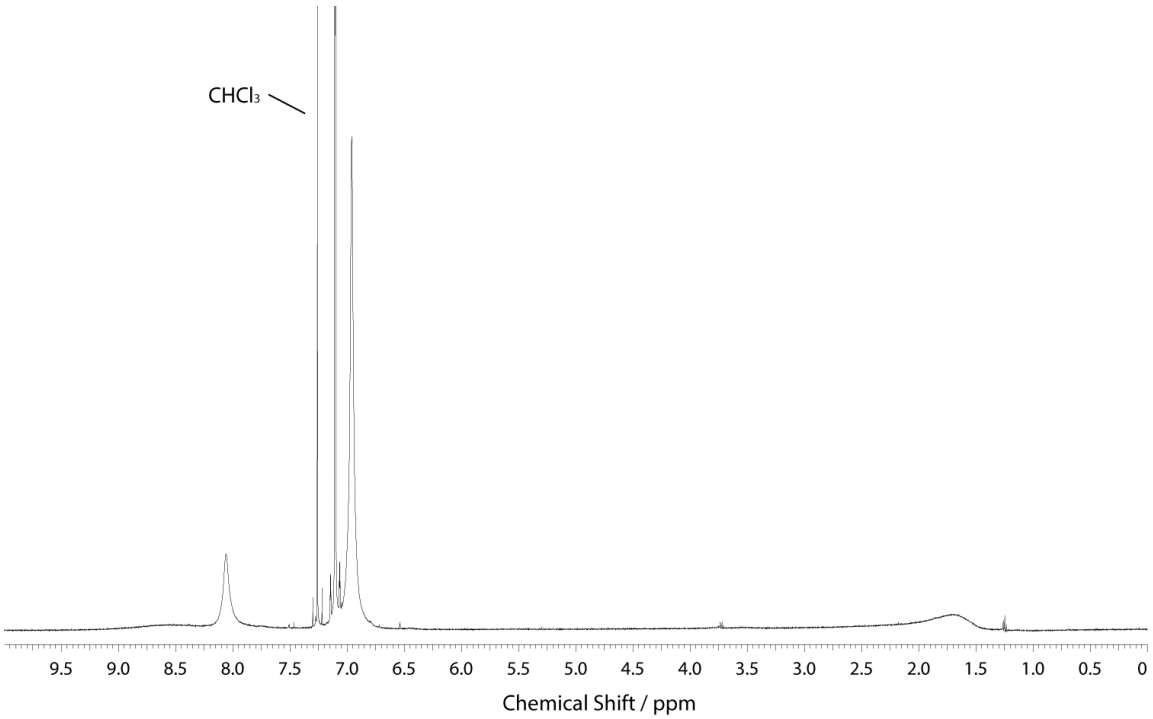

Figure II-11. ^{1}H NMR spectrum of II-S1 recorded in $CDCl_3$ at 23 °C.

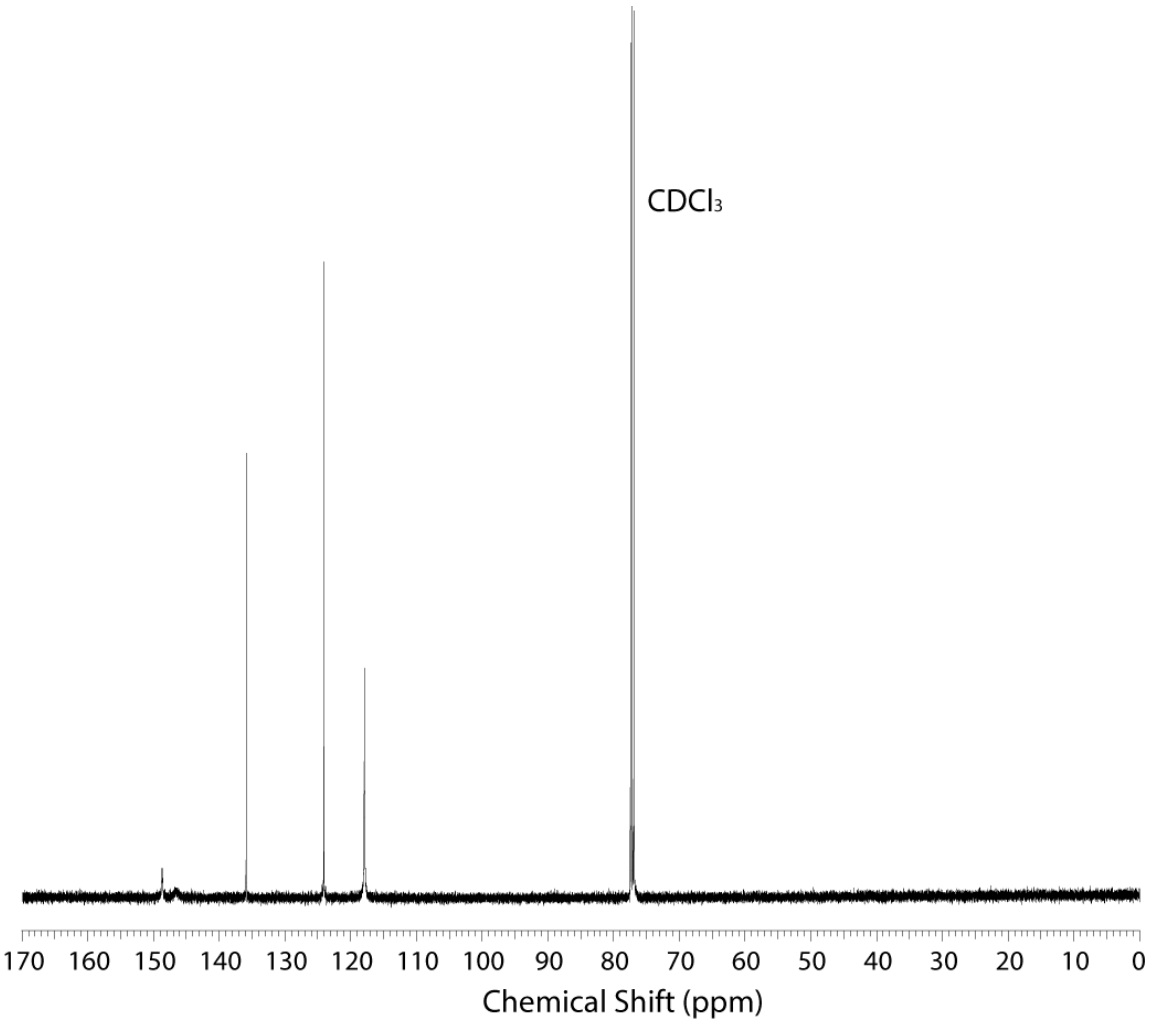

Figure II-12. ^{13}C NMR spectrum of II-S1 recorded in $CDCl_3$ at 23 °C.

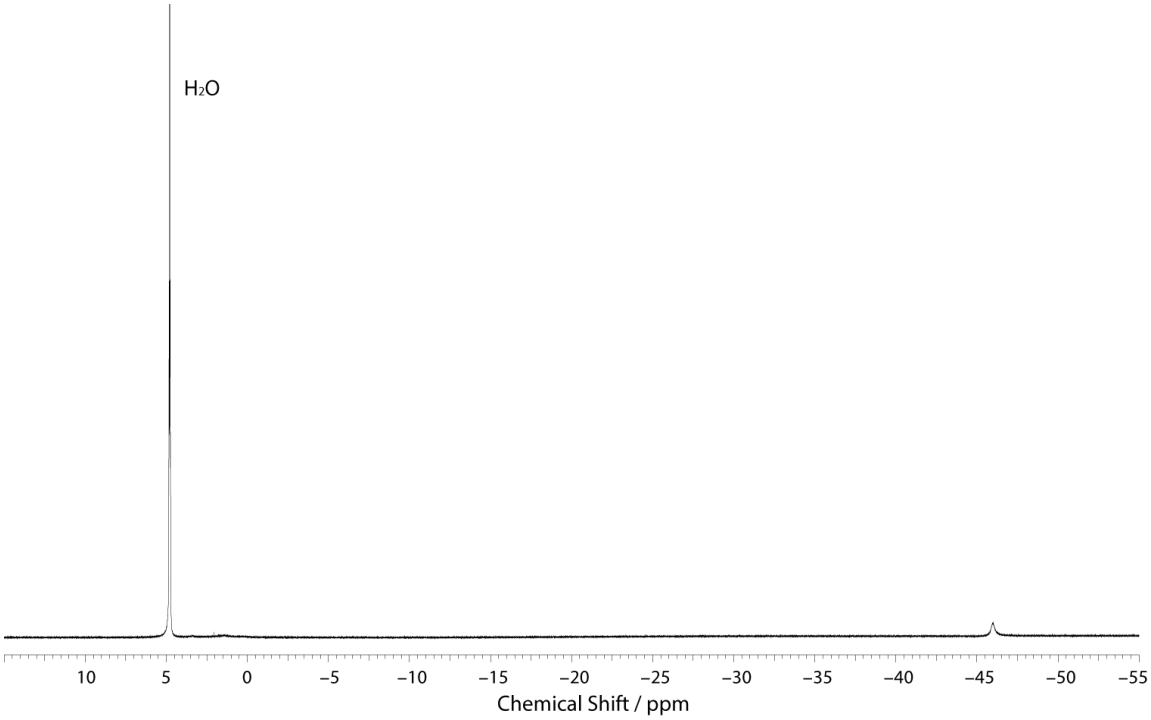

Figure II-13. ^{1}H NMR spectrum of II-S2 recorded in D_2O at 23 °C.

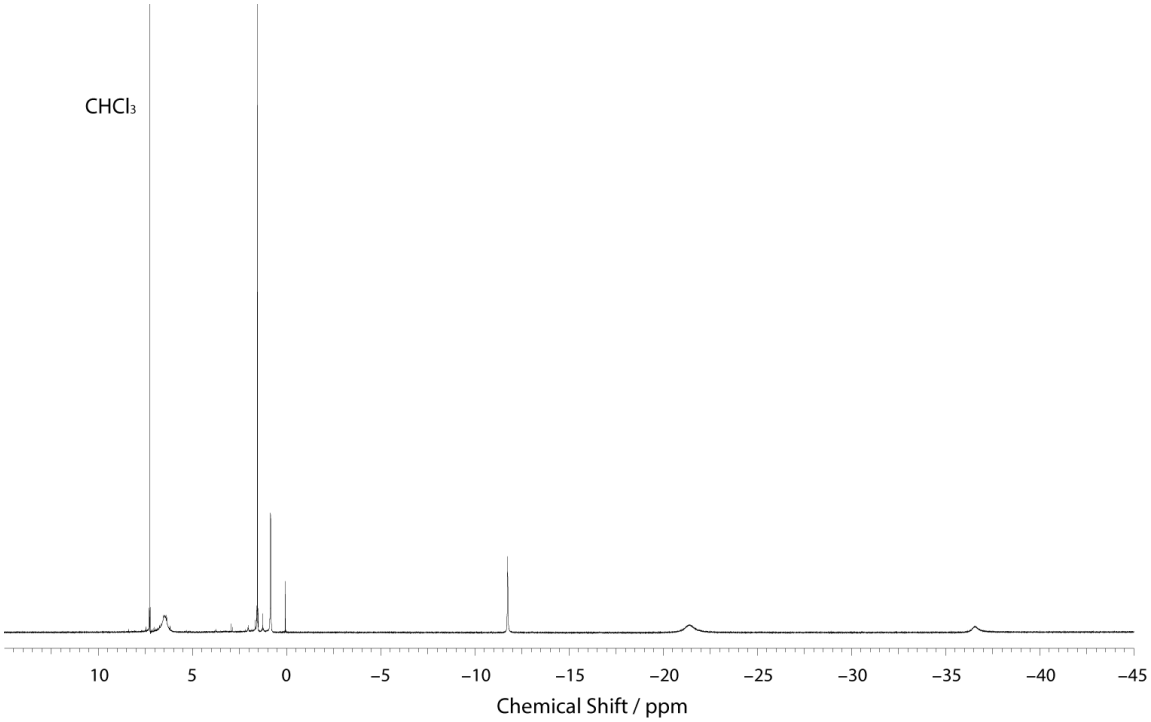

Figure II-14. ^{1}H NMR spectrum of Ru_2 chloride complex II-1 recorded in $CDCl_3$ at 23 °C.

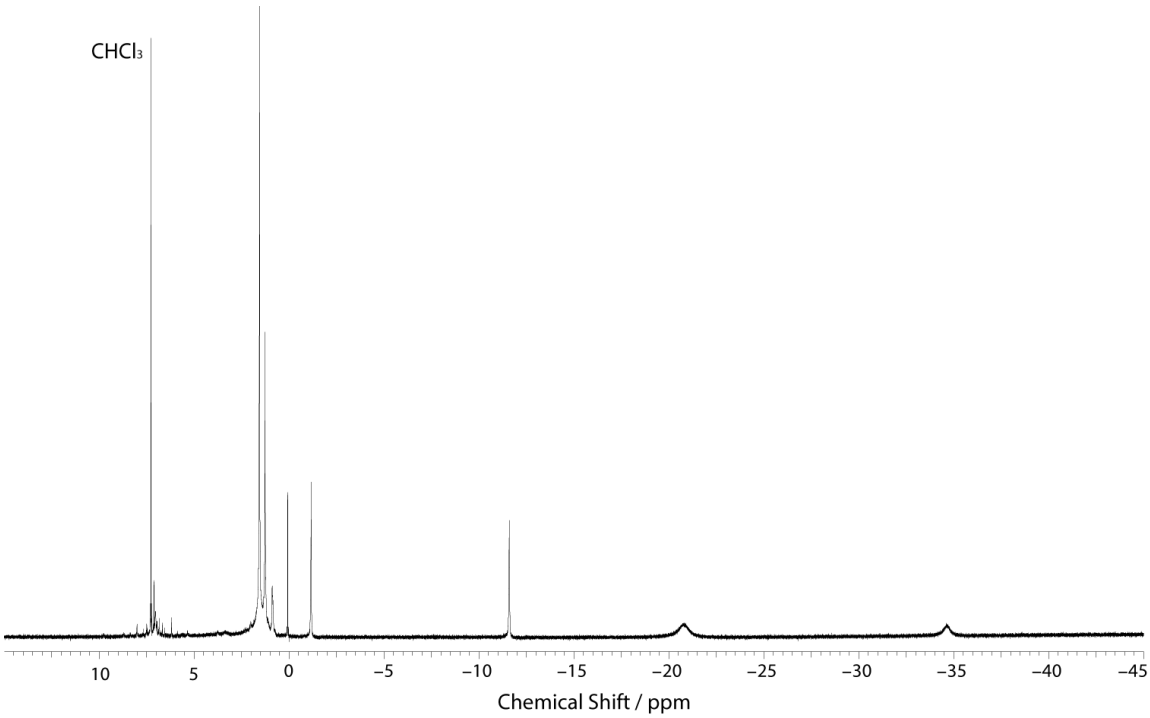

Figure II-15. ^{1}H NMR spectrum of Ru_2 azide complex II-2 recorded in $CDCl_3$ at 23 °C.

CHAPTER III

OBSERVATION OF A PHOTOGENERATED DIRHODIUM NITRENOID INTERMEDIATE IN C–H AMINATION*

III.1. Introduction

Since Kwart and Khan demonstrated that metal nitrenoids participate in C−H amination chemistry in 1967,[188] metal catalyzed nitrogen-group-transfer catalysis has become an important technology for the construction of C−N bonds.[17, 42, 189-194] In particular, Rh_2 nitrenoids, typically generated by the combination of Rh_2 catalysts with iminoiodinane reagents (e.g., PhI–NR), have emerged as powerful intermediates for C−H amination.[44, 58-59, 188, 195-199] The exceptional reactivity of Rh_2 nitrenoids has precluded the spectroscopic or structural characterization of these critical species.[200] Thus, ongoing efforts to develop new amination reactions must rely on computational descriptions of the reactive nitrenoid intermediates.[30, 201]

Characterization of reactive intermediates is inherently challenging due to the fleeting nature of these species. Stable model complexes are often pursued in order to gain insight into the structure and reactivity of reactive intermediates.[155, 202-203] We have been attracted to synthetic photochemistry as a tool to access authentic reactive intermediates under conditions that allow their characterization without attenuating their reactivity.[204] In

* Data, figures, and text in this chapter were adapted with permission from "Observation of a Photogenerated Rh_2 Nitrenoid Intermediate in C–H Amination" by Das, A.; Maher, A. G.; Telser, J.; Powers, D. C. *J. Am. Chem. Soc.* **2018**, *140*, 10412–10415. Copyright 2018 American Chemical Society.

contrast to metal oxo and nitrido complexes, which can be generated by photolysis of metal-bound oxyanions[117, 205] and azido ligands,[156-157] respectively, there are no readily available photoprecursors to metal nitrenoid complexes. In this chapter, we report the development of a new photochemical synthesis of metal nitrenoids, which has enabled the first spectroscopic observation of a Rh_2 nitrenoid intermediate in C−H amination.

We envisioned that a Rh_2 nitrenoid could be generated by photochemical homolysis of an N−X bond in an axially bound *N*-haloamide ligand (**Figure III-1**). Such a transformation would reduce the Rh_2 fragment by one electron, and thus a Rh_2[II,III] precursor is required to access the Rh_2[II,II] nitrenoids that mediate Rh_2-catalyzed C−H amination with iminoiodinanes.[30, 206-207] In contrast to the well-recognized facility of photochemical N−Cl homolysis in *N*-chloroamines to generate nitrogen-centered radicals (i.e., the Hofmann-Löffler-Freytag reaction),[208-213] the photochemistry of transition-metal-bound *N*-chloroamido ligands is less well explored.[214] Here we report the synthesis of a Rh_2 *N*-chloroamide complex and demonstrate that photolysis of this compound unveils a reactive Rh_2 nitrenoid that participates in C−H amination.

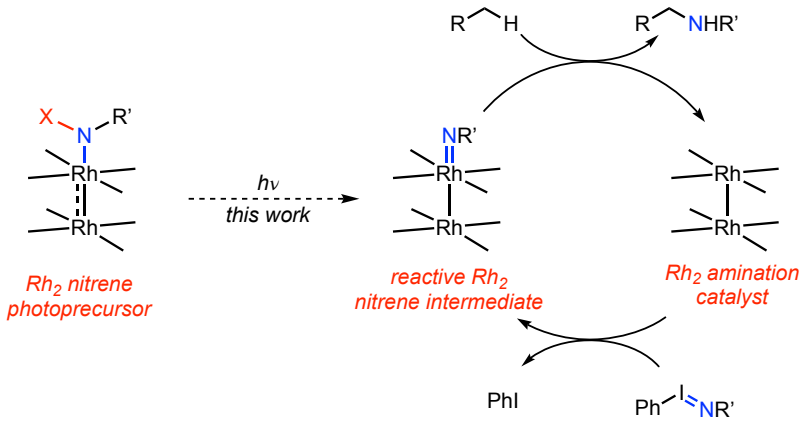

Figure III-1. Synthetic and photochemicaly strategies employed to generate Rh_2 nitrenoid intermediates. Rh_2-catalyzed amination chemistry proceeds through a reactive nitrenoid intermediate generated by nitrene transfer from an iminoiodinane reagent. Here, we demonstrate that photogeneration of a Rh_2 nitrenoid enables direct spectroscopic observation of this critical reactive intermediate.

III.2. Results and Discussions

Treatment of Rh_2[II,III] chloride[206] **III-1** with $AgBF_4$ affords $[Rh_2(espn)_2]BF_4$ (**III-2**). Subsequent exposure of **III-2** to Na[NTsCl] affords Rh_2[II,III] *N*-chloroamido complex **III-3** (**Figure III-2**). Complex **III-3** crystallizes as a red-colored $[Rh_2L_2S_2][Rh_2L_2X_2]$ salt from CH_3CN (L = espn, S = CH_3CN, X = NTsCl); the crystal structure of **III-3** features a cationic Rh_2[II,III] unit with two bound acetonitrile ligands and an anionic Rh_2[II,III] unit with two *N*-chloroamide ligands. For comparison, Rh_2 chloride **III-1** crystallizes from CH_2Cl_2 as extended $(Rh{-}Rh{-}Cl{-})_n$ chains[206] but crystallizes from CH_3CN as a $[Rh_2(espn)_2(CH_3CN)_2][Rh_2(espn)_2Cl_2]$ salt.

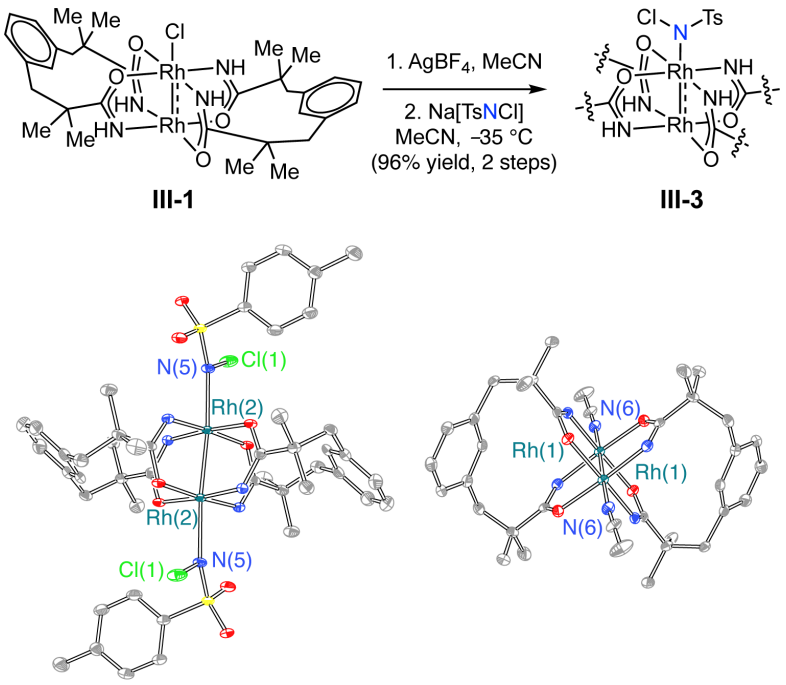

Figure III-2. Synthesis and crystal structure of Rh_2 *N*-chloroamide III-3. Complex **III-3** crystallizes from CH_3CN as a salt of Rh_2[II,III] ions: $[Rh_2(espn)_2(CH_3CN)_2][Rh_2(espn)_2(NTsCl)_2]$.

Based on EPR, IR, and electronic absorption spectroscopies as well as Evans method and dc susceptibility measurements, Rh_2[II,III] complexes **III-1**, **III-2**, and **III-3** share a common S = ½ ground state in which the unpaired electron resides in a Rh−Rh δ* orbital (**Figures III-3–III-6**).[30, 215-216] ESI-MS analysis of a CH_3CN solution of **III-3** displays a signal at 959.168, which is consistent with $[Rh_2(espn)_2(NTsCl)]^+$. The ^1H NMR spectrum of **III-3** measured in CH_3CN displays more features than expected for $[Rh_2(espn)_2(NTsCl)(CH_3CN)]$ (**Figure III-7**). Comparison of the ^1H NMR spectrum of **III-3** with those of $[Rh_2(espn)_2]BF_4$ (**III-2**) and $Na[Rh_2(espn)_2(NTsCl)_2]$ (**III-4**), obtained by treatment of complex **III-1** with excess Na[NTsCl], indicates that the solution structure

of **III-3** is comprised of a ligand-exchange equilibrium mixture of the neutral complex $Rh_2(espn)_2(NTsCl)(CH_3CN)$ and the salt $[Rh_2(espn)_2(CH_3CN)_2][Rh_2(espn)_2(NTsCl)_2]$.

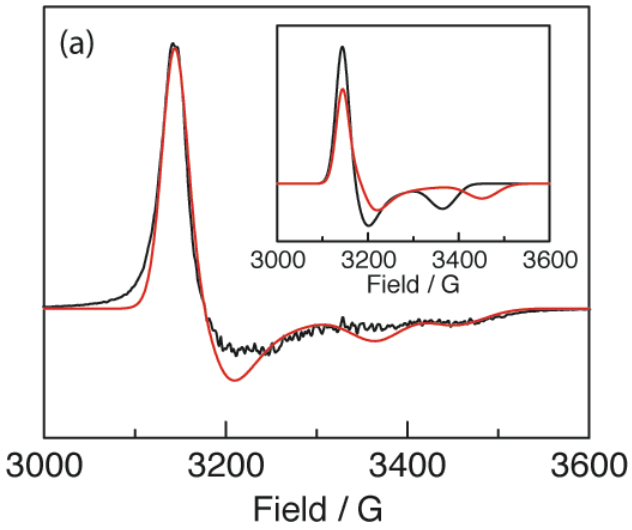

Figure III-3a. X-band EPR spectrum of $[Rh_2(espn)_2]BF_4$ (III-2) in 1:1 CH_3CN:toluene frozen solution phase. Experimental data (—) measured at 4 K, microwave frequency 9.379 GHz, sweep time 90 s and time constant 163.84 ms. Inset: Components of simulated spectrum (—). The data were simulated as the sum of a 1 : 1 admixture of component 1 (—) with g = [2.13, 2.11, 1.99], A(^{103}Rh) × 2 = [25, 25, 70] MHz and W = [40, 80, 60] MHz and component 2 (—) with g = [2.13, 2.10, 1.94], A(^{103}Rh) × 2 = [25, 25, 70] MHz and W = [40, 90, 80] MHz.

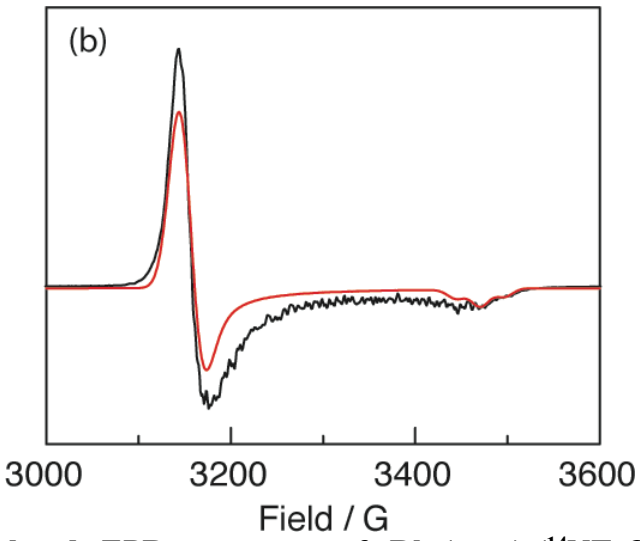

Figure III-3b. X-band EPR spectrum of $Rh_2(espn)_2(^{14}NTsCl)$ (III-3) in 1:1 CH_3CN:toluene frozen solution phase. Experimental data (—) measured at 4 K, microwave frequency 9.378 GHz, sweep time 60 s and time constant 10 ms. Simulated spectrum (—) with g = [2.131, 2.131, 1.935], A(^{103}Rh) × 2 = [25, 25, 70] MHz and W = [40, 40, 30] MHz.

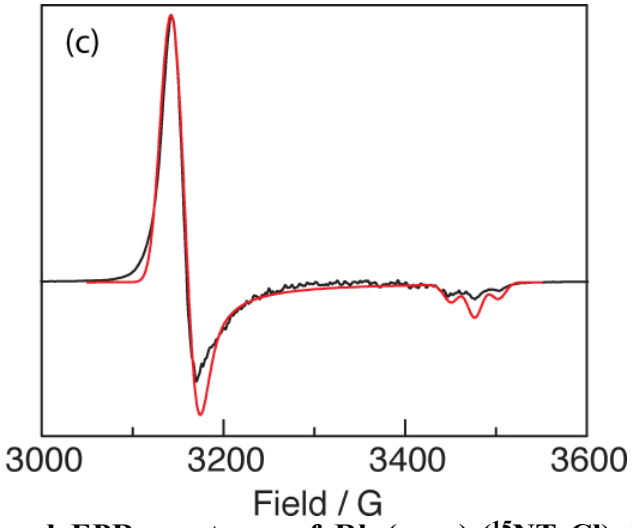

Figure III-3c. X-band EPR spectrum of $Rh_2(espn)_2(^{15}NTsCl)$ ([^{15}N]-III-3) in 1:1 CH_3CN:toluene frozen solution phase. Experimental data (—) measured at 4 K, microwave frequency 9.381 GHz, sweep time 60 s and time constant 10 ms. Simulated spectrum (—) with g = [2.135, 2.120, 1.928], A(^{103}Rh) = A(^{15}N) = [25, 25, 70] MHz and W = [30, 30, 25] MHz. An essentially identical simulation would result using A(^{103}Rh) × 2 = [25, 25, 70] MHz; no distinction can be made between the ^{103}Rh and ^{15}N nuclei at this experimental resolution.

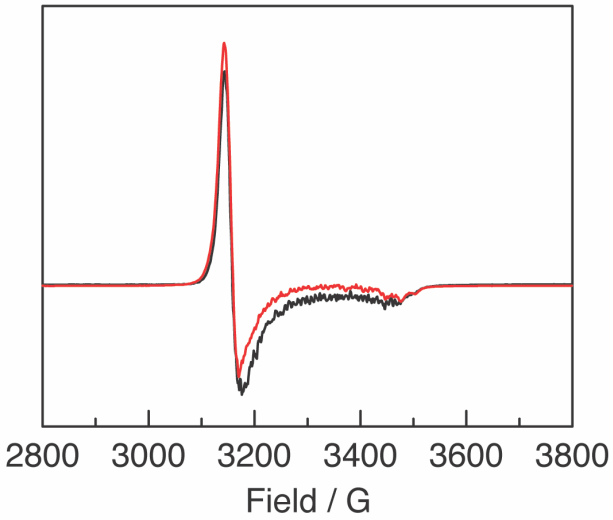

Figure III-3d. X-band EPR spectrum of $Rh_2(espn)_2(^{14}NTsCl)$ (III-3, —) and $Rh_2(espn)_2(^{15}NTsCl)$ ([^{15}N]-III-3, —) in 1:1 CH_3CN:toluene frozen solution phase overlayed for comparison.

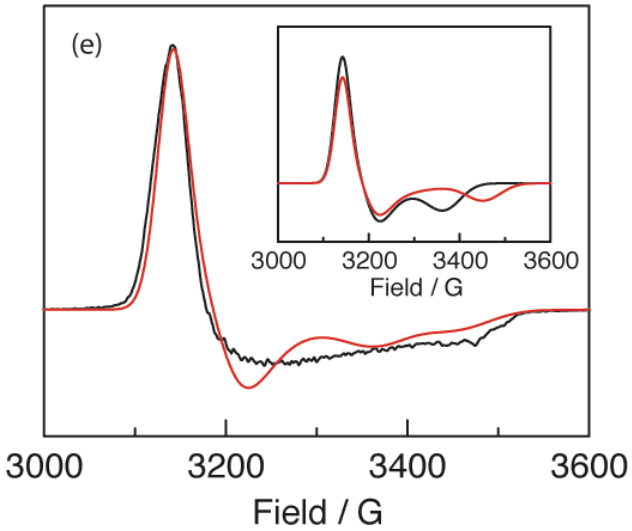

Figure III-3e. X-band EPR spectrum of $Na[Rh_2(espn)_2(NTsCl)_2]$ (III-4) in 1:1 CH_3CN:toluene frozen solution phase. Experimental data (—) measured at 4 K, microwave frequency 9.383 GHz, sweep time 90 s and time constant 163.84 ms. Inset: Components of simulated spectrum (—). The data were simulated as the sum of a 1 : 1 admixture of component 1 (—) with g = [2.132, 2.10, 1.99], A(^{103}Rh) × 2 = [25, 25, 70] MHz and W = [50, 100, 100] MHz and component 2 (—) with g = [2.13, 2.11, 1.94], A(^{103}Rh) × 2 = [25, 25, 70] MHz and W = [50, 100, 100] MHz.

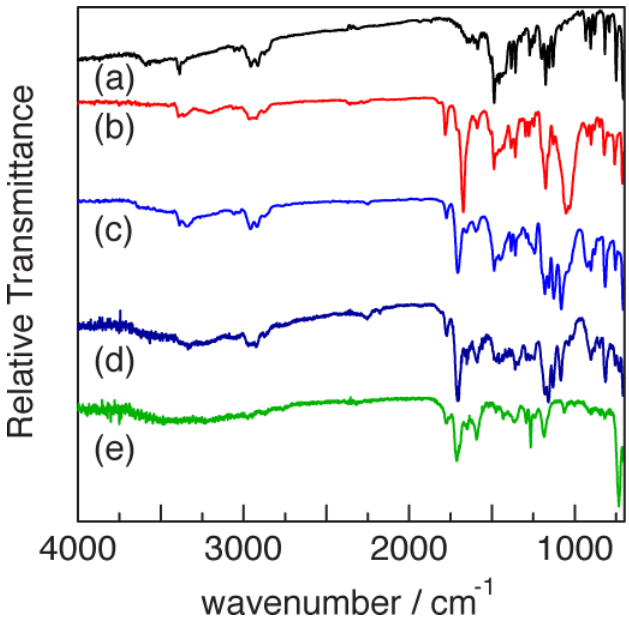

Figure III-4. IR spectra of $Rh_2(espn)_2X$ complexes III-1–III-3 and III-5. IR spectra of (a) $Rh_2(espn)_2Cl$ (**III-1**, —), (b) $Rh_2(espn)_2BF_4$ (**III-2**, —), (c) $Rh_2(espn)_2(NTsCl)$ (**III-3**, —), (d) $Rh_2(espn)_2(^{15}NTsCl)$ ([^{15}N]-**III-3**, —), and (e) $Rh_2(espn)_2$ (**III-5**, —).

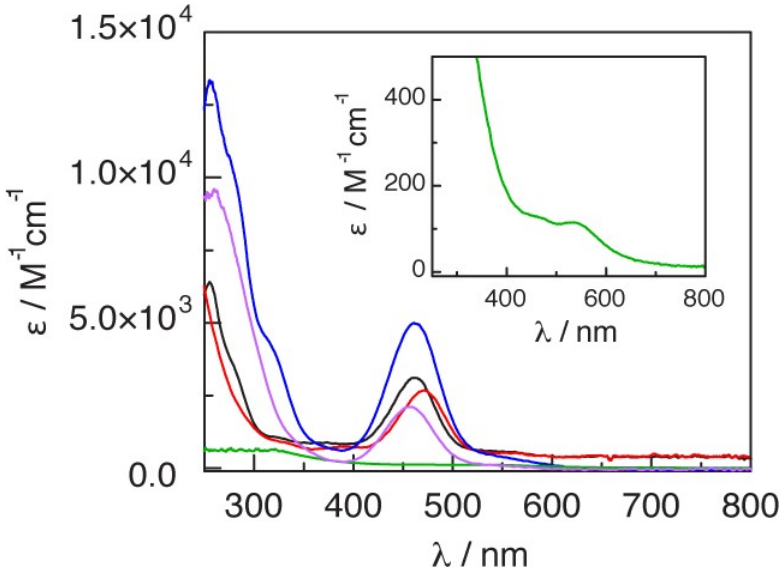

Figure III-5. Electronic absorption spectra of $Rh_2(espn)_2X$ complexes III-1, III-2, III-3, III-4, and III-5. UV-vis spectra of $Rh_2(espn)_2Cl$ (**III-1**, —), $Rh_2(espn)_2BF_4$ (**III-2**, —), $Rh_2(espn)_2(NTsCl)$ (**III-3**, —), $Na[Rh_2(espn)_2(NTsCl)_2]$ (**III-4**, —), and $Rh_2(espn)_2$ (**III-5**, —) in CH_3CN. Inset: expansion of the UV-vis spectrum of $Rh_2(espn)_2$ (**III-5**, —) in CH_3CN.

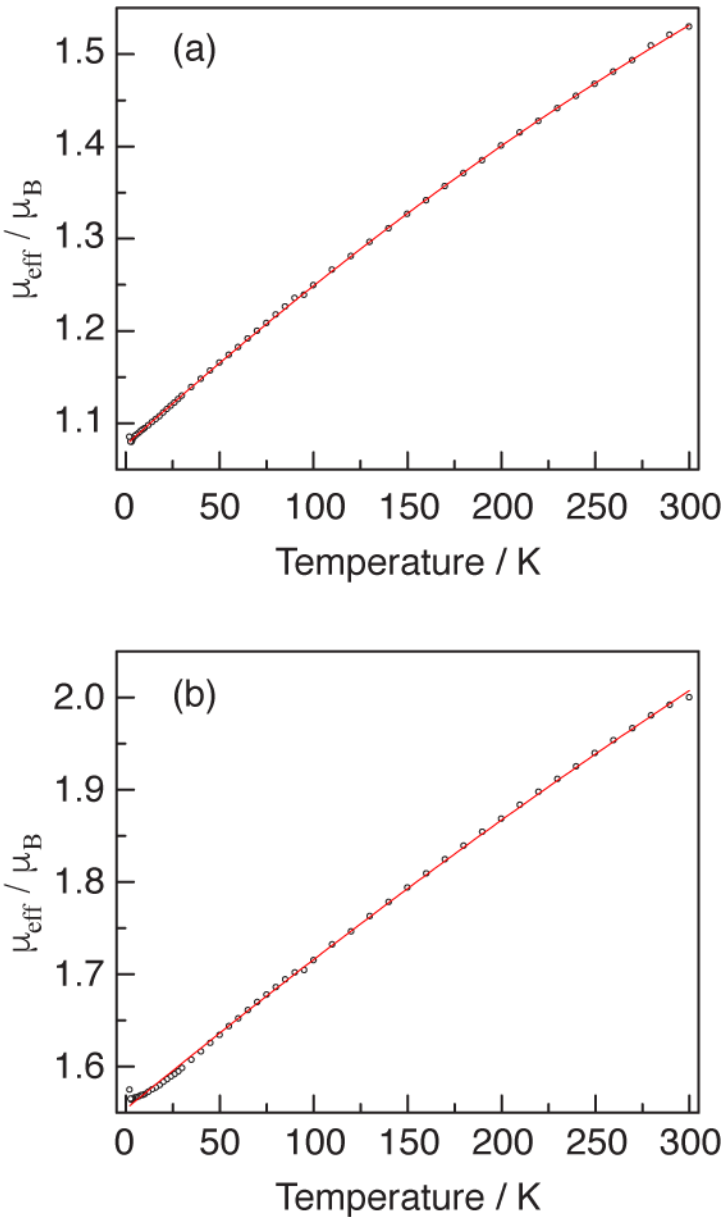

Figure III-6. Plot of μ_{eff} vs. temperature for $Rh_2(espn)_2(NTsCl)$ (III-3). When measured as a (a) powdered sample it has a μ_{eff} of 1.54 at 300 K indicating an S = ½ spin state and (b) crystalline sample it has a μ_{eff} of 1.99 at 300 K also indicating an S = ½ spin state.

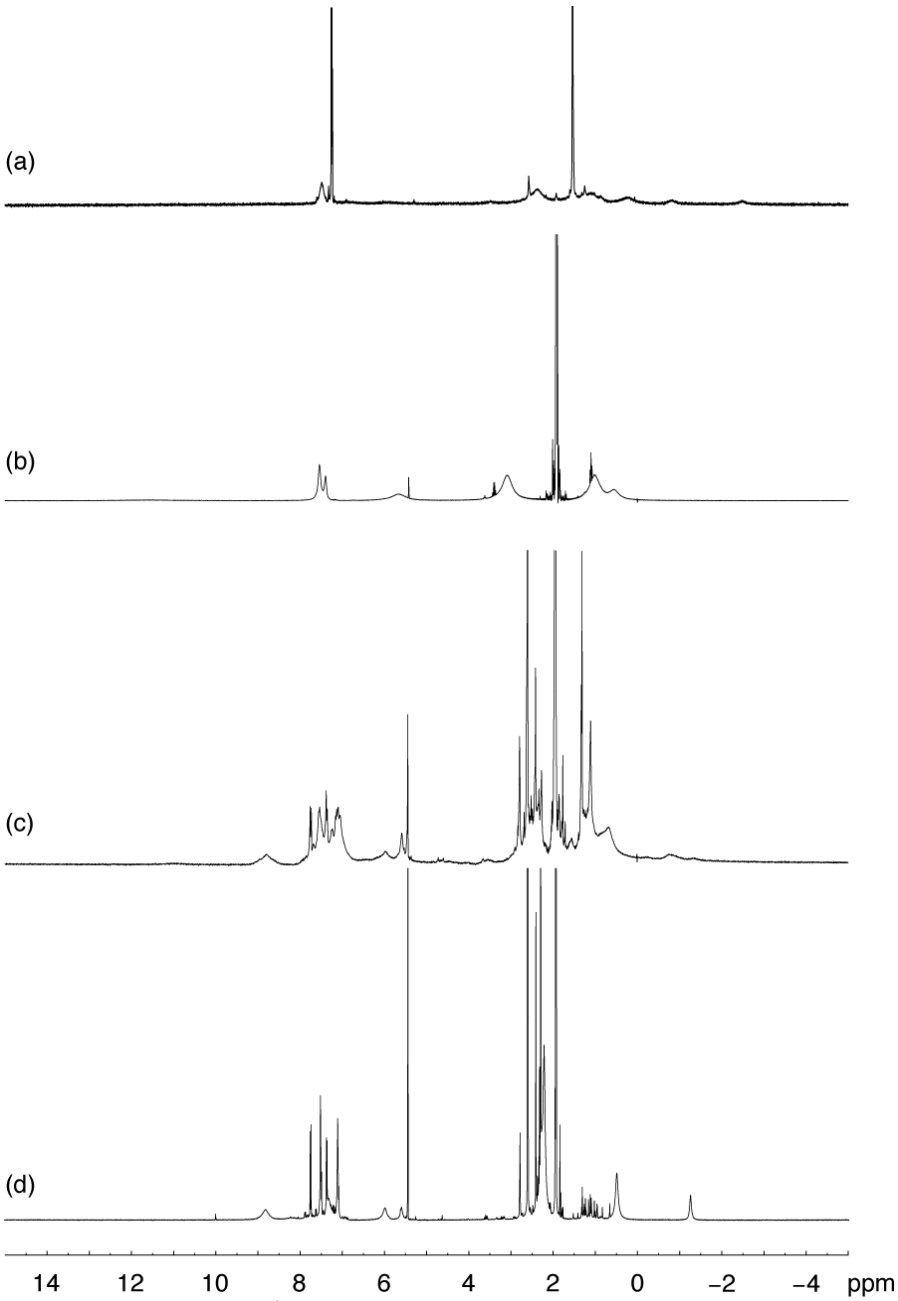

Figure III-7. Comparison of ^{1}H NMR of Rh_2 complexes III-1, III-2, III-3, and III-4. (a) ^{1}H NMR spectrum of $Rh_2(espn)_2Cl$ (**III-1**) in $CDCl_3$ at 23 °C. (b) ^{1}H NMR spectrum of $[Rh_2(espn)_2]BF_4$ (**III-2**) in CD_3CN at 23 °C. (c) ^{1}H NMR spectrum of $Rh_2(espn)_2(NTsCl)$ (**III-3**) in CD_3CN at 23 °C. (d) ^{1}H NMR spectrum of $Na[Rh_2(espn)_2(NTsCl)_2]$ (**III-4**) in CD_3CN at 23 °C.

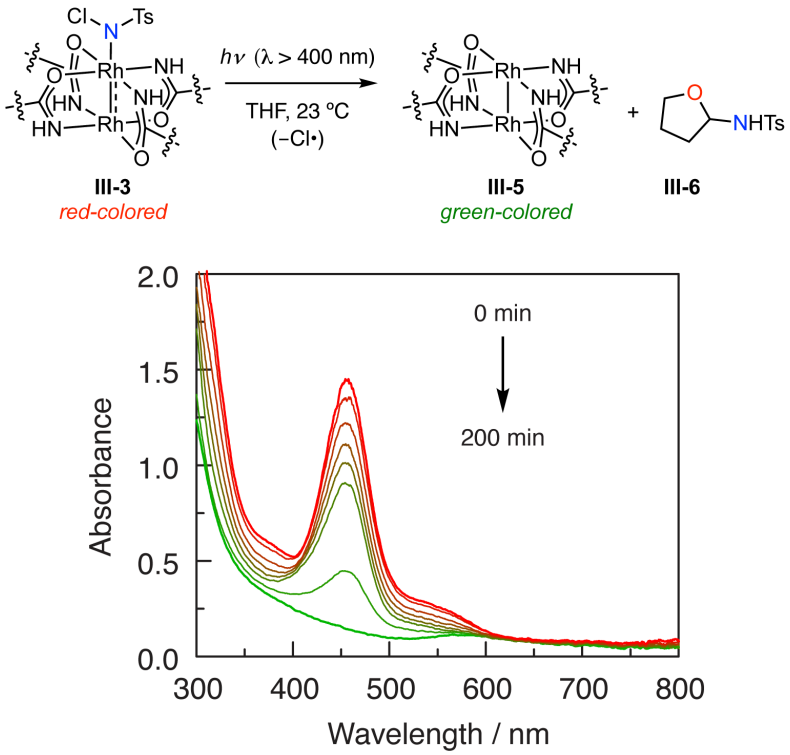

Figure III-8. Monitoring the photolysis of III-3 using UV-vis. Photolysis of red-colored complex **III-3** (λ > 400 nm) results in consumption of **III-3** with concurrent evolution of green-colored Rh_2[II,II] complex **III-5** and amine **III-6**. The observed reaction products, Rh_2[II,II] complex **III-5** and amine **III-6**, are consistent with amination by a photogenerated Rh_2 nitrenoid.

Photolysis of a THF solution of Rh_2 complex **III-3** (λ > 400 nm) results in a red-to-green color change (**Figure III-8**). UV−vis analysis of the reaction mixture following photolysis indicates evolution of green-colored Rh_2[II,II] complex **III-5** (~100%, **Figure III-9**) and ^{1}H NMR analysis of the reaction mixture indicates evolution of **III-6** (47 ± 2%), the product of THF amination (**Figure III-10**). The balance of nitrogen content is accounted for by $TsNH_2$ (45 ± 3%). Rh_2[II,II] complex **III-5** and tosylamide **III-6** are the products expected from initial N−Cl cleavage to generate a Rh_2 nitrenoid and Cl•. Nitrene-transfer from the Rh_2 nitreneoid to THF would generate Rh_2[II,II] complex **III-5** and

amine **III-6** and H-atom abstraction (HAA) between THF and Cl• would generate HCl and THF radicals. We have not detected products derived from THF radicals, but the evolution of HCl was confirmed by the formation of $Et_3N{\cdot}HCl$ upon addition of Et_3N to the photolysis reaction mixture (**Figures III-11–III-12**).

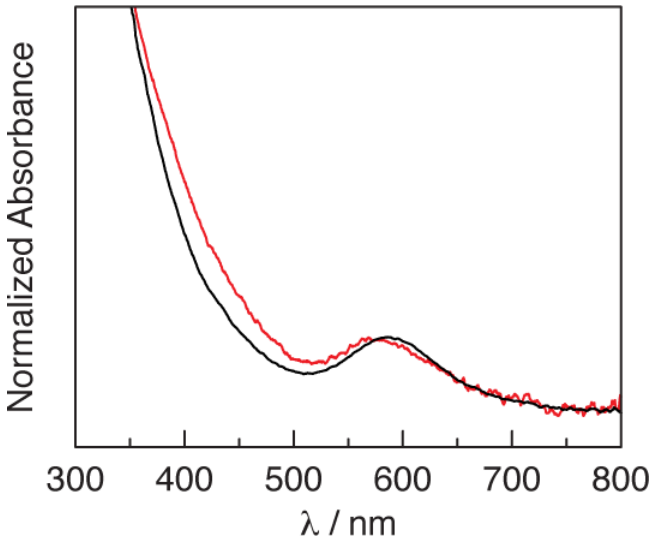

Figure III-9. Comparison of UV-vis spectra of complex III-5 and the end-point of photolysis of III-3. UV spectrum of $Rh_2(espn)_2$ (**III-5**, —) and the reaction mixture following photolysis of $Rh_2(espn)_2(NTsCl)$ (**III-3**, —) measured in THF. The similarity of these spectra indicates that the product of photolysis is Rh_2[II,II] complex **III-5**.

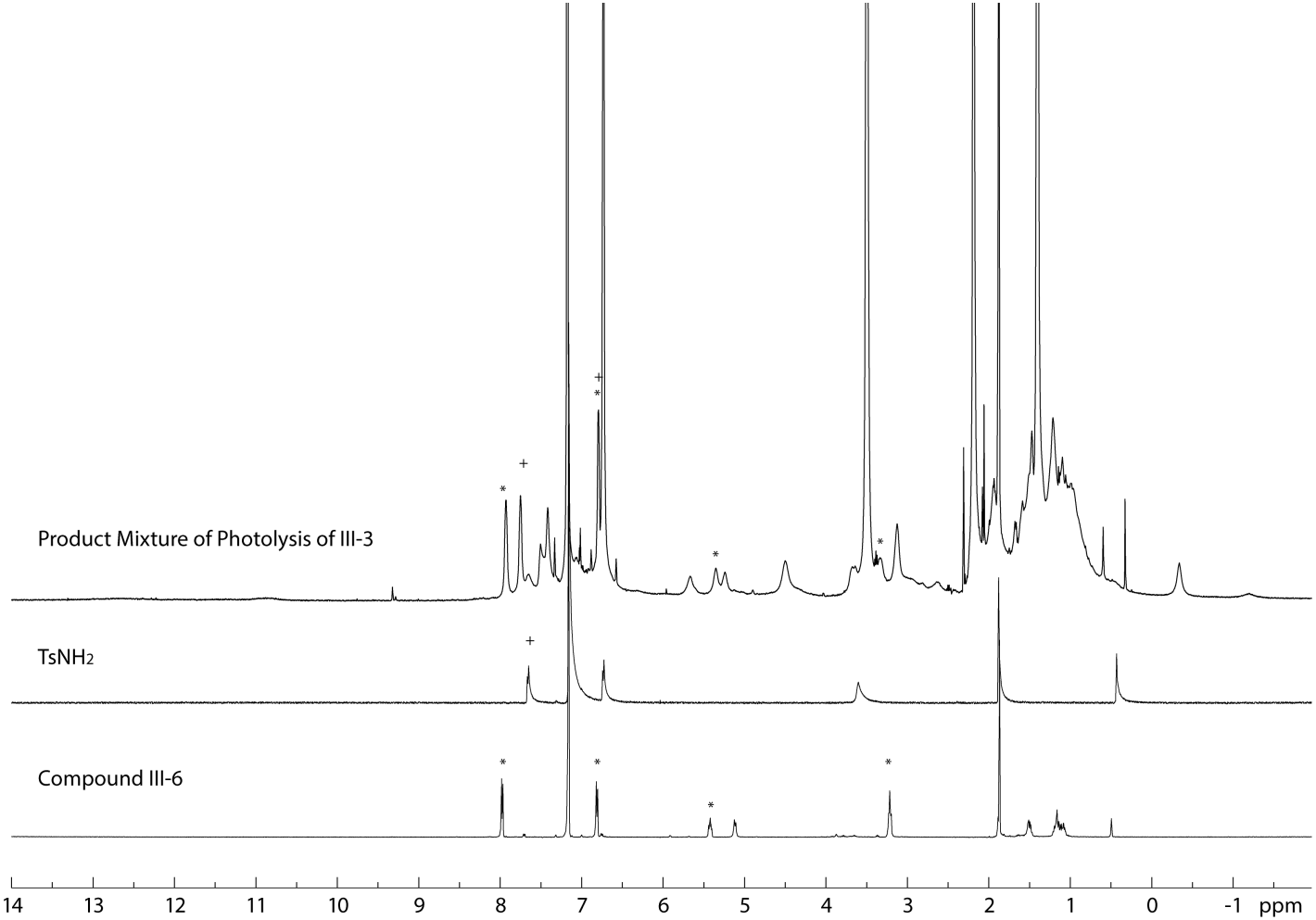

Figure III-10. Comparison of ^{1}H NMR of the end-point of photolysis of III-3 with $TsNH_2$ and III-6. Stacked ^{1}H NMR spectra of (top) product mixture arising from photolysis of $Rh_2(espn)_2(NTsCl)$ (**III-3**) in THF, (middle) $TsNH_2$, and (bottom) tosylamide **III-6**. All spectra are recorded in C_6D_6 at 23 °C. Mesitylene was added to the photolysis product mixture as internal standard.

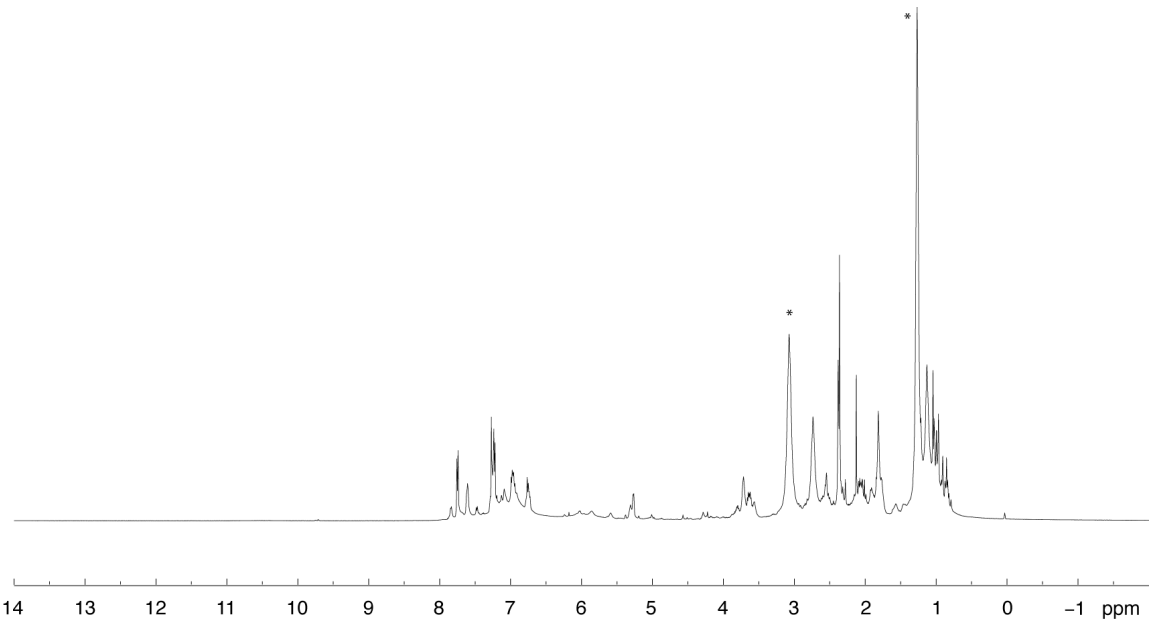

Figure III-11. ^{1}H NMR spectrum obtained following addition of Et_3N to the reaction mixture obtained by photolysis of III-3. The indicated peaks correspond to $Et_3N{\cdot}HCl$.

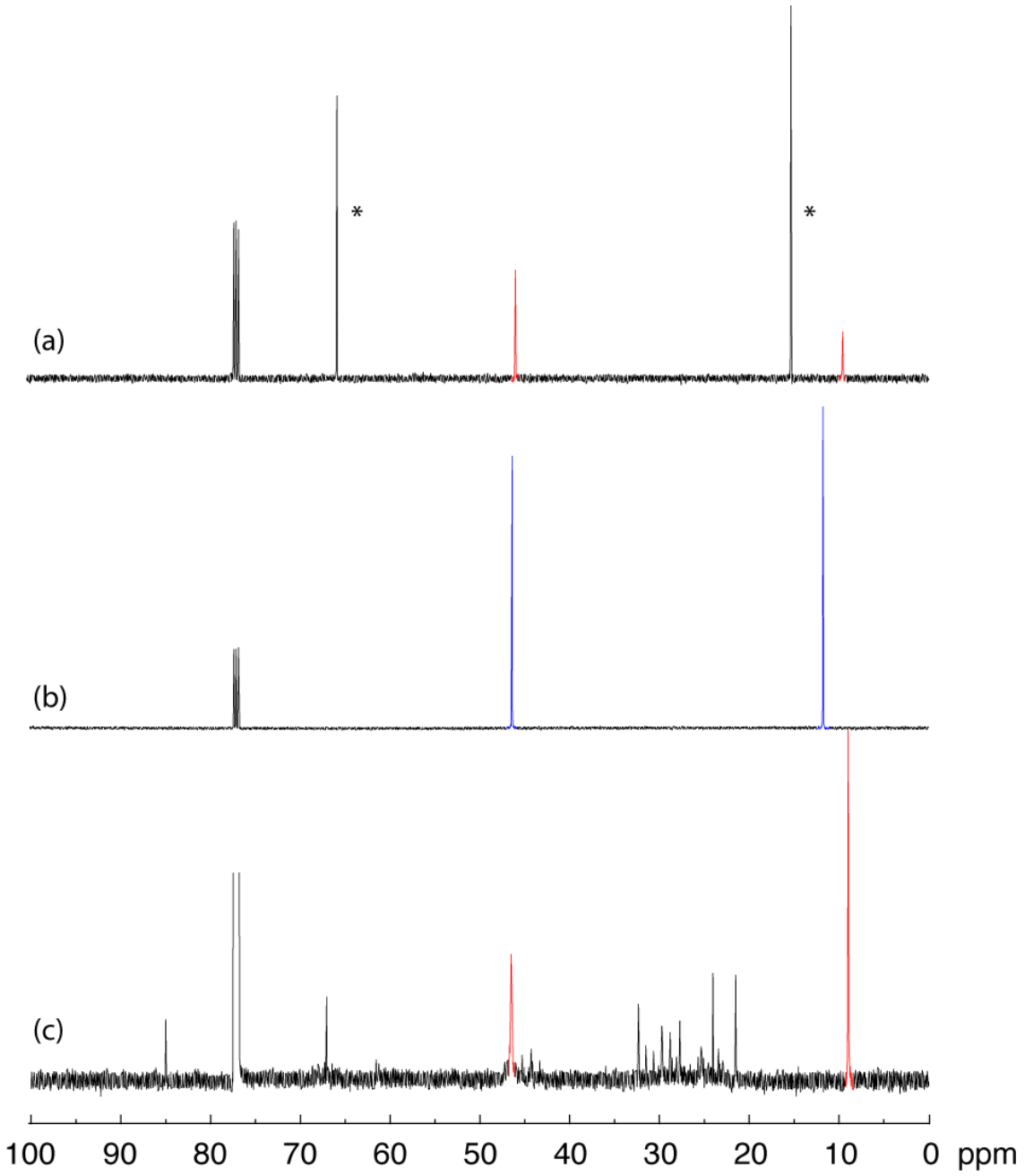

Figure III-12. Comparison of ^{13}C NMR spectrum obtained following addition of Et_3N to the reaction mixture obtained by photolysis of III-3 with $Et_3N{\cdot}HCl$ and Et_3N. ^{13}C NMR spectra (a) of $Et_3N{\cdot}HCl$ (peaks highlighted in red, * = signals from Et_2O, which was the solvent used to add HCl, (b) of Et_3N (peaks highlighted in blue), and (c) obtained following addition of Et_3N to the reaction mixture obtained by photolysis of **III-3**.

In concept, the observed amination of THF could arise from a variety of reactive nitrogen species. For example, initial Rh−N cleavage could generate Rh_2[II,II] complex **III-5** and an aminyl radical that could engage in C−H amination. Alternately, photolysis could generate free tosylnitrene which could also engage in C−H amination. We have carried out a series of kinetic isotope effect (KIE) experiments to interrogate the nature of the reactive nitrogen species generated during photolysis of **III-3** (**Table III-1**). Photolysis of **III-3** in a 1:1 THF/THF-d_8 mixture affords a KIE of 2.72(8). This value is well-matched to KIEs that have been previously measured for Rh_2-catalyzed C−H amination using iminoiodinanes as nitrene sources.[30] In comparison, photolysis of Na[NTsCl] affords tosylamide **III-6** with a KIE of 4.4(3), which is consistent with amination via initial HAA from THF.[217-218] The potential intermediacy of free nitrenes was investigated by photolysis of TsN_3.[219] Analysis of the amination of THF under these conditions affords a KIE of 1.48(2). The similarity of the KIE measured for photochemical amination of THF with that of Rh_2-catalyzed amination, and the dissimilarity with the KIEs measured for amination via aminyl radical and free nitrene intermediates, suggests photolysis of Rh_2 complex **III-3** generates a Rh_2 nitrenoid.

Table III-1. C–H amination KIEs for selected nitrogen sources.

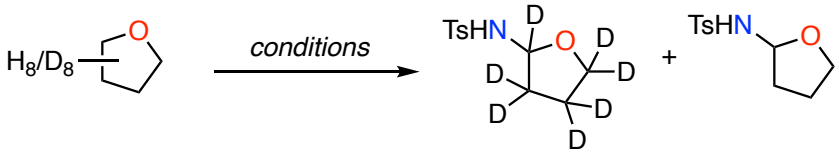

conditions	Yield (**III-6** + d_7-**III-6**) / %	k_H/k_D
III-1, PhINTs	*J. Am. Chem. Soc.* **2016**, *138*, 2327.	2.6
Rh_2 complex **III-3**, hν	48	2.72(8)
Chloramine-T, hν	63	4.4(3)
TsN_3, hν	7	1.48(2)

With a photosynthetic approach to a chemically and kinetically competent Rh_2 nitrenoid in hand, we turned our attention to observation of the reactive intermediate involved in amination chemistry. At low laser intensity, MALDI mass spectrometric analysis of **III-3** displayed an m/z = 754.153, which corresponds to $[Rh_2(espn)_2]^+$. As the laser intensity was increased, we observed the emergence of an m/z signal at 923.458, which corresponds to nitrenoid **III-7** (**Figure III-13a**). Mass spectrometric analysis of ^{15}N-labeled **III-3** displays a shift to 924.555, which is expected for replacement of the ^{14}N with ^{15}N. In addition to the parent ions, m/z signals at 962.464 and 963.547 are also observed, which correspond to the mass of ^{14}N- and ^{15}N-labeled nitrenoid **III-7** with a bound CH_3CN ligand (**Figure III-14**).

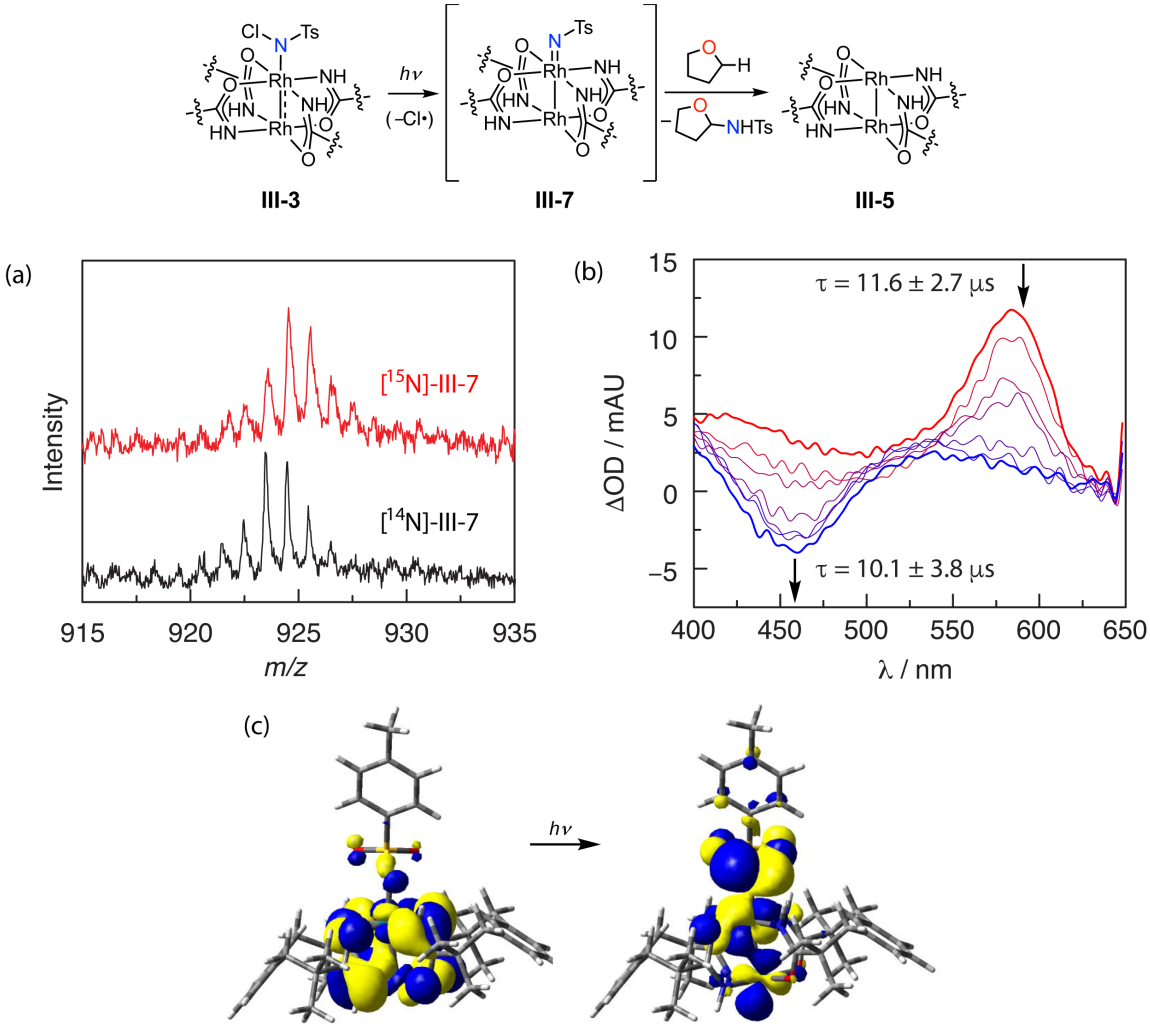

Figure III-13. Spectroscopic characterization of Rh_2 nitrenoid III-7. (a) Rh_2 nitrenoid has been observed by MALDI-MS. MALDI analysis of ^{15}N-labeled **III-3** provides the expected M + 1 m/z shift. (b) TA spectra obtained by laser flash photolysis of a CH_2Cl_2 solution of **III-3** (λ_{pump} = 280 nm). The prompt spectrum (—) displays a transient growth centered at 580 nm that we attribute to Rh_2 nitreneoid **III-7**. The prompt spectrum evolves over the course of 200 μs to a spectrum (—) that displays a spectral bleach that corresponds to consumption of **III-3**. Single wavelength kinetics indicate that the disappearance of the growth at 580 nm and the appearance of the bleach at 450 nm are temporally coupled, suggesting evolution of these two signals is related to the same chemical process. (c) The low-energy feature (580 nm) observed in the spectrum of nitrenoid **III-7** arises from predominantly Rh−Rh π (left) to Rh−N π* (right) excitation.

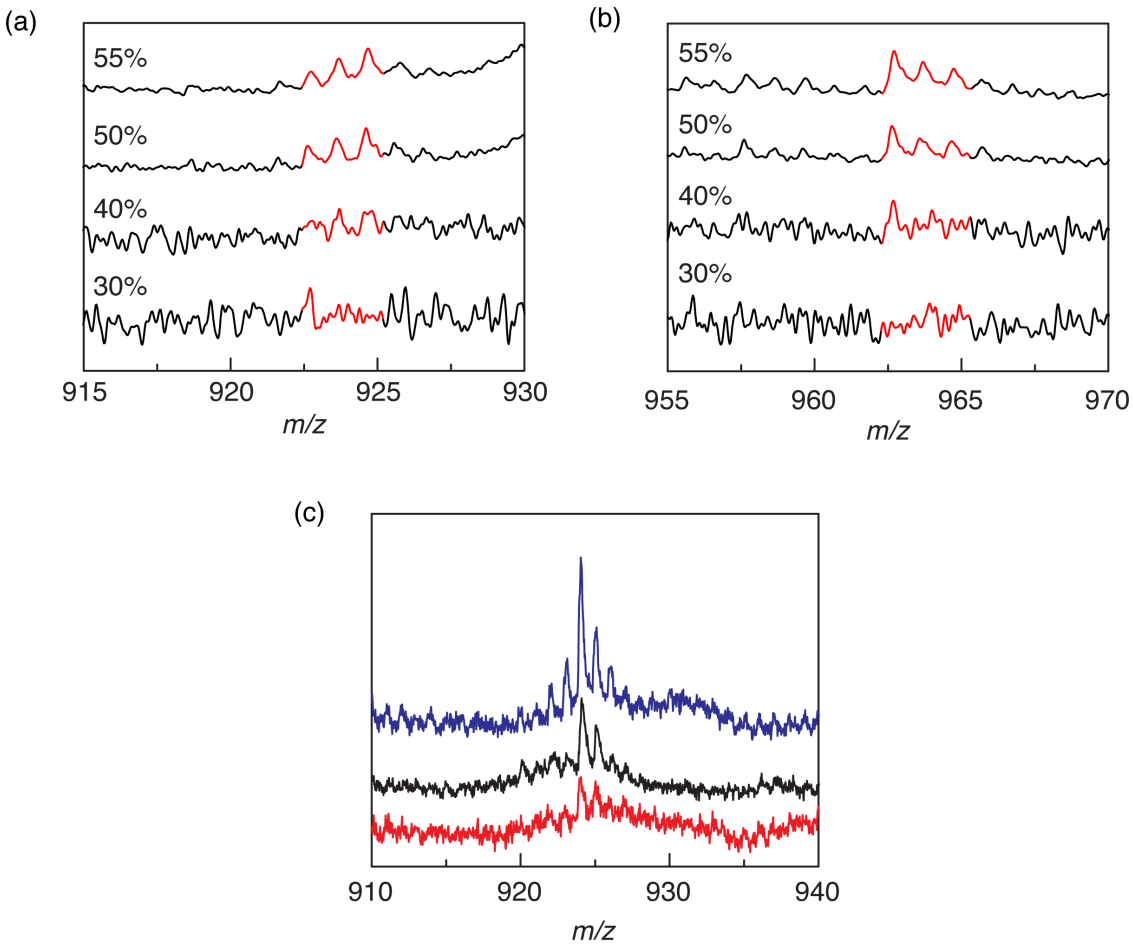

Figure III-14. MALDI-TOF plots for Rh_2 complex III-3. Variable-laser-power MALDI-TOF data that show power-dependent m/z for (a) $Rh_2(espn)_2(NTs)$, and (b) $Rh_2(espn)_2(NTs)(CH_3CN)$. (c) MALDI-TOF data obtained for samples of **III-3** at 65% laser power from different solvents – CH_2Cl_2 (—), THF (—), and THF-d_8 (—) – which show that the signals attributed to nitrenoid **III-7** are solvent independent.

We have carried out transient absorption (TA) experiments to obtain spectroscopic information regarding the reactive intermediate in amination. Laser-flash photolysis (λ = 280 or 355 nm) of Rh_2 complex **III-3** in CH_2Cl_2 reveals a transient growth centered at ~580 nm in the prompt spectrum (red, **Figure III-13b**). The decay of this lower-energy feature is accompanied by the development of a spectral bleach centered at ~450 nm. The

spectrum acquired after a delay of 200 μs corresponds to the difference spectrum expected for consumption of **III-3** and formation of Rh_2[II,II] complex **III-5** (blue, **Figure III-13b**). The time constants for the decay of the feature at 580 nm and for the bleach at 450 nm are 11.6 ± 2.7 μs and 10.1 ± 3.8 μs, respectively. This similarity of the temporal evolution of the two observed transient features suggests that they arise from the same chemical process. Time-dependent density functional theory (TD-DFT) calculations of Rh_2[II,III] complexes **III-1**, **III-2**, **III-3** and nitrenoid **III-7** have been carried out to gain insight into the TA spectra observed (**Figure III-15**). Each of the Rh_2[II,III] complexes **III-1**, **III-2**, and **III-3** share a common absorbance that is primarily derived from a Rh−Rh π to Rh−O π* transition. The computed spectrum of nitrenoid **III-7** shares the absorbance of the Rh_2[II,III] structures as well as a lower energy absorbance that predominantly arises from Rh−Rh π to Rh−N π* excitation. The computed spectra of **III-3** and **III-7** are consistent with the TA spectra that display a prompt low energy growth and the subsequent evolution of a higher energy bleach.

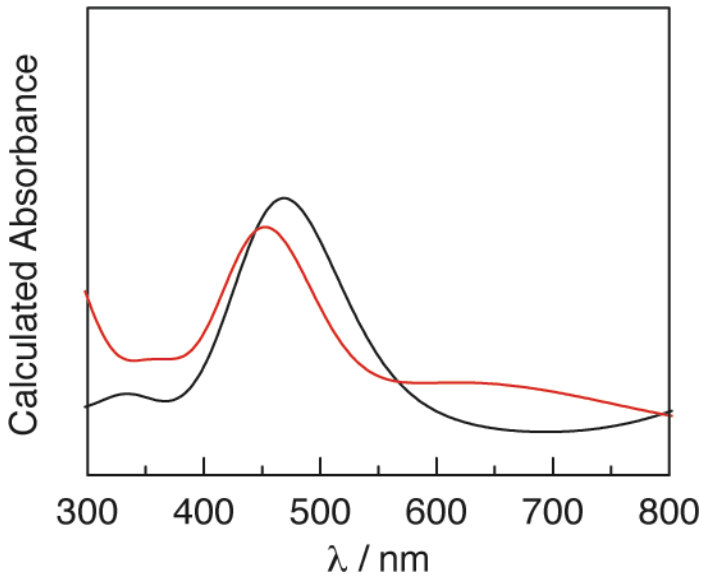

Figure III-15. UV-vis spectra of III-3 and III-7 obtained from TD-DFT calculations. Results of TD-DFT calculations for the absorption spectra of $Rh_2(espn)_2(NTsCl)$ (**III-3**, —) and $Rh_2(espn)_2(NTs)$ nitrenoid (**III-7**, —).

III.3. Conclusion

In conclusion, we have described photogeneration of a Rh_2 nitrenoid intermediate in C−H amination. Based on the observed photochemical C−H amination, the similarity of the KIE for C−H amination to that of Rh_2-catalyzed amination reactions, the observation of m/z for a molecular Rh_2 nitrenoid, and TA spectroscopy correlated with TD-DFT calculations, the developed photochemistry enables the first spectroscopic observation of Rh_2 nitrenoid intermediates (i.e., **III-7**) implicated in amination chemistry. We anticipate that photochemical access to reactive metal nitrenoids will facilitate direct characterization of these critical amination intermediates and thus contribute to the rational development of C−H amination chemistry.

III.4. Experimental Details

III.4.1 General Considerations

Materials Solvents were obtained as ACS reagent grade and used as received. Unless otherwise noted, all chemicals and solvents were used as received. Oxalyl chloride, chloramine-T trihydrate, *N*-chlorosuccinimide (NCS), isobutyronitrile, *n*-butyl lithium (^{n}BuLi), *p*-toluenesulfonyl chloride, hexanes, dichloromethane (CH_2Cl_2), and acetone were obtained from Sigma Aldrich. Trichloroisocyanuric acid and silica gel (0.060–0.200 mm, 60 Å for column chromatography) were obtained from Acros Organics, and silver tetrafluoroborate ($AgBF_4$) was obtained from Strem Chemicals. Dirhodium tetraacetate [$Rh_2(OAc)_4$] was obtained from Ark Pharm and xylylene dibromide was purchased from Bean Town Chemicals. Sodium hydroxide (NaOH), sodium sulfate (Na_2SO_4) and ammonium hydroxide (NH_4OH) were obtained from EMD Millipore. Chlorobenzene (PhCl) was obtained from TCI America. Potassium hydrogen carbonate ($KHCO_3$), diisopropylamine ($^{i}Pr_2NH$), dimethylformamide (DMF), ethyl acetate (EtOAc), diethyl ether (Et_2O), and acetonitrile (CH_3CN) were obtained from Fischer Scientific. NMR solvents and ammonium chloride (^{15}N, 99%) were purchased from Cambridge Isotope Laboratories and were used as received. Anhydrous acetonitrile, THF, and diethyl ether were obtained from a drying column and stored over activated molecular sieves.[180] All reactions were carried out under ambient atmosphere unless otherwise noted.

Characterization Details NMR spectra were recorded on Inova 500 FT NMR operating at 499.53 MHz or Mercury 300 at 299.92 MHz for ^{1}H and ^{13}C acquisitions and were referenced against solvent signals: $CDCl_3$ (7.26 ppm, ^{1}H; 77.16 ppm, ^{13}C), D_2O (4.79

ppm, ^{1}H), d^{8}-THF (3.58 ppm and 1.72 ppm, ^{1}H), CD_3CN (1.94 ppm, ^{1}H), and d^{6}-DMSO (2.50 ppm, ^{1}H).[181] ^{1}H NMR data are reported as follows: chemical shift (δ, ppm), multiplicity (s (singlet), d (doublet), t (triplet), m (multiplet), br (broad)), integration. UV-vis spectra were recorded at 293 K in quartz cuvettes on an Ocean Optics Flame-S miniature spectrometer with DH-mini UV-vis NIR light source (200–900 nm) and Hitachi U-4100 UV-vis-NIR spectrophotometer (200–1200 nm) and were blanked against the appropriate solvent. Solid-state UV-vis spectra were recorded as mineral oil dispersions on glass slides using Hitachi U-4100 UV-vis-NIR spectrophotometer, were blanked against empty glass slides, and were measured in transmittance mode. IR spectra were recorded on a Shimadzu FTIR/IRAffinity-1 spectrometer. Spectra were blanked against air and were determined as the average of 64 scans. IR data are reported as follows: wavenumber (cm^{-1}), peak intensity (s, strong; m, medium; w, weak). Magnetic data was obtained using a Quantum Design MPMS 3 SQUID magnetometer. DC measurements were acquired under a 1000 Oe applied field at a temperature range of 2–300 K. Evans method measurements were carried out using ^{19}F NMR using with trifluorotoluene as the standard. Both DC susceptibility and Evans method measurements were corrected by Pascal's constants.[220] High-resolution mass spectrometry (HRMS) data were measured on a Thermo Scientific Orbitrap Fusion Tribrid in 3kV positive mode at 240000 mass resolution (3 sheath gas, 2 aux gas, 1 sweep gas, 5 μL/min syringe push). MALDI data was obtained using a Bruker Microflex LRF MALDI-TOF using reflectron-TOF modes. The laser power of the MALDI was tuned using the software Bruker Daltonics flexControl pre-installed with the instrument. EPR spectra were recorded at X-band on a Bruker

ELEXSYS Spectrometer with a Cryogen-Free In-Cavity temperature control system. EPR spectra were simulated using the program QPOWA, as modified by J. Telser. Elemental analyses were performed by Atlantic Microlab, Inc., Norcross, GA.

X-ray Diffraction Details Experimental details of crystallization are included in the synthetic procedures for the relevant compounds. Crystal suitable for X-ray diffraction were mounted on a MiTeGen dual thickness micromount and placed under a cold N_2 stream (Oxford). A Bruker APEX 2 Duo X-ray (three-circle) diffractometer was used for crystal screening, unit cell determination, and data collection. The X-ray radiation employed was generated from a Mo sealed X-ray tube (Kα = 0.70173 Å with a potential of 40 kV and a current of 40 mA). Bruker AXS APEX II software was used for data collection and reduction. Absorption corrections were applied using the program SADABS. A solution was obtained using XT/XS in APEX2 and refined in Olex2.[183-184, 221] Hydrogen atoms were placed in idealized positions and were set riding on the respective parent atoms. All non-hydrogen atoms were refined with anisotropic thermal parameters. The structure was refined (weighted least squares refinement on F^2) to convergence.[183-184] Disorder was modeled using two parts and the bond distances and thermal ellipsoids in the disordered molecules were restrained using the SADI and EADP. The restraints SIMU and DELU were also used on the disordered parts. The X-ray crystal structures of **III-3** and **III-4** were collected using synchrotron radiation (0.41328 Å) at ChemMatCARS located at the APS housed at ANL. The data was collected at 100 K (Cryojet N_2 cold stream) using a vertically mounted Bruker D8 three-circle platform goniometer equipped with a PILATUS3 X CdTe 1M detector. Data was collected as a

series of φ and/or ω scans. Data were integrated using SAINT and scaled with a multi-scan absorption correction using SADABS.[221] Structures were solved by intrinsic phasing using SHELXT (Apex2 program suite v2014.1) and refined against F^2 on all data by full matrix least squares with SHELXL97.[221] All non-hydrogen atoms were refined anisotropically. H atoms were placed at idealized positions and refined using a riding model.

Transient Absorption Spectroscopy Details The sample solution was flowed through a 3-mm diameter, 1-cm path length flow cell (Starna, type 585.2) using a peristaltic pump and positive argon pressure. Nanosecond transient absorption (TA) measurements were made with the pump light provided by the third harmonic (355 nm) of a Quanta-Ray Nd:YAG laser (Spectra-Physics) running at 10 Hz. Probe white light was provided by a 75 W Xe-arc lamp (Photon Technologies Inc.). The signal light passed through a Triax 320 spectrometer, where it was dispersed by a 300 nm Å~ 250 nm blazed grating and collected with an intensified gated CCD camera (ICCD, CCD 30-11, Andor Technology, 1024 Å~ 256 pixels, 26 μm). A TTL pulse synchronized with the Q-switch of the Infinity laser was delayed 99 ms before triggering the shutter for the probe light. Electronic delays were created with SRS DG535 delay generators (Stanford Research Systems). These delay boxes, in combination with electronic shutters (Uniblitz), were used to create the necessary pulse sequence.

Computational Details Calculations were performed using the Gaussian 09, Revision D.01 suite of software.[222] Geometry optimizations were carried out with the B3LYP functional[223-226] using the LANL08(f) basis set and corresponding ECP for Rh[227-

[229] and the 6-31G(d) basis set for other atoms. Frequency calculations at this level of theory confirmed that optimized geometries represent ground state structures.

III.4.2 Synthesis and Characterizations

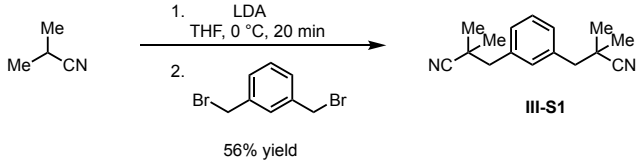

Synthesis of α,α,α',α'-tetramethyl-1,3-benzenedipropionitrile (III-S1) Compound **III-S1** was prepared according to the following modification of literature methods.[230] A 250-mL round-bottom flask was charged with $^{i}Pr_2NH$ (16.0 mL, 114 mmol, 3.49 equiv.) and THF (30.0 mL). ^{n}BuLi (2.50 M, 35.0 mL, 87.5 mmol, 2.68 equiv.) was slowly added to the solution at 0 °C and the reaction mixture was stirred for 10 min at this temperature. Isobutyronitrile (6.00 mL, 66.9 mmol, 2.05 equiv.) was added to the reaction mixture and stirred for 20 min at 0 °C. A solution of xylylene dibromide (8.60 g, 32.6 mmol, 1.00 equiv.) in 10.0 mL THF was slowly added to the reaction mixture at 0 °C and the reaction mixture was allowed to warm to 23 °C and was stirred for 10 h. 1 N HCl (200 mL) was added to the reaction mixture. The phases were separated and the aqueous phase was extracted with EtOAc. The combined organic phases were washed with brine, dried over Na_2SO_4, and concentrated *in vacuo* to obtain a yellow oil. Colorless crystals formed from the yellow oil which were collected over a frit, ground into powder, washed with hexanes and dried *in vacuo* overnight to obtain the title compound as white powder (4.42 g, 56% yield). ^{1}H NMR (δ, 23 °C, $CDCl_3$): 7.32 (t, J = 7.5 Hz, 1H), 7.22 (d, J = 10 Hz, 2H), 7.18

(s, 1H), 2.81 (s, 4H), 1.36 (s, 12H). ^{13}C NMR (δ, 23 °C, $CDCl_3$): 136.0, 132.2, 129.3, 128.6, 124.8, 46.6, 33.7, 26.7. Spectral data are well-matched to those reported in the literature.

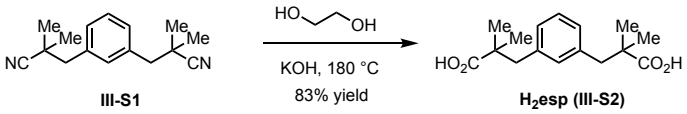

Synthesis of H_2esp (III-S2) Compound (**III-S2**) was prepared according to the following modification of literature methods.[230] A 100-mL Schlenk flask was charged with compound **III-S1** (4.42 g, 18.4 mmol, 1.00 equiv.) and ethylene glycol (10.0 mL). KOH (5.23 g, 93.4 mmol, 2.54 equiv.) was added and reaction mixture was heated at 180 °C for 12 h. The reaction mixture was then cooled to 23 °C and $CHCl_3$ (15.0 mL) and H_2O (15.0 mL) were added. The aqueous phase was separated and acidified (pH = 1) with 6 N HCl. The aqueous layer was extracted with EtOAc and the combined organic phase was sequentially washed with water and brine before being dried over Na_2SO_4. Solvent was removed *in vacuo* to obtain a yellow oil. The yellow oil was layered with hexanes (100 mL) to provide colorless crystals that were collected over a frit, ground into powder and washed with hexanes to obtain the title compound as white powder (4.25 g, 83% yield). ^{1}H NMR (δ, 23 °C, $CDCl_3$): 7.19 (t, J = 7.5 Hz, 1H), 7.01 (m, 3H), 2.83 (s, 4H), 1.18 (s, 12H). ^{13}C NMR (δ, 23 °C, $CDCl_3$): 184.0, 137.5, 131.5, 128.8, 127.7, 51.3, 46.4, 43.7, 24.6. Spectral data are well-matched to those reported in the literature.

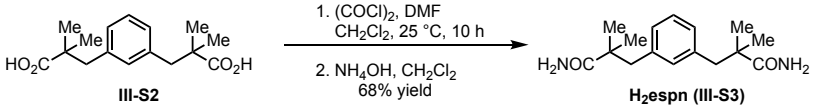

Synthesis of H_2espn (III-S3) Compound (**III-S3**) was prepared according to the following modification of literature methods.[197] A 100-mL Schlenk flask was charged with compound **III-S2** (2.32 g, 8.35 mmol, 1.00 equiv.) and CH_2Cl_2 (30.0 mL). The reaction vessel was purged with N_2 for 15 min. Oxalyl chloride (2.20 mL, 26.0 mmol, 3.11 equiv.) and DMF (0.50 mL) were added and the reaction mixture was stirred under N_2 for 10 h. Solvent was removed in vacuo and the residue was dissolved in CH_2Cl_2 (15.0 mL). The solution was cooled to 0 °C and NH_4OH (7 mL) was added to afford white precipitate. The precipitate was isolated by vacuum filtration and washed with Et_2O. The residue was dissolved in acetone and dried over Na_2SO_4. Solvent was removed *in vacuo* to afford the title compound as white solid (1.57 g, 68% yield). ^{1}H NMR (δ, 23 °C, $CDCl_3$): 7.16 (s, 1H), 7.03 (m, 3H), 5.56 (d, J = 80 Hz, 4H), 2.80 (s, 4H), 1.19 (s, 12H). ^{13}C NMR (δ, 23 °C, $CDCl_3$): 180.1, 137.7, 132.1, 128.6, 127.8, 47.0, 43.6, 25.5. Spectral data are well-matched to those reported in the literature (**Figures III-16–III-17**).

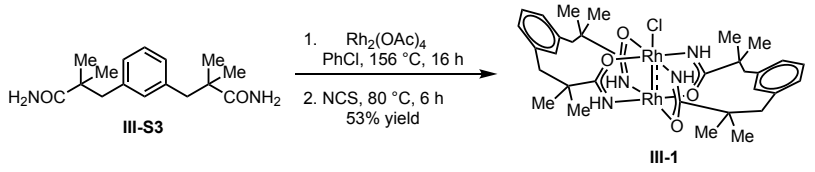

Synthesis of Rh_2(espn)$_2$Cl (III-1) Complex (**III-1**) was prepared according to the following modification of literature methods.[197] A 200-mL round-bottom flask was

charged with $Rh_2(OAc)_4$ (198 mg, 0.448 mmol, 1.00 equiv.) and **III-S3** (305 mg, 1.10 mmol, 2.46 equiv.). Chlorobenzene (50 mL) was added and the resulting mixture was heated to reflux for 16 h. The reaction mixture was cooled to 80 °C and NCS (61.0 mg, 0.459 mmol, 1.02 equiv.) was added and the mixture was stirred for 6 h. The reaction mixture was cooled to 23 °C and solvent was removed *in vacuo*. The residue was purified on a silica gel column with CH_2Cl_2/acetone as a linear gradient eluent system (v/v: 100/0 to 80/20) to afford the title complex as a red powder (0.185 g, 53% yield). Single crystals were obtained by layering a CH_2Cl_2 solution with equal volumes of acetone at 0 °C and the unit cell of these crystals [a = 12.707(1), b = 13.695(1), c = 14.901 (2); α = 71.402(6)°, β = 65.947(6)°, γ = 66.828(6)°, V = 2137.8(4)] was well-matched to the reported unit cell. Crystals with a different unit cell [a = 10.903(2), b = 12.584(2), c = 16.899(2); α = 90.655(2)°, β = 102.953(2)°, γ = 105.320(2)°, V = 2173.1(5)] were obtained by crystallization of **III-1** from a concentrated CH_3CN solution at 0 °C and at –35 °C. μ_{eff} = 1.84 (Evans method). ^{1}H NMR (δ, 23 °C, $CDCl_3$): 7.48 (br), 2.58 (br), 2.35 (br), 1.25 (br), 0.25 (br), –0.83 (br), –2.47 (br). UV-vis (CH_3CN), λ_{max} (nm, ε ($M^{-1}cm^{-1}$)): 463 (2.6×10^3). IR (cm^{-1}): 3582 (w), 3384 (m), 2950 (m), 1588 (m), 1482 (s), 1352 (s), 1261 (s), 1177 (s), 903 (s), 812 (s), 705 (s).

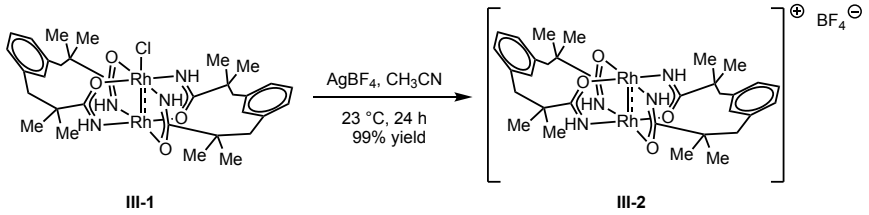

III-1 III-2

Synthesis of $[Rh_2(espn)_2]BF_4$ (III-2) A 100-mL round-bottom flask was charged with $Rh_2(espn)_2Cl$ (**III-2**) (0.352 g, 0.445 mmol, 1.00 equiv.) and CH_3CN (50.0 mL) inside an N_2 glovebox. Separately, a 40-mL vial was charged with $AgBF_4$ (0.0890 g, 0.457 mmol, 1.02 equiv.) and CH_3CN (5.0 mL). The two solutions were combined and the resulting reaction mixture was stirred at 23 °C for 24 h. The reaction mixture was filtered through a Celite plug. Solvent was removed from the filtrate *in vacuo* to obtain the title compound as a dark brown powder (0.410 g, 99% yield). Single crystals of **III-2** were obtained by vapor diffusion of a CH_3CN solution in Et_2O at –35 °C. ^1H NMR (δ, 23 °C, CD_3CN): 11.50 (br), 7.54 (br), 7.39 (br), 5.64 (br), 3.08 (br), 1.00 (br), 0.54 (br). UV-vis (CH_3CN), λ_{max} (nm, ε ($M^{-1}cm^{-1}$)): 469 (2.1×10^3). IR (cm^{-1}): 3369 (m), 3194 (m), 2950 (m), 2349 (w), 1771 (s), 1680 (s), 1482 (s), 1352 (s), 1284 (m), 1170 (s), 1048 (s), 895 (m), 812 (m), 713 (s), 621 (s). Elemental analysis (EA): calculated for $[Rh_2(espn)_2BF_4](CH_3CN)_{2.9}(CH_2Cl_2)_{2.9}$: C, 40.51; H, 4.89, N, 8.01; F, 6.30; found C, 40.01; H, 4.68; N, 8.76; F, 7.13. ^1H NMR confirmed the presence of CH_2Cl_2 in sample.

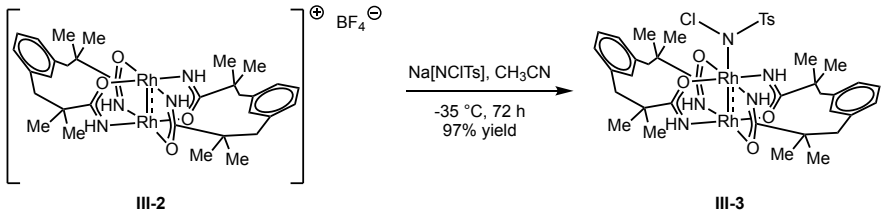

Synthesis of Rh2(espn)2(NTsCl) (III-3) A 100-mL round-bottom flask was charged with $[Rh_2(espn)_2]BF_4$ (**III-2**) (389 mg, 0.421 mmol, 1.00 equiv.) and CH_3CN (50 mL) inside an N_2 glovebox. Separately, a 40-mL vial was charged with Na[NTsCl] (130 mg, 0.462 mmol, 1.09 equiv.) and dissolved in CH_3CN (5 mL). The two solutions were first cooled to –35 °C and then combined and kept at –35 °C for 72 h with occasional shaking. The cold reaction mixture was filtered through a Celite plug and solvent was removed *in vacuo* at –50 °C to obtain the title compound **III-3** as a red powder (410 mg, 97% yield). Single crystals were obtained from a concentrated CH_3CN solution at –35 °C. $\mu_{eff} = 1.55$ (Evans method). ^{1}H NMR (δ, 23 °C, CD_3CN): 8.79 (br), 7.74 (d), 7.54 (br), 7.38 (d), 7.09 (m), 5.97 (br), 5.59 (br), 2.80 (s), 2.60 (s), 2.42 (s), 2.27 (s), 1.77 (s), 1.32 (s), 0.67 (br), –0.76 (br). UV-vis (CH_3CN), λ_{max} (nm, ε ($M^{-1}cm^{-1}$)): 461 (3.5×10^3). IR (cm^{-1}): 3346 (m), 2958 (m), 2243 (w), 1771 (m), 1702 (s), 1482 (s), 1352 (m), 1238 (m), 1177 (s), 1124 (s), 1079 (s), 895 (s), 820 (s), 698 (s), 621 (s). Elemental analysis (EA): calculated for $[Rh_2(espn)_2(NTsCl)](CH_3CN)(CH_2Cl_2)_{0.4}$: C, 48.08; H, 5.34, N, 8.13; Cl, 6.17; found C, 47.62; H, 5.65; N, 7.59; Cl, 6.10. ^{1}H NMR confirmed the presence of CH_2Cl_2 in sample.

Synthesis of $Rh_2(espn)_2(^{15}NTsCl)$ (^{15}N-III-3) Na[^{15}NTsCl] was prepared according to the following two-step procedure, which is modified from literature methods.[231-232] A 25-mL round-bottom flask was charged with *p*-toluenesulfonyl chloride (723 mg, 3.79 mmol,

1.81 equiv.), $^{15}NH_4Cl$ (113 mg, 2.09 mmol, 1.00 equiv.), and distilled water (10 mL). The reaction mixture was heated at 50 °C and $KHCO_3$ (613 mg, 6.13 mmol, 2.93 equiv.) was added. The reaction mixture was then refluxed at 100 °C for 10 h. The reaction mixture was cooled to 0 °C for 4 h. The obtained precipitate was isolated by vacuum filtration, washed with cold water, and dried *in vacuo* to obtain $Ts^{15}NH_2$ as white solid (0.168 g, 47% yield). ^1H NMR (δ, 23 °C, $CDCl_3$): 7.82 (d, J = 9 Hz, 2H), 7.32 (d, J = 6 Hz, 2H), 4.73 (d, J = 81 Hz, 2H), 2.44 (s, 3H). Spectral data are well-matched to those reported in the literature.

An 8-mL vial was charged with $Ts^{15}NH_2$ (160 mg, 0.930 mmol, 1.00 equiv.) and 2N NaOH (1.0 mL). Trichloroisocyanuric acid (165 mg, 0.710 mmol, 0.763 equiv.) was added and the reaction mixture was stirred at 23 °C for 4 h. The reaction mixture was cooled to 0 °C and was stirred at this temperature for 12 h. The resulting precipitate was isolated by vacuum filtration, washed with cold water, and then dried *in vacuo* to afford Na[^{15}NTsCl] as white solid (0.209 mg, 80% yield). ^1H NMR (δ, 23 °C, D_2O): 7.70 (d, J = 9 Hz, 2H), 7.40 (d, J = 9 Hz, 2H), 2.40 (s, 3H). Spectral data are well-matched to those reported in the literature.

A 20-mL round-bottom flask was charged with $[Rh_2(espn)_2]BF_4$ (**III-2**) (69.0 mg, 0.0750 mmol, 1.00 equiv.) and CH_3CN (3.0 mL) inside an N_2 glovebox. Simultaneously, a 20-mL vial was charged with Na[^{15}NTsCl] (23.0 mg, 0.0810 mmol, 1.10 equiv.) and CH_3CN (2.0 mL). The two solutions were first cooled to –35 °C and then combined and kept at –35 °C for 72 h with occasional shaking. The resulting reaction mixture was filtered cold through a Celite plug and solvent was removed *in vacuo* cold to afford ^{15}N-**III-3** as a red

powder (65.0 mg, 87% yield). UV-vis (CH_3CN), λ_{max} (nm, ε ($M^{-1}cm^{-1}$)): 461 (3.5×10^3). IR (cm^{-1}): 2927 (w), 2249 (w), 1775 (m), 1709 (s), 1643 (m), 1585 (m), 1454 (m), 1345 (m), 1250 (m), 1155 (s), 1074 (s), 900 (m), 812 (s), 703 (s), 652 (s). ^1H NMR data were identical to those of the unlabeled complex.

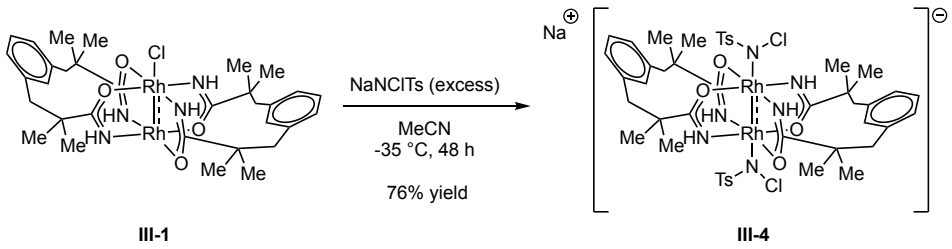

Synthesis of $Na[Rh_2(espn)_2(NTsCl)_2]$ (III-4) A 20-mL vial was charged with $Rh_2(espn)_2Cl$ (**III-1**) (36.0 mg, 0.0460 mmol, 1.00 equiv.) and CH_3CN (2.0 mL) inside an N_2-filled glovebox. A second 20-mL vial was charged with Na[NTsCl] (36.0 mg, 0.128 mmol, 2.78 equiv.) and CH_3CN (3.0 mL). The two solutions were cooled to –35 °C, combined, and kept at –35 °C for 48 h with occasional shaking. The resulting reaction mixture was filtered through a Celite plug at –35 °C and solvent was removed *in vacuo* to afford compound **III-4** as a red powder (42.0 mg, 76% yield). Single crystals were obtained by layering a concentrated CH_2Cl_2 solution with acetone at –35 °C. ^1H NMR (δ, 23 °C, CD_3CN): 8.80 (br), 7.74 (d), 7.51 (d), 7.37 (d), 7.11 (d), 5.99 (br), 5.60 (br), 2.79 (s), 2.60 (s), 2.30 (br), 0.50 (br) -1.25 (br). UV-vis (CH_3CN), λ_{max} (nm, ε ($M^{-1}cm^{-1}$)): 455 (2.1×10^3).

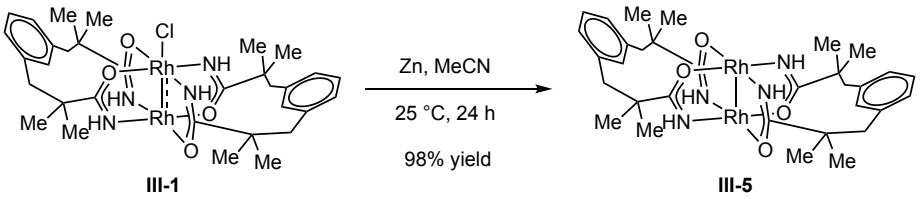

III-1 III-5

Synthesis of $Rh_2(espn)_2$ (III-5) A 20-mL vial was charged with $Rh_2(espn)_2Cl$ (**III-1**) (46.0 mg, 0.0580 mmol, 1.00 equiv.), zinc granules (139 mg, 2.14 mmol, 36.9 equiv.), and CH_3CN (3.0 mL) inside an N_2 glovebox. The reaction mixture was stirred at 23 °C for 24 h and was then filtered through a Celite plug. Solvent was removed *in vacuo* from the obtained filtrate to afford the title compound as green solid (43.0 mg, 98% yield). Single crystals were obtained by slow evaporation of a concentrated CH_3CN solution at –35 °C. ^1H NMR (δ, 23 °C, CD_3CN): 8.91 (br, 4H), 7.24–7.00 (m, 8H), 6.82 (br, 2H), 2.60 (s, 24H), 1.31 (s, 8H). UV-vis (CH_3CN), λ_{max} (nm, ε ($M^{-1}cm^{-1}$)): 535 (1.1×10^2). IR (cm^{-1}): 1782 (m), 1695 (s), 1637 (m), 1585 (m), 1469 (m), 1424 (m), 1359 (m), 1257 (s), 1184 (s), 1053 (m), 732 (s). Elemental analysis (EA): calculated for $[Rh_2(espn)_2](CH_3CN)_4(CH_2Cl_2)_{2.2}$: C, 45.85; H, 5.51, N, 10.14; found C, 45.86; H, 5.37; N, 10.19. ^1H NMR confirmed the presence of CH_2Cl_2 in sample.

III.4.3 Intermolecular C–H amination by photolysis of $Rh_2(espn)_2(NTsCl)$

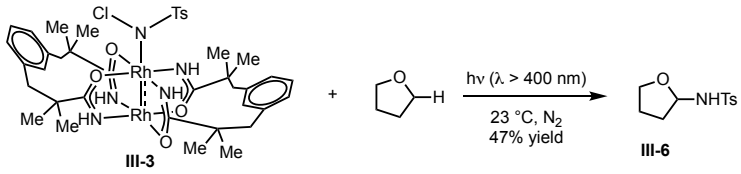

A 20-mL vial was charged with $Rh_2(espn)_2(NTsCl)$ (**III-3**, 25.0 mg, 0.0250 mmol, 1.00 equiv.) and dissolved in THF (4.0 mL) inside an N_2-filled glovebox. The reaction mixture was photolyzed for 10 h while stirring at 23 °C using a 100 W Hg lamp with a 400 nm longpass filter. The reaction mixture was concentrated *in vacuo* and the resulting residue was purified by column chromatography with EtOAc / hexanes as a linear gradient eluent system (v/v: 0/100 to 80/20) to afford tosylamide **III-6** (2.8 mg, 47% yield). The isolated yield agreed with the product yield determined by ^{1}H NMR (against mesitylene added as a standard). Triplicate determination of the reaction yield indicated the yield of **III-6** to be 48 ± 2%. ^{1}H NMR (δ, 23 °C, $CDCl_3$): 7.79 (d, J = 10 Hz, 2H), 7.27 (d, J = 10 Hz, 2H), 5.90 (d, J = 10 Hz, 1H), 5.33 (m, 1H), 3.66 (m, 2H), 2.40 (s, 3H), 2.11 (m, 1H), 1.89 (m, 1H), 1.79 (m, 2H). ^{13}C NMR (δ, 23 °C, $CDCl_3$): 143.3, 138.6, 129.5, 127.1, 85.0, 67.2, 32.6, 24.0, 21.6. Based on the ^{1}H NMR (against mesitylene added as a standard) the yield of free $TsNH_2$ is 45 ± 3%. From the molar absorptivity data and the UV-vis spectra reported in **Figure III-8**, the yield of **III-5** is 100%.

Replacing THF as the reaction solvent with 2-methyltetrahydrofuran (2-Me-THF) resulted in the evolution of 4-methyl-N-(5-methyltetrahydrofuran-2-yl)benzenesulfonamide in 44 ± 1% yield. Use of toluene as the reaction solvent afforded N-benzyl-4-

methylbenzenesulfonamide in 0.5% yield. Yields are based on ^{1}H NMR spectroscopy using mesitylene as internal standard and were measured in triplicate.

III.4.4 KIE Determination for Photochemical Amination

KIE for amination of THF by photolysis of III-3 A 20-mL vial was charged with either Rh_2 complex **III-3** (48.0 mg, 0.0480 mmol, 1.00 equiv.) and dissolved in a 1:1 THF:THF-d_8 mixture (4.0 mL) inside an N_2-filled glovebox. The reaction mixture was photolyzed for 10 h while stirring at 23 °C using a 100 W Hg lamp using a 325–385 nm bandpass filter. Solvent was removed *in vacuo* and the product was purified by preparative TLC using 20% EtOAc : hexanes as eluent. Based on the ^{1}H NMR (against mesitylene added as a standard) the yield of the product was 48 ± 2%. The KIE was determined by integrating the $[M–Na]^+$ peaks at 264.0670 versus 271.1110 using HR-ESI-MS. The reaction was performed in triplicate.

KIE for amination of THF by photolysis of TsN_3 A 20-mL vial was charged with TsN_3 (0.200 g, 1.02 mmol, 1.00 equiv.) and dissolved in a 1:1 THF:THF-d_8 mixture (4.0 mL) inside an N_2-filled glovebox. The reaction mixture was then photolyzed for 10 h while stirring at 23 °C using a 100 W Hg lamp. Solvent was removed *in vacuo* and the product was purified by preparative TLC using 20% EtOAc : hexanes as eluent. Based on the ^{1}H NMR (against mesitylene added as a standard) the yield of the product was 7.2%. The KIE was determined by integrating the $[M–Na]^+$ peaks at 264.0670 versus 271.1110 using HR-ESI-MS. The reaction was performed in triplicate.

KIE for amination of THF by photolysis of Na[NTsCl] A 20-mL vial was charged with Na[NTsCl] (55.0 mg, 0.195 mmol, 1.00 equiv.) and dissolved in a 1:1 THF:THF-d_8 mixture (4.0 mL) inside an N_2-filled glovebox. The reaction mixture was then photolyzed for 10 h while stirring at 23 °C using a 100 W Hg lamp using a 325–385 nm bandpass filter. Solvent was removed *in vacuo* and the product was purified by preparative TLC using 20% EtOAc : hexanes as eluent. Based on the ^{1}H NMR (against mesitylene added as a standard) the yield of the product was 63%. The KIE was determined by integrating the $[M–Na]^+$ peaks at 264.0670 versus 271.1110 using HR-ESI-MS. The reaction was performed in triplicate.

KIE for amination of THF by thermolysis of III-3 A 20-mL vial was charged with Rh_2 complex **III-3** (125 mg, 0.130 mmol, 1.00 equiv.) and dissolved in a 1:1 THF : THF-d_8 mixture (4.0 mL) inside an N_2-filled glovebox. The reaction mixture was kept in dark for 10 h while stirring at 23 °C. Solvent was removed *in vacuo* and the product was purified by preparative TLC using 20% EtOAc : hexanes as eluent. Based on the ^{1}H NMR (against mesitylene added as a standard) the yield of the product was 8.6%. The KIE was determined to be 5.95 by integrating the $[M–Na]^+$ peaks at 264.0670 versus 271.1110 using HR-ESI-MS.

III.4.5 Detection of Photochemical Generation of HCl using NEt_3

A 20-mL vial was charged with $Rh_2(espn)_2(NTsCl)$ (**III-3**, 103.0 mg, 0.107 mmol, 1.00 equiv.) and dissolved in THF (5.0 mL) inside an N_2-filled glovebox. The reaction vial was taken out of the glovebox and photolyzed for 10 h while stirring at 23 °C using a

100 W Hg lamp with a 400 nm longpass filter. Then, NEt_3 (100 μL, 0.718 mmol, 6.71 equiv.) was added to the solution mixture and was stirred for 30 min. Solvent was removed *in vacuo* at 40 °C (to remove excess solvent and NEt_3). The presence of HCl following photolysis was confirmed by formation of triethylammonium hydrochloride which was observed both by ^{1}H (**Figure III-11**) and ^{13}C NMR (**Figure III-12**) spectroscopies, measured in $CDCl_3$.

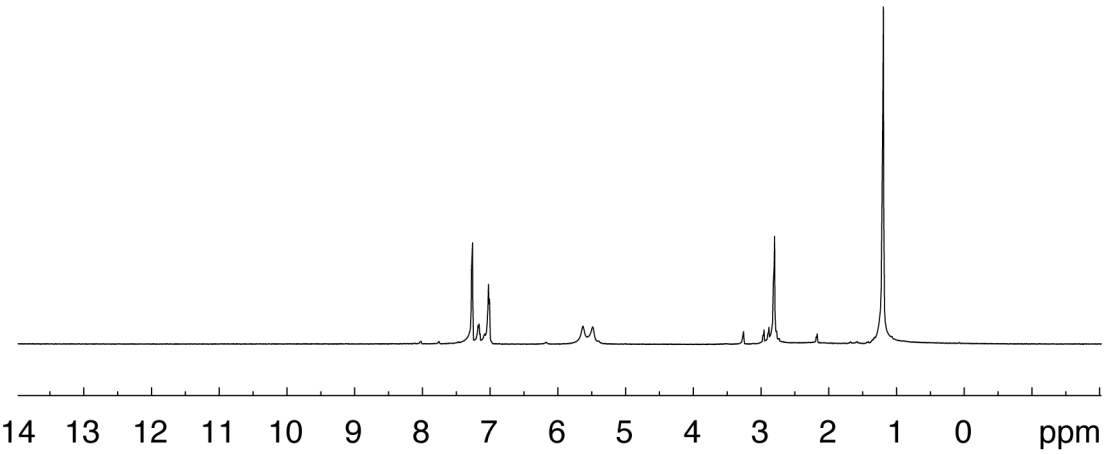

Figure III-16. ^{1}H NMR spectrum of compound III-S3 recorded in $CDCl_3$ at 23 °C.

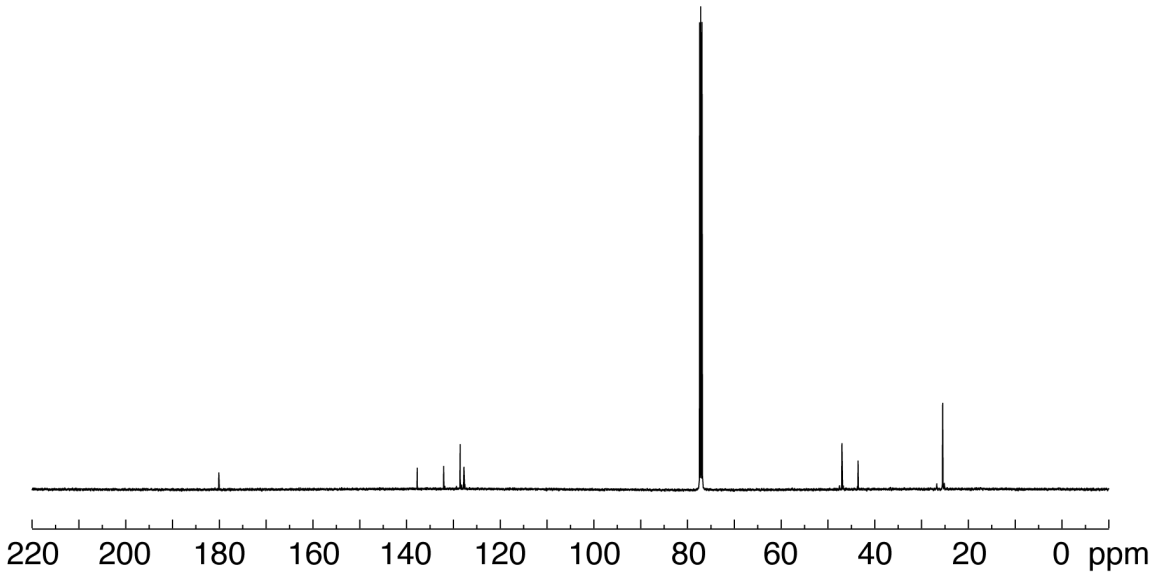

Figure III-17. ^{13}C NMR spectrum of compound III-S3 recorded in $CDCl_3$ at 23 °C.

CHAPTER IV

CHARACTERIZATION OF A REACTIVE DIRHODIUM NITRENOID BY CRYSTALLINE MATRIX ISOLATION*

IV.1. Introduction

Unstabilized nitrenes are reactive, high-energy species that feature a hextet electronic configuration at nitrogen (i.e., N–R species).[31, 233] Nitrenes participate in a diverse reaction manifold, including C–H insertion, addition to C–C multiple bonds, and various unimolecular rearrangements, that render these species challenging to utilize as intermediates in selective synthetic chemistry.[191] Synthetic chemists[17, 49, 189, 192, 234-236] and biologists[63, 190, 237] have advanced selective nitrene-transfer chemistry that is predicated on leveraging the reactivity of transition metal-stabilized nitrenoid intermediates for C–H functionalization and olefin aziridination. In particular, Rh_2-catalysis has emerged as a broadly useful platform in nitrene-transfer catalysis (**Figure IV-1**).[58, 60, 195-196, 198, 238-240] Critical Rh_2 nitrenoid intermediates have been detected by mass spectrometry[200] and time-resolved spectroscopic methods,[241] but due to their fleeting lifetimes, structural data of these transient species has not been available. Significant questions, such as the preferred electronic configuration of Rh_2 nitrenoids, have not been resolved despite extensive theoretical interest.[30, 242-243]

---

* Data, figures, and text in this chapter were adapted with permission from "Characterization of a Reactive Rh_2 Nitrenoid by Crystalline Matrix Isolation" by Das, A.; Chen, Y.-S.; Reibenspies, J. H.; Powers, D. C. *J. Am. Chem. Soc.* **2019**, *141*, 16232–16236. Copyright 2019 American Chemical Society.

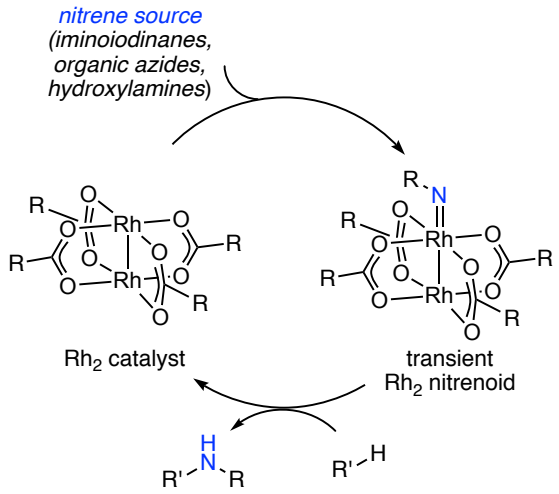

Figure IV-1. Rh_2-catalyzed nitrene transfer chemistry has emerged as a leading method for introducing nitrogen content in organic molecules. These reactions are proposed to proceed via transient Rh_2 nitrenoids, which have thus far eluded structural characterization.

Unambiguous molecular structure determination can be achieved by X-ray diffraction, but requires chemical samples that are sufficiently kinetically stable to be crystallized. The inherently transient nature of reactive intermediates typically precludes application of X-ray diffraction to the characterization of these species. Two methods have been advanced to gain structural information about reactive intermediates in the condensed phase: (1) structural characterization of synthetic derivatives designed to attenuate the reactivity of the intermediate of interest, for example via introduction of sterically encumbering ligands,[202, 244-246] and (2) spectroscopic characterization of photogenerated reactive intermediates by cryogenic matrix isolation.[247] We envisioned that photogeneration of reactive intermediates within a crystalline matrix would combine classical matrix isolation with X-ray diffraction and enable structural characterization of

these species without synthetic derivatization.[204] In this chapter, we demonstrate the successful application of this strategy to the characterization of a Rh_2 nitrenoid generated by N_2 elimination from a Rh_2 alkylazide complex within a crystalline matrix.

IV.2. Results and Discussions

We targeted characterization of a nitrenoid supported by $Rh_2(esp)_2$ (**IV-1**), in which the Rh_2 core is supported by two chelating *bis*-carboxylate ligands,[198] because complex **IV-1** has emerged as a particularly effective, and widely utilized, nitrene-transfer catalyst.[192, 195-196, 239-240] We initiated our studies by exploring the synthesis of Rh_2 complexes with organic azide ligands based on the hypothesis that facile N_2 extrusion would provide access to Rh_2 nitrenoids. Exposure of $Rh_2(esp)_2$ to CH_2Cl_2 solutions of AdN_3 resulted in sequential formation of two Rh_2 azide adducts: $Rh_2(esp)_2(AdN_3)$ (**IV-2a**) and $Rh_2(esp)_2(AdN_3)_2$ (**IV-2b**). Concentration-dependent UV-vis spectra display isosbestic points connecting $Rh_2(esp)_2$ (**IV-1**) and $Rh_2(esp)_2(AdN_3)$ (**IV-2a**) at 0–12 mM [AdN_3] and isosbestic points connecting **IV-2a** and $Rh_2(esp)_2(AdN_3)_2$ (**IV-2b**) at 12–85 mM [AdN_3] implying the absence of steady-state intermediates in these reactions (**Figure IV-2**). Further spectral evolution was not observed upon further addition of AdN_3. Jobs analysis confirms that xx is a 1 : 1 adduct of $Rh_2(esp)_2$ and AdN_3 (**Figure IV-3** and **Table IV-1**). Rapid exchange of free and bound AdN_3 is evident in the room temperature ^1H NMR spectra of **IV-2a** and **IV-2b**. Low-temperature ^1H NMR spectroscopy and electrospray ionization-mass spectrometry (ESI-MS) support the formulation of **IV-2a** and **IV-2b** as mono- and *bis*-azide adducts, respectively (**Figures IV-4–IV-5**). The AdN_3

ligands are weakly bound; titration of a tetrahydrofuran solution of $Rh_2(esp)_2$ with AdN_3 results in no spectral changes, which suggests AdN_3 does not displace bound THF ligands at the apical sites of $Rh_2(esp)_2$.

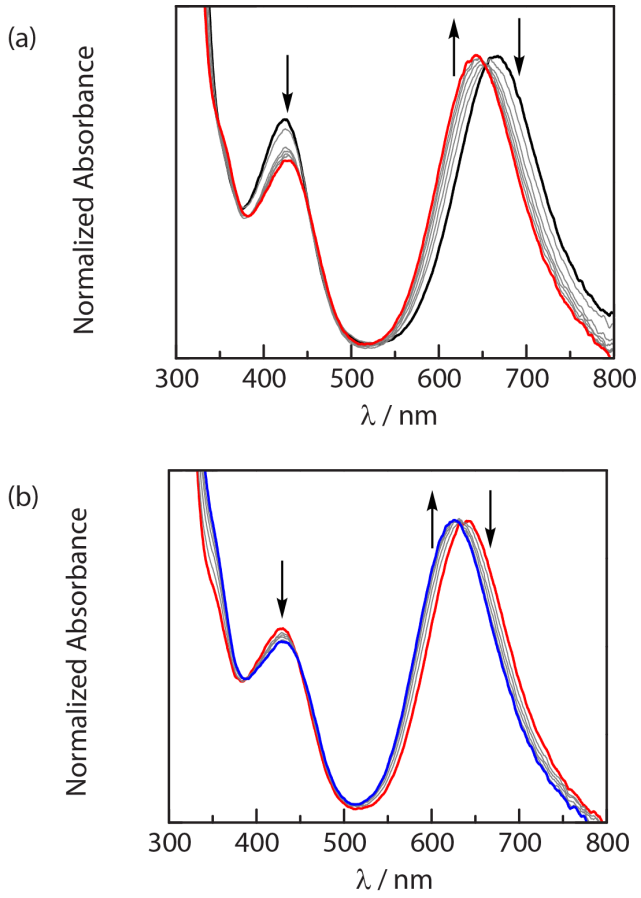

Figure IV-2. UV-vis spectra obtained during titration of Rh_2 complex IV-1 with AdN_3. Spectra were collected in CH_2Cl_2 at 23 °C. The initial concentration of complex **IV-1** was 0.00329 M. (a) UV-vis spectra collected at [AdN_3] of 0–0.0116 M. The well-anchored isosbestic points at 654 and 445 nm indicate the absence of steady-state intermediates in the conversion of **IV-1** (—) to **IV-2a** (—). (b) UV-vis spectra collected at [AdN_3] of 0.0164–0.0847 M. The well-anchored isosbestic points at 634 and 447 nm indicate the absence of steady-state intermediates in the conversion of **IV-2a** (—) to **IV-2b** (—).

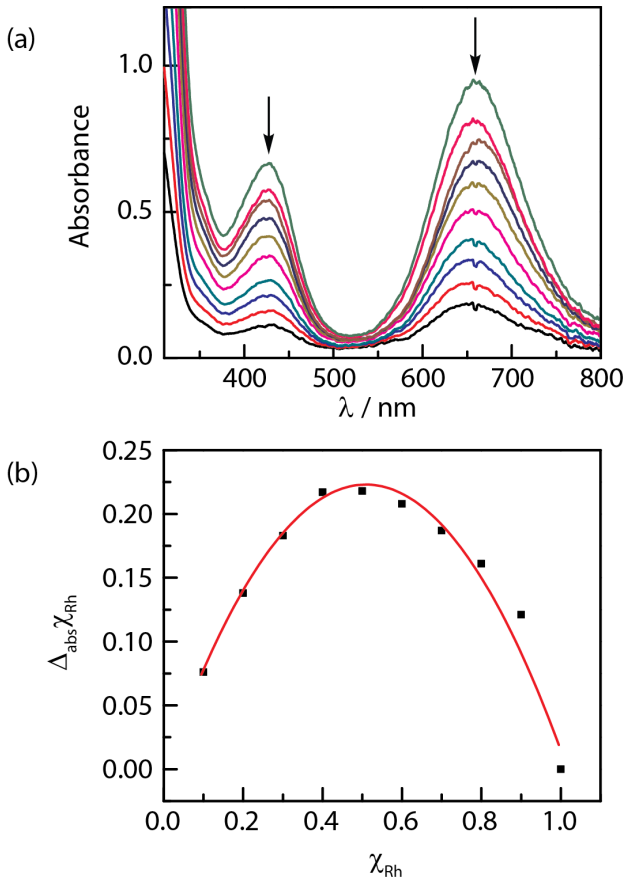

Figure IV-3. Jobs plot generated from addition of AdN_3 to compound IV-1. (a) UV-vis obtained in CH_2Cl_2 at 23 °C with [**IV-1** + AdN_3] = 3.520 mM. (b) Plot of absorbance at 667 nm as a function of χ_{Rh}. The absorbance data is tabulated in Table IV-1. The Jobs plot suggests a 1:1 complex of **IV-1** with AdN_3. The maximum is slightly less than χ_{Rh} due to the presence of more than two equilibrating species (i.e., **IV-1**, **IV-2a**, and **IV-2b**).[248-249]

Table IV-1. Absorbance at 667 nm of IV-1 as a function of χ_{Rh}. Spectra were recorded at 23 °C in CH_2Cl_2 with [**IV-1** + AdN_3] = 3.520 mM.

Entry	χ_{Rh}	[**IV-1**] mM	[AdN_3] mM	Absorbance	Δ_{abs}
1	1.0	3.520	0	0.943	0.000
2	0.9	3.168	0.352	0.809	0.134
3	0.8	2.816	0.704	0.742	0.201
4	0.7	2.464	1.056	0.676	0.267
5	0.6	2.112	1.408	0.596	0.347
6	0.5	1.760	1.760	0.507	0.436
7	0.4	1.408	2.112	0.400	0.543
8	0.3	1.056	2.464	0.333	0.610
9	0.2	0.704	2.816	0.253	0.690
10	0.1	0.352	3.168	0.186	0.757

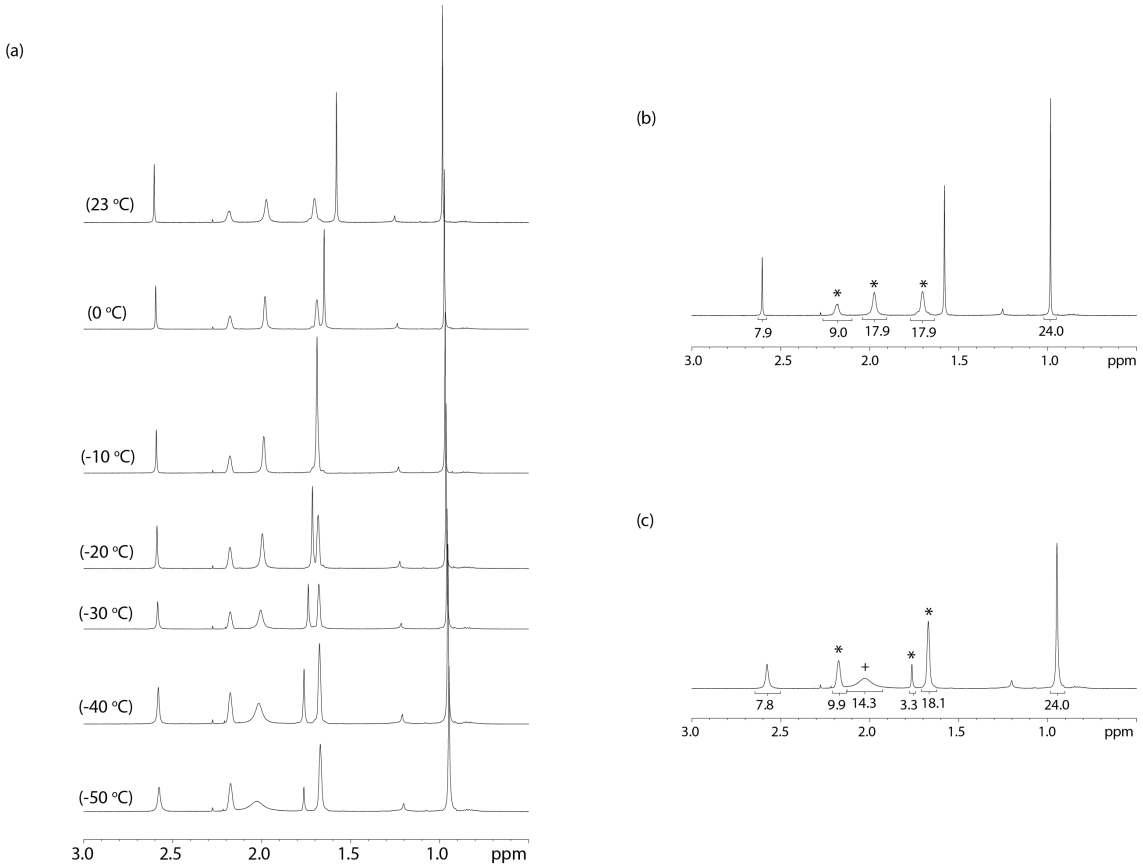

Figure IV-4. Temperature-dependent ^{1}H NMR spectra of IV-2a in $CDCl_3$. (a) Expansion of the spectral window from 3.0–0.5 ppm depicting the change in resonance signals for the coordinated and uncoordinated AdN_3. (b) Expansion of the spectral window from 3.0–0.5 ppm for **IV-2a** at 23 °C. The indicated peaks are attributed to AdN_3. (c) Expansion of the spectral window from 3.0–0.5 ppm for **IV-2a** at −50 °C. The peaks indicated by (*) are attributed to free AdN_3 and (+) are for coordinated AdN_3. The integration of the resonances attributed to AdN_3 at 23 °C indicate that, coordinated and free AdN_3 are indistinguishable as they are in equilibrium, whereas, at −50 °C they can be distinguished.

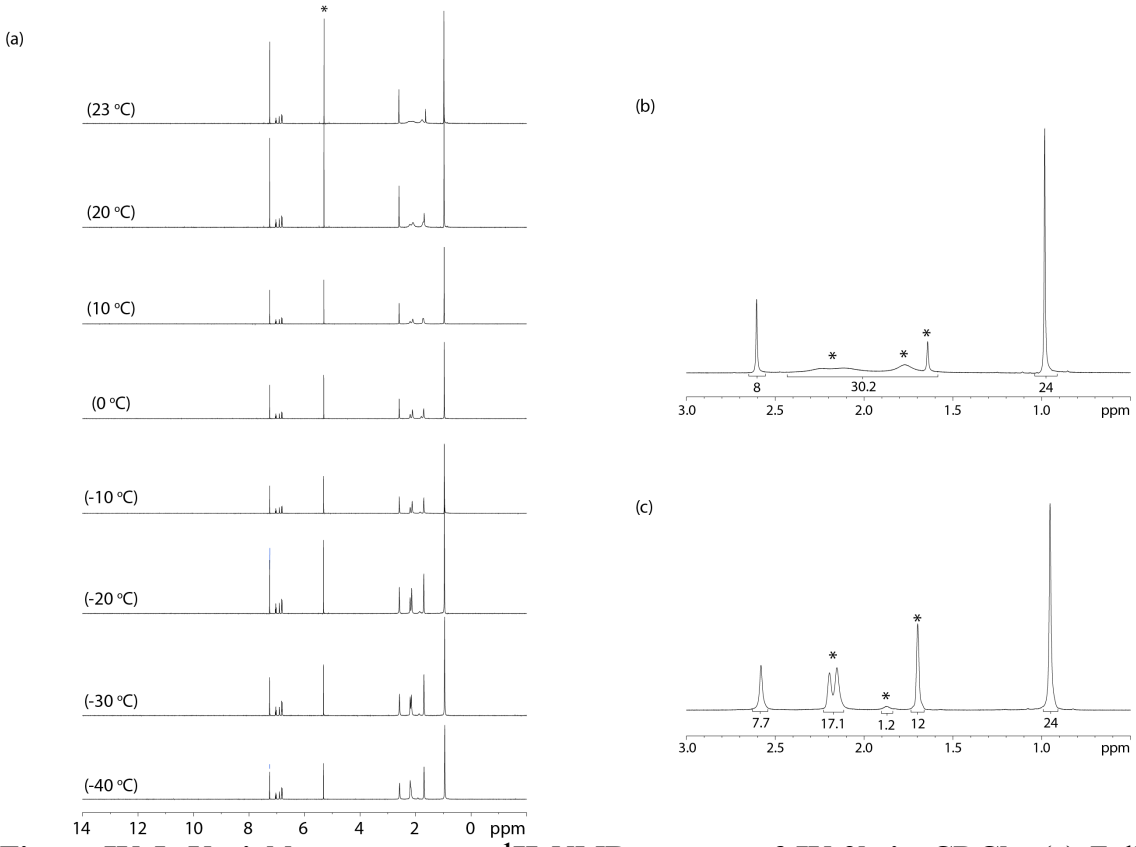

Figure IV-5. Variable-temperature ^{1}H NMR spectra of IV-2b in $CDCl_3$. (a) Full spectral range; the signals attributable to AdN_3 sharpen as the temperature is reduced. The indicated peak corresponds to CH_2Cl_2 that is present in the crystal structure. (b) Expansion of the spectral window from 3.0–0.5 ppm for **IV-2b** at 23 °C. The indicated peak corresponds to coordinated AdN_3. (c) Expansion of the spectral window from 3.0–0.5 ppm for **IV-2b** at –40 °C. The indicated peak corresponds to coordinated AdN_3. The integration of the resonances attributed to AdN_3 at both 23 °C and –40 °C reflect the binding of two AdN_3 ligands as depicted in the structure of **IV-2b**.

Single crystals of **IV-2b** were obtained from cooling a CH_2Cl_2 solution of $Rh_2(esp)_2$ and AdN_3. X-ray diffraction analysis revealed the structure depicted in **Figure IV-6a** in which two symmetry-equivalent AdN_3 ligands are bound to the Rh_2 core via N(α). Efforts to crystallize **IV-2a** by lowering the AdN_3 loading consistently provided *bis*-

azide adduct **IV-2b** as the exclusive crystallization product, which suggests the preferential crystallization of **IV-2b** over mono-azide adduct **IV-2a**. The Rh–Rh distance in **IV-2b** (2.3968(8) Å) is similar to that previously reported for $Rh_2(esp)_2L_2$ complexes (L = solvent-derived ligands, see **Table IV-2**). The N_3 fragment of the AdN_3 ligand is nearly linear (N(1)–N(2)–N(3) = 176.2(4)°), the N(1)–N(2) and N(2)–N(3) distances are similar to those in free AdN_3, and the infrared (IR) spectrum of **IV-2b** displays ν_{N3} at 2120 and 2093 cm^{-1} (**Figure IV-7**). These metrics are consistent with AdN_3 binding as a σ-donor with insignificant π-backbonding.[250-252]

Table IV-2. Analysis of the Rh–Rh distance in $Rh_2(esp)_2L_2$ complexes.

Ligand	Rh–Rh / Å	Reference
Acetone	2.382	*J. Am. Chem. Soc.* **2004**, *126*, 15378.
Chloride	2.360	*Chem. Eur. J.* **2011**, *17*, 5827.
Pyridine	2.402	*Inorg. Chem.* **2015**, *54*, 8817.
3-methylpyridine	2.406	*Inorg. Chem.* **2015**, *54*, 8817.
2,6-dimethylpyridine	2.421	*Inorg. Chem.* **2015**, *54*, 8817.
CH_3CN	2.392	*Inorg. Chem.* **2015**, *54*, 8817.
CH_3OH	2.377	*Inorg. Chem.* **2015**, *54*, 8817.
CH_3COOH	2.378	*Eur. J. Inorg. Chem.* **2012**, 562.
1-methoxy-2-(methylsulfinyl)benzene (O-bound)	2.380	*J. Org. Chem.* **2016**, *81*, 129.
1-methoxy-2-(methylsulfinyl)benzene (S-bound)	2.410	*J. Org. Chem.* **2016**, *81*, 129.
(2,2,2-trichloroethoxysulfonyl)amide	2.407	*ChemPhotoChem* **2017**, *1*, 562.
Average	2.392 ± 0.018	

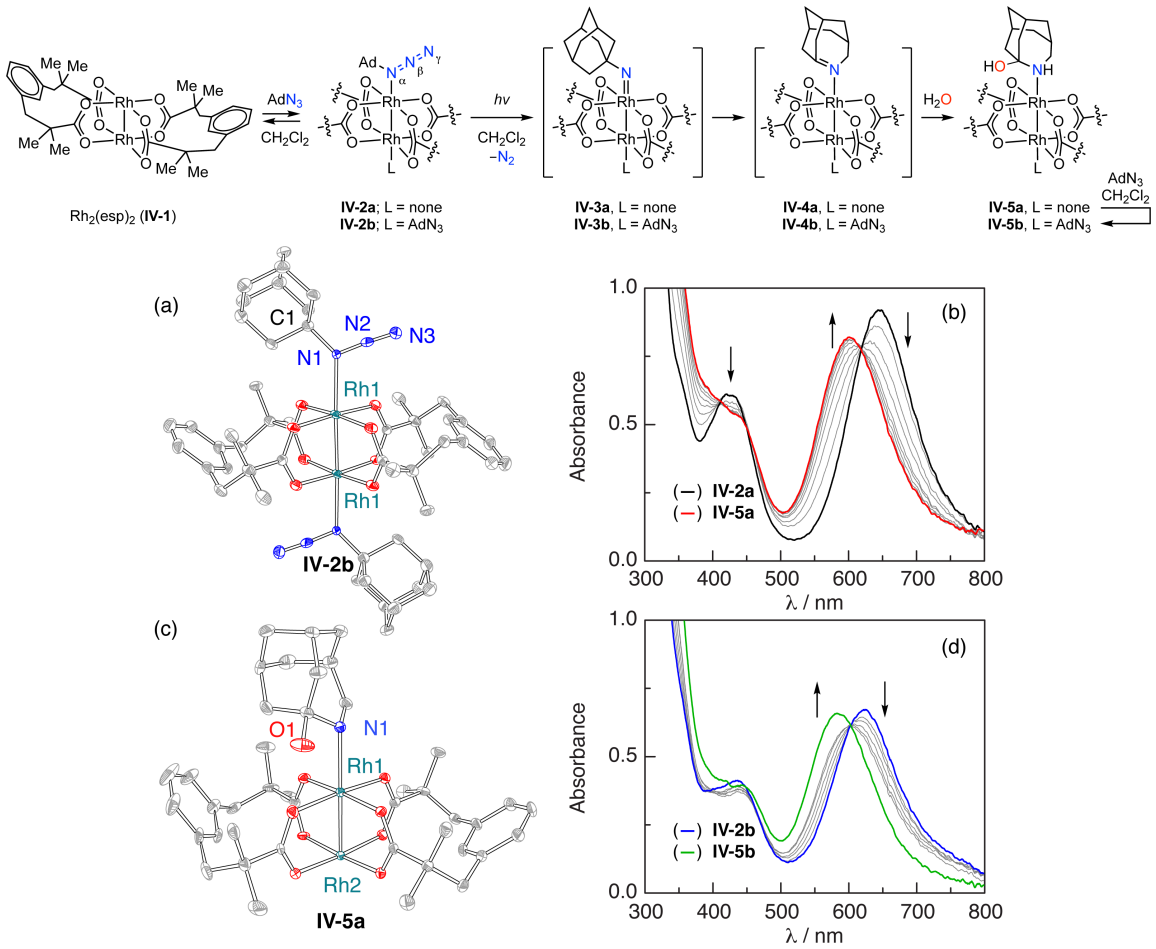

Figure IV-6. Synthesis and steady-state photochemistry of organoazide complexes of $Rh_2(esp)_2$ (IV-1). Treatment of $Rh_2(esp)_2$ (**IV-1**) with AdN_3 results in sequential formation of $Rh_2(esp)_2(AdN_3)$ (**IV-2a**) and $Rh_2(esp)_2(AdN_3)_2$ (**IV-2b**). (a) Thermal ellipsoid plot of **IV-2b** drawn at 50% probability with H atoms and solvent removed for clarity. Rh(1)−Rh(1): 2.3968(8) Å, Rh(1)−N(1): 2.335(3) Å, N(1)−C(1): 1.509(5) Å, N(1)−N(2): 1.254(5) Å, N(2)−N(3): 1.135(5) Å, N(1)−N(2)−N(3): 176.1(4)°. (b) UV−vis spectra collected during the photolysis of Rh_2 complex **IV-2a** in CH_2Cl_2 (335 nm < λ < 610 nm). Isosbestic points are observed at 411, 455, and 618 nm, which indicate the lack of a steady-state intermediate in the conversion of **IV-2a** to **IV-5a**. (c) Thermal ellipsoid plot of **IV-5a** drawn at 50% probability with H atoms and solvent removed for clarity. Selected metrical parameters: Rh(1)−Rh(2): 2.3959(5) Å; Rh(1)−N(1): 2.303(4) Å. (d) UV−vis spectra collected during the photolysis of Rh_2 complex **IV-2b** in CH_2Cl_2 (335 nm < λ < 610 nm). An isosbestic point is observed at 603 nm, which indicates the lack of a steady-state intermediate in the conversion of **IV-2b** to **IV-5b**.

Rh_2 complexes **IV-2a** and **IV-2b** are photoprecursors to Rh_2 nitrenoids. Photolysis of a CH_2Cl_2 solution of **IV-2a** (335 nm < λ < 610 nm) resulted in new spectral features that are accessed via well-anchored isosbestic points at 411, 455, and 618 nm (**Figure IV-6b**). Crystallization of the photolysis reaction mixture afforded a single crystal of **IV-5a** (**Figure IV-6c**). Compound **IV-5a** can be envisioned as arising from C–to–N migration within an adamantyl nitrene ligand to generate a transient 2-azahomoadamant-3-ene ligand and subsequent trapping with adventitious water to give rise to the observed hemiaminal ligand (see **Figure IV-8**). The observed structure is consistent both with the known low-temperature rearrangement of adamantyl nitrene and with the electrophilicity of highly strained anti-Bredt imines.[253-255] The UV-vis spectrum of a CH_2Cl_2 solution of **IV-5a** is well-matched to the UV-vis spectrum obtained following photolysis of **IV-2a** (**Figure IV-9**). Similarly, photolysis of complex **IV-2b** (335 nm < λ < 610 nm) proceeds via a well-anchored isosbestic point at 603 nm (**Figure IV-6d**). The product of photolysis was assigned as **IV-5b** by comparison of the final UV-vis spectrum obtained from photolysis of **IV-2b** with the spectrum generated by addition of AdN_3 to **IV-5a** (**Figure IV-10**).

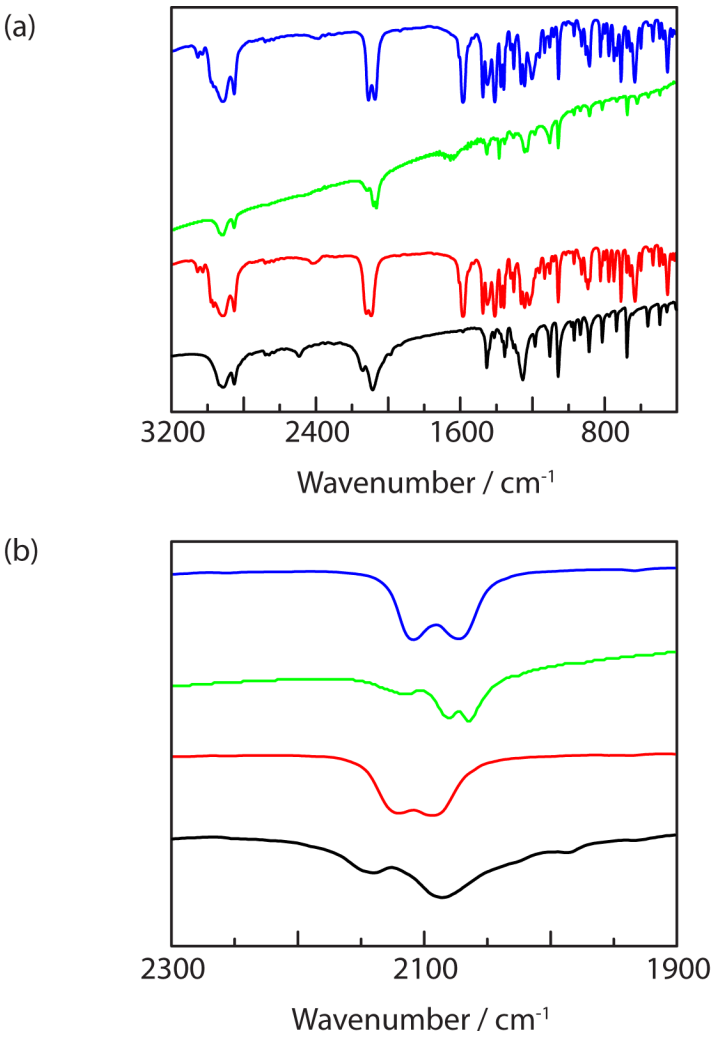

Figure IV-7. IR spectra of Rh_2 complexes IV-2b and [^{15}N]-IV-2b. (a) IR spectra of AdN_3 (—), **IV-2b** (—), $Ad^{15}NN_2$ (—) and [^{15}N]- **IV-2b** (—) recorded in KBr pellets at 23 °C. (b) Expansion of the spectral window depicting the azide region for AdN_3 (—), **IV-2b** (—), $Ad^{15}NN_2$ (—) and [^{15}N]-**IV-2b** (—).

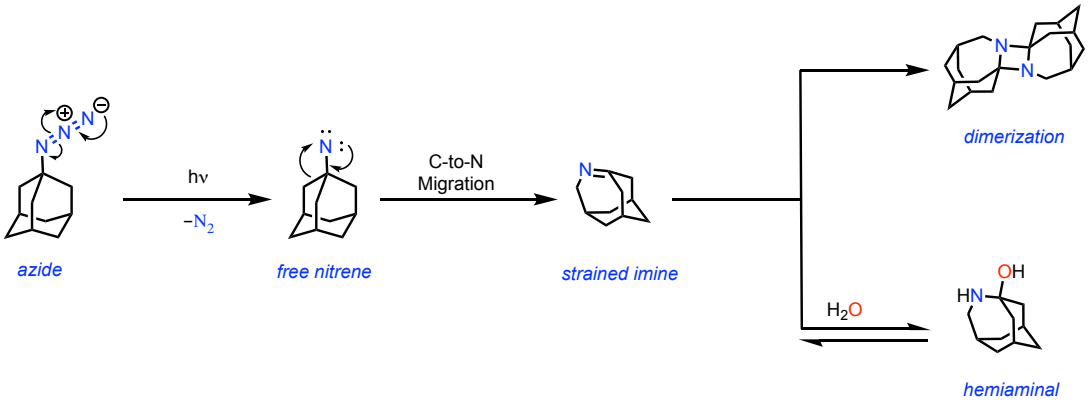

Figure IV-8. Depiction of the generation of adamantyl nitrene and the reaction pathways available to this reactive intermediate. C-to-N migration generates 2-azahomoadamant-3-ene, which has been observed to participate in both [2+2] cycloaddition and reaction with nucleophiles,[256-258] such as water, to generate adducts with concurrent release of the strain associated with the anti-Bredt imine.

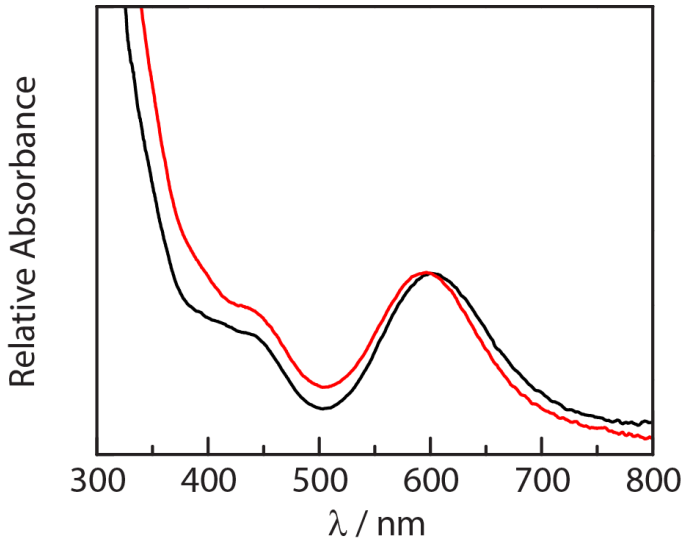

Figure IV-9. UV-vis spectra of crystals of IV-5a dissolved in CH_2Cl_2 (—), and the end point of photolysis of IV-2a in CH_2Cl_2 (—).

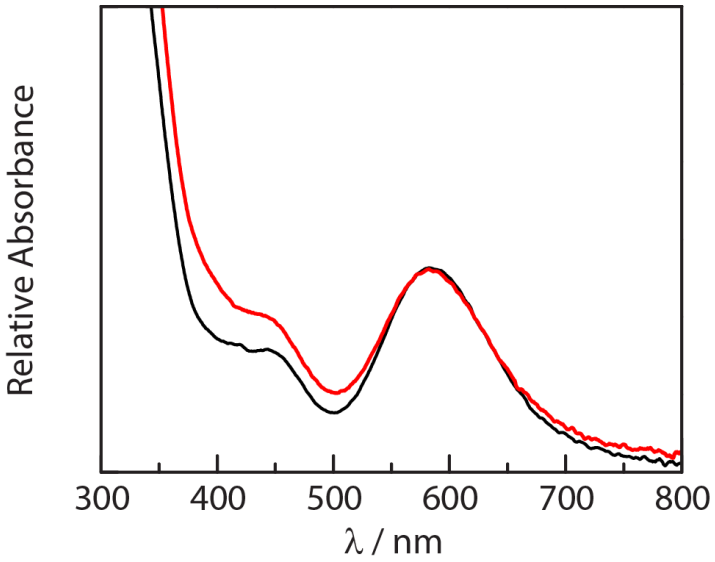

Figure IV-10. UV-vis spectra (a) following addition of AdN_3 to IV-5a in CH_2Cl_2 (—), and (b) the end point of photolysis of IV-2b in CH_2Cl_2 after 1 hour (—).

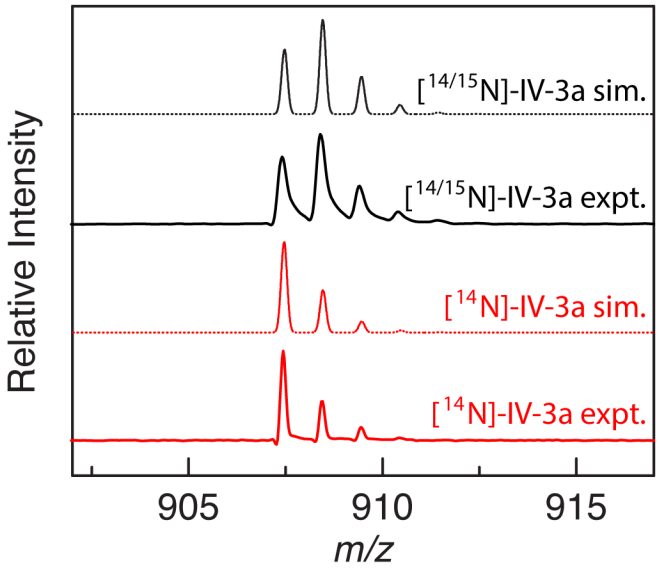

Figure IV-11. Mass spectrometry evidence for N_2 loss from Rh_2 complexes IV-2a to generate IV-3a. MALDI-MS data were acquired for ablation of samples of **IV-2a** and [^{15}N]-**IV-2a**, which indicate the facile loss of N_2 from these complexes to generate $Rh_2(esp)_2(AdN)$ fragments.

Matrix-assisted laser desorption-mass spectrometry (MALDI-MS) data provided additional evidence for facile N_2 elimination from **IV-2a** (**Figure IV-11**). Ablation of a sample of **IV-2a** produces an ion at m/z = 907.5, which is well matched to the expected mass of $Rh_2(esp)_2(AdN)^+$ (calc = 907.2), and displays the expected isotopic distribution. Ablation of a sample of [^{15}N]-**IV-2a**, prepared from monolabeled [^{15}N]-AdN_3, provided the expected +1 m/z (m/z = 908.4 (expt); 908.2 (calc)) and displays the isotope pattern expected for a 1 : 1 mixture of **IV-3a** and [^{15}N]-**IV-3a**, which results from incorporation of 50% ^{15}N at each of N(α) and N(γ) in [^{15}N]-AdN_3. *In situ* IR analysis of both photolyzed or thermolyzed KBr pellets of **IV-2b** further indicate facile N_2 loss from **IV-2b** (**Figures IV-12–Figure IV-13**).

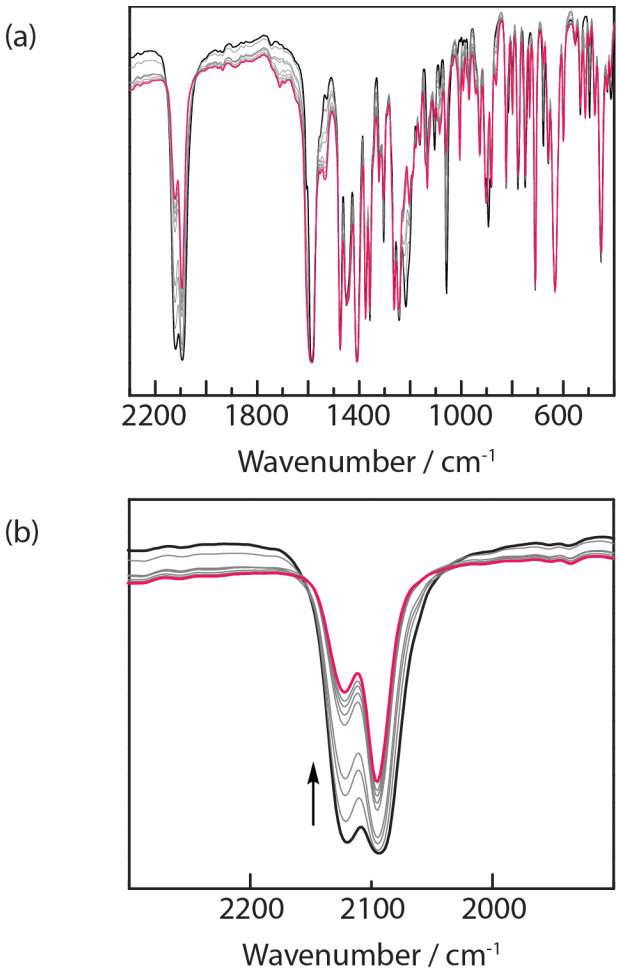

Figure IV-12. IR spectra collected during the photolysis ($335 < \lambda < 610$ nm) of IV-2b in a KBr pellet. (a) Full spectral range, and (b) expansion of the spectral window depicting the change in the azide region. The evolution is consistent with the evolution of **IV-2b**, which displays both symmetric and antisymmetric modes about the two azide ligands, to **IV-5b**, which displays only one stretching mode.

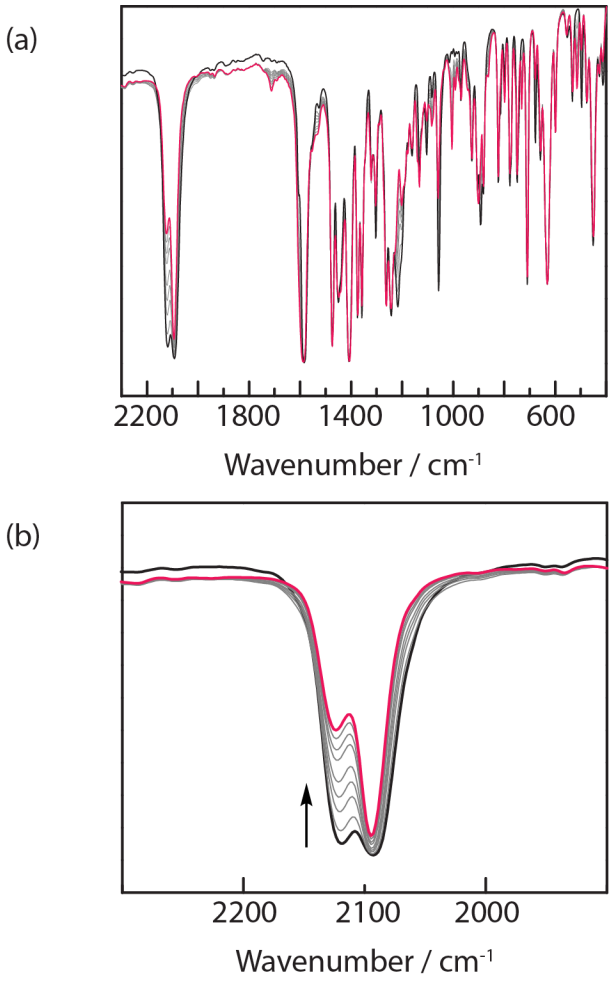

Figure IV-13. *In situ* IR spectra collected during the thermolysis of IV-2b in a KBr pellet at 95 °C. (a) Full spectral range, and (b) expansion of the spectral window depicting the change in the azide region. The evolution is consistent with the evolution of **IV-2b**, which displays both symmetric and antisymmetric modes about the two azide ligands, to **IV-5b**, which displays only one stretching mode.

We hypothesized that low-temperature N_2 extrusion from **IV-2b** within a single crystal habit would enable direct structural characterization of nitrenoid **IV-3b**. To this end, we examined the *in situ* structural evolution of a single-crystal of **IV-2b** by X-ray diffraction during irradiation with a 365 nm light source. Data was collected at 100 K with 50 keV synchrotron radiation.[259] Solid-state reaction progress was monitored by free

refinement of the nitrogen occupancies, which indicate that while the occupancy of N(α) was unchanged with time, the occupancy of N(β) decreased. Concurrently, the space group was observed to transition from monoclinic $P2_1/c$ to $P2_1/n$.[260] Refinement of the resulting data indicated elimination of a molecule of N_2 to afford Rh_2 nitrenoid **IV-3b**·N_2 (**Figure IV-14**). Upon N_2 extrusion, Rh(1)–N(1B) (i.e., the nitrenoid linkage) contracts from 2.335(3) Å (**IV-2b**) to 2.12(1) Å (**IV-3b**). Concurrent with N_2 extrusion and Rh(1)–N(1B) contraction, significant contraction of N(1B)–C(1) (i.e., the N–C bond in the adamantyl nitrene fragment) is also observed from 1.509(5) Å (IV-2b) to 1.41(2) Å (**IV-3b**). Importantly, the conversion of **IV-2b** to **IV-3b** is accompanied by a significant expansion of the Rh(1)–N(B)–C(1) angle from 129.1° to 147.2°. No substantial changes in the C–C distances of the adamantyl fragment were observed, and both Rh(1)–Rh(1) (2.3968(8) Å (**IV-2b**); 2.3903(4) Å (**IV-3b**)) and Rh(1)–N(1A) (i.e., the Rh–N(Ad)N_2 linkage; 2.335(3) (**IV-2b**); 2.346(4) Å (**IV-3b**)) are essentially unchanged. The Rh centers in **IV-3b**·N_2 are symmetry equivalent, and thus following loss of N_2 the AdN_3 and AdN ligands of **IV-3b** are compositionally disordered (i.e., 50% occupancy of each AdN and AdN_3 on each of the Rh centers). Solid-state conversion of up to 70% are well accommodated within the single crystal. Attempts to achieve higher conversions or to promote loss of a second equivalent of N_2 to generate a *bis*-nitrenoid by prolonged irradiation were unsuccessful due to loss of crystallinity.

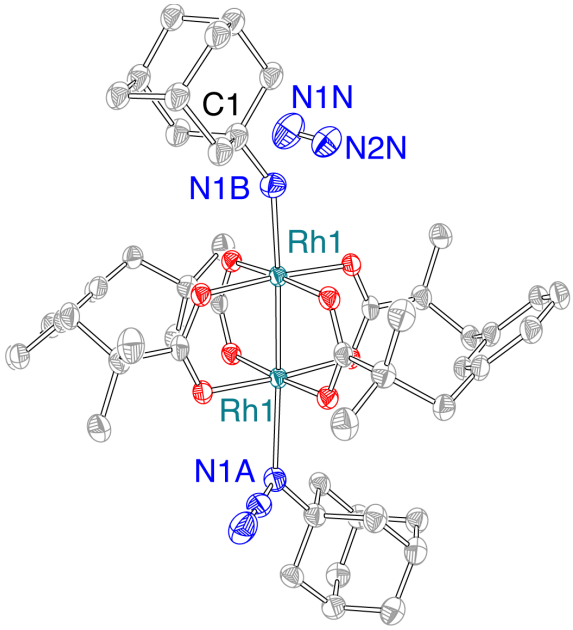

	IV-3b expt.	^{3}[**IV-3b**] comp.	^{1}[**IV-3b**] comp.
Rh(1)–N(1B) / Å	2.12(2)	2.094	1.924
Rh(1)–N(1A) / Å	2.346(4)	2.408	2.534
Rh(1)–Rh(1) / Å	2.3903(4)	2.438	2.465
Rh(1)–N(1B)–C(1) / °	147.2(9)	136.9	126.8

Figure IV-14. Solid-state structure of reactive Rh_2 nitrenoid IV-3b. Thermal ellipsoid plot of **IV-3b**·N_2 generated by solid-state N_2 elimination from **IV-2b**. Ellipsoids are drawn at 50% probability. H atoms and solvent are removed for clarity. The structure illustrated here results from refinement of a data set collected at 46% conversion; higher conversions can be achieved but at the expense of crystallinity. Comparison of the bond metrics derived from the X-ray structure with those computed for ^{3}[**IV-3b**] and ^{1}[**IV-3b**] indicate excellent agreement with the triplet electronic configuration.

Density Functional Theory (DFT) optimization of the geometry of **IV-3b** has been pursued both as a singlet and as a triplet electronic configuration (i.e., ^{1}[**IV-3b**] and ^{3}[**IV-3b**]; M06 functional, LANL2DZ basis set for Rh, 6-31G** for other atoms).[201] The calculated Rh(1)–Rh(1), Rh(1)–N(1A), Rh(1)–N(1B), and N(1B)–C(1) distances and Rh(1)–N(1B)–C(1) angle for ^{3}[**IV-3b**] are in excellent agreement with the experimentally defined parameters (**Figure IV-14**). In contrast, the optimized structure of ^{1}[**IV-3b**]

substantially underestimates both the Rh(1)–N(1B) distance (1.924 Å (comp.); 2.12(2) Å (expt.)) and Rh(1)–N(1B)–C(1) angle (126.8° (comp.); 147.2° (expt.)) and substantially overestimates the Rh(1)–N(1A) distance (2.534 Å (comp.); 2.346(4) Å (expt.)). The observation of ^{3}[**IV-3b**] is consistent with the relative stabilities computed for the ^{1}[**IV-3b**] and ^{3}[**IV-3b**]; the singlet structure is calculated to be 5.5 kcal/mol above the triplet.[17] One might expect that a singlet nitrene would be best stabilized in a bent geometry that maximizes back-bonding into a vacant p-orbital. We speculate that the observed linearization of the nitrenoid fragment in **IV-3b** enables the triplet nitrene to be stabilized by two half-order π-bonds generated by overlap of filled Rh–Rh π^* orbitals with partially occupied *N*-centered orbitals.[201]

IV.3. Conclusion

In closing, the characterization of nitrenoid **IV-3b** reported here establishes the electronic and three-dimensional structures of this critical intermediate. Typically, structural characterization of the transient intermediates involved in the intimate bond-forming and -breaking processes during catalysis is not possible, and thus investigations of reaction mechanisms often rely on computational characterization of reactive intermediates using methods optimized for isolated catalyst intermediates. We anticipate that direct characterization of reactive nitrenoid intermediates will inform rational development of C–H amination chemistry. Further, the demonstration of crystalline matrix confinement as a platform for the structural characterization of reactive intermediates raises the tantalizing possibility that proper design of photoactive molecular precursors

may represent a general strategy to directly characterize reactive species generated by elimination of small molecules within crystalline samples.

IV.4. Experimental Details

IV.4.1. General Considerations

Materials Solvents were obtained as ACS reagent grade and used as received. Unless otherwise noted, all chemicals and solvents were used as received. Isobutyronitrile, *n*-butyl lithium (^{n}BuLi) (2.5 M in hexanes), 1-azidoadamantane (AdN_3), 1-adamantanol (AdOH), ethylene glycol, hexanes, dichloromethane (CH_2Cl_2), and acetone were obtained from Sigma Aldrich. Silica gel (0.06–0.20 mm, 60 Å for column chromatography) was obtained from Acros Organics and chlorobenzene (PhCl) was obtained from TCI America. Dirhodium tetraacetate [$Rh_2(OAc)_4$] was obtained from Ark Pharm and xylylene dibromide from BTC. Potassium hydroxide (KOH) and sulfuric acid (H_2SO_4) were obtained from EMD Millipore. Diisopropylamine ($^{i}Pr_2NH$) was obtained from Fisher Scientific. NMR solvents and sodium azide (1-^{15}N, 98%) were purchased from Cambridge Isotope Laboratories and were used as received. Anhydrous dichloromethane was obtained from a drying column and stored over activated molecular sieves.[180] All reactions were carried out at 23 °C unless otherwise noted. α,α,α',α'-Tetramethyl-1,3-benzenedipropionic acid (H_2esp)[241] was prepared according to the literature.

Characterization Details NMR spectra were recorded on Bruker Avance NEO 400 NMR operating at 400.09 MHz for ^{1}H and ^{13}C acquisitions and were referenced against solvent signals: $CDCl_3$ (7.26 ppm, ^{1}H; 77.16 ppm, ^{13}C) and CD_2Cl_2 (5.32 ppm, ^{1}H;

53.84 ppm, ^{13}C).[181] ^{1}H NMR data are reported as follows: chemical shift (δ, ppm), multiplicity (s (singlet), d (doublet), t (triplet), m (multiplet), br (broad)), integration. UV-vis spectra were recorded at 293 K in quartz cuvettes on an Ocean Optics Flame-S miniature spectrometer with DH-mini UV-vis NIR light source (200–900 nm) and were blanked against the appropriate solvent. Attenuated total reflectance-infrared (ATR-IR) spectra were recorded on a Shimadzu FTIR/IRAffinity-1S spectrometer. *In situ* IR spectra were measured in a KBr pellet with a Bruker VERTEX 70. Spectra were blanked against air and were determined as the average of 64 scans. IR data are reported as follows: wavenumber (cm^{-1}), peak intensity (s, strong; m, medium; w, weak). Mass spectrometry measurements were recorded with either an Orbitrap Fusion™ Tribrid™ mass spectrometer or a Q Exactive™ Focus Hybrid Quadrupole-Orbitrap™ mass spectrometer. MALDI data was obtained using a Bruker Microflex LRF MALDI-TOF using reflectron-TOF modes. The laser power of the MALDI was tuned using Bruker Daltonics flexControl software that was pre-installed with the instrument.

X-Ray Diffraction Details Experimental details of crystallization are included in the synthetic procedures for the relevant compounds. A Bruker APEX 2 Duo X-ray (three-circle) diffractometer was used for crystal screening, unit cell determination, and data collection for the X-ray crystal structures of **IV-5a**. Crystal suitable for X-ray diffraction were mounted on a MiTeGen dual-thickness micro-mount and placed under a cold N_2 stream (Oxford). The X-ray radiation employed was generated from a Mo sealed X-ray tube (Kα = 0.70173 Å with a potential of 40 kV and a current of 40 mA). Bruker AXS APEX II software was used for data collection and reduction. Absorption corrections were

applied using the program SADABS. A solution was obtained using XT/XS in APEX2 and refined in Olex2.[183-184, 221] Hydrogen atoms were placed in idealized positions and were set riding on the respective parent atoms. All non-hydrogen atoms were refined with anisotropic thermal parameters. The structure was refined (weighted least squares refinement on F^2) to convergence.[183-184]

The X-ray crystal structures **IV-2b** and **IV-3b**·N_2 were collected using synchrotron radiation (both 0.24796 Å and 0.33062 Å) at ChemMatCARS located at the Advanced Photon Source (APS) housed at Argonne National Laboratory (ANL). Crystals suitable for X-ray diffraction were mounted on a glass fiber. The data was collected at 100 K (Cryojet N_2 cold stream) using a vertically mounted Bruker D8 three-circle platform goniometer equipped with a PILATUS3 X CdTe 1M detector. Data was collected as a series of φ and/or ω scans. Data were integrated using SAINT and scaled with a multi-scan absorption correction using SADABS. Structures were solved by intrinsic phasing using SHELXT (Apex2 program suite v2014.1) and refined against F^2 on all data by full matrix least squares with SHELXL97. All non-hydrogen atoms were refined anisotropically. H atoms were placed at idealized positions and refined using a riding model. Disorder was modeled using two parts and the bond distances and thermal ellipsoids in the disordered molecules were restrained using the SADI, EADP and ISOR. The restraints SIMU, DELU, SAME, and CHIV were also used on the disordered parts. The N–N bond distance in the generated N_2 molecule was fixed to 1.09 Å using DFIX command.

Computational Details Calculations were performed using the Gaussian 09, Revision D.01 suite of software.[225] A variety of basis sets and functionals have previously been employed in the analysis of Rh_2 nitrenoid chemistry.[30, 196, 201, 242-243, 261-267] We have carried out geometry optimizations using a suite of these methods in order to obtain a satisfactory reproduction of critical metrical parameters. Methods employed include the M06,[268] B3LYP,[223-226] and BP86[269] functionals implemented with LANL2DZ,[229, 270] LANL08(f),[227-229] or TZVP[271] basis sets for Rh (with accompanying effective core potentials), and 6-31G(d,p) for light atoms. Stationary points were characterized with frequency calculations using the same basis set and functionals. Given the demonstration that hybrid functionals can substantially overestimate the stabilities of open-shell electronic configurations,[272-273] we have evaluated the singlet-triplet gap using the B97D3[274] functional in combination with the basis sets used for optimization. NBO calculations were carried out with the NBO 6.0 suite.[275]

IV.4.2. Synthesis and Characterization

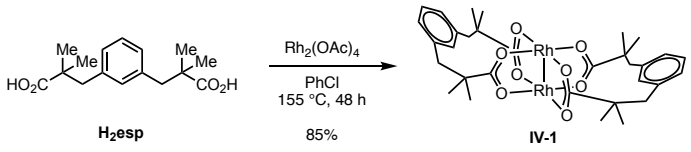

Synthesis of $Rh_2(esp)_2$ (IV-1) Complex **IV-1** was prepared according to the following modification of literature method.[276] A 200-mL round-bottom flask was charged with $Rh_2(OAc)_4$ (565 mg, 1.29 mmol, 1.00 equiv.) and H_2esp (863 mg, 3.10 mmol, 2.40 equiv.). Chlorobenzene (50 mL) was added and the reaction mixture was heated at 155 °C for 48

h. The reaction mixture was cooled to 23 °C and the solvent was removed *in vacuo*. The green residue was purified by SiO_2 chromatography with CH_2Cl_2/acetone as a linear gradient eluent system (v/v: 100/0 to 90/10) to afford a dark-green powder. Solvent was removed *in vacuo* and the resulting powder was further heated under active vacuum at 60 °C to afford the title complex as light-green powder (827 mg, 85% yield). ^{1}H NMR (δ, 23 °C, $CDCl_3$): 7.08 (t, J = 8.0 Hz, 2H), 6.97 (s, 2H), 6.86 (d, J = 8.0 Hz, 4H), 2.66 (s, 8H), 1.02 (s, 24H). ^{13}C NMR ((δ, 23 °C, $CDCl_3$): 196.8, 138.1, 131.1, 128.1, 127.0, 47.1, 46.6, 25.8. IR (ATR, cm^{-1}): 2962 (m), 2920 (m), 1731 (m), 1681 (m), 1584 (s), 1469 (s), 1406 (s), 1372 (s), 1240 (s), 900 (s), 745 (s), 708 (s), 628 (s). UV-vis (CH_2Cl_2), λ_{max} (nm, ε ($M^{-1}cm^{-1}$)): 425 (177), 667 (227) (Figure IV-15). The recorded ^{1}H and ^{13}C NMR spectra are shown in **Figure IV-16b** and **Figure IV-17b** respectively.

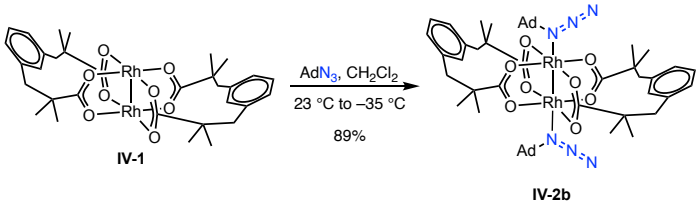

Synthesis of $Rh_2(esp)_2(N_3Ad)_2$ (IV-2b) A 20-mL vial was charged with complex **IV-1** (40.0 mg, 0.0528 mmol, 1.00 equiv.), AdN_3 (30.0 mg, 0.169 mmol, 3.19 equiv.), and CH_2Cl_2 (3.0 mL) inside a N_2-filled glovebox and the reaction mixture was stirred at 23 °C for 2 h. The reaction mixture was cooled to –35 °C, at which temperature the mixture was maintained for 24 h to afford dark-green crystals. The supernatant was decanted and the crystals were washed with pentane and dried *in vacuo* at 23 °C to afford the title compound

IV-2b (59.5 mg, 89% yield). ^{1}H NMR (δ, 23 °C, $CDCl_3$): 7.04 (t, J = 8.0 Hz, 2H), 6.92 (s, 2H), 6.83 (d, J = 8.0 Hz, 4H), 2.61 (s, 8H), 2.26–1.79 (br, 27H), 1.61 (s, 3H), 0.99 (s, 24H). ^{13}C NMR ((δ, 23 °C, $CDCl_3$): 196.1, 138.2, 131.2, 127.9, 126.7, 53.6, 47.2, 46.3, 36.3, 30.4, 25.9. IR (ATR, cm^{-1}): 2917 (s), 2850 (s), 2103 (s), 2079 (m), 1571 (s), 1470 (s), 1446 (s), 1404 (s), 1368 (s), 1260 (s), 1189 (s), 1045 (s), 889 (m), 728 (s). IR (KBr pellet, cm^{-1}): 2918 (s), 2850 (s), 2120 (s), 2093 (s), 1586 (s), 1472 (s), 1407 (s), 1375 (s), 1356 (s), 1305 (m), 1244 (s), 1054 (s), 893 (s), 707 (s), 632 (s). UV-vis (CH_2Cl_2), λ_{max} (nm, ε ($M^{-1}cm^{-1}$)): 438 (150), 625 (236) (**Figure IV-15**). For **IV-2a** HR-ESI-MS: $[M]^+$ = 935.2096 (expt.) and 935.2099 (calc.). For **IV-2b** HR-ESI-MS: $[M+H]^+$ = 1113.3430 (expt.) and 1113.3438 (calc.). The recorded ^{1}H and ^{13}C NMR spectra are shown in **Figure IV-16c** and **Figure IV-17c** respectively.

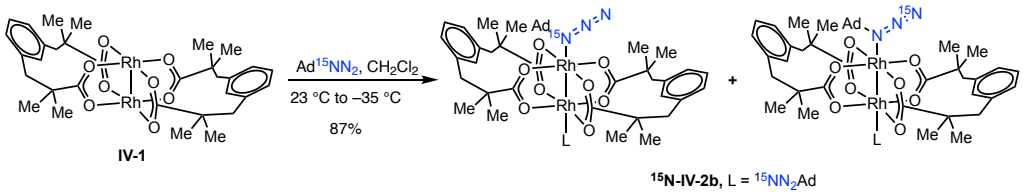

Synthesis of $Rh_2(esp)_2(^{15}NN_2Ad)_2$ ([^{15}N]-IV-2b) $Ad^{15}NN_2$ was prepared according to the following modification of literature methods.[277] A 25-mL round-bottom flask was charged with 1-adamantanol (99.7 mg, 0.656 mmol, 1.00 equiv.) and $CHCl_3$ (1.0 mL) and cooled to 0 °C using an ice-bath. H_2SO_4 (65 wt% in H_2O, 2.5 mL) was added to the reaction solution dropwise at 0 °C and the resulting reaction mixture was stirred at this temperature for 15 min. $Na^{15}NN_2$ (88.0 mg, 1.33 mmol, 2.02 equiv.) was added to the reaction mixture

in portions at 0 °C while stirring. The reaction mixture was allowed to warm to 23 °C, at which temperature the mixture was stirred for 12 h. The phases were separated and the aqueous phase was extracted with $CHCl_3$ (30.0 mL). The organic phases were combined, dried over Na_2SO_4, and concentrated *in vacuo* to afford a white solid. The residue was purified by SiO_2 chromatography with hexanes as the eluent to afford $Ad^{15}NN_2$ as a white solid (23.0 mg, 20% yield). ^{1}H NMR (δ, 23 °C, $CDCl_3$): 2.14 (s, 3H), 1.80–1.63 (m, 12H). ^{13}C NMR ((δ, 23 °C, $CDCl_3$): 45.5, 41.7, 36.2, 36.1, 30.9, 29.9. IR (KBr pellet, cm^{-1}): 2917 (s), 2854 (m), 2113 (w), 2081 (s), 2064 (s), 1451 (s), 1383 (s), 1245 (s), 1230 (s), 1104 (s), 1056 (s), 883 (m), 674 (m).

A 20-mL vial was charged with **IV-1** (30.0 mg, 0.0396 mmol, 1.00 equiv.), $Ad^{15}NN_2$ (20.0 mg, 0.112 mmol, 2.87 equiv.), and CH_2Cl_2 (3.0 mL) in an N_2-filled glovebox. The reaction mixture was stirred at 23 °C for 2 h after which time the reaction was cooled to –35 °C and maintained at this temperature for 24 h to yield dark-green crystals. The supernatant was decanted and the crystals were washed with pentane and dried overnight *in vacuo* at 23 °C to afford the title compound [^{15}N]-**IV-2b** (43.6 mg, 87% yield). IR (KBr pellet, cm^{-1}): 2914 (s), 2850 (s), 2109 (s), 2073 (s), 1585 (s), 1476 (s), 1448 (s), 1408 (s), 1375 (s), 1358 (s), 1304 (m), 1263 (s), 1243 (s), 1202 (m), 1057 (m), 881(m), 707 (s), 631 (s).

IV.4.3. Photolysis of Compound IV-2a

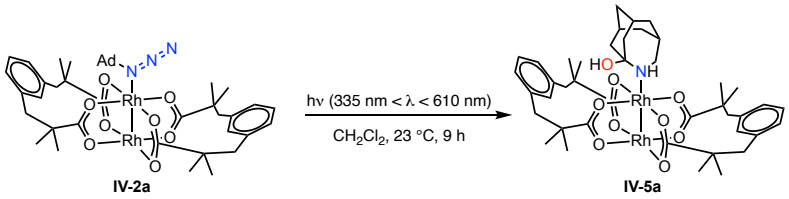

IV-2a **IV-5a**

A 20-mL vial was charged with compound **IV-1** (15.0 mg, 0.0198 mmol, 1.00 equiv.) and CH_2Cl_2 (6.0 mL). A second 20-mL vial was charged with AdN_3 (90.0 mg, 0.508 mmol, 26.7 equiv.) and CH_2Cl_2 (1.0 mL). A quartz cuvette was charged with the stock solution of **IV-1** (3.0 mL) and the stock solution of AdN_3 (0.07 mL). The UV-vis spectrum was recorded and indicated the exclusive presence of compound **IV-2a**. The solution was photolyzed and the reaction was monitored via UV-vis until the spectrum stopped evolving. Solvent was then removed *in vacuo* and the residue was taken up in $CDCl_3$ for NMR analysis (**Figures IV-18–IV-9**). Single crystals of **IV-5a** were obtained from concentrated $CDCl_3$ solution at 23 °C.

IV.4.4. Photolysis of Compound IV-2b

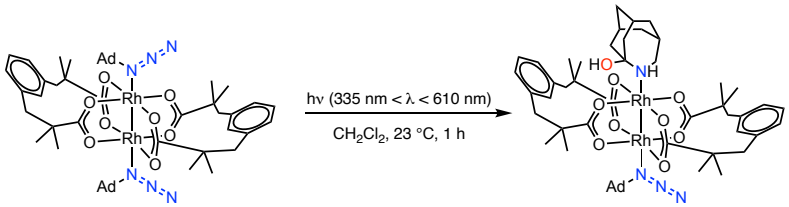

IV-2b **IV-5b**

A 20-mL vial was charged with compound **IV-1** (15.0 mg, 0.0198 mmol, 1.00 equiv.) and CH_2Cl_2 (6.0 mL). A second 20-mL vial was charged with AdN_3 (90.0 mg, 0.508 mmol, 26.7 equiv.) and CH_2Cl_2 (1.0 mL). A cuvette was charged with the stock solution of **IV-1**

(3.0 mL) and the stock solution of AdN_3 (0.6 mL). The UV-vis spectrum was recorded and indicated the exclusive presence of compound **IV-2b**. The solution was photolyzed and the reaction was monitored via UV-vis until the spectrum stopped evolving. The final product obtained in this photolysis displayed spectral features that overlayed with the spectrum obtained by addition of AdN_3 to the product of **IV-2a** photolysis (**Figure IV-10**).

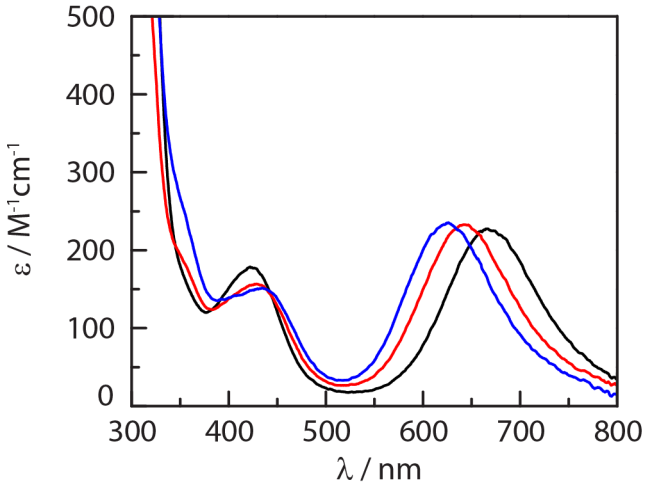

Figure IV-15. Molar absorptivity plots for Rh_2 complexes IV-1 (—), IV-2a (—), and IV-2b (—) in CH_2Cl_2.

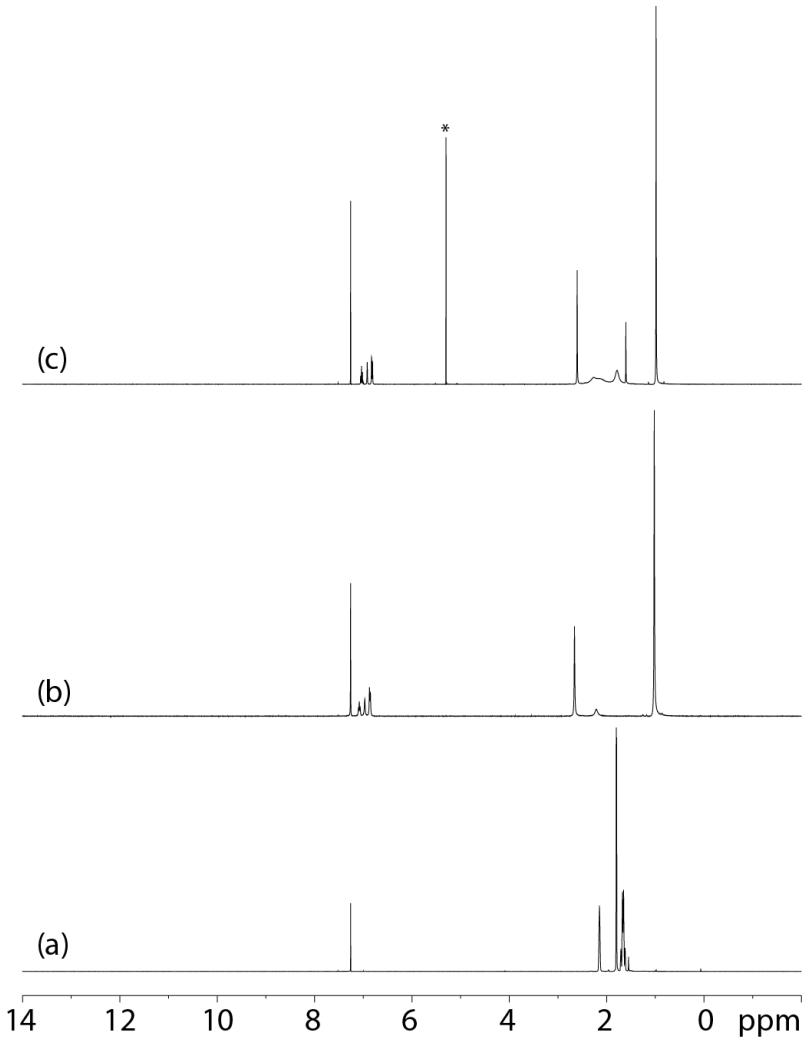

Figure IV-16. ^{1}H NMR spectra of Rh_2 complexes IV-1 and IV-2b. ^{1}H NMR spectra of (a) AdN_3, (b) Rh_2 complex **IV-1**, and (c) and dissolved crystals of Rh_2 complex **IV-2b**. Spectra were measured in $CDCl_3$ at 23 °C. The indicated peak (*) corresponds to CH_2Cl_2 that is present in the crystal structure.

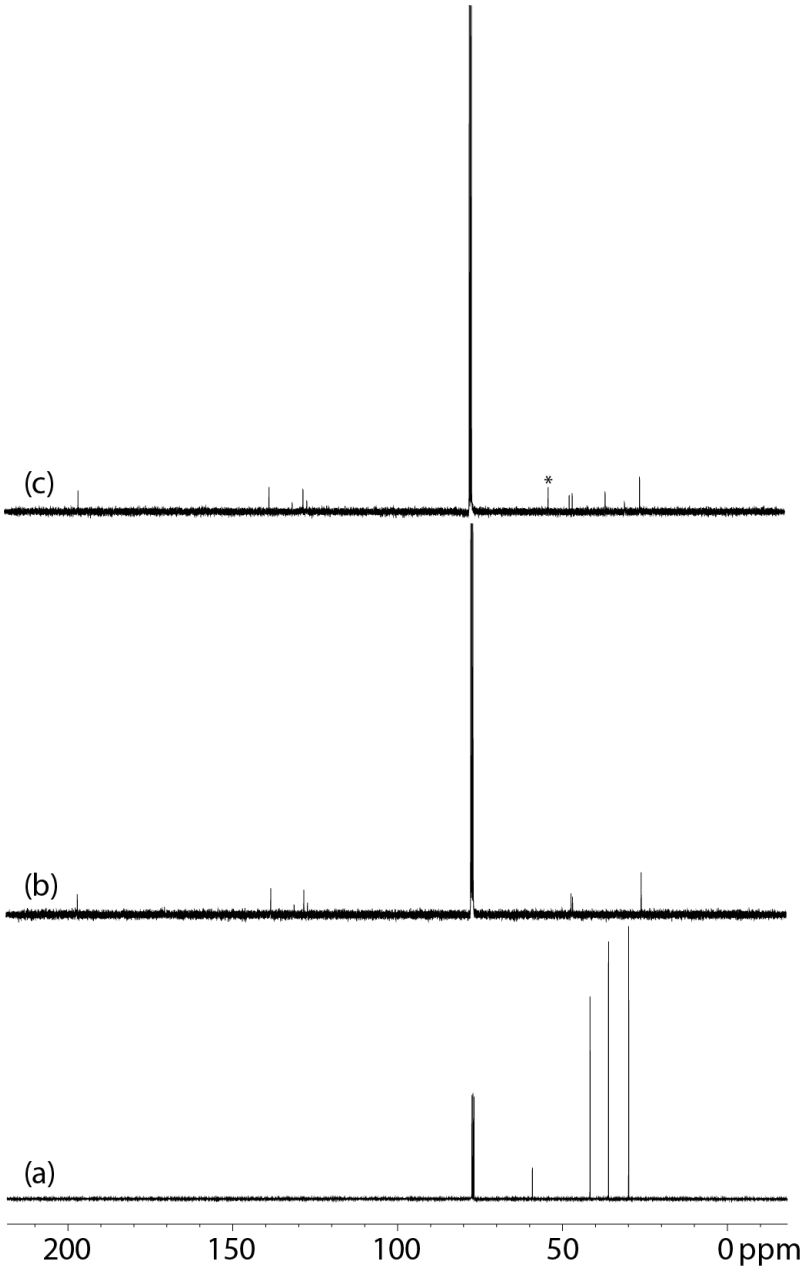

Figure IV-17. ^{13}C NMR spectra of Rh_2 complexes IV-1 and IV-2b. ^{13}C NMR spectra of (a) AdN_3, (b) Rh_2 complex **IV-1**, and (c) and dissolved crystals of Rh_2 complex **IV-2b**. Spectra were measured in $CDCl_3$ at 23 °C. The indicated peak (*) corresponds to CH_2Cl_2 that is present in the crystal structure.

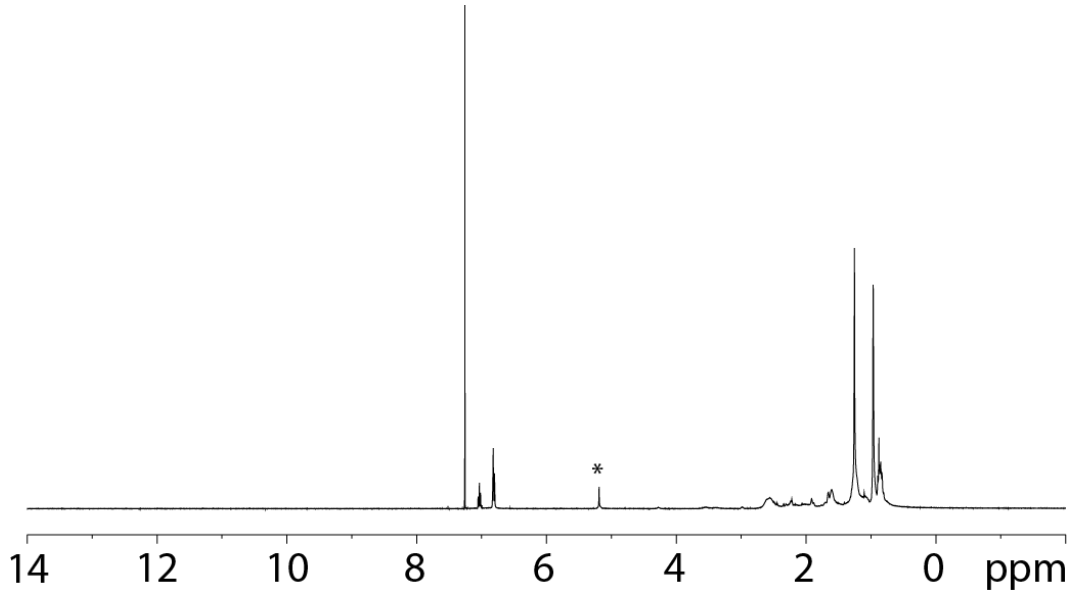

Figure IV-18. ^{1}H NMR spectra of dissolved crystals of Rh_2 complex IV-5a recorded in $CDCl_3$ at 23 °C. The indicated peak (*) corresponds to CH_2Cl_2 that is present in the crystal structure.

CHAPTER V

IN CRYSTALLO SNAPSHOTS OF DIRHODIUM-CATALYZED C–H AMINATION*

V.1. Introduction

X-ray and electron diffraction-based experiments are routinely employed to elucidate the chemical structures that are required for the rational design and optimization of small molecule catalysts.[278-279] While crystallography is routinely utilized to examine ligand-induced structural variation in kinetically stable coordination complexes and pre-catalysts, application to the characterization of reactive intermediates, which are intimately involved in the bond-making and -breaking in catalysis, is typically stymied by the kinetic lability of these species.[64, 110, 155, 203, 280] As a result, experimental evaluation of the impact of ligand structure, and coordinating additives present during catalysis, is typically not possible. In this chapter, we demonstrate *in crystallo* synthesis of reactive Rh_2 nitrenes that mediate intramolecular C–H amination. This strategy allows experimental evaluation of the impact of ligand perturbation on the structures of transient reactive intermediates in catalysis.

Nitrene transfer catalysis represents a leading approach for the construction of C–N bonds via C–H amination and olefin aziridination reactions.[17, 48, 63, 194, 281-286] In this context, reactive Rh_2 nitrenes, which are generated by combination of nitrene transfer

* Data, figures, and text in this chapter were adapted from "*In Crystallo* Snapshots of Rh_2-Catalyzed C–H Amination" by Das, A.; Wang, C.-H.; Van Trieste III, G. P.; Sun, C.-J.; Chen, Y.-S.; Reibenspies, J. H.; Powers, D. C. *J. Am. Chem. Soc.* **2020**, *ASAP*. Copyright 2020 American Chemical Society.

reagents (i.e., iminoiodinanes, organoazides, or hydroxylamines) with Rh_2 catalysts, are critical reactive intermediates in a variety of synthetically important C–H amination methodologies (**Figure V-1a**).[195-196, 198] Despite the ubiquity of Rh_2 nitrene intermediates in nitrene transfer catalysis, the structures of Rh_2 nitrenes that participate in C–H amination have eluded experimental scrutiny.

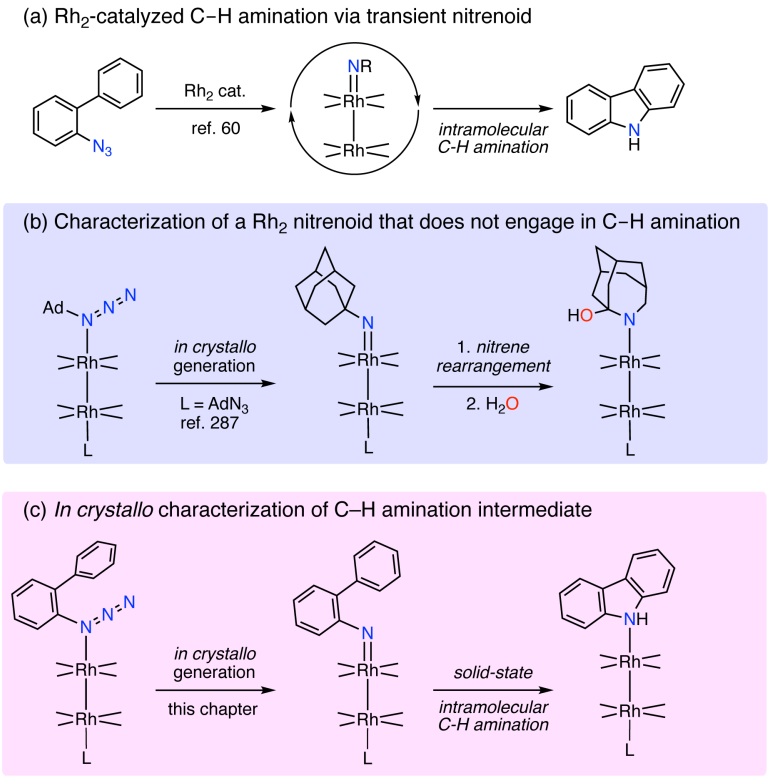

Figure V-1. Intramolecular C–H amination mediated by Rh_2 nitrenoids. (a) Rh_2-catalyzed nitrene transfer from organic azide precursors has been developed for intramolecular C–H amination catalysis via transient Rh_2 nitrene intermediates. (b) *In situ* generation of Rh_2 adamantyl nitrene enabled crystallographic characterization, but rearrangement of the nitrene fragment prevents observation of C–H functionalization. (c) Here, we characterize two Rh_2 nitrene complexes that participate in intramolecular C–H amination, which has enabled direct characterization of the impact of coordinating ligands on the structures of reactive intermediates. Ad = adamantyl.

We have been interested in the direct structural characterization of transient intermediates involved in C–H functionalization reactions enabled by *in crystallo* synthesis.[204] This approach represents a crystallographically addressable analogue of classic matrix isolation experiments.[143, 145-147] In chapter IV, we demonstrated that *in crystallo* N_2 extrusion from a Rh_2 adamantyl azide complex enabled structural characterization of a transient triplet nitrene adduct of Rh_2, however, rearrangement of the nitrene fragment prevented observation of C–H amination in this system (**Figure V-1b**).[287] We hypothesized that generation of a Rh_2 nitrene bearing a proximal C–H bond would enable characterization of transient nitrene intermediates that were competent intermediates for intramolecular C–H amination (**Figure V-1c**). Here, we demonstrate the characterization of a pair of transient Rh_2 nitrenes that participate in solid-state C–H amination. These structural snapshots of a C–H amination reaction provide an opportunity to directly evaluate the impact of coordinating ligands on the structure of reactive intermediates in C–H functionalization.

V.2. Results and Discussions

We initiated our studies by examining the coordination chemistry of $Rh_2(esp)_2$ (**V-1**) with *o*-biphenyl azide (**V-2**) (esp = α,α,α',α'-tetramethyl-1,3-benzenedipropionate). These substrates were selected because $Rh_2(esp)_2$ (**V-1**), in which the two Rh centers are bridged by two chelating bis-carboxylate ligands, is among the most widely used catalysts for nitrene transfer chemistry, and Driver *et al.* demonstrated Rh_2-catalyzed intramolecular amination of o-biphenyl azides.[60, 239, 242, 288] An equimolar mixture of **V-1** and **V-2** in

$CDCl_3$ displays ^1H NMR spectral features consistent with a 1 : 1 adduct, i.e., $Rh_2(esp)_2(C_{12}H_{10}N_3)$ (**V-3a**, **Figures V-2–V-4**). IR analysis of **V-3a** in a KBr pellet displays stretching modes at 2129 cm^{-1} and 2101 cm^{-1}, which arises from the N_3 functionality (for comparison, 2125 cm^{-1} and 2089 cm^{-1} in **V-2**) (**Figure V-5**). Single crystals of **V-3a** were obtained by slow evaporation of a CH_2Cl_2 solution of 1 : 1 mixture of **V-1** and **V-2** at –35 °C (**Figure V-2b**). The metrical parameters of the Rh_2 fragment in **V-3a** are similar to those of $Rh_2(esp)_2$ (Rh–Rh: **V-1** = 2.3817(9) Å;[198] **V-3a** = 2.3850(4) Å) and the biphenyl azide moiety metrics are typical of unbound **V-2**.[289]

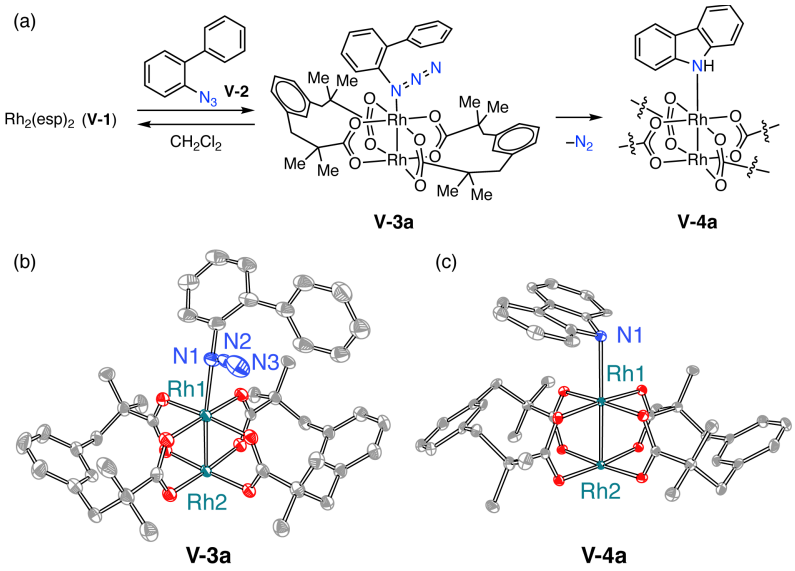

Figure V-2. Synthesis and reaction chemistry of Rh_2 o-biphenylazide complex V-3a. (a) Solid-state, intramolecular C–H amination from **V-3a** can be promoted either thermally (i.e., heating to 60 °C) or photochemically ($335 < \lambda < 610$ nm). (b) Thermal ellipsoid plot of **V-3a** drawn at 50% probability. H-atoms and solvent are omitted for clarity. Selected metrical parameters: Rh(1)–N(1) = 2.244(3) Å, N(1)–C(1) = 1.441(5) Å, Rh(1)–Rh(2) = 2.3850(4) Å, Rh(1)–N(1)–C(1) = 125.0(2)°. (c) Thermal ellipsoid plot of **V-4a** drawn at 50% probability. Selected metrical parameters: Rh(1)–N(1) = 2.341(3) Å, Rh(1)–Rh(2) = 2.3835(3) Å. H-atoms and solvent are omitted for clarity; esp = α,α,α',α'-tetramethyl-1,3-benzenedipropionate.

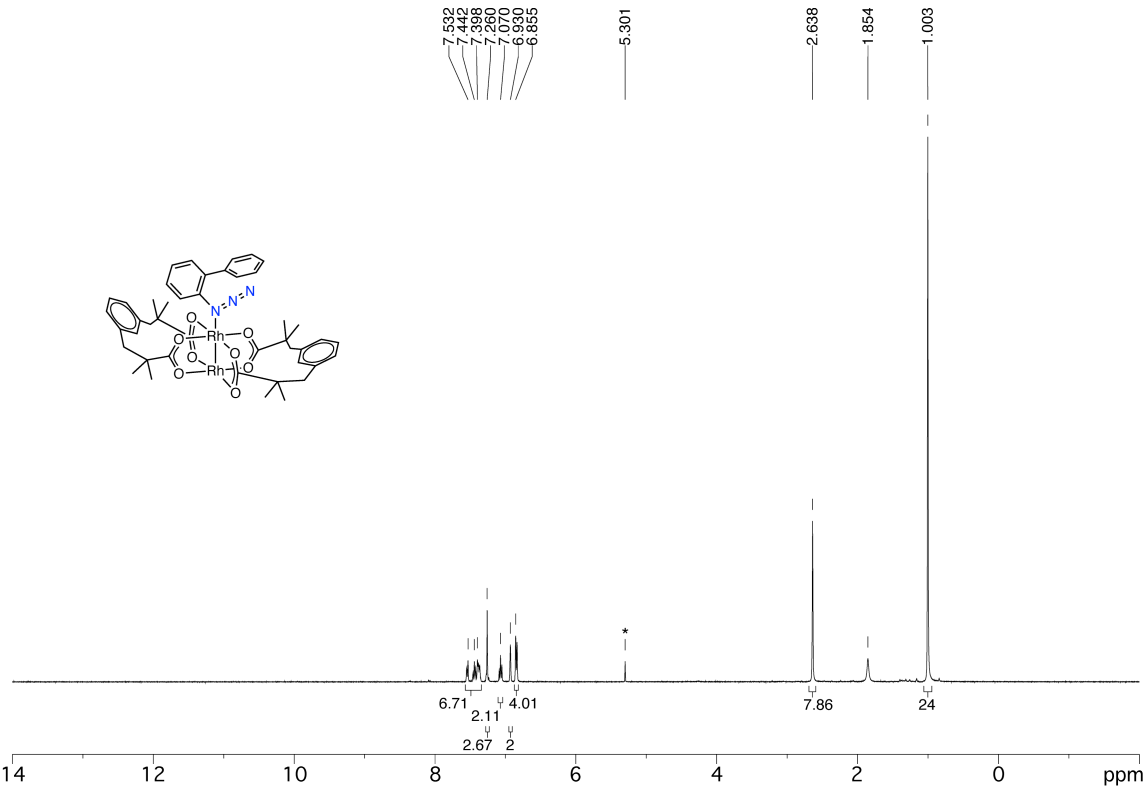

Figure V-3. ^{1}H NMR spectrum of V-3a recorded in $CDCl_3$ at 23 °C. The indicated peak (*) corresponds to CH_2Cl_2 that is present in the crystal structure. Integration indicates the formation of a 1 : 1 adduct of **V-2** with **V-1**.

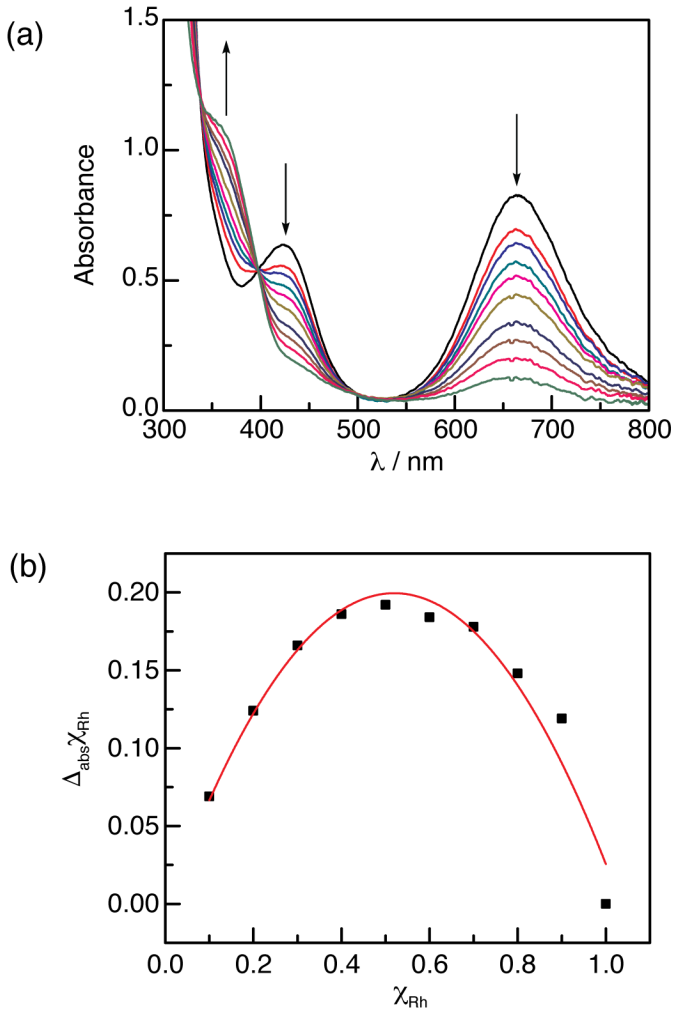

Figure V-4. Jobs plot generated from the titration of $Rh_2(esp)_2$ (V-1) with 2-azidobiphenyl (V-2). (a) UV-vis spectra obtained in CH_2Cl_2 at 23 °C with [**V-2** + **V-1**] = 3.078 M. (b) Plot of absorbance at 667 nm as a function of χ_{Rh}. The plot indicates formation of a 1 : 1 adduct of **V-2** with **V-1**.

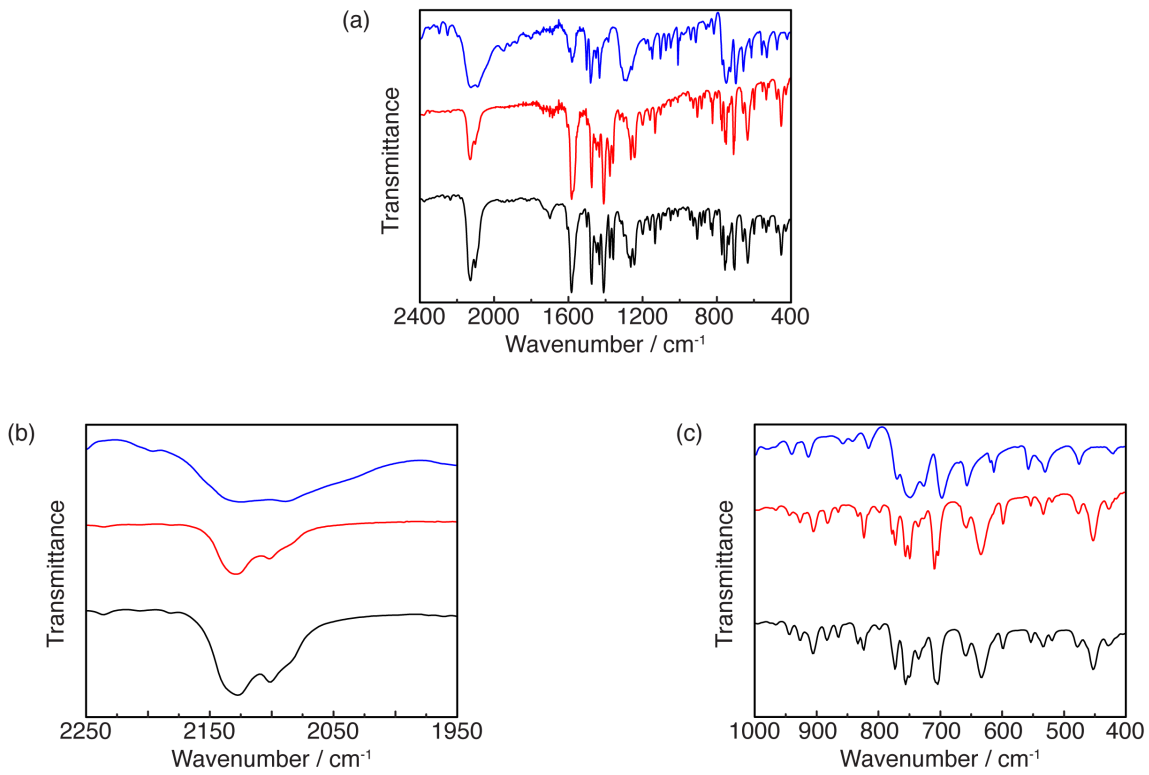

Figure V-5. IR spectra Rh_2 complexes V-3a and V-3b. (a) IR spectra of **V-2** (—), **V-3a** (—), and **V-3b** (—) recorded in KBr pellets at 23 °C. (b) Expansion of the spectral window depicting the azide region for **V-2** (—), **V-3a** (—), and **V-3b** (—). (c) Expansion of the spectral window depicting the fingerprint region for **V-2** (—), **V-3a** (—), and **V-3b** (—).

Complex **V-3a** participates in intramolecular C–H amination chemistry in the solid state. Either photolysis ($335 < \lambda < 610$ nm) or thermolysis (60 °C) of a KBr pellet of complex **V-3a** results in the formation of carbazole complex **V-4a** (**Figure V-2**).[290] Solid-state conversion was evidenced by the disappearance of the N_3 stretching frequencies at 2129 and 2101 cm^{-1} and the appearance of new peaks at 726, 575, and 508 cm^{-1} (**Figures V-6–V-7**). The final IR spectrum overlays with that of an authentic sample of carbazole complex **V-4a**, which could be independently prepared by treatment of $Rh_2(esp)_2$ with carbazole (**Figures V-8–V-9**). The formation of **V-4a** was further confirmed by ^1H NMR

analysis following extraction of either a photolyzed or thermolyzed KBr pellet with $CDCl_3$ (**Figures V-10–V-11**).

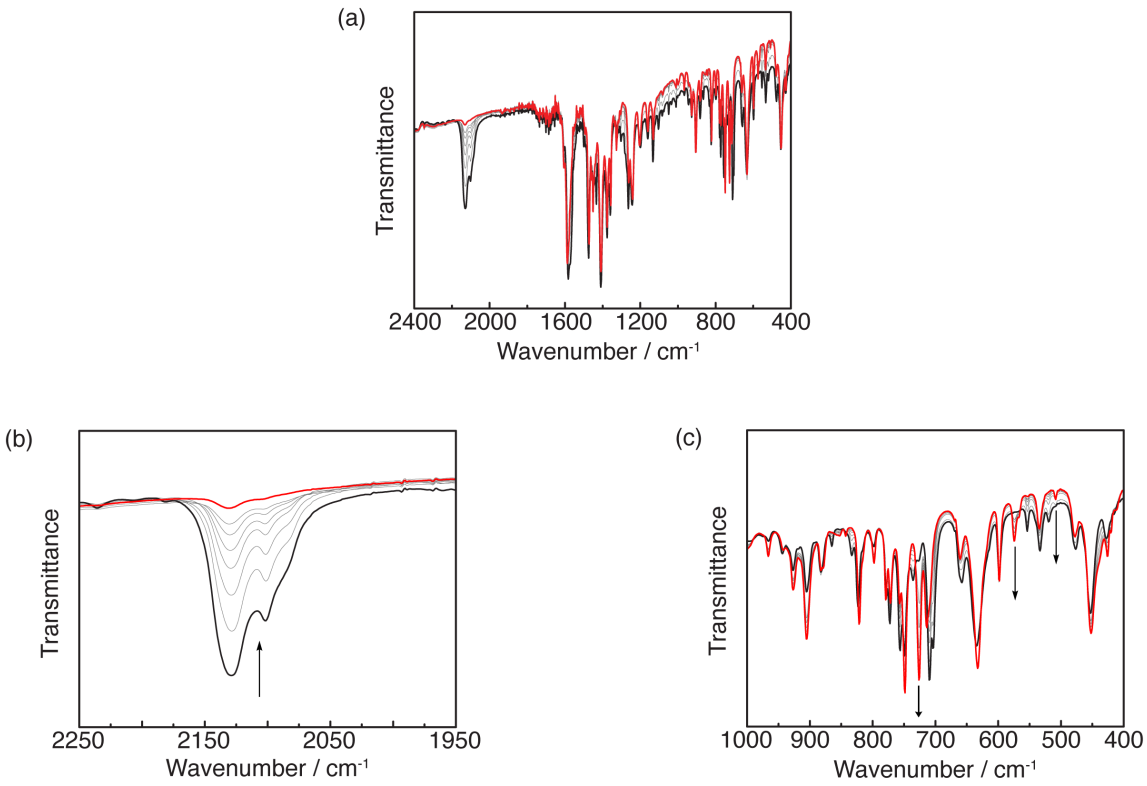

Figure V-6. *In situ* IR of the solid-state thermolysis of compound V-3a. (a) IR spectra collected during the thermolysis of a KBr pellet of **V-3a** at 60 °C from 0 min (—) to 70 min (—). (b) Expansion of the spectral window depicting the azide region shows the disappearance of the azide peaks at 2129 and 2101 cm^{-1}. (c) Expansion of the spectral window depicting the fingerprint region shows the formation of new peaks at 726, 574, and 508 cm^{-1}.* These observations are consistent with the thermally promoted, solid-state conversion of **V-3a** to **V-4a**.

* Baseline correction was performed to display the changes in the spectral features.

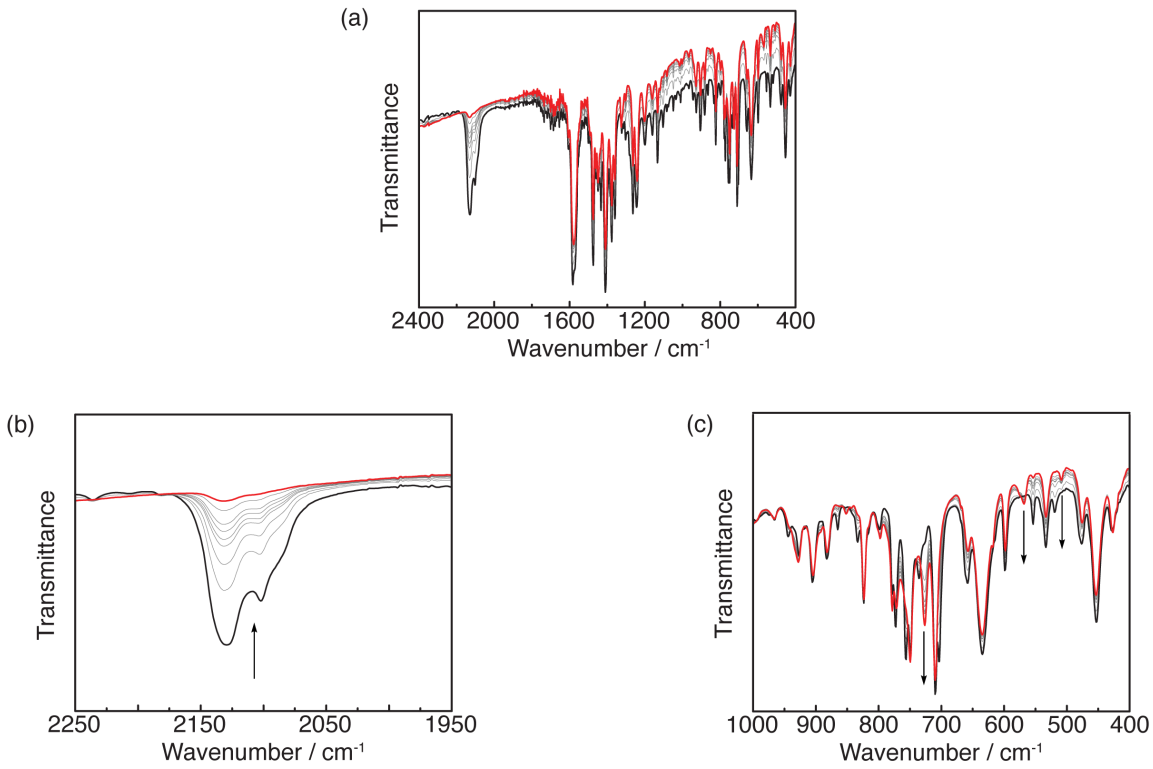

Figure V-7. *In situ* IR of the solid-state photolysis of compound V-3a. (a) IR spectra collected during the thermolysis of a KBr pellet of **V-3a** at 60 °C from 0 min (—) to 100 min (—). (b) Expansion of the spectral window depicting the azide region shows the disappearance of the azide peaks at 2129 and 2101 cm^{-1}. (c) Expansion of the spectral window depicting the fingerprint region shows the formation of new peaks at 726, 575, and 508 cm^{-1}.* These observations are consistent with the thermally promoted, solid-state conversion of **V-3a** to **V-4a**.

* Baseline correction was performed to display the changes in the spectral features.

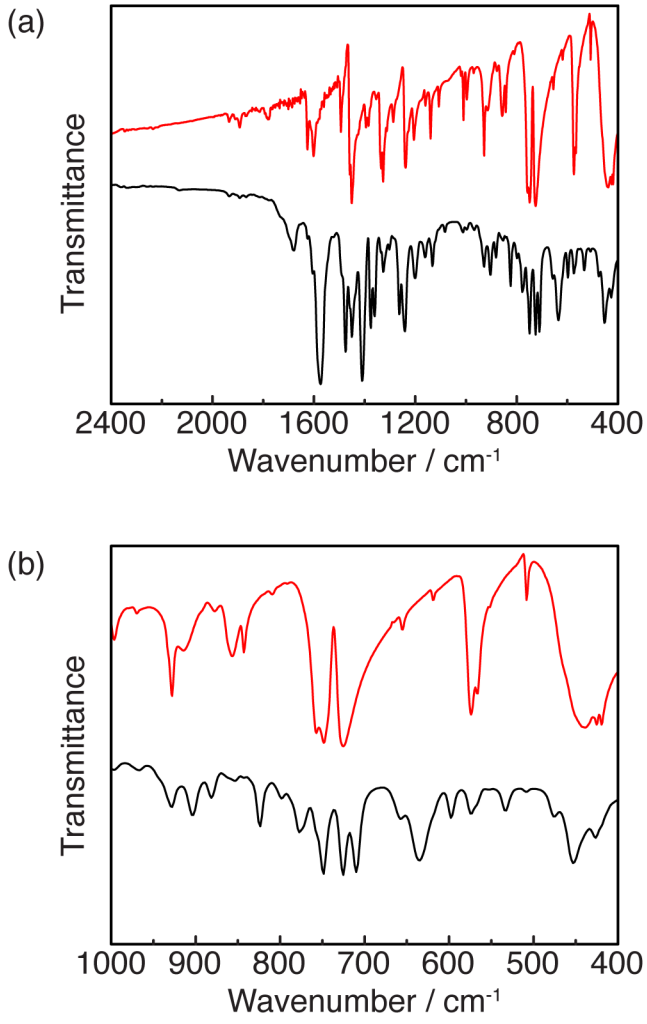

Figure V-8. IR spectra of Rh_2 complex V-4a. (a) IR spectra of carbazole (—) and **V-4a** (—) recorded as KBr pellets at 23 °C. (b) Expansion of the spectral window depicting the fingerprint region for carbazole (—) and **V-4a** (—).

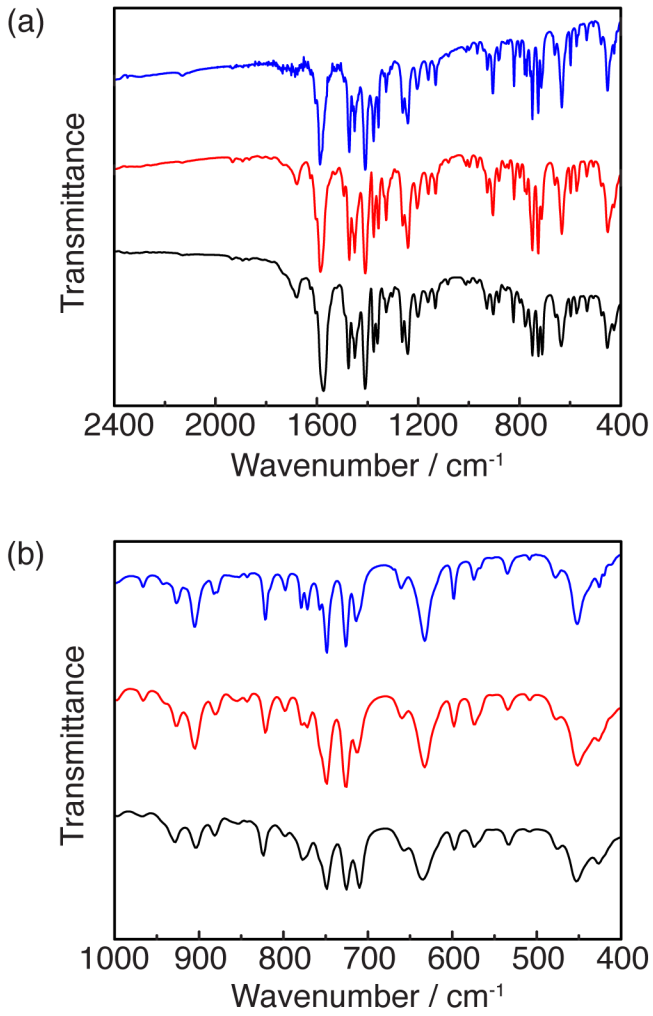

Figure V-9. Comparison of IR spectra of the end point of thermolysis of V-3a and V-3b with V-4a. (a) IR spectra of **V-4a** (—), following thermolysis of **V-3a** (—), and following thermolysis of **V-3b** (—) recorded in KBr pellets at 23 °C. (b) Expansion of the spectral window depicting the fingerprint region for of **V-4a** (—), following thermolysis of **V-3a** (—), and following thermolysis of **V-3b** (—).

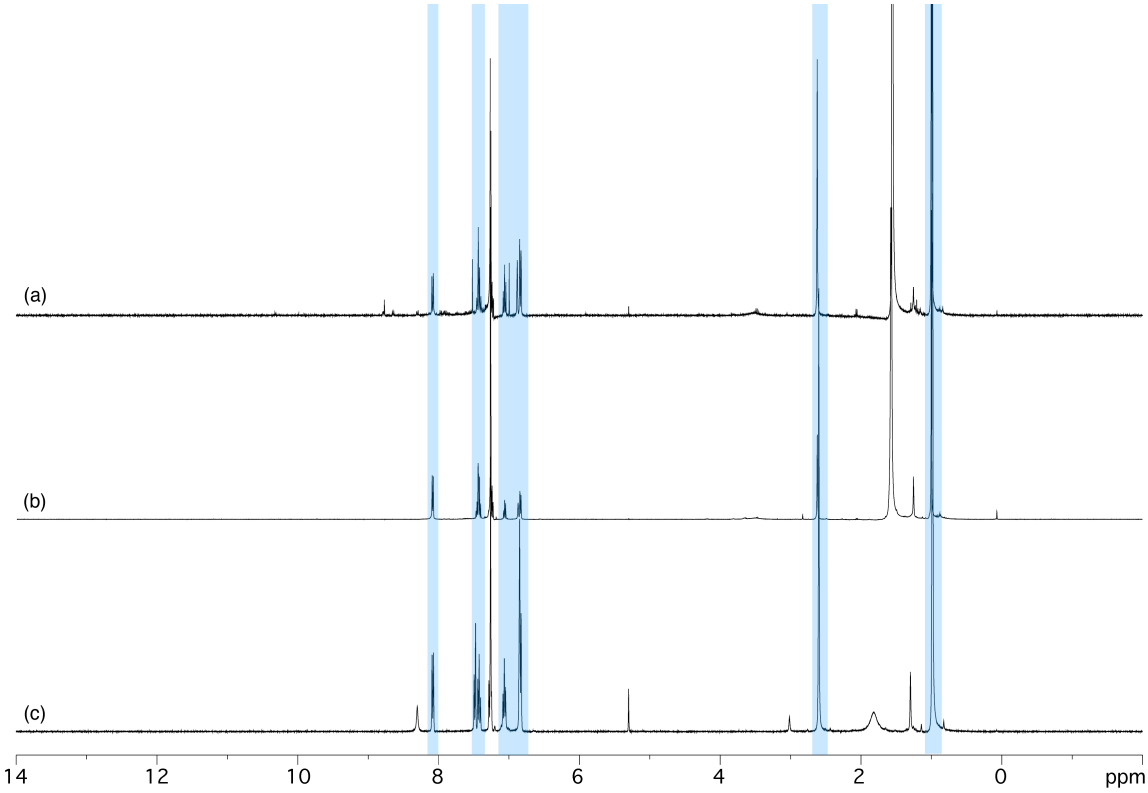

Figure V-10. Comparison of ^{1}H NMR spectra of the end point of thermolysis of V-3a and V-3b with V-4a. ^{1}H NMR spectra obtained following of (a) extraction of the KBr pellet of **V-3a** that was thermalized at 60 °C, (b) extractions of the KBr pellet of **V-3b** that was thermalized at 60 °C and (c) Rh_2 complex **V-4a**. Spectra were recorded in $CDCl_3$ at 23 °C.

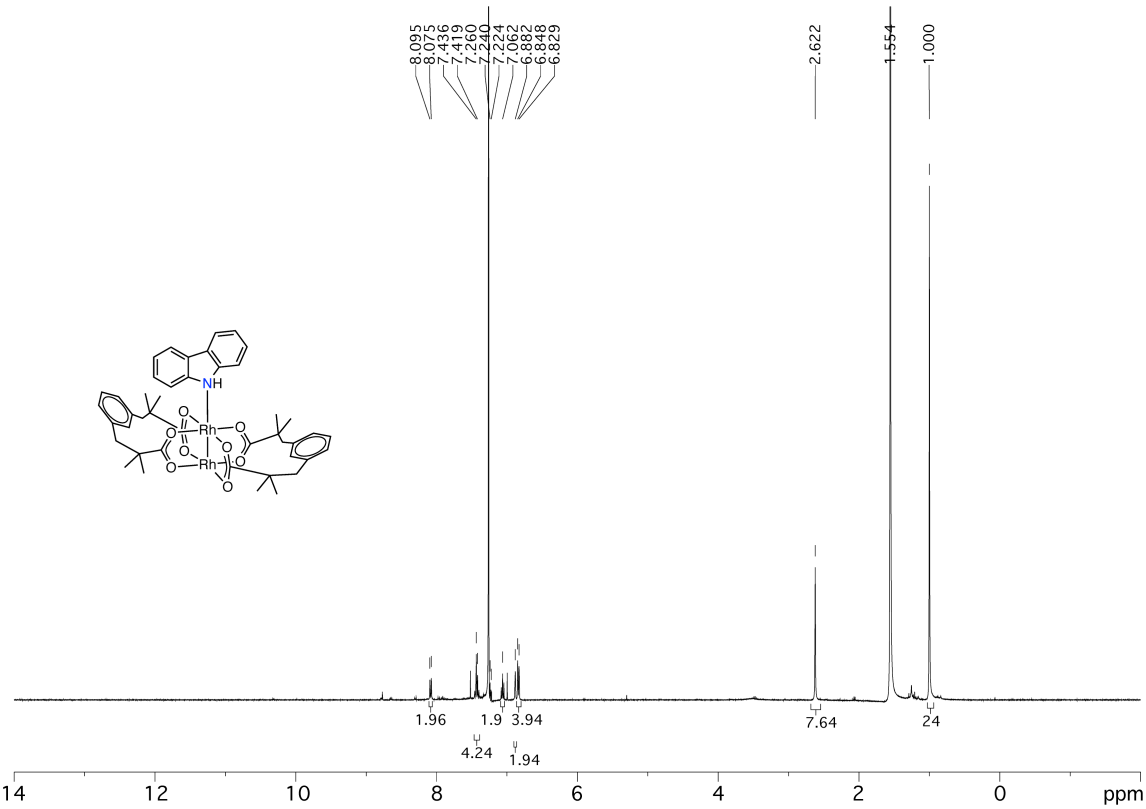

Figure V-11. ^{1}H NMR spectrum obtained following extraction of a thermolyzed (60 °C) KBr pellet of V-3a. This spectrum is the same as that presented in Figure V-10a. The spectrum was recorded in $CDCl_3$ at 23 °C. Integration of the peaks corresponding to carbazole and the $Rh_2(esp)_2$ moiety respectively, indicate that they are present as 1:1 ratio.

Intramolecular C–H amination within the coordination sphere of **V-3a** to generate **V-4a** presumably proceeds via the intermediates of Rh_2 nitrene **V-5a** (**Figure V-12a**). Evidence of facile N_2 elimination from **V-3a** was obtained from flux-dependent matrix-assisted laser-desorption ionization-mass spectrometry (MALDI-MS) measurements (**Figure V-12b**): A signal corresponding to $Rh_2(esp)_2^+$ (m/z = 758.3599, calc. 758.0828) was observed at low laser power; as the flux of the ablation laser was increased, a new signal, which corresponds to nitrene fragment $Rh_2(esp)_2(C_{12}H_{10}N)^+$ (m/z = 924.5538, calc. 925.1563) emerged.

Photolysis (λ= 365 nm) of a single crystal of **V-3a** under cryogenic conditions (100 K) promoted the *in crystallo* synthesis and crystallographic characterization of Rh_2 nitrene **V-5a**·N_2 (**Figure V-12c**). *In crystallo* reaction progress was monitored by periodic collection of X-ray crystal structures (synchrotron radiation λ = 0.41328 Å). Refinement of the resulting data indicated the extrusion of N_2 to generate the Rh_2 nitrenoid **V-5a**·N_2 with 90% chemical conversion (**Figure 12**).[291] Elimination of N_2 from **V-3a** is accompanied by the contraction of Rh(1)–N(1) from 2.244(3) Å in **V-3a** to 2.055(4) Å in **V-5a**·N_2. Concurrently, significant contraction of N(1)–C(1) (i.e. the N–C linkage in biphenyl nitrene) from 1.441(5) Å in **V-3a** to 1.335(7) Å in **V-5a**·N_2 and expansion of the Rh(1)–N(1)–C(1) bond angle from 125.0(2)° in **V-3a** to 140.6(4)° in **V-5a**·N_2 are observed. The Rh(1)–Rh(2) bond distance remained unchanged (i.e., **V-3a**: 2.3850(4) Å, **V-5a**·N_2: 2.3953(4) Å). The evolved N_2 was refined at 90% occupancy, which is consistent with the measured chemical conversion of **V-3a** to **V-5a**·N_2. *In crystallo* conversion of **V-3a** to **V-5a**·N_2 could also be accomplished more slowly by sustained exposure to synchrotron radiation (λ = 0.41328 Å) without photolysis. This observation is similar to X-ray stimulated N_2 extrusion reactions previously observed in both Rh_2-[287] and Co-azide[292] complexes, and a variety of other X-ray stimulated chemical reactions.[279,280] While the N(1)–C(12) distance (i.e., the N–C bond formed during carbazole formation) decreased from 3.190(5) Å (**V-3a**) to 3.019(8) Å (**V-5a**·N_2), we were unsuccessful in observing the conversion of nitrene **V-5a**·N_2 to carbazole adduct **V-4a** via a second single-crystal-to-single-crystal transformation, presumably due to thermally promoted N_2 mobility which led to destruction of sample crystallinity.

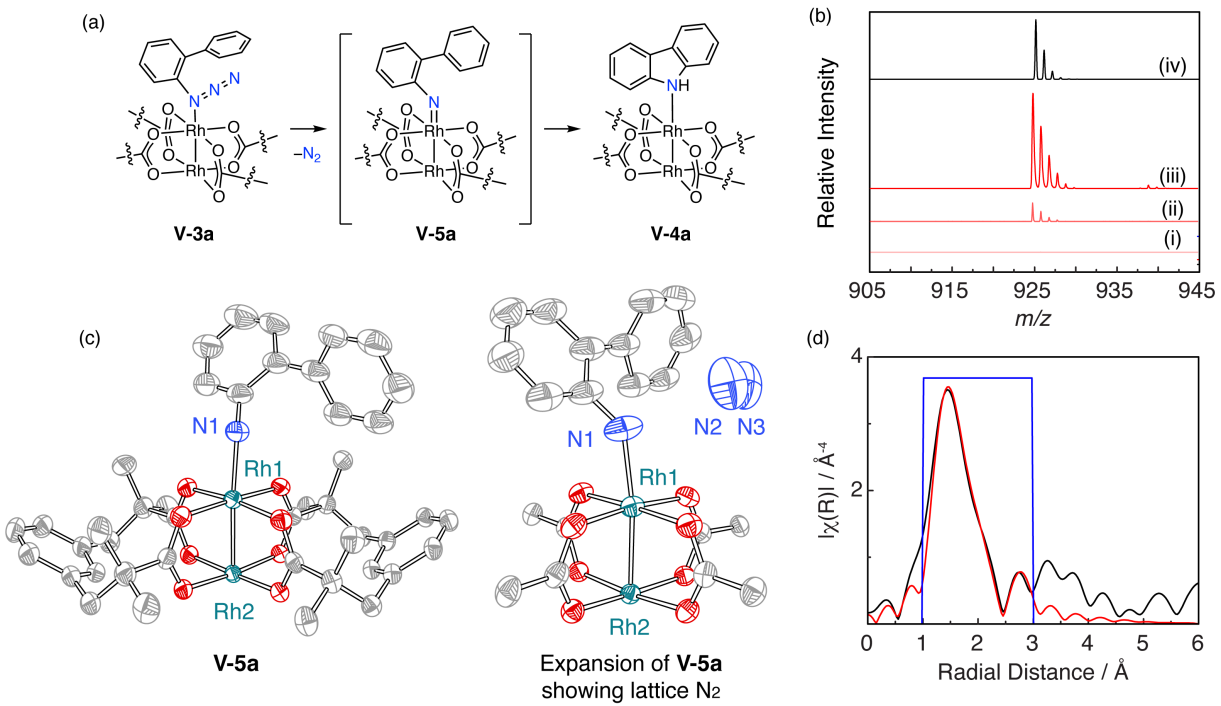

Figure V-12. Characterization of the Rh_2 nitrenoid V-5a. (a) Thermally or photochemically promoted loss of N_2 from complex **V-3a** affords the transient Rh_2 complex **V-5a**, which participates in intramolecular C–H amination to generate carbazole complex **V-4a**. (b) (i–iii) Flux-dependent MALDI-MS data shows an ion corresponding to $Rh_2(esp)_2(C_{12}H_{10}N)^+$; (iv) simulated isotopic distribution for $Rh_2(esp)_2(C_{12}H_{10}N)^+$. (c) Left: Thermal ellipsoid plot of **V-5a** drawn at 50% probability. H-atoms, N_2 and solvent are omitted for clarity. Right: Thermal ellipsoid plot of **V-5a** drawn at 50% probability by rotating the left structure by 90°. H-atoms, esp ligand and solvent are omitted for clarity. Selected metrical parameters: Rh(1)–N(1) = 2.055(4) Å, N(1)–C(1) = 1.335(7) Å, Rh(1)–Rh(1) = 2.3953(4) Å, Rh(1)–N(1)–C(1) = 140.6(4)°. (d) Rh K-edge EXAFS data (spectral fitting window range 1.0–3.0 Å (—)) of $Rh_2(esp)_2(C_{12}H_9N)$ (**V-5a**, experimental data (—) and fitted data (—)) that was generated by synchrotron irradiation (λ = 0.41328 Å) at 100 K for 2 h. Fitting statistics are compiled in Table V-2.

Rh K-edge Extended X-ray Fine Structure (EXAFS) analysis of $Rh_2(esp)_2(C_{12}H_{10}N_3)$ (**V-3a**) indicates the coordination environment around Rh is comprised of four Rh–O interactions with 2.01(2) Å, one Rh–Rh interaction with 2.36(3) Å, and a half-occupied Rh–N vector of 2.26(2) Å, which is in excellent agreement with the metrical parameters derived from single-crystal X-ray analysis (**Figure V-13** and **Table V-1**). Similar analysis of nitrene **V-5a**, which was generated by sustained (2 h) exposure of a boron nitride pellet of **V-3a** to synchrotron radiation (λ = 0.41328 Å), was fit with four Rh–O interactions with 2.03(2) Å, one Rh–Rh interaction with 2.400(9) Å, and one-half Rh–N interaction with 2.063(9) Å (**Figure V-14** and **Table V-2**). These metrical parameters are consistent with the metrics obtained from *in crystallo* synthesis of **V-5a**·N_2. Analysis of the edge-energy and spectral intensity from successive measurements indicates that significant chemical conversion is not observed on the time scale of the experiment. Comparison of the X-ray absorption near edge structure (XANES) data of **V-1**, **V-3a**, and **V-5a** indicates that all complexes share a common Rh_2[II,II] core (**Figure V-15**).

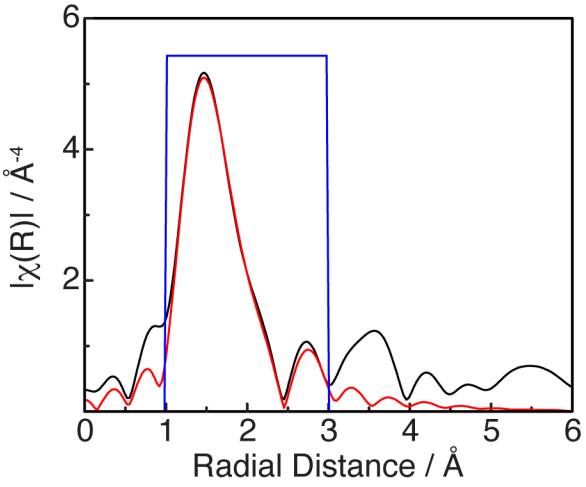

Figure V-13. Rh K-edge EXAFS data (spectral fitting window range 1.0–3.0 Å) of V-3a (experimental data (—) and fitted data (—)). Fitting statistics are compiled in Table V-1.

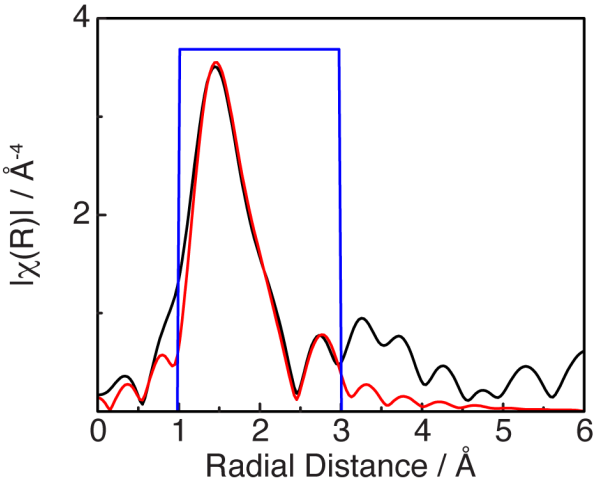

Figure V-14. Rh K-edge EXAFS data (spectral fitting window range 1.0–3.0 Å) of V-5a (experimental data (—) and fitted data (—)) that was generated by synchrotron irradiation (l = 0.41328 Å) at 100 K for 2 h. Fitting statistics are compiled in Table V-2.

Table V-1. EXAFS fitting results for $Rh_2(esp)_2(C_{12}H_9N_3)$ (V-3a).

	Path	R / Å	CN	σ^2 / Å^2	ΔE / eV	R-Factor	Independent points	Variables	Reduced χ^2
V-3a	Rh–O	2.01(2)	4.0	0.0025(7)	–3(4)	0.007	8.6875	7	2.79
	Rh–N	2.26(2)	0.5	0.0025(7)					
	Rh–Rh	2.36(3)	1.0	0.004(1)					
	Rh–C	2.88(2)	4.0	0.003(3)					
	Rh–N	2.99(2)	0.5	0.0025(7)					
	Rh–O	3.05(2)	4.0	0.0025(7)					
	Rh–OC	3.08(1)	8.0	0.003(1)					
	Rh–C	3.30(2)	0.5	0.003(3)					

Table V-2. EXAFS fitting results for *in situ* generated $Rh_2(esp)_2(C_{12}H_9N)$ (V-5a).

	Path	R / Å	CN	σ^2 / Å^2	ΔE / eV	R-Factor	Independent points	Variables	Reduced χ^2
V-5a	Rh–O	2.03(2)	4.0	0.0076(8)	–4(2)	0.010	8.6875	6	16.73
	Rh–N	2.063(9)	0.5	0.004(2)					
	Rh–Rh	2.400(9)	1.0	0.007(2)					
	Rh–C	2.889(9)	2.0	0.004(2)					
	Rh–C	2.918(9)	2.0	0.004(2)					
	Rh–O	3.05(2)	1.0	0.0051(5)					
	Rh–OC	3.08(2)	8.0	0.0076(8)					
	Rh–O	3.078(9)	3.0	0.0051(5)					

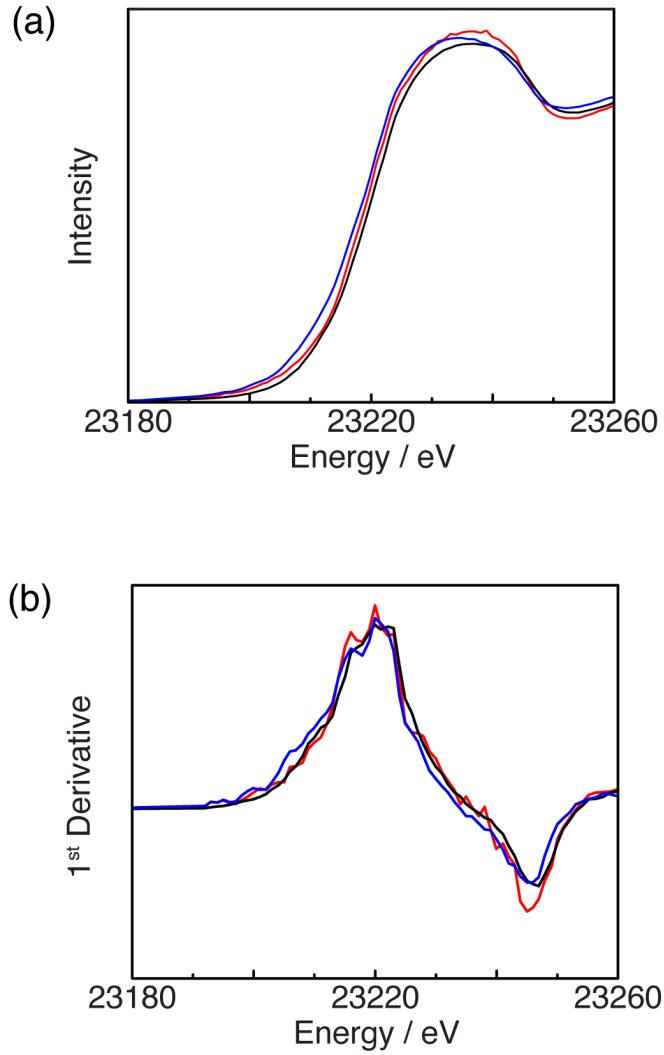

Figure V-15. XANES Spectra of Rh_2 complexes V-1, V-3a and V-5a. (a) Rh K-edge XANES spectra of $Rh_2(esp)_2$ (**V-1**, —), $Rh_2(esp)_2(C_{12}H_9N_3)$ (**V-3a**, —) and $Rh_2(esp)_2(C_{12}H_9N)$ (**V-5a**, —) that was generated by synchrotron irradiation ($\lambda = 0.41328$ Å) at 100 K for 2h. (b) First derivative plot of the Rh K-edge XANES data of $Rh_2(esp)_2$ (**V-1**, —), $Rh_2(esp)_2(C_{12}H_9N_3)$ (**V-3a**, —) and $Rh_2(esp)_2(C_{12}H_9N)$ (**V-5a**, —). The XANES data obtained for **V-1**, **V-3a** and **V-5a** is consistent with a common Rh_2[II,II] core.

The experimentally determined metrical parameters from photocrystallography and *in situ* EXAFS for **V-5a** are in excellent agreement with geometry optimization calculations of the triplet electronic configuration (i.e., ^{3}[**V-5a**]) carried out by Density

Functional Theory at the wB97XD[293]/ SDD (Rh),[294-296] 6-31G(d) (light atoms)[297-298] level of theory.[299] Consistent with the assigned electronic configuration, the triplet configuration was calculated to be 12.2 kcal·mol^{-1} more stable than the corresponding singlet. Significantly, comparison of a variety of computational strategies that have been used in the past to examine Rh_2-catalyzed reactions revealed that while the optimized structures of **V-1** and **V-3a** were well captured by several popular method, the optimized geometry of reactive intermediate **V-5a** displayed significant variation (**Tables V-3–V-5**).

Table V-3. Comparison of computed and experimental bond lengths for $Rh_2(esp)_2(C_{12}H_9N_3)$ (V-3a). Experimental distances are derived from the X-ray structure of compound **V-3a**. Computed distances are derived from optimization of $Rh_2(esp)_2(C_{12}H_9N_3)$ at the indicated level of theory.

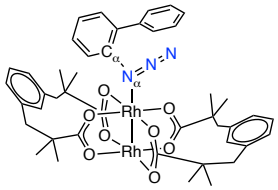

	Rh–Rh / Å	**Rh–N$_\alpha$ / Å**	**N$_\alpha$–C$_\alpha$ / Å**	**Rh–N$_\alpha$–C$_\alpha$ / °**
Experiment	2.3850(4)	2.244(3)	1.441(5)	125.0(2)
wB97XD SDD (Rh) 6-31G(d) (light atoms)	2.39696	2.25478	1.43710	124.87870
uM06 LANL2DZ	2.44148	2.20523	1.44500	124.36860
CAM-B3LYP LANL2DZ (Rh) 6-31G(d) (light atoms)	2.39245	2.28451	1.43910	130.15470
BP86 SDD (Rh) 6-31+G(d,p) (light atoms)	2.41433	2.30256	1.44518	131.51866
M06L SDD (Rh) 6-31+G(d,p) (light atoms)	2.40543	2.31820	1.43368	121.86388
BP86 def2TZVP	2.39994	2.31718	1.44131	131.88760
M06L def2TZVP	2.39712	2.31813	1.42949	123.04460
M06L def2SVP	2.39574	2.31735	1.42726	121.61240

Table V-4. Comparison of computed and experimental bond lengths for $Rh_2(esp)_2(C_{12}H_9N)$ (V-5a). Experimental distances are derived from the X-ray structure of compound **V-5a**. Computed distances are derived from optimization of $Rh_2(esp)_2(C_{12}H_9N)$ at the indicated level of theory.

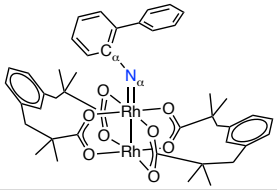

		Rh–Rh / Å	Rh–N$_\alpha$ / Å	N$_\alpha$–C$_\alpha$ / Å	Rh–N$_\alpha$–C$_\alpha$ / °
Experiment		2.3953(4)	2.055(4)	1.335(7)	140.6(4)
wB97XD SDD (Rh) 6-31G(d) (light atoms)	Singlet	2.44127	1.98514	1.31602	125.90780
	Triplet	2.41189	2.05864	1.32141	139.14460
uM06 LANL2DZ	Singlet	2.49000	1.98148	1.34825	125.48241
	Triplet	2.45225	2.03499	1.34525	141.92290
CAM-B3LYP LANL2DZ (Rh) 6-31G(d) (light atoms)	Singlet	2.43985	2.01481	1.30487	127.91396
	Triplet	2.40350	2.10745	1.31153	157.86428
BP86 SDD (Rh) 6-31+G(d,p) (light atoms)	Singlet	2.44931	1.96383	1.34594	127.31661
	Triplet	2.42601	1.97287	1.33446	141.26718
M06L SDD (Rh) 6-31+G(d,p) (light atoms)	Singlet	2.45074	1.96605	1.33706	123.30204
	Triplet	2.42395	1.99299	1.32610	137.27385
BP86 def2TZVP	Singlet	2.43512	1.95050	1.33808	128.12910
	Triplet	2.41036	1.95949	1.32628	142.29010
M06L def2TZVP	Singlet	2.43640	1.94466	1.32671	124.96320
	Triplet	2.41267	1.97282	1.31675	140.41850
M06L def2SVP	Singlet	2.44286	1.95607	1.33327	123.92180
	Triplet	2.41416	1.98499	1.32317	138.02930

Table V-5. Analysis of the relative stabilities of ^{1}[V-5a] and ^{3}[V-5a]. In all the calculations, the triplet state was lower in energy.

wB97XD SDD (Rh) 6-31G(d) (light atoms)	**ΔE**	**ΔH**	**ΔG**
^{1}[**V-5a**]	–2582.524539 E_h	–2582.523595 E_h	–2582.658467 E_h
^{3}[**V-5a**]	–2582.542076 E_h	–2582.541132 E_h	–2582.677973 E_h
Δ(^{3}[**V-5a**]– ^{1}[**V-5a**])	–11.005 kcal·mol^{-1}	–11.005 kcal·mol^{-1}	–12.240 kcal·mol^{-1}
uM06 LANL2DZ	**ΔE**	**ΔH**	**ΔG**
^{1}[**V-5a**]	–2579.165594 E_h	–2579.164650 E_h	–2579.298399 E_h
^{3}[**V-5a**]	–2579.175733 E_h	–2579.174789 E_h	–2579.311011 E_h
Δ(^{3}[**V-5a**]– ^{1}[**V-5a**])	–6.4 kcal·mol^{-1}	–6.4 kcal·mol^{-1}	–7.9 kcal·mol^{-1}
CAM-B3LYP LANL2DZ (Rh) 6-31G(d) (light atoms)	**ΔE**	**ΔH**	**ΔG**
^{1}[**V-5a**]	–2579.707311 E_h	–2579.706367 E_h	–2579.841947 E_h
^{3}[**V-5a**]	–2579.725921 E_h	–2579.724977 E_h	–2579.862564 E_h
Δ(^{3}[**V-5a**]– ^{1}[**V-5a**])	–11.7 kcal·mol^{-1}	–11.7 kcal·mol^{-1}	–12.9 kcal·mol^{-1}
BP86 SDD (Rh) 6-31+G(d,p) (light atoms)	**ΔE**	**ΔH**	**ΔG**
^{1}[**V-5a**]	–2583.558481 E_h	–2583.557537 E_h	–2583.699214 E_h
^{3}[**V-5a**]	–2583.559700 E_h	–2583.558756 E_h	–2583.702181 E_h
Δ(^{3}[**V-5a**]– ^{1}[**V-5a**])	–0.8 kcal·mol^{-1}	–0.8 kcal·mol^{-1}	–1.9 kcal·mol^{-1}
M06L SDD (Rh) 6-31+G(d,p) (light atoms)	**ΔE**	**ΔH**	**ΔG**
^{1}[**V-5a**]	–2583.227090 E_h	–2583.226146 E_h	–2583.361200 E_h
^{3}[**V-5a**]	–2583.231218 E_h	–2583.230274 E_h	–2583.367814 E_h
Δ(^{3}[**V-5a**]– ^{1}[**V-5a**])	–2.6 kcal·mol^{-1}	–2.6 kcal·mol^{-1}	–4.2 kcal·mol^{-1}
BP86 def2TZVP	**ΔE**	**ΔH**	**ΔG**
^{1}[**V-5a**]	–2584.395272 E_h	–2584.394328 E_h	–2584.535707 E_h
^{3}[**V-5a**]	–2584.397037 E_h	–2584.396093 E_h	–2584.538597 E_h
Δ(^{3}[**V-5a**]– ^{1}[**V-5a**])	–1.1 kcal·mol^{-1}	–1.1 kcal·mol^{-1}	–1.8 kcal·mol^{-1}
M06L def2TZVP	**ΔE**	**ΔH**	**ΔG**
^{1}[**V-5a**]	–2584.002248 E_h	–2584.001304 E_h	–2584.136008 E_h
^{3}[**V-5a**]	–2584.005491 E_h	–2584.004547 E_h	–2584.141444 E_h
Δ(^{3}[**V-5a**]– ^{1}[**V-5a**])	–2.0 kcal·mol^{-1}	–2.0 kcal·mol^{-1}	–3.4 kcal·mol^{-1}
M06L def2SVP	**ΔE**	**ΔH**	**ΔG**
^{1}[**V-5a**]	–2581.415596 E_h	–2581.414652 E_h	–2581.550808 E_h
^{3}[**V-5a**]	–2581.423401 E_h	–2581.422457 E_h	–2581.558345 E_h
Δ(^{3}[**V-5a**]– ^{1}[**V-5a**])	–4.9 kcal·mol^{-1}	–4.9 kcal·mol^{-1}	–4.7 kcal·mol^{-1}

During C–H amination catalysis, substrate **V-2** is present in significant excess with respect to Rh_2 catalyst **V-1**, and thus multiple equivalents of coordinating substrate could bind to the Rh_2 catalyst. Slow evaporation of a $CHCl_3$ solution of **V-1** that contained an excess of biphenylazide **V-2** afforded single crystals of **V-3b** in which each of the Rh centers is coordinated by an azide ligand (i.e., 2 : 1 adduct, **Figure V-16**). The metrical parameters of complex **V-3b** are similar to those obtained for **V-3a**, except the Rh(1)–N(1) bond distance (2.280(4) Å) is longer than the corresponding distance in **V-3a** (2.244(3) Å), which is consistent with a through Rh–Rh bond structural trans influence of the coordinated azide ligand. The IR spectrum of **V-3b** is similar to that of **V-3a**, except the intensity of the azide stretching modes in **V-3b** are twice that of **V-3a** (**Figure V-5**).

Similar to the solid-state chemistry of **V-3a**, bis-azide complex **V-3b** also participates in both photochemically ($335 < \lambda < 610$ nm) and thermally (60 °C) promoted intramolecular C–H amination in the solid state. IR spectra obtained during either photolysis or thermolysis of a KBr pellet of **V-3b** revealed that the disappearance of the N_3 stretching frequency at 2129 and 2101 cm^{-1} was accompanied by the evolution of new peaks at 726, 575 and 508 cm^{-1} (**Figures V-17–V-18**). ^1H NMR analysis following extraction of either the photolyzed or thermolyzed KBr pellet with $CDCl_3$ revealed a 2:1 ratio of carbazole to $Rh_2(esp)_2$ (**Figures V-10** and **V-19**), which indicates that under these conditions, both azide ligands eventually undergo cyclization to carbazole.

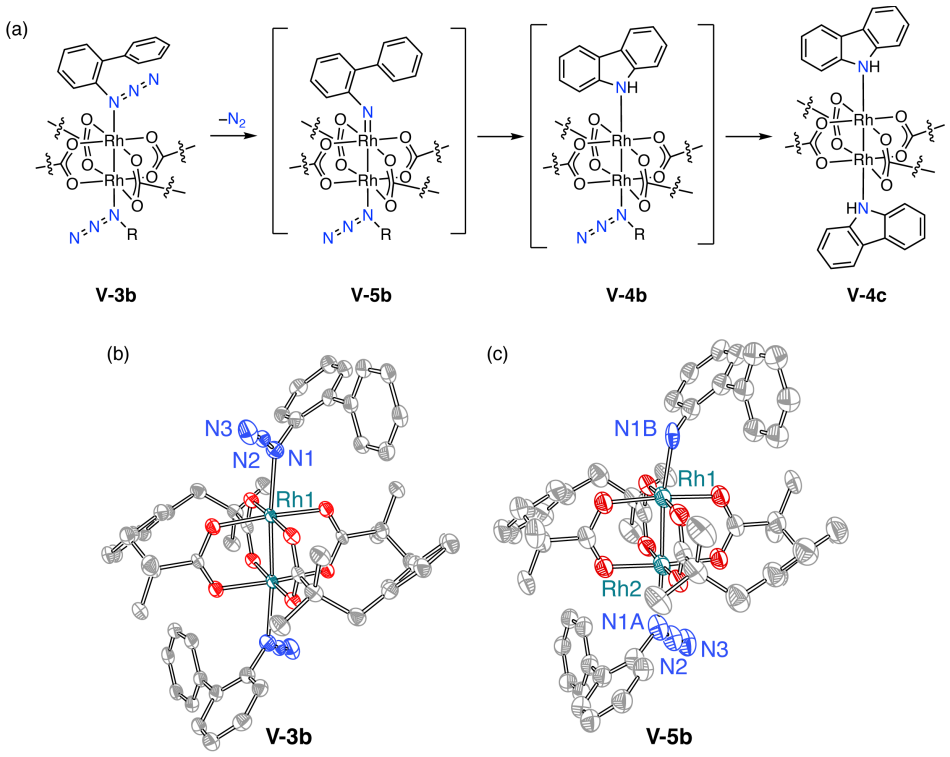

Figure V-16. Synthesis and photochemistry of Rh_2 bis-azide complex V-3b. (a) Solid-state, intramolecular C–H amination from **V-3b** can be promoted either thermally (i.e., heating to 60 °C) or photochemically ($335 < \lambda < 610$ nm). (b) Thermal ellipsoid plot of **V-3b** drawn at 50% probability. H-atoms and solvent are omitted for clarity. Selected metrical parameters: Rh(1)–N(1) = 2.280(4) Å, N(1)–C(1) = 1.436(6) Å, Rh(1)–Rh(1) = 2.3872(6) Å, Rh(1)–N(1)–C(1) = 125.1(3)°. (c) Thermal ellipsoid plot of **V-5b**·N_2 drawn at 50% probability. H-atoms and solvent are omitted for clarity. Selected metrical parameters: Rh(1)–N(1) = 2.10(4) Å, N(1)–C(1) = 1.36(4) Å, Rh(1)–Rh(1) = 2.4061(8) Å, Rh(1)–N(1)–C(1) = 127(2)°.

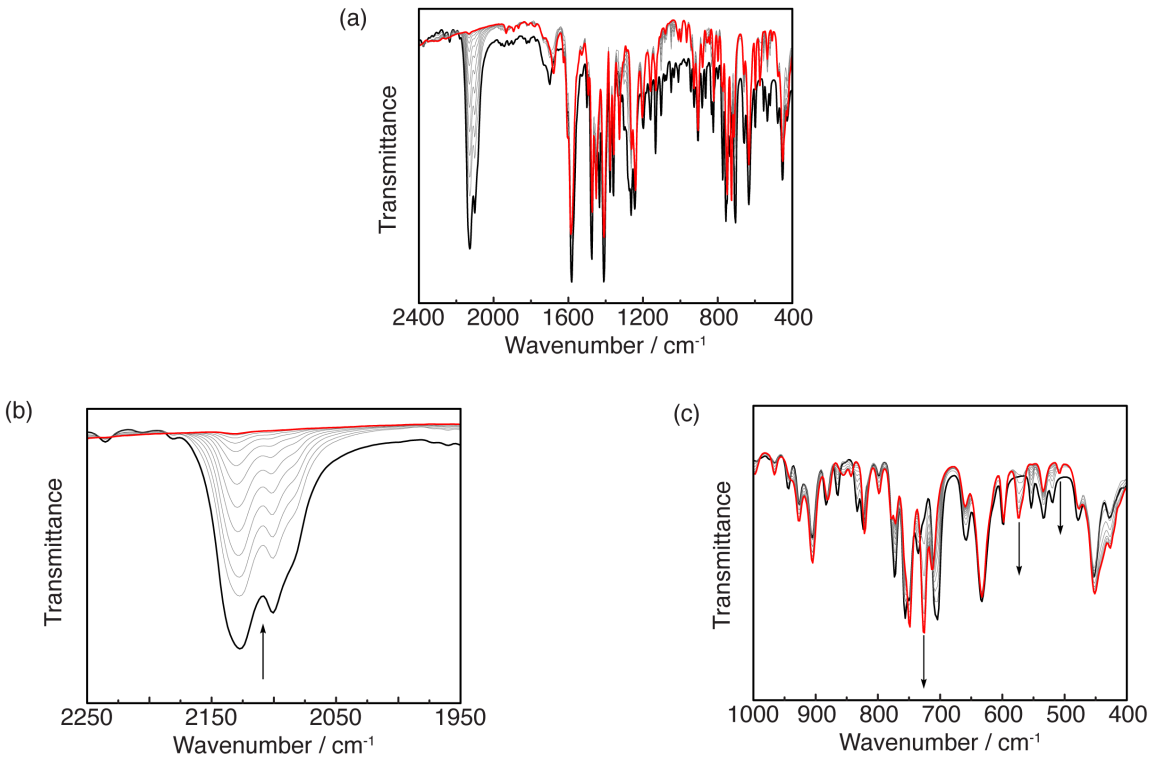

Figure V-17. *In situ* IR of solid-state thermolysis of compound V-3b. (a) IR spectra collected during the thermolysis of a KBr pellet of **V-3b** at 60 °C from 0 min (—) to 120 min (—). (b) Expansion of the spectral window depicting the azide region shows the disappearance of the azide peaks at 2129 and 2101 cm^{-1}. (c) Expansion of the spectral window depicting the fingerprint region shows the formation of new peaks at 726, 574, and 508 cm^{-1}.*

* Baseline correction was performed to display the changes in the spectral features.

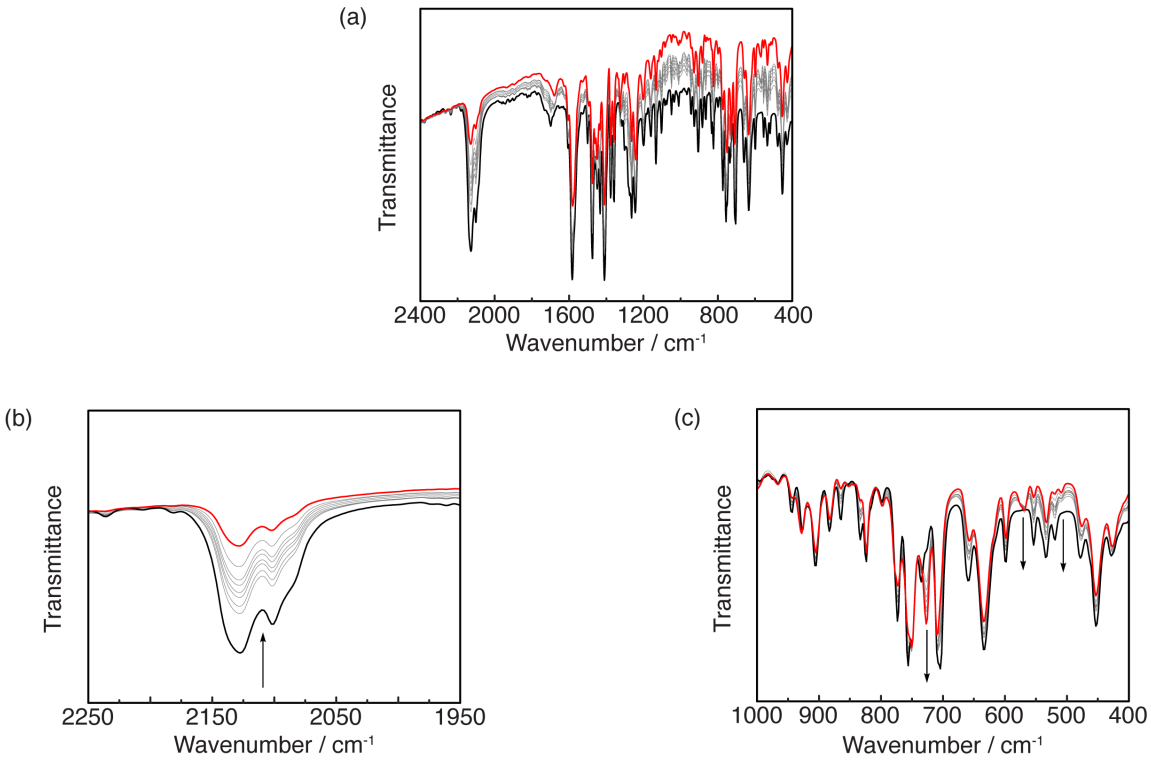

Figure V-18. *In situ* IR of solid-state photolysis of compound V-3b. (a) IR spectra collected during the photolysis ($335 < \lambda < 610$ nm) of a KBr pellet of **V-3b** in a KBr pellet at 23 °C from 0 min (—) to 120 min (—). (b) Expansion of the spectral window depicting the azide region shows the disappearance of the azide peaks at 2129 and 2101 cm^{-1}. (c) Expansion of the spectral window depicting the fingerprint region shows the formation of new peaks at 726, 575, and 508 cm^{-1}.*

* Baseline correction was performed to display the changes in the spectral features.

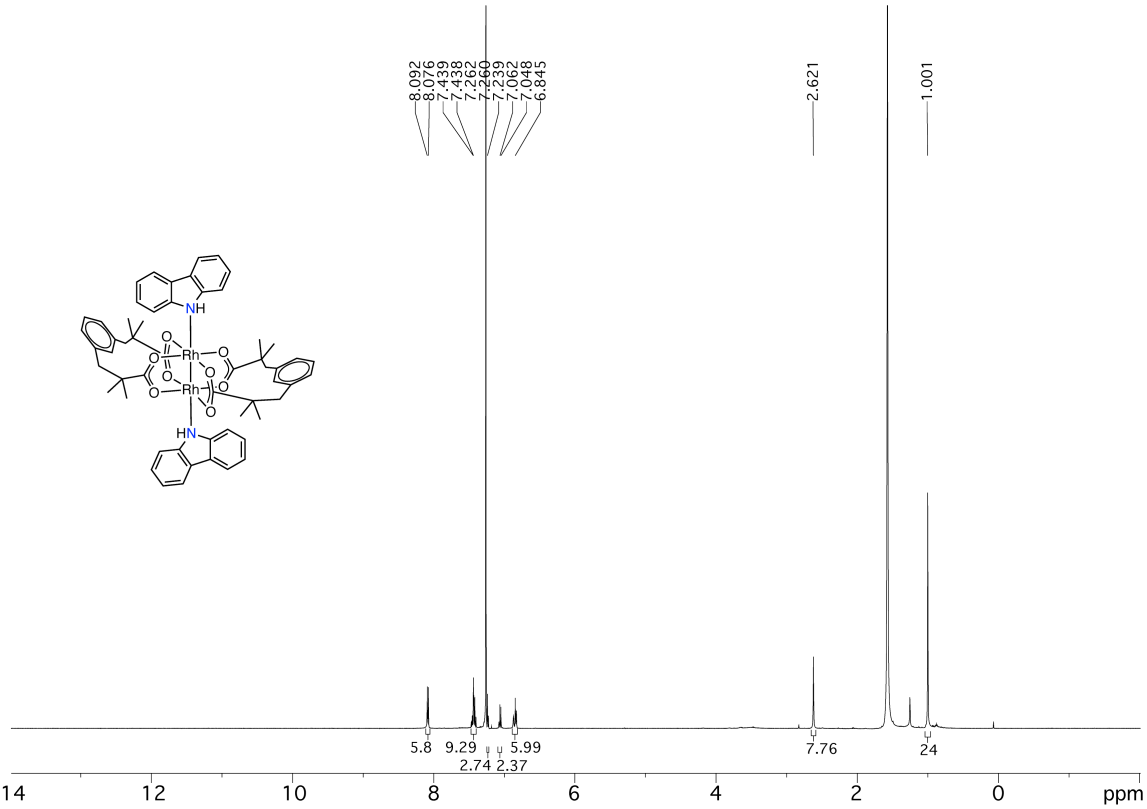

Figure V-19. ^{1}H NMR spectra obtained following extraction of a thermolyzed (60 °C) KBr pellet of V-3b. This spectrum is the same as that presented in Figure V-10b. The spectrum was recorded in $CDCl_3$ at 23 °C. Integration of the peaks corresponding to carbazole and the $Rh_2(esp)_2$ moiety respectively, indicate that they are present as 2:1 ratio.

In crystallo N_2 expulsion from **V-3b** enabled the characterization of Rh_2 nitrene **V-5b**·N_2, which differs from **V-5a**·N_2 by the presence of a coordinated biphenylazide ligand (i.e., **V-2**) on the distal Rh center (**Figure V-16c**). Similar to the synthesis of **V-5a**, *in crystallo* reaction progress was monitored by periodic collection of X-ray crystal structures (synchrotron radiation λ = 0.41328 Å). Refinement of the resulting data indicated the extrusion of N_2 to generate the Rh_2 nitrenoid **V-5b**·N_2 with 43% chemical

conversion; higher conversions led to loss in sample crystallinity (**Figure V-16**).[300] The Rh centers in both **V-3b** and **V-5b**·N_2 are symmetry equivalent, and thus loss in N_2 results in positional disorder of the unreacted biphenyl azide and newly generated biphenyl nitrene moieties (i.e., the generated nitrene is modeled as 50% occupancy of $C_{12}H_{10}N_3$ and $C_{12}H_{10}N$ at each Rh center). Extrusion of N_2 from **V-3b** resulted in the contraction of Rh(1)–N(1) from 2.280(4) Å in **V-3b** to 2.10(4) in Å **V-5b**·N_2. Concurrent with the expulsion of N_2 and the contraction of Rh(1)–N(1) bond, N(1)–C(1) (i.e., the N–C linkage in biphenyl nitrene) contracted from 1.436(6) Å to 1.36(4) Å and the Rh(1)–N(1)–C(1) bond angle expanded from 125.1(3)° to 127(2)°. The Rh(1)–Rh(1) bond distance remained essentially unchanged (i.e., from 2.3872(6) Å (**V-3b**) to 2.4061(8) Å (**V-5b**·N_2)). We were unable to locate the evolved N_2 in the structure of **V-5b** because it is disordered with a lattice $CHCl_3$ molecule that is present in the crystal structure of **V-3b**.

DFT geometry optimization of ^{3}[**V-5b**] are well-matched to the experimental data; computed metrics of ^{1}[**V-5b**] reveal a significantly shorter nitrene linkage. This observation is supported by the relative energies computed for singlet and triplet configurations ($\Delta E_{triplet–singlet}$ = –16.8 kcalmol^{-1}). The only significant deviation between experiment and theory was the Rh–N–C angle, which is measured to be 127(2)° and computed to be 148.4° (this deviation is consistent across computational methods examined) (see **Tables V-6–V-8**). We hypothesize that the observed deviation arises from crystal packing restrictions on *in crystallo* structural reorganization, which prevent full relaxation of **V-5b** to the minimum geometry in the solid state. Consistent with this

hypothesis, the energy cost of bending the nitrene linkage on the triplet surface is < 2 kcalmol^{-1} (see **Table V-9**).

Table V-6. Comparison of computed and experimental bond lengths for $Rh_2(esp)_2(C_{12}H_9N_3)_2$ (V-3b). Experimental distances are derived from the X-ray structure of compound **V-3b**. Computed distances are derived from optimization of $Rh_2(esp)_2(C_{12}H_9N_3)_2$ at the indicated level of theory.

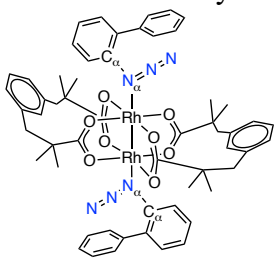

	Rh–Rh / Å	**Rh–N$_\alpha$ / Å**	**N$_\alpha$–C$_\alpha$ / Å**	**Rh–N$_\alpha$–C$_\alpha$ / °**
Experiment	2.3872(6)	2.280(4)	1.436(6)	125.1(3)
wB97XD SDD (Rh) 6-31G(d) (light atoms)	2.39990	2.31859	1.43398	122.46682
uM06 LANL2DZ	2.44739	2.26743	1.44387	122.50163
CAM-B3LYP LANL2DZ (Rh) 6-31G(d) (light atoms)	2.39907	2.34974	1.43582	129.30695
BP86 SDD (Rh) 6-31+G(d,p) (light atoms)	2.42601	2.34400	1.44318	130.35206
M06L SDD (Rh) 6-31+G(d,p) (light atoms)	2.41212	2.35438	1.43264	121.08717

Table V-7. Comparison of computed and experimental bond lengths for $Rh_2(esp)_2(C_{12}H_9N)(C_{12}H_9N_3)$ (V-5b). Experimental distances are derived from the X-ray structure of compound **V-5b**. Computed distances are derived from optimization of $Rh_2(esp)_2(C_{12}H_9N)(C_{12}H_9N_3)$ at the indicated level of theory.

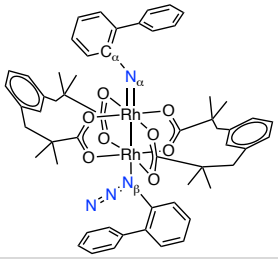

		Rh–Rh / Å	Rh–N_α / Å	N_α–C_α / Å	Rh–N_α / Å	Rh–N_α–C_α / °
Experiment		2.4061(8)	2.10(4)	1.36(4)	2.23(4)	127(2)
wB97XD SDD (Rh) 6-31G(d) (light atoms)	Singlet	2.44055	2.02612	1.32139	2.40763	125.48642
	Triplet	2.41362	2.11733	1.32153	2.33384	148.38231
uM06 LANL2DZ	Singlet	2.49234	2.01129	1.35229	2.37091	124.24656
	Triplet	2.45840	2.10849	1.35068	2.27359	143.98358
CAM-B3LYP LANL2DZ (Rh) 6-31G(d) (light atoms)	Singlet	2.43590	2.04567	1.30645	2.50678	128.29143
	Triplet	2.40843	2.17141	1.31521	2.37465	149.69664
BP86 SDD (Rh) 6-31+G(d,p) (light atoms)	Singlet	2.45406	1.97389	1.34309	2.53175	128.34550
	Triplet	2.43857	2.00280	1.33347	2.42436	147.86257
M06L SDD (Rh) 6-31+G(d,p) (light atoms)	Singlet	2.45580	1.98254	1.33851	2.49654	123.18068
	Triplet	2.42714	2.03868	1.32694	2.39295	145.57042

Table V-8. Analysis of the relative stabilities of ^{1}[V-5b] and ^{3}[V-5b]. In all the calculations, the triplet state was lower in energy.

wB97XD SDD (Rh) 6-31G(d) (light atoms)	**ΔE**	**ΔH**	**ΔG**
^{1}**[V-5b]**	–3209.018206 E_h	–3209.017262 E_h	–3209.181738 E_h
^{3}**[V-5b]**	–3209.043637 E_h	–3209.042693 E_h	–3209.208667 E_h
Δ(^{3}**[V-5b]**– ^{1}**[V-5b]**)	–15.958 kcal·mol^{-1}	–15.958 kcal·mol^{-1}	–16.898 kcal·mol^{-1}
uM06 LANL2DZ	**ΔE**	**ΔH**	**ΔG**
^{1}**[V-5b]**	–3205.313247 E_h	–3205.312303 E_h	–3205.473865 E_h
^{3}**[V-5b]**	–3205.330989 E_h	–3205.330044 E_h	–3205.493846 E_h
Δ(^{3}**[V-5b]**– ^{1}**[V-5b]**)	–11.1 kcal·mol^{-1}	–11.1 kcal·mol^{-1}	–12.5 kcal·mol^{-1}
CAM-B3LYP LANL2DZ (Rh) 6-31G(d) (light atoms)	**ΔE**	**ΔH**	**ΔG**
^{1}**[V-5b]**	–3206.050678 E_h	–3206.049734 E_h	–3206.217120 E_h
^{3}**[V-5b]**	–3206.074680 E_h	–3206.073736 E_h	–3206.242017 E_h
Δ(^{3}**[V-5b]**– ^{1}**[V-5b]**)	–15. 1 kcal·mol^{-1}	–15. 1 kcal·mol^{-1}	–15.6 kcal·mol^{-1}
BP86 SDD (Rh) 6-31+G(d,p) (light atoms)	**ΔE**	**ΔH**	**ΔG**
^{1}**[V-5b]**	–3210.293300 E_h	–3210.292356 E_h	–3210.468508 E_h
^{3}**[V-5b]**	–3210.294991 E_h	–3210.294047 E_h	–3210.470597 E_h
Δ(^{3}**[V-5b]**– ^{1}**[V-5b]**)	–1. 1 kcal·mol^{-1}	–1. 1 kcal·mol^{-1}	–1.3 kcal·mol^{-1}
M06L SDD (Rh) 6-31+G(d,p) (light atoms)	**ΔE**	**ΔH**	**ΔG**
^{1}**[V-5b]**	–3209.908668 E_h	–3209.907724 E_h	–3210.070670 E_h
^{3}**[V-5b]**	–3209.915109 E_h	–3209.914165 E_h	–3210.079483 E_h
Δ(^{3}**[V-5b]**– ^{1}**[V-5b]**)	–4.0 kcal·mol^{-1}	–4.0 kcal·mol^{-1}	–5.5 kcal·mol^{-1}

Table V-9. Analysis of the bending of Rh–N$_\alpha$–C bond angle of nitrene moiety in ^{3}[V-5b].

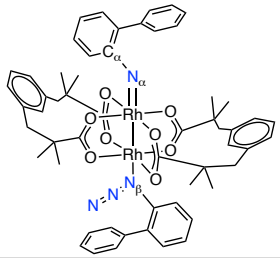

Rh–N$_\alpha$–C / °	Rh–N$_\alpha$ / Å	Rh–N$_\alpha$ / Å	Energy / E$_h$
120	2.22001	2.30647	–3210.15959
125	2.18283	2.31359	–3210.160711
130	2.15815	2.31906	–3210.161478
135	2.14195	2.32377	–3210.161877
140	2.13097	2.32871	–3210.162184
145	2.12105	2.33212	–3210.162386
150	2.11708	2.33370	–3210.162345
155	2.12441	2.33349	–3210.162260
160	2.11887	2.33856	–3210.162366
165	2.11631	2.34045	–3210.162501
170	2.11444	2.34014	–3210.162543
175	2.11535	2.34028	–3210.162406

The availability of experimental structures for both Rh_2 nitrene **V-5a**·N_2 and **V-5b**·N_2 reveals the impact of coordinated axial ligands on the structure of the reactive intermediate responsible for intramolecular C–H amination. In the absence of a trans axial ligand to the nitrene in **V-5a**, the Rh(1)–N(1) bond is 2.055(4) Å; in the presence of a trans axial azide ligand to the nitrene in **V-5b**, the Rh(1)–N(1) bond distance increases to 2.10(4) Å, which is consistent with a significant structural trans effect through the M–M bond (see **Table V-10**).[301-305] In addition to elongating the Rh–nitrene bond, the presence of an axial ligand significantly increases the spin density on the nitrene nitrogen atom: Natural bond order (NBO) analysis of ^{3}[**V-5a**] and ^{3}[**V-5b**] indicates that while there is significant *N*-centered spin density in **V-5a** (1.16 e$^-$), coordination of a distal azide ligand under

catalytically relevant conditions increases the *N*-centered spin density to 1.48 e$^-$ in **V-5b** (**Figure V-20**).

Table V-10. Analysis of the elongation of Rh–N$_\beta$ bond distance in ^{3}[V-5b].

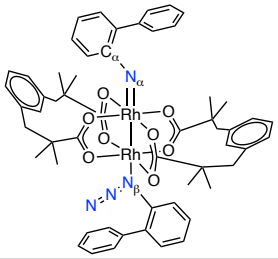

Entry	Rh–N$_\beta$ / Å	Rh–Rh / Å	Rh–N$_\beta$ / Å	Energy / E$_h$
V-5b (Expt)	2.23(4)	2.4061(8)	2.10(4)	–
V-5a (Expt)	–	2.3953(4)	2.055(4)	–
1	2.10	2.42562	2.15225	–3210.157104
2	2.20	2.41939	2.13634	–3210.160983
3	2.30	2.41462	2.12285	–3210.162318
4	2.40	2.41131	2.11141	–3210.162076
5	2.50	2.40898	2.10167	–3210.161014
6	2.60	2.40735	2.09210	–3210.159455
7	2.70	2.40628	2.08476	–3210.157736
8	2.80	2.40528	2.07893	–3210.156013
9	2.90	2.40675	2.07384	–3210.154411
10	3.00	2.41151	2.07528	–3210.154612
11	3.10	2.41221	2.07437	–3210.154763
12	3.20	2.41209	2.07384	–3210.155360
13	3.30	2.41292	2.07452	–3210.155993
14	3.40	2.41385	2.07513	–3210.156602

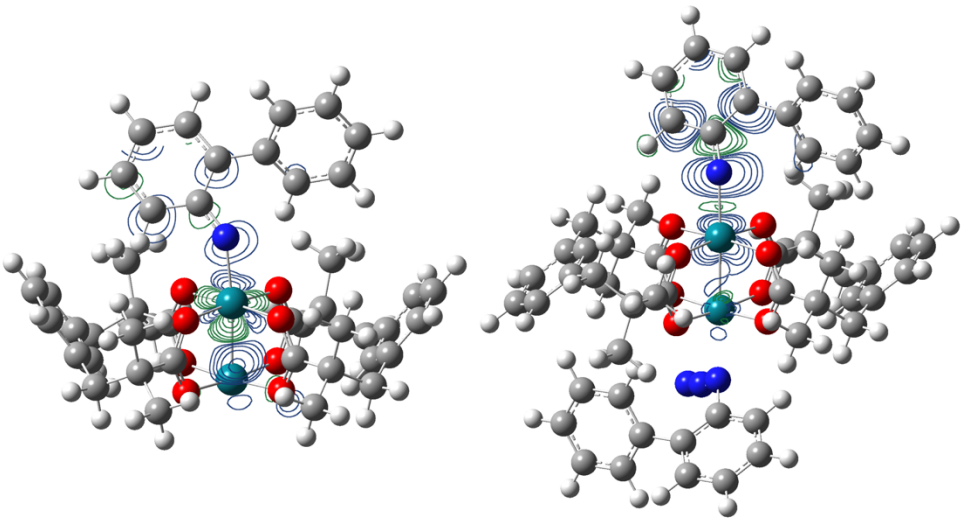

Figure V-20. Spin density plots for Rh_2 nitrenoid complexes V-5a and V-5b. Plots are drawn at the isolevel = 0.004, and show significant spin density on the nitrene *N*-atom in both ^{3}[**V-5a**] and ^{3}[**V-5b**]. Binding of an axial biphenyl azide ligand in **V-5b** significantly enhances *N*-centered spin density.

V.3. Conclusion

In this chapter, we have described the structural characterization of a pair of Rh_2 nitrenes that mediate intramolecular C–H amination chemistry. *In crystallo* confinement enables direct characterization of the species that are intimately involved in bond-breaking and -making in catalysis. In addition, we were able to experimentally evaluate the structural trans effect of coordination substrates, which are present during catalysis. Importantly, by having access to experimentally derived metrical parameters, we were able to evaluate the fidelity of various commonly-employed computational approaches to the description of Rh_2-catalyzed processes, which provides critical, but previously unavailable insight, into the fidelity of these models to experiment. In conclusion, we demonstrate *in situ* crystallography as a powerful tool for characterizing the actual reactive

intermediates relevant towards C–H activation catalysis, without the need for synthetic derivatization.

V.4. Experimental Details

V.4.1. General Considerations

Materials Unless otherwise noted, all chemicals and solvents (ACS reagent grade) were used as received. Isobutyronitrile, *n*-butyl lithium (^{n}BuLi) (2.5 M in hexanes), ethylene glycol, hexanes, dichloromethane (CH_2Cl_2), ethyl acetate (EtOAc), chloroform ($CHCl_3$), and molecular sieves (4 Å, MS) were obtained from Sigma Aldrich. Silica gel (0.06–0.20 mm, 60 Å for column chromatography), 2-aminobiphenyl, and carbazole were obtained from Acros Organics. Chlorobenzene (PhCl) and acetic acid (AcOH) were obtained from TCI America. Dirhodium tetraacetate ($Rh_2(OAc)_4$), xylylene dibromide, sodium nitrite ($NaNO_2$), and sodium azide (NaN_3) purchased from BTC. Potassium hydroxide (KOH), potassium carbonate (K_2CO_3), sodium chloride (NaCl), and sodium sulfate (Na_2SO_4) were obtained from EMD Millipore. Diisopropylamine ($^{i}Pr_2NH$) and tetrahydrofuran (THF) were obtained from Fisher Scientific. NMR solvents were purchased from Cambridge Isotope Laboratories and were used as received. Anhydrous THF was obtained from a drying column and stored over activated molecular sieves.[180] All reactions were carried out at 23 °C unless otherwise noted. α,α,α',α'-Tetramethyl-1,3-benzenedipropionic acid (H_2esp) and $Rh_2(esp)_2$ (**V-1**) were prepared according to literature methods.[241, 287]

Characterization Details NMR spectra were recorded on Bruker Avance NEO 400 NMR operating at 400.09 MHz for ^{1}H and 100.02 MHz for ^{13}C acquisitions and Inova 500 FT NMR operating at 499.53 MHz for ^{1}H acquisitions and 125.62 MHz for ^{13}C acquisitions. The NMR spectra were referenced against solvent signals: $CDCl_3$ (7.26 ppm, ^{1}H; 77.16 ppm, ^{13}C).[181] ^{1}H NMR data are reported as follows: chemical shift (δ, ppm), multiplicity (s (singlet), d (doublet), t (triplet), m (multiplet), br (broad)), integration. UV-vis spectra were recorded at 293 K in quartz cuvettes on an Ocean Optics Flame-S miniature spectrometer with DH-mini UV-vis NIR light source (200–900 nm) and were blanked against the appropriate solvent. IR spectra were recorded on a Shimadzu FTIR/IRAffinity-1 Spectrometer. Spectra were blanked against air and were determined as the average of 32 scans. *In situ* IR spectra were measured in a KBr pellet with a Bruker VERTEX 70. Spectra were blanked against air and were determined as the average of 64 scans. IR data are reported as follows: wavenumber (cm^{-1}), peak intensity (s, strong; m, medium; w, weak). MALDI data was obtained using a Bruker Microflex LRF MALDI-TOF using reflectron-TOF modes. The laser power of the MALDI was tuned using Bruker Daltonics flexControl software that was pre-installed with the instrument.

X-Ray Diffraction Details Experimental details of crystallization are included in the synthetic procedures for the respective compounds.

Routine Crystallography: A Bruker APEX 2 Duo X-ray (three-circle) diffractometer was used for crystal screening, unit cell determination, and data collection for the X-ray crystal structure of **V-4a**. A crystal suitable for X-ray diffraction was mounted on a MiTeGen dual-thickness micro-mount and placed under a cold N_2 stream

(Oxford). The X-ray radiation employed was generated from a Mo sealed X-ray tube (Kα = 0.70173 Å with a potential of 40 kV and a current of 40 mA). Bruker AXS APEX II software was used for data collection and reduction. Absorption corrections were applied using the program SADABS. A solution was obtained using XT/XS in APEX2 and refined in Olex2.[183-184, 221] Hydrogen atoms were placed in idealized positions and were set riding on the respective parent atoms. All non-hydrogen atoms were refined with anisotropic thermal parameters. The structure was refined (weighted least squares refinement on F^2) to convergence.

In Situ Crystallography: The X-ray crystal structures **V-3a**, **V-3b**, **V-5a**·N_2 and **V-5b**·N_2 were collected using synchrotron radiation (λ = 0.41328 Å) at ChemMatCARS located at the Advanced Photon Source (APS) housed at Argonne National Laboratory (ANL). Crystals suitable for X-ray diffraction were mounted on a glass fiber. The data was collected at 100 K (Cryojet N_2 cold stream) using a vertically mounted Bruker D8 three-circle platform goniometer equipped with a PILATUS3 X CdTe 1M detector. Data was collected as a series of φ and/or ω scans. Data were integrated using SAINT and scaled with a multi-scan absorption correction using SADABS. Structures were solved by intrinsic phasing using SHELXT (Apex2 program suite v2014.1) and refined against F^2 on all data by full matrix least squares with SHELXL97.[221] All non-hydrogen atoms were refined anisotropically. H-atoms were placed at idealized positions and refined using a riding model.

X-Ray Absorption Spectroscopy (XAS) Details Rh K-edge data for **V-1**, **V-3a** and **V-5a** were recorded at beamline 20-ID-C of Advanced Photon Source at Argonne

National Laboratory, using the Si(111) double crystal monochromator to scan the energy. The spectra were collected in transmission mode using synchrotron radiation (λ = 0.41328 Å) at 100 K and energy calibrations were done using Rh foil as reference. The reported spectra for **V-1**, **V-3a** and **V-5a** are an average of five repeated measurements. *In situ* generation of **V-5a** was achieved by irradiating **V-3a** with synchrotron radiation (λ = 0.41328 Å) at 100 K for 2 h prior to data collection.

The data were processed with the Athena and Artemis programs of the IFEFFIT package.[306] Reference foil data were aligned to the first zero-crossing of the second derivative of normalized μ(E) data, which was calibrated to the literature E_0 value for the Rh K-edge. Spectra were averaged in μ(E) prior to normalization. Background removal was achieved by spline fitting. EXAFS data were extracted above the threshold energy, E_0. FEFF6[307] was used to calculate theoretical phases and amplitudes from structure models consisting of crystal structures. All data were initially fitted with simultaneous k-weighting of 1, 2, and 3, then finalized with k^3-weighting in R-space. Fit windows in k-space were determined based on the lowest quality data collected. Rh data sets were from 3.0 to 10 $Å^{-1}$ (k-space) and 1.0 to 3.0 Å (R-space). Structural parameters that were determined by the fit include the bond distance (R), the mean square relative displacement of the scattering element (σ^2) and the energy shift of the photoelectron(ΔE_0).

Computational Details Calculations were performed using the Gaussian 09, Revision D.01 suite of software[225] that was executed using the Terra cluster available at Texas A&M High Performance Research Computing (TAMU-HPRC) facility. Geometry optimizations were carried out using a variety of basis sets and functionals that have

previously been employed in the analysis of Rh_2 nitrenoid chemistry,[30, 196, 242-243, 267, 299] in order to obtain a satisfactory reproduction of critical metrical parameters. Methods employed include the wB97XD,[293] uM06,[268] BP86,[269] M06L,[268, 308] and CAM-B3LYP[309] functionals implemented with SDD,[294-296] LANL2DZ,[229, 270] def2TZVP,[271, 310] and def2SVP[271] basis sets for Rh (with accompanying effective core potentials), and 6-31G(d)[297-298] and 6-31+G(d,p)[297-298] for light atoms. Stationary points were characterized with frequency calculations using the same basis set and functionals with SMD for solvents. The computed metrical parameters and energies of $Rh_2(esp)_2(C_{12}H_{10}N_3)$ (**V-3a**, **Table V-3**), $Rh_2(esp)_2(C_{12}H_{10}N)$ (**V-5a**, **Tables V-4–V-5**), $Rh_2(esp)_2(C_{12}H_{10}N_3)_2$ (**V-3b**, **Tables V-6**), and $Rh_2(esp)_2(C_{12}H_{10}N)(C_{12}H_{10}N_3)$ (**V-5b**, **Tables V-7–V-8**) are collected in the indicated Tables. NBO calculations were carried out with the NBO 6.0 suite.[275]

V.4.2. Synthesis and Characterization

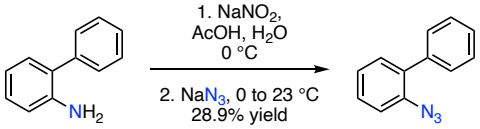

V-2

Synthesis of 2-Azidobiphenyl (V-2) 2-Azidobephenyl (**V-2**) was prepared according to the following modification of the literature method.[311] A 500-mL round-bottom flask was charged with 2-aminobiphenyl (2.99 g, 17.7 mmol, 1.00 equiv.), AcOH (60.0 mL), and H_2O (30.0 mL) and the reaction vessel was cooled to 0 °C. $NaNO_2$ (1.61 g, 23.3 mmol, 1.32 equiv.) was slowly added in portions and the reaction mixture was stirred at 0 °C for 1 h. NaN_3 (1.63 g, 25.1 mmol, 1.42 equiv.) was added slowly in portions at 0 °C. The

reaction mixture was then warmed to 23 °C and stirred for 1 h. The reaction mixture was diluted with H_2O (100.0 mL) and CH_2Cl_2 (100.0 mL) and neutralized with K_2CO_3. The phases were separated and the aqueous phase was extracted with CH_2Cl_2 (2 × 100 mL). The combined organic layers were washed with brine, dried over Na_2SO_4, and concentrated *in vacuo*. The residue was purified by SiO_2 chromatography with EtOAc/hexanes as a linear gradient eluent system (v/v: 0/100 to 30/70) to afford the title compound, which was obtained as a light-yellow oil that crystallized upon storage in the freezer (1.00 g, 28.9% yield).

^{1}H NMR (δ, 23 °C, $CDCl_3$): 7.46–7.35 (m, 7H), 7.29–7.20 (m, 2H). ^{13}C NMR (δ, 23 °C, $CDCl_3$): 138.3, 137.2, 133.9, 131.4, 129.6, 128.8, 128.2, 127.6, 125.0, 118.9. IR (KBr pellet, cm^{-1}):* 2125 (s), 2089 (s), 1579 (m), 1501 (m), 1479 (s), 1450 (w), 1431 (s), 1298 (s), 1285 (s), 1148 (m), 1102 (m), 1073 (m), 1048 (m), 1009 (m), 940 (w), 913 (w), 816 (w), 749 (s), 696 (s), 656 (m), 612 (m), 558 (m), 530 (m), 475 (m), 420(w). UV-vis (CH_2Cl_2), λ_{max} (nm, ε ($M^{-1}cm^{-1}$)): 260 (6.83×10^3). Spectral data are well-matched with those available in the literature.[311]

* An ATR-IR spectrum of **V-2** displayed the same peaks as that acquired in a KBr pellet.

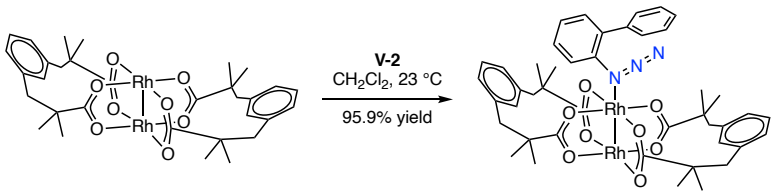

Synthesis of $Rh_2(esp)_2(C_{12}H_{10}N_3)$ (V-3a) A 20-mL scintillation vial was charged with $Rh_2(esp)_2$ (**V-1**, 50.7 mg, 0.0668 mmol, 1.00 equiv.), compound **V-2** (13.0 mg, 0.0666 mmol, 0.997 equiv.), and CH_2Cl_2 (2.0 mL) inside a N_2-filled glovebox and the reaction mixture was stirred for 30 min at 23 °C. Solvent was removed *in vacuo* to afford **V-3a** as green powder (61.1 mg, 95.9% yield). Single crystals of **V-3a** were obtained by slow evaporation of a CH_2Cl_2 solution at –35 °C.

^{1}H NMR (δ, 23 °C, $CDCl_3$): 7.54 (d, J = 6.8 Hz, 2H), 7.46–7.39 (m, 5H), 7.07 (t, J = 7.2 Hz, 2H), 6.93 (s, 2H), 6.84 (d, J = 7.6 Hz, 4H), 2.64 (s, 8H), 1.00 (s, 24). ^{13}C NMR ((δ, 23 °C, $CDCl_3$): 196.6, 138.1, 137.1, 134.5, 131.3, 129.5, 128.7, 128.5, 128.0, 127.8, 126.9, 126.1, 125.6, 120.5, 47.1, 46.5, 25.8. IR (KBr pellet, cm^{-1}): 2129 (s), 2101 (m), 1583 (s), 1474 (s), 1434 (w), 1409 (s), 1376 (m), 1358 (m), 1263 (m), 1243 (m), 1131 (w), 905 (w), 823 (w), 770 (m), 756 (m), 750 (m), 709 (m), 634 (m), 533 (w), 452 (m). UV-vis (CH_2Cl_2), λ_{max} (nm, ε ($M^{-1}cm^{-1}$)): 372 (716), 666 (163).

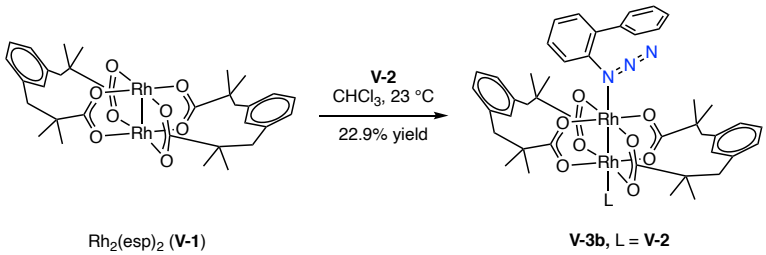

Synthesis of $Rh_2(esp)_2(C_{12}H_{10}N_3)_2$ (V-3b) A 20-mL scintillation vial was charged with $Rh_2(esp)_2$ (**V-1**, 52.5 mg, 0.0692 mmol, 1.00 equiv.), compound **V-2** (151 mg, 0.772 mmol, 11.2 equiv.), and $CHCl_3$ (2.0 mL) inside a N_2-filled glovebox and the reaction mixture was stirred for 30 min at 23 °C. Single crystals of **V-3b** were obtained by slow evaporation of the $CHCl_3$ solution at –35 °C (18.3 mg, 22.9% yield).

^{1}H NMR (δ, 23 °C, $CDCl_3$): 7.48 (d, J = 10 Hz, 4H), 7.43 (t, J = 7.5 Hz, 4H), 7.40–7.39 (m, 8H), 7.23 (t, J = 7.5 Hz, 2H), 7.07 (t , J = 7.0 Hz, 2H), 6.90 (s, 2H), 6.84 (d, J = 8.0 Hz, 4H), 2.63 (s, 8H), 0.99 (s, 24H). ^{13}C NMR ((δ, 23 °C, $CDCl_3$): 196.6, 138.2, 138.1, 137.2, 134.3, 131.4, 131.0, 129.5, 128.8, 128.3, 128.0, 127.7, 126.9, 126.0, 125.3, 120.5, 119.8, 111.1, 47.1, 46.5, 25.8. IR (KBr pellet, cm^{-1}): 2129 (s), 2101 (m), 1583 (s), 1474 (s), 1434 (w), 1409 (s), 1376 (m), 1358 (m), 1263 (m), 1243 (m), 1131 (w), 905 (w), 823 (w), 770 (m), 756 (m), 750 (m), 709 (m), 634 (m), 533 (w), 452 (m). The IR spectrum of **V-3b** is similar to that of **V-3a** (**Figure V-5**) with the exception that the N_3 stretching frequency (2129 and 2101 cm^{-1}) is more intense in **V-3b**.

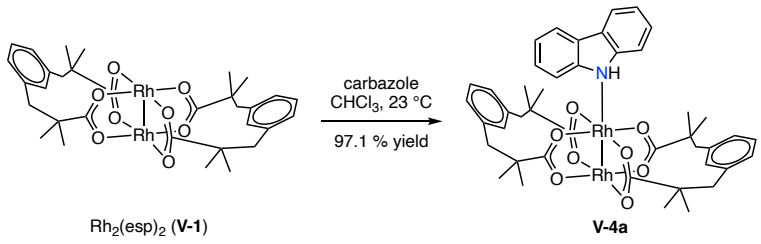

$Rh_2(esp)_2$ (**V-1**) **V-4a**

Synthesis of $Rh_2(esp)_2(C_{12}H_8NH)$ (V-4a) A 20-mL scintillation vial was charged with $Rh_2(esp)_2$ (**V-1**, 50.5 mg, 0.0666 mmol, 1.00 equiv.), carbazole (11.5 mg, 0.0688 mmol, 1.03 equiv.), and $CHCl_3$ (2.0 mL) inside a N_2-filled glovebox and the reaction mixture was stirred for 2 h at 23 °C. Solvent was removed *in vacuo* to afford **V-4a** as green powder (59.9 mg, 97.1% yield). Single crystals of **V-4a** were obtained by slow evaporation of a $CHCl_3$ solution at 23 °C.

^{1}H NMR (δ, 23 °C, $CDCl_3$): 8.30 (br, 1H), 8.08 (d, J = 7.6 Hz, 2H), 7.49–7.40 (m, 4H), 7.07 (t, J = 7.6 Hz, 2H), 6.83 (d, J = 7.6 Hz, 6H), 2.59 (s, 8H), 0.98 (s, 24H). ^{13}C NMR ((δ, 23 °C, $CDCl_3$): 196.6, 140.4, 138.1, 131.0, 128.1, 126.9, 126.1, 124.2, 120.5, 120.1, 111.4, 47.0, 46.5, 25.8. IR (KBr pellet, cm^{-1}): 1680 (m), 1573 (s), 1473 (s), 1410 (s), 1376 (s), 1240 (s), 1200 (m), 1132 (m), 929 (m), 903 (m), 880 (m), 852 (w), 842 (w), 824 (m), 776 (s), 748 (s), 726 (s), 710 (s), 657 (m), 634 (s), 597 (m), 572 (m), 533 (m), 508 (w), 452 (s). UV-vis (CH_2Cl_2), λ_{max} (nm, ε ($M^{-1}cm^{-1}$)): 427 (1.68×10^2), 667 (2.16×10^2).

V.4.3. Isolation of 4a from carbazole-forming reaction

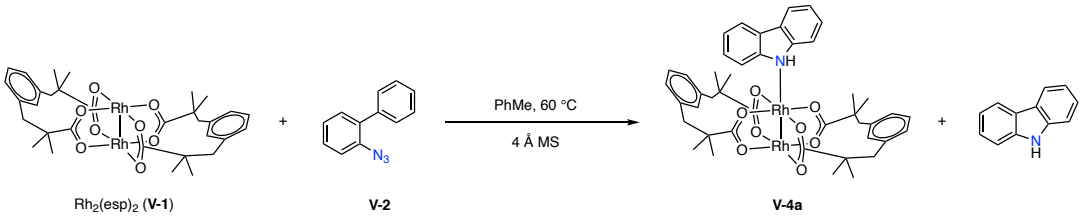

A 50-mL round-bottomed flask was charged with **V-1** (22.8 mg, 0.0300 mmol, 1.00 equiv.), compound **V-2** (105 mg, 0.540 mmol, 18.0 equiv.), 4 Å molecular sieves (MS, 300 mg), and PhMe (20.0 mL), and the reaction mixture was stirred for 16 h at 60 °C.[311] The reaction mixture was cooled to 23 °C, filtered through a frit and the filtrate was concentrated *in vacuo* to obtain a light-green solid. Slow evaporation of a $CHCl_3$ solution of this light-green solid afforded two different single crystals — a green colored crystal and a colorless crystal. Unit cell collection determined the green crystals as **V-4a** [a = 15.66 Å, b = 17.29 Å, c = 19.65 Å, a = 111.58 °, b = 94.52 °, g = 96.20 °, V = 4878 $Å^3$, Triclinic P] and the colorless crystals as carbazole [a = 5.66 Å, b = 7.63 Å, c = 19.00 Å, a = b = g = 90 °, V = 822 $Å^3$, Orthorhombic P]. Purification by SiO_2 chromatography with EtOAc/hexanes as a linear gradient eluent system (v/v: 0/100 to 40/60) afforded carbazole as a light brown powder (84.9 mg, 94.1% yield) and **V-1** as a green powder (20.1 mg, 88.3% yield).

Carbazole: ^{1}H NMR (δ, 23 °C, $CDCl_3$): 8.08 (d, 2H), 8.05 (br, 1H), 7.45–7.40 (m, 4H), 7.26–7.22 (m, 2H). ^{13}C NMR ((δ, 23 °C, $CDCl_3$): 139.6, 125.9, 123.5, 120.5, 119.6, 110.7. IR (KBr pellet, cm^{-1}): 1625 (m), 1602 (m), 1493 (m), 1450 (s), 1395 (w), 1384 (w), 1335 (m), 1327 (m), 1287 (w), 1239 (m), 1204 (m), 1139 (m), 1108 (w), 1010 (m), 927 (m),

857 (m), 842 (m), 758 (s), 748 (s), 725 (s), 573 (s), 508 (w), 439 (s). UV-vis (CH_2Cl_2), λ_{max} (nm, ε ($M^{-1}cm^{-1}$)): 258 (7.01×10^3), 294 (7.91×10^3), 322 (1.71×10^3), 335 (1.43×10^3). Spectral data are well-matched with those available in the literature.[311]

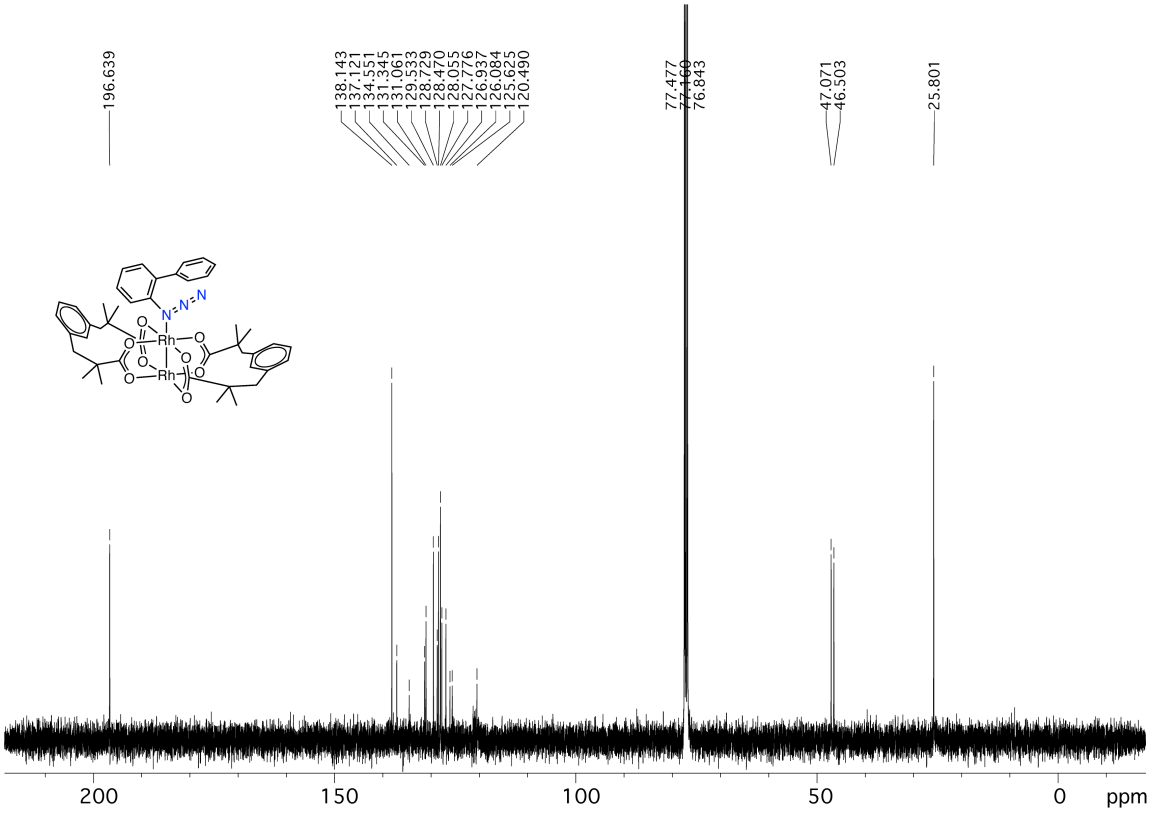

Figure V-21. ^{13}C NMR spectrum of V-3a recorded in $CDCl_3$ at 23 °C.

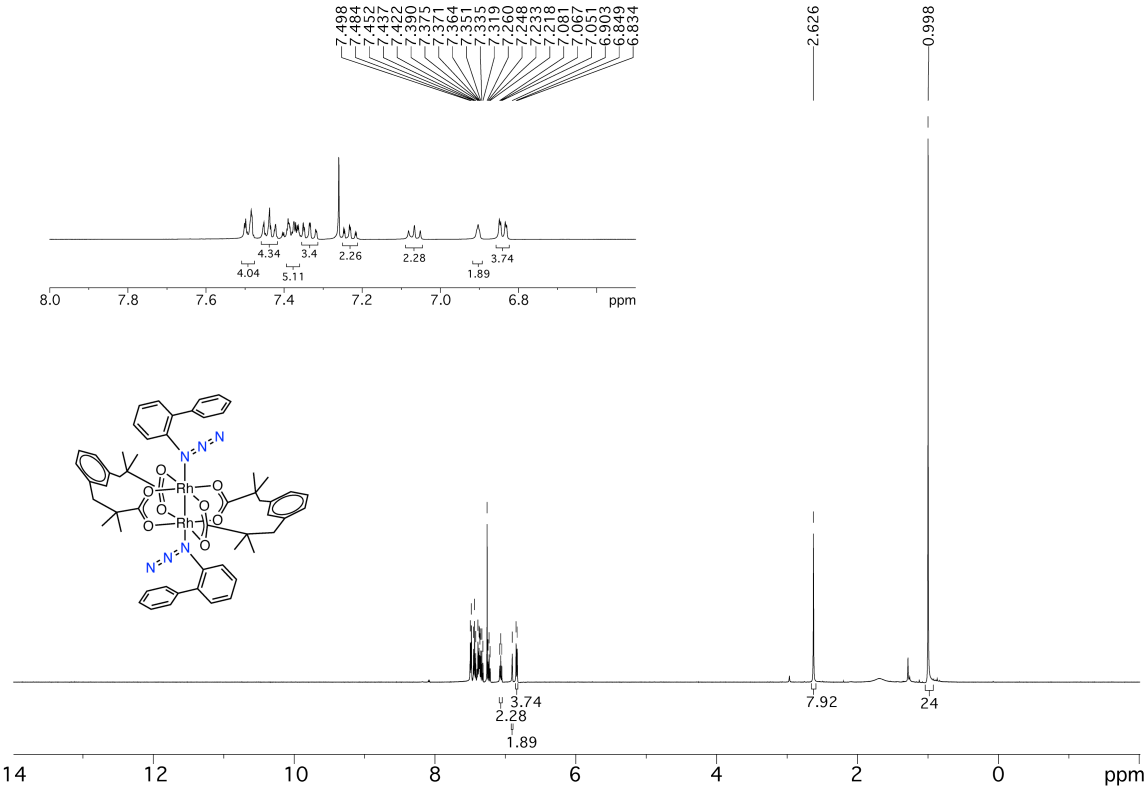

Figure V-22. ^{1}H NMR spectrum of V-3b recorded in $CDCl_3$ at 23 °C. Inset: Expansion of the aromatic region highlighting the splitting pattern and integration.

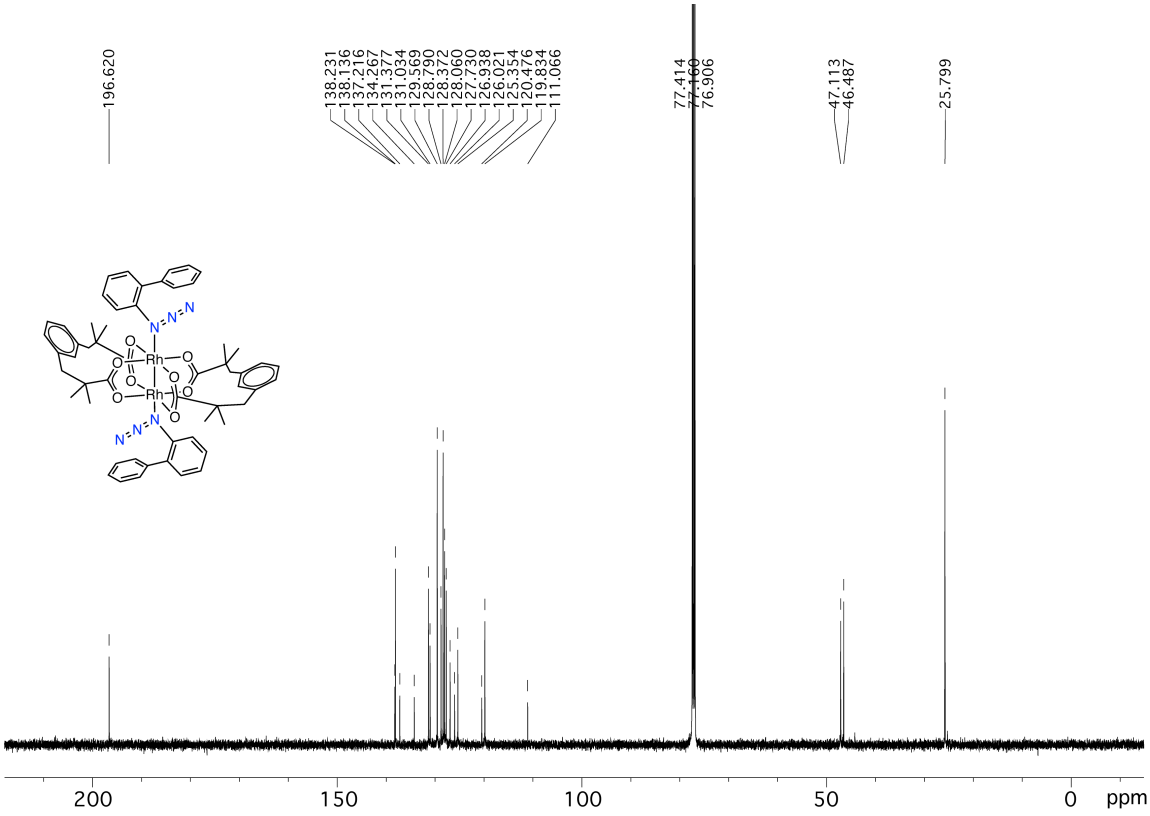

Figure V-23. ^{13}C NMR spectrum of V-3b recorded in $CDCl_3$ at 23 °C.

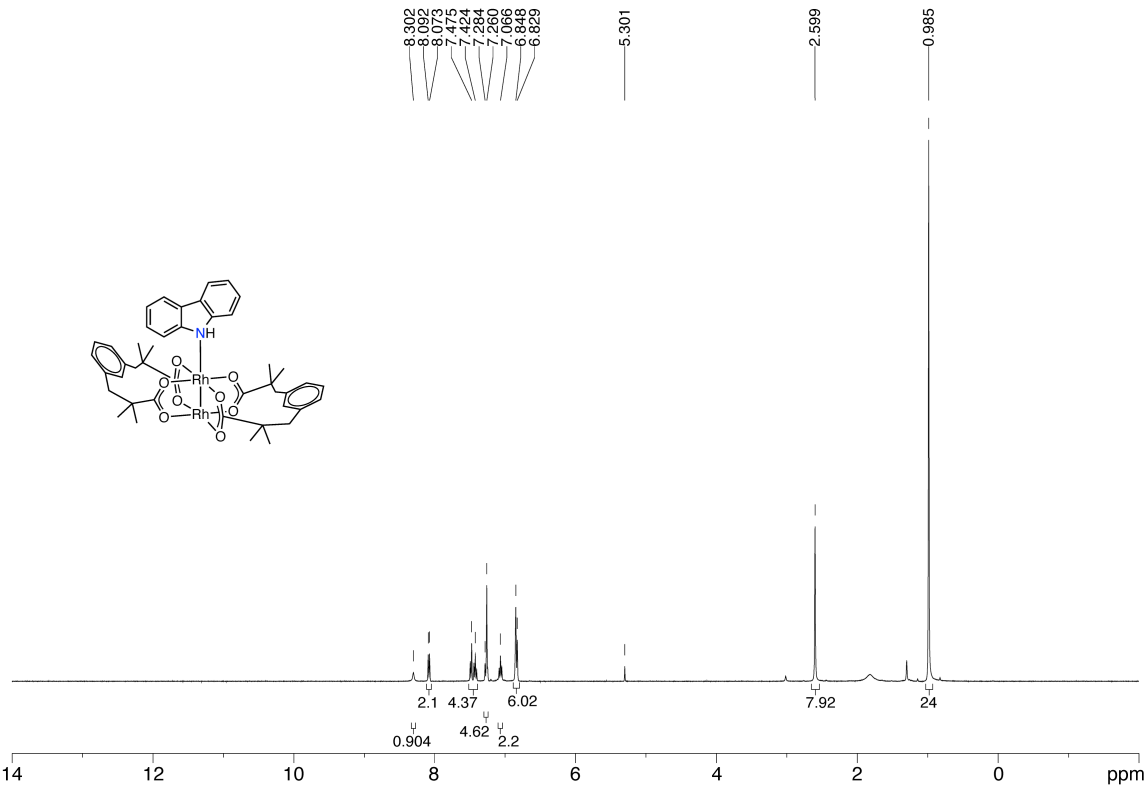

Figure V-24. ^{1}H NMR spectrum of V-4a recorded in $CDCl_3$ at 23 °C.

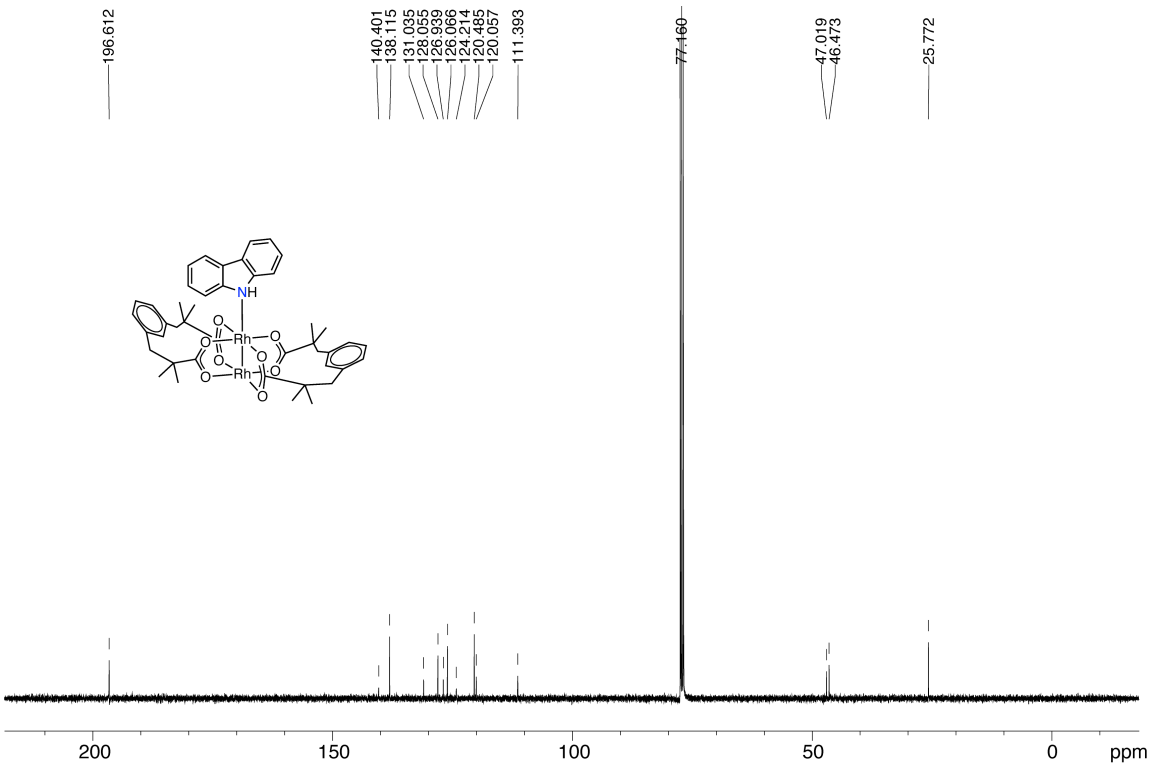

Figure V-25. ^{13}C NMR spectrum of V-4a recorded in $CDCl_3$ at 23 °C.

CHAPTER VI

CONCLUSIONS AND FUTURE DIRECTION*

In the preceding chapters, we have described various strategies that have emerged for the study of reactive M–L multiply bonded species. We have demonstrated photocrystallographic experiments to provide new tools in the study of the chemical structures of transient reactive species, including the ones relevant during selective C–H activation catalysis. We view this line of research as an opportunity to advance the structural characterization of reactive species without necessitating synthetic derivatization and the attendant attenuation of reactivity. This technique would extend the available structural data to significantly more reactive species than are currently available, and in the process would resolve questions of the relevant electronic structures and the relationship between structure and activity in these complexes. In order to realize this potential, development of robust photoprecursors, demonstration of solid-state generation of a greater variety of intermediates, and extension to time-resolved methods to capture structural data of increasingly reactive species are viewed as significant outstanding challenges.

VI.1. Development of Robust Photoprecursors

The differences between the solid-state photochemistry of Rh_2 chloroamide complex **III-3** in Chapter III and the adamantyl azide complex **IV-2b** in Chapter IV highlights the impact of appropriately designed photo-leaving groups for photocrystallographic studies: In the former, chlorine radicals caused rapid sample decomposition which precluded high-resolution structure determination while the latter participates in complete N_2 extrusion to generate nitrene **IV-3b**. Based on available data, the elimination of closed-shell small molecules, such as N_2, appear to most often be well

* Data, figures, and text in this chapter were adapted with permission from "Crystallography of Reactive Intermediates" by Das, A.; Van Trieste III, G. P.; Powers, D. C. *Comment. Inorg. Chem.* **2020**, *40*, 116–158. Copyright 2020 Taylor & Francis.

tolerated. The extent to which the crystal packing must be optimized to accommodate the evolution of small molecules is also yet to be fully established.

Related to the development of photoprecursors is the need to more fully understand the various activation modes available for *in situ* crystallographic experiments. For example, each of the examples presented thus far can be stimulated by photolysis of single crystals with an appropriate wavelength of light. During examination of the photochemistry of Rh_2 adamantyl azide complex **IV-3b** we also observed that N_2 loss could be stimulated without visible irradiation but solely by bombardment with high energy X-ray flux.[287] A similar set of observation was made during studies of Co(II) azide **VI-1**.[292] In this system, no chemical conversion was observed during photolysis, but N_2 was cleanly extruded to afford Co(III) iminyl radical **VI-2** (Co–N bond contracts from 2.045(3) Å (in VI-1) to 1.856(9) Å (in VI-2)) (**Figure VI-1**). These observations mirror the common observation in protein crystallography that weak bonds (e.g. disulfide linkages) are cleaved under extended X-ray bombardment,[312] the observation by Ohashi and co-workers who demonstrated X-ray induced Co–C bond cleavage in a cobaloxime derivative, and the more general observation that third generation synchrotron sources promote chemical transformation in small-molecule crystallography.[279]

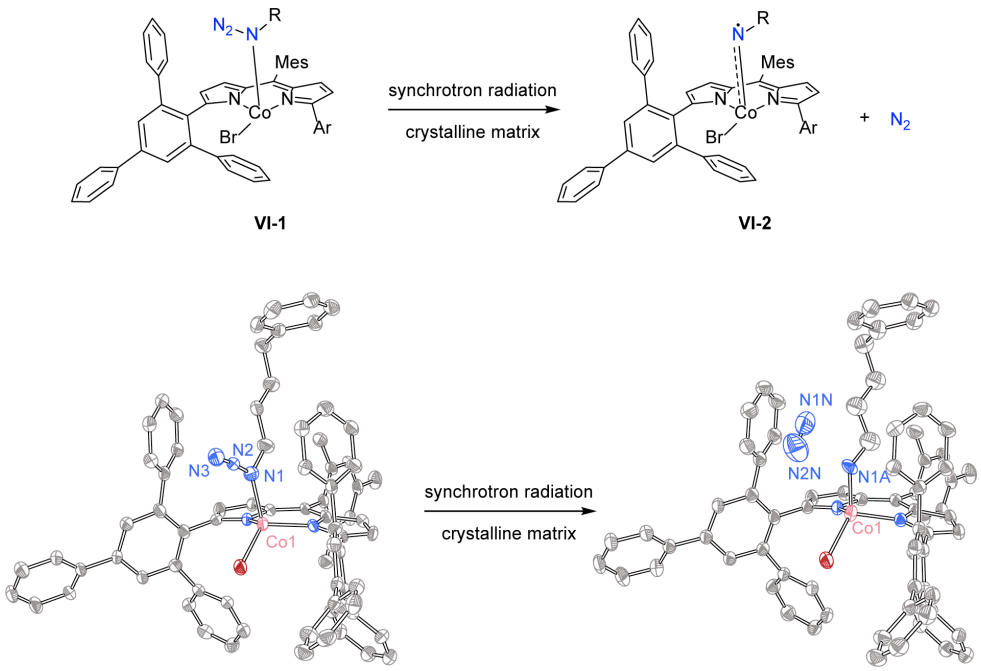

Figure VI-1. Conversion of Co(II) azide complex VI-1 to Co(III) iminyl radical complex VI-2 by high-flux X-ray bombardment.

VI.2. Extension to Characterization of Other Reactive Species

The impact of photocrystallography in the study of reactive species depends on the structural diversity that can be evaluated with the method. Beyond exploring the generality of *in crystallo* nitride and nitrene photochemistry, extension to the characterization of metal oxo fragments would critically expand the scope of crystalline matrix isolation chemistry. While the oxyanion chemistry advanced by Newcomb appear to be viable initial platforms, identification of appropriate ligand classes for efficient solid-state chemistry will be critical. For example, O_2 extrusion by photolysis of metal ozone adducts, or N_2 extrusion via photolysis of metal N_2O adduct could act as potential photoprecursors for metal oxos.[313-320] Similarly, we anticipate that appropriate design of photoprecursor molecules may enable characterization of hitherto unobserved reactive species, such as reactive carbyne (CR^{3-}),[321-325] phosphinidene (PR^{2-})[326-331] or phosphide (P^{3-}) complexes. For example, CO extrusion by photolysis of a phosphaketene **VI-3** (**Figure VI-2a**),[332] anthracene extrusion from adducts such as **VI-5** (**Figure VI-2b**),[333] or N_2 extrusion from

metal diazo complexes such as **VI-6** (**Figure VI-2c**)[334] would appear to be potential launching points for these efforts.

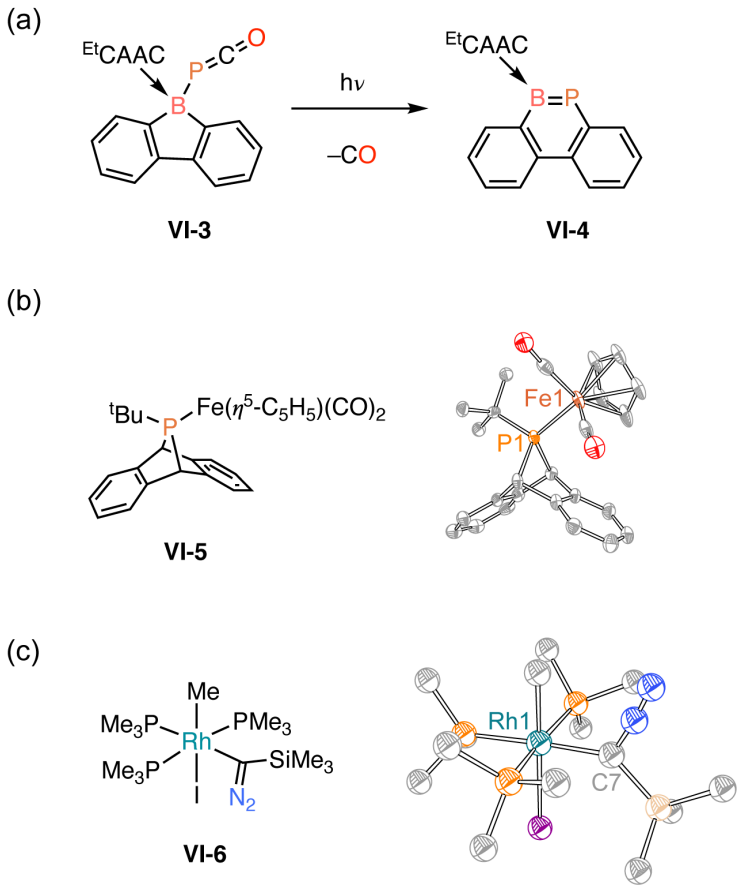

Figure VI-2. Photoprecursor candidates for generating reactive phosphinidene and carbyne species. (a) Photolysis of phosphaketene **VI-3** results in the formation of **VI-4** along with the extrusion of CO via the presumable intermediacy of a transient phosphinidene. (b) A potential iron phosphinidene photoprecursor (**VI-5**). (c) A potential rhodium carbyne photoprecursor (**VI-6**).

VI.3. Extension to Time-Resolved Crystallography

Each of the examples described above resulted from steady-state photochemical experiments in which a photoreaction was driven to completion (or near completion) and the product structure was evaluated by refinement of the resulting diffraction data. The

applicability of steady-state photocrystallographic experiments is inherently limited by the lifetime of the fragments of interest under the experimental conditions. In order to extend the characterization of reactive intermediates beyond those that can be stabilized on the timescale of minutes to hours (typical of data acquisition in steady-state experiments), translation of steady-state photocrystallographic experiments to time-resolved strategies will be critical. Photocrystallographic experiments have also been carried out in time-resolved contexts. For example, Coppens reported the characterization of the excited-state of $Pt_2(pop)_4$ (**VI-7** to **VI-7***) complex by combining laser flash photolysis with time-resolved acquisition of X-ray data (pop = $P_2O_7H_2$).[335-337] Photocrystallographic data revealed the decrease in Pt–Pt bond distance from 2.9126(2) Å to 2.63(9) Å, which matched with the data available in the literature (**Figure VI-3**).[147]

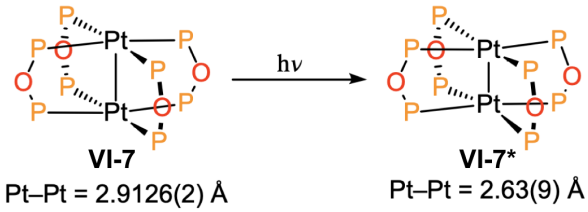

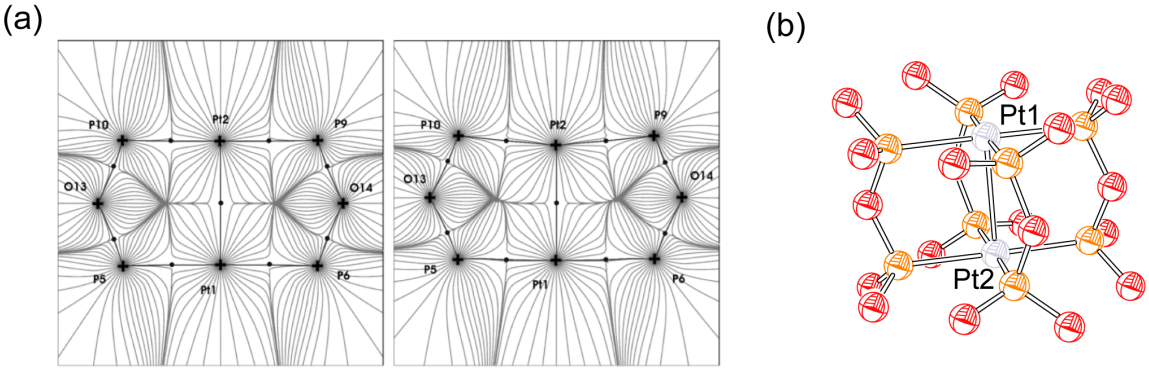

Figure VI-3. Photo-excitation of a Pt(III,III) dimer to a triplet excited state displays a Pt–Pt bond contraction. (a) Theoretically generated charge density maps of **VI-7** (left) and **VI-7*** (right) are in accordance with the experimentally observed bond contraction after photo-excitation. (b) Thermal ellipsoid plot of complex **VI-7** drawn at 50% confidence. Figure VI-3a reprinted with permission from reference 147. Copyright 2003 American Chemical Society.

A serious barrier to employing time-resolved photocrystallography to characterize reactive species is that in contrast to the pumping of an excited state, the photoreactions that generate these species are irreversible and thus sample degradation is likely to be a substantial challenge. However, if technical issues can be addressed and the photosynthetic chemistry generalized, crystalline matrix isolation promises to provide structural insights into the species that are at the heart of important catalytic reactions.

REFERENCES

1. Duan, L.; Bozoglian, F.; Mandal, S.; Stewart, B.; Privalov, T.; Llobet, A.; Sun, L., A Molecular Ruthenium Catalyst with Water-Oxidation Activity Comparable to that of Photosystem II. *Nat. Chem.* **2012**, *4*, 418–423.
2. Mano, N.; de Poulpiquet, A., O_2 Reduction in Enzymatic Biofuel Cells. *Chem. Rev.* **2018**, *118*, 2392–2468.
3. Hoffman, B. M.; Lukoyanov, D.; Yang, Z.-Y.; Dean, D. R.; Seefeldt, L. C., Mechanism of Nitrogen Fixation by Nitrogenase: The Next Stage. *Chem. Rev.* **2014**, *114*, 4041–4062.
4. Zhong, C.; Hu, W. B.; Cheng, Y. F., Recent Advances in Electrocatalysts for Electro-oxidation of Ammonia. *J. Mater. Chem. A* **2013**, *1*, 3216–3238.
5. Rittle, J.; Green, M. T., Cytochrome P450 Compound I: Capture, Characterization, and C–H Bond Activation Kinetics. *Science* **2010**, *330*, 933–937.
6. Nam, W., High-Valent Iron(IV)–Oxo Complexes of Heme and Non-Heme Ligands in Oxygenation Reactions. *Acc. Chem. Res.* **2007**, *40*, 522–531.
7. Bell, S. R.; Groves, J. T., A Highly Reactive P450 Model Compound I. *J. Am. Chem. Soc.* **2009**, *131*, 9640–9641.
8. Meunier, B.; de Visser, S. P.; Shaik, S., Mechanism of Oxidation Reactions Catalyzed by Cytochrome P450 Enzymes. *Chem. Rev.* **2004**, *104*, 3947–3980.
9. Meinhold, P.; Peters, M. W.; Chen, M. M. Y.; Takahashi, K.; Arnold, F. H., Direct Conversion of Ethane to Ethanol by Engineered Cytochrome P450 BM3. *Chem. Bio. Chem.* **2005**, *6*, 1765–1768.

10. Castillo, R. G.; Banerjee, R.; Allpress, C. J.; Rohde, G. T.; Bill, E.; Que, L.; Lipscomb, J. D.; DeBeer, S., High-Energy-Resolution Fluorescence-Detected X-ray Absorption of the Q Intermediate of Soluble Methane Monooxygenase. *J. Am. Chem. Soc.* **2017**, *139*, 18024–18033.
11. Qian, J.; An, Q.; Fortunelli, A.; Nielsen, R. J.; Goddard, W. A., Reaction Mechanism and Kinetics for Ammonia Synthesis on the Fe(111) Surface. *J. Am. Chem. Soc*. **2018**, *140*, 6288–6297.
12. van der Ham, C. J. M.; Koper, M. T. M.; Hetterscheid, D. G. H., Challenges in Reduction of Dinitrogen by Proton and Electron Transfer. *Chem. Soc. Rev.* **2014**, *43*, 5183–5191.
13. Surendranath, Y.; Nocera, D. G., Oxygen Evolution Reaction Chemistry of Oxide-Based Electrodes. *In Prog. Inorg. Chem.*, Karlin, K. G., Ed. John Wiley & Sons, Inc.,: Hoboken, NJ, **2011**; *57*, 505–560.
14. Gunay, A.; Theopold, K. H., C−H Bond Activations by Metal Oxo Compounds. *Chem. Rev.* **2010**, *110*, 1060–1081.
15. Davies, H. M. L.; Beckwith, R. E. J., Catalytic Enantioselective C−H Activation by Means of Metal−Carbenoid-Induced C−H Insertion. *Chem. Rev.* **2003**, *103*, 2861–2904.
16. Davies, H. M. L.; Liao, K., Dirhodium Tetracarboxylates as Catalysts for Selective Intermolecular C–H Functionalization. *Nat. Rev. Chem.* **2019**, *3*, 347–360.
17. Davies, H. M. L.; Manning, J. R., Catalytic C–H Functionalization by Metal Carbenoid and Nitrenoid Insertion. *Nature* **2008**, *451*, 417–424.

18. Liao, K.; Yang, Y.-F.; Li, Y.; Sanders, J. N.; Houk, K. N.; Musaev, D. G.; Davies, H. M. L., Design of Catalysts for Site-Selective and Enantioselective Functionalization of Non-Activated Primary C–H Bonds. *Nat. Chem.* **2018**, *10*, 1048–1055.

19. Caballero, A.; Despagnet-Ayoub, E.; Mar Díaz-Requejo, M.; Díaz-Rodríguez, A.; González-Núñez, M. E.; Mello, R.; Muñoz, B. K.; Ojo, W.-S.; Asensio, G.; Etienne, M.; Pérez, P. J., Silver-Catalyzed C–C Bond Formation Between Methane and Ethyl Diazoacetate in Supercritical CO_2. *Science* **2011**, *332*, 835–838.

20. Wang, Z.; Herraiz, A. G.; del Hoyo, A. M.; Suero, M. G., Generating Carbyne Equivalents with Photoredox Catalysis. *Nature* **2018**, *554*, 86–91.

21. Wang, Z.; Jiang, L.; Sarró, P.; Suero, M. G., Catalytic Cleavage of $C(sp^2)$–$C(sp^2)$ Bonds with Rh-Carbynoids. *J. Am. Chem. Soc.* **2019**, *141*, 15509–15514.

22. Zhang, R. K.; Chen, K.; Huang, X.; Wohlschlager, L.; Renata, H.; Arnold, F. H., Enzymatic Assembly of Carbon–Carbon Bonds via Iron-Catalysed sp^3 C–H Functionalization. *Nature* **2019**, *565*, 67–72.

23. Chen, K.; Huang, X.; Kan, S. B. J.; Zhang, R. K.; Arnold, F. H., Enzymatic Construction of Highly Strained Carbocycles. *Science* **2018**, *360*, 71–75.

24. Zhu, D.; Chen, L.; Fan, H.; Yao, Q.; Zhu, S., Recent Progress on Donor and Donor–Donor Carbenes. *Chem. Soc. Rev.* **2020**, *49*, 908–950.

25. Ballhausen, C. J.; Gray, H. B., The Electronic Structure of the Vanadyl Ion. *Inorg. Chem.* **1962**, *1*, 111–122.

26. Mayer, J. M., Metal–Oxygen Multiple Bond Lengths: A Statistical Study. *Inorg. Chem.* **1988**, *27*, 3899–3903.

27. Betley, T. A.; Wu, Q.; Van Voorhis, T.; Nocera, D. G., Electronic Design Criteria for O−O Bond Formation via Metal−Oxo Complexes. *Inorg. Chem.* **2008**, *47*, 1849–1861.

28. Winkler, J. R.; Gray, H. B., Electronic Structure of Metal–Oxo Ions. *In Struct. Bond.*, Mingos, D. M. P.; Day, P.; Dahl, J. P., Eds. Springer Berlin Heidelberg: Berlin, Heidelberg, **2012**; *142*, 17–28.

29. Darcy, J. W.; Koronkiewicz, B.; Parada, G. A.; Mayer, J. M., A Continuum of Proton-Coupled Electron Transfer Reactivity. *Acc. Chem. Res.* **2018**, *51*, 2391–2399.

30. Varela-Álvarez, A.; Yang, T.; Jennings, H.; Kornecki, K. P.; Macmillan, S. N.; Lancaster, K. M.; Mack, J. B. C.; Du Bois, J.; Berry, J. F.; Musaev, D. G., Rh_2(II,III) Catalysts with Chelating Carboxylate and Carboxamidate Supports: Electronic Structure and Nitrene Transfer Reactivity. *J. Am. Chem. Soc.* **2016**, *138*, 2327–2341.

31. Wentrup, C., Carbenes and Nitrenes: Recent Developments in Fundamental Chemistry. *Angew. Chem. Int. Ed.* **2018**, *57*, 11508–11521.

32. Platz, M.; Gritsan, N. P., Organic Azides: Syntheses and Applications. John Wiley & Sons: West Sussex, United Kingdom, **2010**.

33. Dielmann, F.; Back, O.; Henry-Ellinger, M.; Jerabek, P.; Frenking, G.; Bertrand, G., A Crystalline Singlet Phosphinonitrene: A Nitrogen Atom–Transfer Agent. *Science* **2012**, *337*, 1526–1528.

34. Hinsberg, W. D.; Dervan, P. B., Synthesis and Direct Spectroscopic Observation of a 1,1-Dialkyldiazene. Infrared and Electronic Spectrum of *N*-(2,2,6,6-tetramethylpiperidyl)nitrene. *J. Am. Chem. Soc.* **1978**, *100*, 1608–1610.

35. Hinsberg, W. D.; Schultz, P. G.; Dervan, P. B., Direct Studies of 1,1-Diazenes. Syntheses, Infrared and Electronic Spectra, and Kinetics of the Thermal Decomposition of *N*-(2,2,6,6-tetramethylpiperidyl)nitrene and *N*-(2,2,5,5-tetramethylpyrrolidyl)nitrene. *J. Am. Chem. Soc.* **1982**, *104*, 766–773.
36. Schultz, P. G.; Dervan, P. B., Synthesis and Direct Spectroscopic Observation of *N*-(2,2,5,5-tetramethylpyrrolidinyl)nitrene. Comparison of Five- and Six-Membered Cyclic 1,1-Dialkyldiazenes. *J. Am. Chem. Soc.* **1980**, *102*, 878–880.
37. Meyer, D.; Roth, K. C., Discovery of Interstellar NH. *Astrophys. J.* **1991**, *376*, L49–L52.
38. Klima, R. F.; Gudmundsdóttir, A. D., Intermolecular Triplet-Sensitized Photolysis of Alkyl Azides: Trapping of Triplet Alkyl Nitrenes. *J. Photoch. Photobio. A* **2004**, *162*, 239–247.
39. Grote, D.; Sander, W., Photochemistry of Fluorinated 4-Iodophenylnitrenes: Matrix Isolation and Spectroscopic Characterization of Phenylnitrene-4-yls. *J. Org. Chem.* **2009**, *74*, 7370–7382.
40. Nunes, C. M.; Knezz, S. N.; Reva, I.; Fausto, R.; McMahon, R. J., Evidence of a Nitrene Tunneling Reaction: Spontaneous Rearrangement of 2-Formyl Phenylnitrene to an Imino Ketene in Low-Temperature Matrixes. *J. Am. Chem. Soc.* **2016**, *138*, 15287–15290.
41. Abramovitch, R. A.; Challand, S. R.; Yamada, Y., Addition of Aryl Nitrenes to Olefins. *J. Org. Chem.* **1975**, *40*, 1541–1547.

42. Zalatan, D. N.; Bois, J. D., Metal-Catalyzed Oxidations of C–H to C–N Bonds. *In C-H Activation*, Yu, J.-Q.; Shi, Z., Eds. Springer Berlin Heidelberg: Berlin, Heidelberg, **2010**; 347–378.

43. Breslow, R.; Gellman, S. H., Tosylamidation of Cyclohexane by a Cytochrome P-450 Model. *J. Chem. Soc., Chem. Commun.* **1982**, 1400–1401.

44. Breslow, R.; Gellman, S. H., Intramolecular Nitrene Carbon-Hydrogen Insertions Mediated by Transition-Metal Complexes as Nitrogen Analogs of Cytochrome P-450 Reactions. *J. Am. Chem. Soc.* **1983**, *105*, 6728–6729.

45. Pearce, A. J.; See, X. Y.; Tonks, I. A., Oxidative Nitrene Transfer from Azides to Alkynes via Ti(II)/Ti(IV) redox catalysis: Formal [2+2+1] Synthesis of Pyrroles. *Chem. Commun.* **2018**, *54*, 6891–6894.

46. Gilbert, Z. W.; Hue, R. J.; Tonks, I. A., Catalytic Formal [2+2+1] Synthesis of Pyrroles from Alkynes and Diazenes via Ti^{II}/Ti^{IV} Redox Catalysis. *Nat. Chem.* **2016**, *8*, 63–68.

47. Kawakita, K.; Beaumier, E. P.; Kakiuchi, Y.; Tsurugi, H.; Tonks, I. A.; Mashima, K., Bis(imido)vanadium(V)-Catalyzed [2+2+1] Coupling of Alkynes and Azobenzenes Giving Multisubstituted Pyrroles. *J. Am. Chem. Soc.* **2019**, *141*, 4194–4198.

48. Clark, J. R.; Feng, K.; Sookezian, A.; White, M. C., Manganese-Catalysed Benzylic $C(sp^3)$–H Amination for Late-Stage Functionalization. *Nat. Chem.* **2018**, *10*, 583–591.

49. Svastits, E. W.; Dawson, J. H.; Breslow, R.; Gellman, S. H., Functionalized Nitrogen Atom Transfer Catalyzed by Cytochrome P-450. *J. Am. Chem. Soc.* **1985**, *107*, 6427–6428.

50. Wang, Z.; Zhang, Y.; Fu, H.; Jiang, Y.; Zhao, Y., Efficient Intermolecular Iron-Catalyzed Amidation of C−H Bonds in the Presence of *N*-Bromosuccinimide. *Org. Lett.* **2008**, *10*, 1863–1866.

51. Goswami, M.; Lyaskovskyy, V.; Domingos, S. R.; Buma, W. J.; Woutersen, S.; Troeppner, O.; Ivanović-Burmazović, I.; Lu, H.; Cui, X.; Zhang, X. P.; Reijerse, E. J.; DeBeer, S.; van Schooneveld, M. M.; Pfaff, F. F.; Ray, K.; de Bruin, B., Characterization of Porphyrin-Co(III)-'Nitrene Radical' Species Relevant in Catalytic Nitrene Transfer Reactions. *J. Am. Chem. Soc.* **2015**, *137*, 5468–5479.

52. Jin, L.-M.; Lu, H.; Cui, Y.; Lizardi, C. L.; Arzua, T. N.; Wojtas, L.; Cui, X.; Zhang, X. P., Selective Radical Amination of Aldehydic C(sp^2)–H Bonds with Fluoroaryl Azides via Co(II)-based Metalloradical Catalysis: Synthesis of *N*-fluoroaryl Amides from Aldehydes under Neutral and Nonoxidative Conditions. *Chem. Sci.* **2014**, *5*, 2422–2427.

53. Powers, I. G.; Andjaba, J. M.; Luo, X.; Mei, J.; Uyeda, C., Catalytic Azoarene Synthesis from Aryl Azides Enabled by a Dinuclear Ni Complex. *J. Am. Chem. Soc.* **2018**, *140*, 4110–4118.

54. Evans, D. A.; Faul, M. M.; Bilodeau, M. T.; Anderson, B. A.; Barnes, D. M., Bis(oxazoline)-copper Complexes as Chiral Catalysts for the Enantioselective Aziridination of Olefins. *J. Am. Chem. Soc.* **1993**, *115*, 5328–5329.

55. Hamilton, C. W.; Laitar, D. S.; Sadighi, J. P., Oxidation-Resistant, Sterically Demanding Phenanthrolines as Supporting Ligands for Copper(I) Nitrene Transfer Catalysts. *Chem. Commun.* **2004**, 1628–1629.

56. Bhuyan, R.; Nicholas, K. M., Efficient Copper-Catalyzed Benzylic Amidation with Anhydrous Chloramine-T. *Org. Lett.* **2007**, *9*, 3957–3959.

57. Harvey, M. E.; Musaev, D. G.; Du Bois, J., A Diruthenium Catalyst for Selective, Intramolecular Allylic C–H Amination: Reaction Development and Mechanistic Insight Gained through Experiment and Theory. *J. Am. Chem. Soc.* **2011**, *133*, 17207–17216.

58. Espino, C. G.; Wehn, P. M.; Chow, J.; Du Bois, J., Synthesis of 1,3-Difunctionalized Amine Derivatives through Selective C−H Bond Oxidation. *J. Am. Chem. Soc.* **2001**, *123*, 6935–6936.

59. Fiori, K. W.; Du Bois, J., Catalytic Intermolecular Amination of C−H Bonds: Method Development and Mechanistic Insights. *J. Am. Chem. Soc.* **2007**, *129*, 562–568.

60. Stokes, B. J.; Dong, H.; Leslie, B. E.; Pumphrey, A. L.; Driver, T. G., Intramolecular C−H Amination Reactions: Exploitation of the Rh_2(II)-Catalyzed Decomposition of Azidoacrylates. *J. Am. Chem. Soc.* **2007**, *129*, 7500–7501.

61. Cui, Y.; He, C., A Silver-Catalyzed Intramolecular Amidation of Saturated C–H Bonds. *Angew. Chem. Int. Ed.* **2004**, *43*, 4210–4212.

62. Gómez-Emeterio, B. P.; Urbano, J.; Díaz-Requejo, M. M.; Pérez, P. J., Easy Alkane Catalytic Functionalization. *Organometallics* **2008**, *27*, 4126–4130.

63. Prier, C. K.; Zhang, R. K.; Buller, A. R.; Brinkmann-Chen, S.; Arnold, F. H., Enantioselective, Intermolecular Benzylic C–H Amination Catalysed by an Engineered Iron-Haem Enzyme. *Nat. Chem.* **2017**, *9*, 629–634.

64. Carsch, K. M.; DiMucci, I. M.; Iovan, D. A.; Li, A.; Zheng, S.-L.; Titus, C. J.; Lee, S. J.; Irwin, K. D.; Nordlund, D.; Lancaster, K. M.; Betley, T. A., Synthesis of a Copper-Supported Triplet Nitrene Complex Pertinent to Copper-Catalyzed Amination. *Science* **2019**, *365*, 1138–1143.

65. DiMucci, I. M.; Lukens, J. T.; Chatterjee, S.; Carsch, K. M.; Titus, C. J.; Lee, S. J.; Nordlund, D.; Betley, T. A.; MacMillan, S. N.; Lancaster, K. M., The Myth of d8 Copper(III). *J. Am. Chem. Soc.* **2019**, *141*, 18508–18520.

66. Ye, S.; Neese, F., Nonheme Oxo-Iron(IV) Intermediates form an Oxyl Radical upon Approaching the C–H Bond Activation Transition State. *Proc. Natl. Acad. Sci. U.S.A.* **2011**, *108*, 1228–1233.

67. Vilella, L.; Conde, A.; Balcells, D.; Díaz-Requejo, M. M.; Lledós, A.; Pérez, P. J., A Competing, Dual Mechanism for Catalytic Direct Benzene Hydroxylation from Combined Experimental-DFT Studies. *Chem. Sci.* **2017**, *8*, 8373–8383.

68. Corona, T.; Pfaff, F. F.; Acuña-Parés, F.; Draksharapu, A.; Whiteoak, C. J.; Martin-Diaconescu, V.; Lloret-Fillol, J.; Browne, W. R.; Ray, K.; Company, A., Reactivity of a Nickel(II) Bis(amidate) Complex with *meta*-Chloroperbenzoic Acid: Formation of a Potent Oxidizing Species. *Chem. Eur. J.* **2015**, *21*, 15029–15038.

69. Shimoyama, Y.; Kojima, T., Metal–Oxyl Species and Their Possible Roles in Chemical Oxidations. *Inorg. Chem.* **2019**, *58*, 9517–9542.

70. Kobayashi, K.; Ohtsu, H.; Wada, T.; Kato, T.; Tanaka, K., Characterization of a Stable Ruthenium Complex with an Oxyl Radical. *J. Am. Chem. Soc.* **2003**, *125*, 6729–6739.

71. Birk, T.; Bendix, J., Atom Transfer as a Preparative Tool in Coordination Chemistry. Synthesis and Characterization of Cr(V) Nitrido Complexes of Bidentate Ligands. *Inorg. Chem.* **2003**, *42*, 7608–7615.

72. Bucinsky, L.; Breza, M.; Lee, W.-T.; Hickey, A. K.; Dickie, D. A.; Nieto, I.; DeGayner, J. A.; Harris, T. D.; Meyer, K.; Krzystek, J.; Ozarowski, A.; Nehrkorn, J.; Schnegg, A.; Holldack, K.; Herber, R. H.; Telser, J.; Smith, J. M., Spectroscopic and Computational Studies of Spin States of Iron(IV) Nitrido and Imido Complexes. *Inorg. Chem.* **2017**, *56*, 4751–4768.

73. Jacobs, B. P.; Wolczanski, P. T.; Jiang, Q.; Cundari, T. R.; MacMillan, S. N., Rare Examples of Fe(IV) Alkyl-Imide Migratory Insertions: Impact of Fe—C Covalency in $(Me_2IPr)Fe(=NAd)R_2$ (R = ^{neo}Pe, 1-nor). *J. Am. Chem. Soc.* **2017**, *139*, 12145–12148.

74. Piro, N. A.; Figueroa, J. S.; McKellar, J. T.; Cummins, C. C., Triple-Bond Reactivity of Diphosphorus Molecules. *Science* **2006**, *313*, 1276–1279.

75. Figueroa, J. S.; Piro, N. A.; Clough, C. R.; Cummins, C. C., A Nitridoniobium(V) Reagent that Effects Acid Chloride to Organic Nitrile Conversion: Synthesis via Heterodinuclear (Nb/Mo) Dinitrogen Cleavage, Mechanistic Insights, and Recycling. *J. Am. Chem. Soc.* **2006**, *128*, 940–950.

76. Jenkins, D. M.; Betley, T. A.; Peters, J. C., Oxidative Group Transfer to Co(I) Affords a Terminal Co(III) Imido Complex. *J. Am. Chem. Soc.* **2002**, *124*, 11238–11239.

77. Mehn, M. P.; Brown, S. D.; Jenkins, D. M.; Peters, J. C.; Que, L., Vibrational Spectroscopy and Analysis of Pseudo-tetrahedral Complexes with Metal Imido Bonds. *Inorg. Chem.* **2006**, *45*, 7417–7427.

78. Fout, A. R.; Kilgore, U. J.; Mindiola, D. J., The Progression of Synthetic Strategies to Assemble Titanium Complexes Bearing the Terminal Imide Group. *Chem. Eur. J.* **2007**, *13*, 9428–9440.

79. Hay-Motherwell, R. S.; Wilkinson, G.; Hussain-Bates, B.; Hursthouse, M. B., Synthesis and X-ray crystal Structure of Oxotrimesityliridium(V). *Polyhedron* **1993**, *12*, 2009–2012.

80. Goetz, M. K.; Hill, E. A.; Filatov, A. S.; Anderson, J. S., Isolation of a Terminal Co(III)-Oxo Complex. *J. Am. Chem. Soc.* **2018**, *140*, 13176–13180.

81. MacBeth, C. E.; Golombek, A. P.; Young, V. G.; Yang, C.; Kuczera, K.; Hendrich, M. P.; Borovik, A. S., O_2 Activation by Nonheme Iron Complexes: A Monomeric Fe(III)–Oxo Complex Derived From O_2. *Science* **2000**, *289*, 938–941.

82. Shook, R. L.; Peterson, S. M.; Greaves, J.; Moore, C.; Rheingold, A. L.; Borovik, A. S., Catalytic Reduction of Dioxygen to Water with a Monomeric Manganese Complex at Room Temperature. *J. Am. Chem. Soc.* **2011**, *133*, 5810–5817.

83. Betley, T. A.; Peters, J. C., A Tetrahedrally Coordinated $L_3Fe{-}N_x$ Platform that Accommodates Terminal Nitride (Fe^{IV}:N) and Dinitrogen ($Fe^{I}{-}N_2{-}Fe^{I}$) Ligands. *J. Am. Chem. Soc.* **2004**, *126*, 6252–6254.

84. Hendrich, M. P.; Gunderson, W.; Behan, R. K.; Green, M. T.; Mehn, M. P.; Betley, T. A.; Lu, C. C.; Peters, J. C., On the Feasibility of N_2 Fixation via a Single-Site Fe^{I}/Fe^{IV} Cycle: Spectroscopic Studies of $Fe^{I}(N_2)Fe^{I}$, Fe^{IV}–N, and Related Species. *Proc. Natl. Acad. Sci. U.S.A.* **2006**, *103*, 17107–17112.

85. Vogel, C.; Heinemann, F. W.; Sutter, J.; Anthon, C.; Meyer, K., An Iron Nitride Complex. *Angew. Chem. Int. Ed.* **2008**, *47*, 2681–2684.

86. Scepaniak, J. J.; Fulton, M. D.; Bontchev, R. P.; Duesler, E. N.; Kirk, M. L.; Smith, J. M., Structural and Spectroscopic Characterization of an Electrophilic Iron Nitrido Complex. *J. Am. Chem. Soc.* **2008**, *130*, 10515–10517.

87. Scepaniak, J. J.; Young, J. A.; Bontchev, R. P.; Smith, J. M., Formation of Ammonia from an Iron Nitrido Complex. *Angew. Chem. Int. Ed.* **2009**, *48*, 3158–3160.

88. Scepaniak, J. J.; Vogel, C. S.; Khusniyarov, M. M.; Heinemann, F. W.; Meyer, K.; Smith, J. M., Synthesis, Structure, and Reactivity of an Iron(V) Nitride. *Science* **2011**, *331*, 1049–1052.

89. Kropp, H.; King, A. E.; Khusniyarov, M. M.; Heinemann, F. W.; Lancaster, K. M.; DeBeer, S.; Bill, E.; Meyer, K., Manganese Nitride Complexes in Oxidation States III, IV, and V: Synthesis and Electronic Structure. *J. Am. Chem. Soc.* **2012**, *134*, 15538–15544.

90. Brown, S. D.; Betley, T. A.; Peters, J. C., A Low-Spin d^5 Iron Imide: Nitrene Capture by Low-Coordinate Iron(I) Provides the 4-Coordinate Fe(III) Complex $[PhB(CH_2PPh_2)_3]Fe{:}N$-p-tolyl. *J. Am. Chem. Soc.* **2003**, *125*, 322–323.

91. Cowley, R. E.; Bontchev, R. P.; Sorrell, J.; Sarracino, O.; Feng, Y.; Wang, H.; Smith, J. M., Formation of a Cobalt(III) Imido from a Cobalt(II) Amido Complex. Evidence for Proton-Coupled Electron Transfer. *J. Am. Chem. Soc.* **2007**, *129*, 2424–2425.

92. Poverenov, E.; Efremenko, I.; Frenkel, A. I.; Ben-David, Y.; Shimon, L. J. W.; Leitus, G.; Konstantinovski, L.; Martin, J. M. L.; Milstein, D., Evidence for a Terminal Pt(IV)-Oxo Complex Exhibiting Diverse Reactivity. *Nature* **2008**, *455*, 1093–1096.

93. Searles, K.; Fortier, S.; Khusniyarov, M. M.; Carroll, P. J.; Sutter, J.; Meyer, K.; Mindiola, D. J.; Caulton, K. G., A *cis*-Divacant Octahedral and Mononuclear Iron(IV) Imide. *Angew. Chem. Int. Ed.* **2014**, *53*, 14139–14143.

94. Sun, J.; Abbenseth, J.; Verplancke, H.; Diefenbach, M.; de Bruin, B.; Hunger, D.; Würtele, C.; Joris, v. S., Joris; Holthausen, M. C.; Schneider, S., A Platinum(II) Metallonitrene with a Triplet Ground State. *Nat. Chem.* **2020**.

95. Mansuy, D.; Mahy, J.-P.; Dureault, A.; Bedi, G.; Battioni, P., Iron- and Manganese-Porphyrin Catalysed Aziridination of Alkenes by Tosyl- and Acyl-Iminoiodobenzene. *J. Chem. Soc., Chem. Commun.* **1984**, 1161–1163.

96. Mahy, J. P.; Bedi, G.; Battioni, P.; Mansuy, D., Allylic Amination of Alkenes by Tosyliminoiodobenzene: Manganese Porphyrins as Suitable Catalysts. *Tetrahedron Lett.* **1988**, 1927–1930.

97. Alcover-Fortuny, G.; Caballol, R.; Pierloot, K.; de Graaf, C., Role of the Imide Axial Ligand in the Spin and Oxidation State of Manganese Corrole and Corrolazine Complexes. *Inorg. Chem.* **2016**, *55*, 5274–5280.

98. Eikey, R. A.; Khan, S. I.; Abu-Omar, M. M., The Elusive Terminal Imido of Manganese(V). *Angew. Chem. Int. Ed.* **2002**, *41*, 3591–3595.

99. Lansky, D. E.; Kosack, J. R.; Narducci Sarjeant, A. A.; Goldberg, D. P., An Isolable, Nonreducible High-Valent Manganese(V) Imido Corrolazine Complex. *Inorg. Chem.* **2006**, *45*, 8477–8479.

100. Badiei, Y. M.; Dinescu, A.; Dai, X.; Palomino, R. M.; Heinemann, F. W.; Cundari, T. R.; Warren, T. H., Copper–Nitrene Complexes in Catalytic C–H Amination. *Angew. Chem. Int. Ed.* **2008**, *47*, 9961–9964.

101. McGhee, W. D.; Foo, T.; Hollander, F. J.; Bergman, R. G., Synthesis and Chemistry of a Dinuclear Iridium Bis-μ-Oxo Complex. Observation of Oxygen Transfer and Phosphorus-Carbon Bond Cleavage. *J. Am. Chem. Soc.* **1988**, *110*, 8543–8545.

102. Dobbs, D. A.; Bergman, R. G., Synthesis and Reactivity of Bridging Imido and Imido-Oxo Complexes of Iridium. Water-Catalyzed and -Uncatalyzed Dimerization of Terminal Iridium Imido Complexes. *Organometallics* **1994**, *13*, 4594–4605.

103. Wilding, M. J. T.; Iovan, D. A.; Betley, T. A., High-Spin Iron Imido Complexes Competent for C–H Bond Amination. *J. Am. Chem. Soc.* **2017**, *139*, 12043–12049.

104. Jones, C.; Schulten, C.; Rose, R. P.; Stasch, A.; Aldridge, S.; Woodul, W. D.; Murray, K. S.; Moubaraki, B.; Brynda, M.; La Macchia, G.; Gagliardi, L., Amidinato– and Guanidinato–Cobalt(I) Complexes: Characterization of Exceptionally Short Co–Co Interactions. *Angew. Chem. Int. Ed.* **2009**, *48*, 7406–7410.

105. Grapperhaus, C. A.; Mienert, B.; Bill, E.; Weyhermüller, T.; Wieghardt, K., Mononuclear (Nitrido)iron(V) and (Oxo)iron(IV) Complexes via Photolysis of

[(cyclam-acetato)$Fe^{III}(N_3)]^+$ and Ozonolysis of [(cyclam-acetato)$Fe^{III}(O_3SCF_3)]^+$ in Water/Acetone Mixtures. *Inorg. Chem.* **2000**, *39*, 5306–5317.

106. Aghazada, S.; Miehlich, M.; Messelberger, J.; Heinemann, F. W.; Munz, D.; Meyer, K., A Terminal Iron Nitrilimine Complex: Accessing the Terminal Nitride through Diazo N−N Bond Cleavage. *Angew. Chem. Int. Ed.* **2019**, *58*, 18547–18551.

107. Odom, A. L.; Cummins, C. C.; Protasiewicz, J. D., Nitric Oxide Cleavage: Synthesis of Terminal Chromium(VI) Nitrido Complexes via Nitrosyl Deoxygenation. *J. Am. Chem. Soc.* **1995**, *117*, 6613–6614.

108. Morimoto, Y.; Shimaoka, Y.; Ishimizu, Y.; Fujii, H.; Itoh, S., Direct Observation of Primary C−H Bond Oxidation by an Oxido-Iron(IV) Porphyrin π-Radical Cation Complex in a Fluorinated Carbon Solvent. *Angew. Chem. Int. Ed.* **2019**, *58*, 10863–10866.

109. Schaub, S.; Miska, A.; Becker, J.; Zahn, S.; Mollenhauer, D.; Sakshath, S.; Schünemann, V.; Schindler, S., Synthesis of an Iron(IV) Aqua–Oxido Complex Using Ozone as an Oxidant. *Angew. Chem. Int. Ed.* **2018**, *57*, 5355–5358.

110. Werlé, C.; Goddard, R.; Fürstner, A., The First Crystal Structure of a Reactive Dirhodium Carbene Complex and a Versatile Method for the Preparation of Gold Carbenes by Rhodium-to-Gold Transmetalation. *Angew. Chem. Int. Ed.* **2015**, *54*, 15452–15456.

111. Seidel, G.; Fürstner, A., Structure of a Reactive Gold Carbenoid. *Angew. Chem. Int. Ed.* **2014**, *53*, 4807–4811.

112. Maxwell, J.; Kodadek, T., Organometallic Chemistry of Porphyrins: Spectroscopic and Chemical Characterization of a Rhodium Porphyrin-Ethyl Diazoacetate Adduct. *Organometallics* **1991**, *10*, 4–6.

113. Caballero, A.; Pérez, P. J., Dimensioning the Term Carbenoid. *Chem. Eur. J.* **2017**, *23*, 14389–14393.

114. Sarkar, S. K.; Sawai, A.; Kanahara, K.; Wentrup, C.; Abe, M.; Gudmundsdottir, A. D., Direct Detection of a Triplet Vinylnitrene, 1,4-Naphthoquinone-2-ylnitrene, in Solution and Cryogenic Matrices. *J. Am. Chem. Soc.* **2015**, *137*, 4207–4214.

115. Pan, Z.; Wang, Q.; Sheng, X.; Horner, J. H.; Newcomb, M., Highly Reactive Porphyrin−Iron−Oxo Derivatives Produced by Photolyses of Metastable Porphyrin−Iron(IV) Diperchlorates. *J. Am. Chem. Soc.* **2009**, *131*, 2621–2628.

116. Zhang, R.; Horner, J. H.; Newcomb, M., Laser Flash Photolysis Generation and Kinetic Studies of Porphyrin−Manganese−Oxo Intermediates. Rate Constants for Oxidations Effected by Porphyrin−Mn^{V}−Oxo Species and Apparent Disproportionation Equilibrium Constants for Porphyrin−Mn^{IV}−Oxo Species. *J. Am. Chem. Soc.* **2005**, *127*, 6573–6582.

117. Zhang, R.; Newcomb, M., Laser Flash Photolysis Generation of High-Valent Transition Metal−Oxo Species: Insights from Kinetic Studies in Real Time. *Acc. Chem. Res.* **2008**, *41*, 468–477.

118. Newcomb, M.; Zhang, R.; Pan, Z.; Harischandra, D. N.; Chandrasena, R. E. P.; Horner, J. H.; Martinez, E., Laser Flash Photolysis Production of Metal-Oxo

Derivatives and Direct Kinetic Studies of their Oxidation Reactions. *Catal. Today* **2006**, *117*, 98–104.

119. Andrews, L.; Citra, A.; Chertihin, G. V.; Bare, W. D.; Neurock, M., Reactions of Laser-Ablated Co and Ni Atoms with Nitrogen Atoms and Molecules. Infrared Spectra and DFT Calculations of Metal Nitride Molecular Species and Complexes. *J. Phys. Chem. A* **1998**, *102*, 2561–2571.

120. Citra, A.; Andrews, L., Reactions of Laser-Ablated Osmium and Ruthenium Atoms with Nitrogen. Matrix Infrared Spectra and Density Functional Calculations of Osmium and Ruthenium Nitrides and Dinitrides. *J. Phys. Chem. A* **2000**, *104*, 1152–1161.

121. Long, A. K. M.; Timmer, G. H.; Pap, J. S.; Snyder, J. L.; Yu, R. P.; Berry, J. F., Aryl C–H Amination by Diruthenium Nitrides in the Solid State and in Solution at Room Temperature: Experimental and Computational Study of the Reaction Mechanism. *J. Am. Chem. Soc.* **2011**, *133*, 13138–13150.

122. Musch Long, A. K.; Yu, R. P.; Timmer, G. H.; Berry, J. F., Aryl C−H Bond Amination by an Electrophilic Diruthenium Nitride. *J. Am. Chem. Soc.* **2010**, *132*, 12228–12230.

123. Timmer, G. H.; Berry, J. F., Electrophilic Aryl C–H Amination by Dimetal Nitrides: Correlating Electronic Structure with Reactivity. *Chem. Sci.* **2012**, *3*, 3038–3052.

124. Pap, J. S.; DeBeer George, S.; Berry, J. F., Delocalized Metal–Metal and Metal–Ligand Multiple Bonding in a Linear Ru–Ru≡N Unit: Elongation of a Traditionally Short Ru≡N Bond. *Angew. Chem. Int. Ed.* **2008**, *47*, 10102–10105.

125. Zolnhofer, E. M.; Käß, M.; Khusniyarov, M. M.; Heinemann, F. W.; Maron, L.; van Gastel, M.; Bill, E.; Meyer, K., An Intermediate Cobalt(IV) Nitrido Complex and its N-Migratory Insertion Product. *J. Am. Chem. Soc.* **2014**, *136*, 15072–15078.

126. Hu, X.; Meyer, K., Terminal Cobalt(III) Imido Complexes Supported by Tris(Carbene) Ligands: Imido Insertion into the Cobalt−Carbene Bond. *J. Am. Chem. Soc.* **2004**, *126*, 16322–16323.

127. Scheibel, M. G.; Wu, Y.; Stückl, A. C.; Krause, L.; Carl, E.; Stalke, D.; de Bruin, B.; Schneider, S., Synthesis and Reactivity of a Transient, Terminal Nitrido Complex of Rhodium. *J. Am. Chem. Soc.* **2013**, *135*, 17719–17722.

128. Scheibel, M. G.; Askevold, B.; Heinemann, F. W.; Reijerse, E. J.; de Bruin, B.; Schneider, S., Closed-Shell and Open-Shell Square-Planar Iridium Nitrido Complexes. *Nat. Chem.* **2012**, *4*, 552–558.

129. Xiao, D. J.; Bloch, E. D.; Mason, J. A.; Queen, W. L.; Hudson, M. R.; Planas, N.; Borycz, J.; Dzubak, A. L.; Verma, P.; Lee, K.; Bonino, F.; Crocellà, V.; Yano, J.; Bordiga, S.; Truhlar, D. G.; Gagliardi, L.; Brown, C. M.; Long, J. R., Oxidation of Ethane to Ethanol by N_2O in a Metal–Organic Framework with Coordinatively Unsaturated Iron(II) Sites. *Nat. Chem.* **2014**, *6*, 590–595.

130. Gallagher, A. T.; Lee, J. Y.; Kathiresan, V.; Anderson, J. S.; Hoffman, B. M.; Harris, T. D., A Structurally-Characterized Peroxomanganese(IV) Porphyrin from

Reversible O_2 Binding within a Metal–Organic Framework. *Chem. Sci.* **2018**, *9*, 1596–1603.

131. Pike, S. D.; Thompson, A. L.; Algarra, A. G.; Apperley, D. C.; Macgregor, S. A.; Weller, A. S., Synthesis and Characterization of a Rhodium(I) σ-Alkane Complex in the Solid State. *Science* **2012**, *337*, 1648–1651.

132. Kawamichi, T.; Haneda, T.; Kawano, M.; Fujita, M., X-Ray Observation of a Transient Hemiaminal Trapped in a Porous Network. *Nature* **2009**, *461*, 633–635.

133. Ohashi, Y., Direct Observation of Unstable Reaction Intermediates by Acid-Base Complex Formation. *Chem. Rec.* **2013**, *13*, 303–325.

134. Zheng, S.-L.; Wang, Y.; Yu, Z.; Lin, Q.; Coppens, P., Direct Observation of a Photoinduced Nonstabilized Nitrile Imine Structure in the Solid State. *J. Am. Chem. Soc.* **2009**, *131*, 18036–18037.

135. Harada, J.; Uekusa, H.; Ohashi, Y., X-ray Analysis of Structural Changes in Photochromic Salicylideneaniline Crystals. Solid-State Reaction Induced by Two-Photon Excitation. *J. Am. Chem. Soc.* **1999**, *121*, 5809–5810.

136. Kawano, M., X-ray Direct Observation of Reactions and Labile Species on the Basis of Crystal Design. *Bull. Chem. Soc. Jpn.* **2014**, *87*, 577–592.

137. Kawano, M.; Kobayashi, Y.; Ozeki, T.; Fujita, M., Direct Crystallographic Observation of a Coordinatively Unsaturated Transition-Metal Complex *in situ* Generated within a Self-Assembled Cage. *J. Am. Chem. Soc.* **2006**, *128*, 6558–6559.

138. Cole, J. M., Single-Crystal X-Ray Diffraction Studies of Photo-Induced Molecular Species. *Chem. Soc. Rev.* **2004**, *33*, 501–513.

139. Novozhilova, I. V.; Coppens, P.; Lee, J.; Richter-Addo, G. B.; Bagley, K. A., Experimental and Density Functional Theoretical Investigations of Linkage Isomerism in Six-Coordinate {FeNO}^{6} Iron Porphyrins with Axial Nitrosyl and Nitro Ligands. *J. Am. Chem. Soc.* **2006**, *128*, 2093–2104.

140. Kovalevsky, A. Y.; Bagley, K. A.; Coppens, P., The First Photocrystallographic Evidence for Light-Induced Metastable Linkage Isomers of Ruthenium Sulfur Dioxide Complexes. *J. Am. Chem. Soc.* **2002**, *124*, 9241–9248.

141. Fomitchev, D. V.; Coppens, P., X-Ray Diffraction Analysis of Geometry Changes upon Excitation: The Ground-State and Metastable-State Structures of $K_2[Ru(NO_2)_4(OH)(NO)]$. *Inorg. Chem.* **1996**, *35*, 7021–7026.

142. Kovalevsky, A. Y.; King, G.; Bagley, K. A.; Coppens, P., Photoinduced Oxygen Transfer and Double-Linkage Isomerism in a *cis*-$(NO)(NO_2)$ Transition-Metal Complex by Photocrystallography, FT-IR Spectroscopy and DFT Calculations. *Chem. Eur. J.* **2005**, *11*, 7254–7264.

143. Kawano, M.; Sano, T.; Abe, J.; Ohashi, Y., The First *in Situ* Direct Observation of the Light-Induced Radical Pair from a Hexaarylbiimidazolyl Derivative by X-ray Crystallography. *J. Am. Chem. Soc.* **1999**, *121*, 8106–8107.

144. Koshima, H.; Kawanishi, H.; Nagano, M.; Yu, H.; Shiro, M.; Hosoya, T.; Uekusa, H.; Ohashi, Y., Absolute Asymmetric Photocyclization of Isopropylbenzophenone Derivatives Using a Cocrystal Approach Involving Single-Crystal-to-Single-Crystal Transformation. *J. Org. Chem.* **2005**, *70*, 4490–4497.

145. Kawano, M.; Hirai, K.; Tomioka, H.; Ohashi, Y., Structure Analysis of a Transient Triplet Carbene Trapped in a Crystal. *J. Am. Chem. Soc.* **2001**, *123*, 6904–6908.

146. Kawano, M.; Takayama, T.; Uekusa, H.; Ohashi, Y.; Ozawa, Y.; Matsubara, K.; Imabayashi, H.; Mitsumi, M.; Toriumi, K., Structure Analysis of Photo-induced Triplet Phenylnitrene Using Synchrotron Radiation. *Chem. Lett.* **2003**, *32*, 922–923.

147. Novozhilova, I. V.; Volkov, A. V.; Coppens, P., Theoretical Analysis of the Triplet Excited State of the $[Pt_2(H_2P_2O_5)_4]^{4-}$ Ion and Comparison with Time-Resolved X-ray and Spectroscopic Results. *J. Am. Chem. Soc.* **2003**, *125*, 1079–1087.

148. Pressprich, M. R.; White, M. A.; Coppens, P., Single-Crystal X-Ray Analysis of an Electronic Excited State: The Structure Determination of a Metastable State of Sodium Nitroprusside. *J. Am. Chem. Soc.* **1993**, *115*, 6444–6445.

149. Saouma, C. T.; Peters, J. C., M≡E and M=E Complexes of Iron and Cobalt that Emphasize Three-Fold Symmetry (E=O, N, NR). *Coord. Chem. Rev.* **2011**, *255*, 920–937.

150. Ortiz de Montellano, P. R., Hydrocarbon Hydroxylation by Cytochrome P450 Enzymes. *Chem. Rev.* **2010**, *110*, 932–948.

151. Que, L., The Road to Non-Heme Oxoferryls and Beyond. *Acc. Chem. Res.* **2007**, *40*, 493–500.

152. Holm, R. H.; Berg, J. M., Toward Functional Models of Metalloenzyme Active Sites: Analog Reaction Systems of the Molybdenum Oxo Transferases. *Acc. Chem. Res.* **1986**, *19*, 363–370.

153. Nugent, W. A.; Mayer, J. M., Metal Ligand Multiple Bonds. Wiley & Sons: New York, NY: **1988**.

154. Mayer, J. M., Why are there no Terminal Oxo Complexes of the Late Transition Metals? or The Importance of Metal–Ligand π Antibonding Interactions. *Comment. Inorg. Chem.* **1988**, *8*, 125–135.

155. Rohde, J.-U.; In, J. H.; Lim, M. H.; Brennessel, W. W.; Bukowski, M. R.; Stubna, A.; Munck, E.; Nam, W.; Que, L., Jr., Crystallographic and Spectroscopic Characterization of a Nonheme Fe(IV)=O Complex. *Science* **2003**, *299*, 1037–1039.

156. Smith, J. M., Reactive Transition Metal Nitride Complexes. *In Prog. Inorg. Chem.*, John Wiley & Sons, Inc.: **2014**; *58*, 417–470.

157. Berry, J. F., Terminal Nitrido and Imido Complexes of the Late Transition Metals. *Comment. Inorg. Chem.* **2009**, *30*, 28–66.

158. Eikey, R. A.; Abu-Omar, M. M., Nitrido and Imido Transition Metal Complexes of Groups 6–8. *Coord. Chem. Rev.* **2003**, *243*, 83–124.

159. Hojilla Atienza, C. C.; Bowman, A. C.; Lobkovsky, E.; Chirik, P. J., Photolysis and Thermolysis of Bis(imino)pyridine Cobalt Azides: C−H Activation from Putative Cobalt Nitrido Complexes. *J. Am. Chem. Soc.* **2010**, *132*, 16343–16345.

160. Knobloch, D. J.; Lobkovsky, E.; Chirik, P. J., Dinitrogen Cleavage and Functionalization by Carbon Monoxide Promoted by a Hafnium Complex. *Nat. Chem.* **2010**, *2*, 30–35.

161. Schöffel, J.; Šušnjar, N.; Nückel, S.; Sieh, D.; Burger, P., 4d vs. 5d – Reactivity and Fate of Terminal Nitrido Complexes of Rhodium and Iridium. *Eur. J. Inorg. Chem.* **2010**, *2010*, 4911–4915.

162. Schlangen, M.; Neugebauer, J.; Reiher, M.; Schröder, D.; Lopez, J. P.; Haryono, M.; Heinemann, F. W.; Grohmann, A.; Schwarz, H., Gas-Phase C−H and N−H Bond Activation by a High Valent Nitrido-Iron Dication and 〈NH〉 -Transfer to Activated Olefins. *J. Am. Chem. Soc.* **2008**, *130*, 4285–4294.

163. Chen, W.-Z.; De Silva, V.; Lin, C.; Abellard, J.; Marcus, D. M.; Ren, T., Azidotetrakis(diarylformamidinate)diruthenium(II,III) Compounds: Synthesis, Molecular Structures and Voltammetric Properties; Linear Free Energy Relationships in Dinuclear Compounds VII. *J. Clust. Sci.* **2005**, *16*, 151–165.

164. Buschhorn, D.; Pink, M.; Fan, H.; Caulton, K. G., Nitrogen-Ligated Iron Complexes: Photolytic Approach to the FeN^{+} Moiety. *Inorg. Chem.* **2008**, *47*, 5129–5135.

165. Ingleson, M. J.; Pink, M.; Fan, H.; Caulton, K. G., Redox Chemistry of the Triplet Complex (PNP)Co^{I}. *J. Am. Chem. Soc.* **2008**, *130*, 4262–4276.

166. Rohde, J.-U.; Betley, T. A.; Jackson, T. A.; Saouma, C. T.; Peters, J. C.; Que, L., XAS Characterization of a Nitridoiron(IV) Complex with a Very Short Fe−N Bond. *Inorg. Chem.* **2007**, *46*, 5720–5726.

167. Abe, J.; Sano, T.; Kawano, M.; Ohashi, Y.; Matsushita, M. M.; Iyoda, T., EPR and Density Functional Studies of Light-Induced Radical Pairs in a Single Crystal of a Hexaarylbiimidazolyl Derivative. *Angew. Chem. Int. Ed.* **2001**, *40*, 580–582.

168. Kawano, M.; Hirai, K.; Tomioka, H.; Ohashi, Y., Structure Determination of Triplet Diphenylcarbenes by in Situ X-ray Crystallographic Analysis. *J. Am. Chem. Soc.* **2007**, *129*, 2383–2391.

169. Carducci, M. D.; Pressprich, M. R.; Coppens, P., Diffraction Studies of Photoexcited Crystals: Metastable Nitrosyl-Linkage Isomers of Sodium Nitroprusside. *J. Am. Chem. Soc.* **1997**, *119*, 2669–2678.

170. Kawano, M.; Ishikawa, A.; Morioka, Y.; Tomizawa, H.; Miki, E.-i.; Ohashi, Y., X-Ray Diffraction and Spectroscopic Studies of the Light-Induced Metastable State of a Ethylenediamine Nitrosyl Ruthenium Complex. *J. Chem. Soc., Dalton Trans.* **2000**, 2425–2431.

171. Bowes, K. F.; Cole, J. M.; Husheer, S. L. G.; Raithby, P. R.; Savarese, T. L.; Sparkes, H. A.; Teat, S. J.; Warren, J. E., Photocrystallographic Structure Determination of a New Geometric Isomer of $[Ru(NH_3)_4(H_2O)([\eta^1$-OSO)$][MeC_6H_4SO_3]$. *Chem. Commun.* **2006**, 2448–2450.

172. Warren, M. R.; Brayshaw, S. K.; Johnson, A. L.; Schiffers, S.; Raithby, P. R.; Easun, T. L.; George, M. W.; Warren, J. E.; Teat, S. J., Reversible 100 % Linkage Isomerization in a Single-Crystal–to–Single-Crystal Transformation: Photocrystallographic Identification of the Metastable [Ni(dppe)(η^1-ONO)Cl] Isomer. *Angew. Chem. Int. Ed.* **2009**, *48*, 5711–5714.

173. Yoshiki, O.; Madoka, T.; Minoru, M.; Koshiro, T.; Nobuhiro, Y.; Hidehiro, U.; Yuji, O., Photoexcited Crystallography of Diplatinum Complex by Multiple-exposure IP Method. *Chem. Lett.* **2003**, *32*, 62–63.

174. Walstrom, A.; Pink, M.; Yang, X.; Tomaszewski, J.; Baik, M.-H.; Caulton, K. G., A Facile Approach to a d^4 Ru:N: Moiety. *J. Am. Chem. Soc.* **2005**, *127*, 5330−5331.

175. Man, W.-L.; Tang, T.-M.; Wong, T.-W.; Lau, T.-C.; Peng, S.-M.; Wong, W.-T., Highly Electrophilic (Salen)ruthenium(VI) Nitrido Complexes. *J. Am. Chem. Soc.* **2004**, *126*, 478–479.

176. Chen, N. Y.; Degnan, T. F., Jr.; Smith, C. M., Molecular Transport and Reaction in Zeolites. VCH Publishers: New York, NY, **1994**.

177. Schmøkel, M. S.; Kamiński, R.; Benedict, J. B.; Coppens, P., Data Scaling and Temperature Calibration in Time-Resolved Photocrystallographic Experiments. *Acta Crystallogr. A* **2010**, *66*, 632–636.

178. Svendsen, H.; Overgaard, J.; Chevallier, M.; Collet, E.; Iversen, B. B., Photomagnetic Switching of the Complex $[Nd(dmf)_4(H_2O)_3(\mu\text{-}CN)Fe(CN)_5]\cdot H_2O$ Analyzed by Single-Crystal X-Ray Diffraction. *Angew. Chem. Int. Ed.* **2009**, *48*, 2780−2783.

179. Angaridis, P.; Cotton, F. A.; Murillo, C. A.; Villagrán, D.; Wang, X., Structural and Magnetic Evidence Concerning Spin Crossover in Formamidinate Compounds with Ru_2^{5+} Cores. *J. Am. Chem. Soc.* **2005**, *127*, 5008–5009.

180. Pangborn, A. B.; Giardello, M. A.; Grubbs, R. H.; Rosen, R. K.; Timmers, F. J., Safe and Convenient Procedure for Solvent Purification. *Organometallics* **1996**, *15*, 1518-1520.

181. Fulmer, G. R.; Miller, A. J. M.; Sherden, N. H.; Gottlieb, H. E.; Nudelman, A.; Stoltz, B. M.; Bercaw, J. E.; Goldberg, K. I., NMR Chemical Shifts of Trace

Impurities: Common Laboratory Solvents, Organics, and Gases in Deuterated Solvents Relevant to the Organometallic Chemist. *Organometallics* **2010**, *29*, 2176–2179.

182. AXS, B. Apex II, Bruker AXS: Madison, Wisconsin, **2009**.

183. Sheldrick, G., A short history of SHELX. *Acta Crystallogr. A* **2008**, *64*, 112–122.

184. Sheldrick, G., Crystal structure refinement with SHELXL. *Acta Crystallogr. C* **2015**, *71*, 3–8.

185. Krackl, S.; Inoue, S.; Driess, M.; Enthaler, S., Intermolecular Hydrogen–Fluorine Interaction in Dimolybdenum Triply Bonded Complexes Modified by Fluorinated Formamidine Ligands for the Construction of 2D- and 3D-Networks. *Eur. J. Inorg. Chem.* **2011**, *2011*, 2103–2111.

186. Mitchell, R. W.; Spencer, A.; Wilkinson, G., Carboxylato-Triphenylphosphine Complexes of Ruthenium, Cationic Triphenylphosphine Complexes Derived from them, and their Behaviour as Homogeneous Hydrogenation Catalysts for Alkenes. *J. Chem. Soc., Dalton Trans.* **1973**, 846–854.

187. Lin, C.; Ren, T.; Valente, E. J.; Zubkowski, J. D.; Smith, E. T., Continuous Spectroscopic and Redox Tuning of Dinuclear Compounds: Chlorotetrakis(μ-*N,N′*-diarylformamidinato)diruthenium(II,III). *Chem. Lett.* **1997**, *26*, 753–754.

188. Kwart, H.; Khan, A. A., Copper-Catalyzed Decomposition of Benzenesulfonyl Azide in Cyclohexene Solution. *J. Am. Chem. Soc.* **1967**, *89*, 1951–1953.

189. Park, Y.; Kim, Y.; Chang, S., Transition Metal-Catalyzed C−H Amination: Scope, Mechanism, and Applications. *Chem. Rev.* **2017**, *117*, 9247–9301.

190. Brandenberg, O. F.; Fasan, R.; Arnold, F. H., Exploiting and Engineering Hemoproteins for Abiological Carbene and Nitrene Transfer Reactions. *Curr. Opin. Biotech.* **2017**, *47*, 102–111.

191. Deqquirez, G.; Pons, V.; Dauben, P., Nitrene Chemistry in Organic Synthesis: Still in its Infancy? *Angew. Chem. Int. Ed.* **2012**, *51*, 7384–7395.

192. Roizen, J. L.; Harvey, M. E.; Du Bois, J., Metal-Catalyzed Nitrogen-Atom Transfer Methods for the Oxidation of Aliphatic C−H Bonds. *Acc. Chem. Res.* **2012**, *45*, 911–922.

193. Du Bois, J., Rhodium-Catalyzed C–H Amination. An Enabling Method for Chemical Synthesis. *Org. Process Res. Dev.* **2011**, *15*, 758–762.

194. Godula, K.; Sames, D., C–H Bond Functionalization in Complex Organic Synthesis. *Science* **2006**, *312*, 67–72.

195. Paudyal, M. P.; Adebesin, A. M.; Burt, S. R.; Ess, D. H.; Ma, Z.; Kürti, L.; Falck, J. R., Dirhodium-Catalyzed C–H Arene Amination using Hydroxylamines. *Science* **2016**, *353*, 1144–1147.

196. Jat, J. L.; Paudyal, M. P.; Gao, H.; Xu, Q.-L.; Yousufuddin, M.; Devarajan, D.; Ess, D. H.; Kürti, L.; Falck, J. R., Direct Stereospecific Synthesis of Unprotected N–H and N–Me Aziridines from Olefins. *Science* **2014**, *343*, 61–65.

197. Kornecki, K. P.; Berry, J. F., Introducing a Mixed-Valent Dirhodium(II,III) Catalyst with Increased Stability in C–H Amination. *Chem. Commun.* **2012**, *48*, 12097–12099.

198. Espino, C. G.; Fiori, K. W.; Kim, M.; Du Bois, J., Expanding the Scope of C–H Amination through Catalyst Design. *J. Am. Chem. Soc.* **2004**, *126*, 15378–15379.

199. Müller, P.; Baud, C.; Jacquier, Y., A Method for Rhodium(II)-Catalyzed Aziridination of Olefins. *Tetrahedron* **1996**, *52*, 1543–1548.

200. Perry, R. H.; Cahill, T. J.; Roizen, J. L.; Du Bois, J.; Zare, R. N., Capturing Fleeting Intermediates in a Catalytic C–H Amination Reaction Cycle. *Proc. Natl. Acad. Sci. U.S.A.* **2012**, *109*, 18295–18299.

201. Varela-Álvarez, A.; Haines, B. E.; Musaev, D. G., Key Mechanistic Insights into the Intramolecular C-H Bond Amination and Double Bond Aziridination in Sulfamate Esters Catalyzed by Dirhodium Tetracarboxylate Complexes. *J. Organometallic Chem.* **2018**, *867*, 183–192.

202. Iovan, D. A.; Betley, T. A., Characterization of Iron-Imido Species Relevant for N-Group Transfer Chemistry. *J. Am. Chem. Soc.* **2016**, *138*, 1983–1993.

203. Kornecki, K. P.; Briones, J. F.; Boyarskikh, V.; Fullilove, F.; Autschbach, J.; Schrote, K. E.; Lancaster, K. M.; Davies, H. M. L.; Berry, J. F., Direct Spectroscopic Characterization of a Transitory Dirhodium Donor-Acceptor Carbene Complex. *Science* **2013**, *342*, 351–354.

204. Das, A.; Reibenspies, J. H.; Chen, Y.-S.; Powers, D. C., Direct Characterization of a Reactive Lattice-Confined Ru_2 Nitride by Photocrystallography. *J. Am. Chem. Soc.* **2017**, *139*, 2912–2915.

205. Corcos, A. R.; Pap, J. S.; Yang, T.; Berry, J. F., A Synthetic Oxygen Atom Transfer Photocycle from a Diruthenium Oxyanion Complex. *J. Am. Chem. Soc.* **2016**, *138*, 10032–10040.

206. Kornecki, K. P.; Berry, J. F., Evidence for a One-Electron Mechanistic Regime in Dirhodium-Catalyzed Intermolecular C–H Amination. *Chem. Eur. J.* **2011**, *17*, 5827–5832.

207. Zalatan, D. N.; Du Bois, J., Understanding the Differential Performance of $Rh_2(esp)_2$ as a Catalyst for C−H Amination. *J. Am. Chem. Soc.* **2009**, *131*, 7558–7559.

208. Stateman, L. M.; Nakafuku, K. M.; Nagib, D. A., Remote C–H Functionalization via Selective Hydrogen Atom Transfer. *Synthesis* **2018**, *50*, 1569–1686.

209. Zard, S. Z., Recent Progress in the Generation and use of Nitrogen-Centred Radicals. *Chem. Soc. Rev.* **2008**, *37*, 1603–1618.

210. Neale, R. S., Nitrogen Radicals as Synthesis Intermediates. *N*-Halamide Rearrangements and Additions to Unsaturated Hydrocarbons. *Synthesis* **1971**, *1971*, 1–15.

211. Wolff, M. E., Cyclization of N-Halogenated Amines (The Hofmann-Löffler Reaction). *Chem. Rev.* **1963**, *63*, 55–64.

212. Evans, J. C.; Jackson, S. K.; Rowlands, C. C.; Barratt, M. D., An Electron Spin Resonance Study of Radicals from Chloramine-T–1 : Spin Trapping of Radicals Produced in Acid Media. *Tetrahedron* **1985**, *41*, 5191–5194.

213. Evans, J. C.; Jackson, S. K.; Rowlands, C. C.; Barratt, M. D., An Electron Spin Resonance Study of Radicals from Chloramine-T—2 : Spin Trapping of Photolysis Products of Chloramine-T at Alkaline pH. *Tetrahedron* **1985**, *41*, 5195–5200.

214. Shcherbakov, V. I.; Kuznetsova, V. P.; Chuprunov, E. V.; Ovsetsina, T. I.; Stolyarova, N. E.; Zakharov, L. N.; Novgorod, N., Reaction of Di- (IV) and Trialkylstannyl Chlorides (II) with Chloroamine (I) in an Aqueous Medium. Crystal Structure of *N*-Chloro-*N*- trimethylstannyl-4-chlorob enzenesulfonamide. *Metalloorg. Khim.* **1991**, *4*, 1350–1354.

215. Lutterman, D. A.; Degtyareva, N. N.; Johnston, D. H.; Gallucci, J. C.; Eglin, J. L.; Turro, C., Photoinduced One-Electron Reduction of Alkyl Halides by Dirhodium(II,II) Tetraformamidinates and a Related Complex with Visible Light. *Inorg. Chem.* **2005**, *44*, 5388–5396.

216. Kawamura, T.; Maeda, M.; Miyamoto, M.; Usami, H.; Imaeda, K.; Ebihara, M., Geometrical Difference and Electron Configuration of Lantern-Type Rh_2^{4+} and Rh_2^{5+} Complexes: X-ray Structural and DFT Study. *J. Am. Chem. Soc.* **1998**, *120*, 8136–8142.

217. Martínez, C.; Muñiz, K., An Iodine-Catalyzed Hofmann–Löffler Reaction. *Angew. Chem. Int. Ed.* **2015**, *54*, 8287–8291.

218. Corey, E. J.; Hertler, W. R., A Study of the Formation of Haloamines and Cyclic Amines by the Free Radical Chain Decomposition of *N*-Haloammonium Ions (Hofmann-Löffler Reaction). *J. Am. Chem. Soc.* **1960**, *82*, 1657–1668.

219. Shainyan, B. A.; Kuzmin, A. V., Sulfonyl Nitrenes from Different Sources: Computational Study of Formation and Transformations. *J. Phys. Org. Chem.* **2014**, *27*, 156–162.

220. Bain, G. A.; Berry, J. F., Diamagnetic Corrections and Pascal's Constants. *J. Chem. Educ.* **2008**, *85*, 532–536.

221. Dolomanov, O. V.; Bourhis, L. J.; Gildea, R. J.; Howard, J. A. K.; Puschmann, H., OLEX2: A Complete Structure Solution, Refinement and Analysis Program. *J. Appl. Crystallogr.* **2009**, *42*, 339–341.

222. Frisch, M. J.; Trucks, G. W.; Schlegel, H. B.; Scuseria, G. E.; Robb, M. A.; Cheeseman, J. R.; Scalmani, G.; Barone, V.; Mennucci, B.; Petersson, G. A.; Nakatsuji, H.; Caricato, M.; Li, X.; Hratchian, H. P.; Izmaylov, A. F.; Bloino, J.; Zheng, G.; Sonnenberg, J. L.; Hada, M.; Ehara, M.; Toyota, K.; Fukuda, R.; Hasegawa, J.; Ishida, M.; Nakajima, T.; Honda, Y.; Kitao, O.; Nakai, H.; Vreven, T.; Montgomery, J. A., Jr.; Peralta, J. E.; Ogliaro, F.; Bearpark, M.; Heyd, J. J.; Brothers, E.; Kudin, K. N.; Staroverov, V. N.; Keith, T.; Kobayashi, R.; Normand, J.; Raghavachari, K.; Rendell, A.; Burant, J. C.; Iyengar, S. S.; Tomasi, J.; Cossi, M.; Rega, N.; Millam, J. M.; Klene, M.; Knox, J. E.; Cross, J. B.; Bakken, V.; Adamo, C.; Jaramillo, J.; Gomperts, R.; Stratmann, R. E.; Yazyev, O.; Austin, A. J.; Cammi, R.; Pomelli, C.; Ochterski, J. W.; Martin, R. L.; Morokuma, K.; Zakrzewski, V. G.; Voth, G. A.; Salvador, P.; Dannenberg, J. J.; Dapprich, S.; Daniels, A. D.; Farkas, O.; Foresman, J. B.; Ortiz, J. V.; Cioslowski, J.; Fox, D. J. Gaussian 09, revision D.01, Gaussian, Inc.: Wallingford, CT, **2009**.

223. Stephens, P. J.; Devlin, F. J.; Chabalowski, C. F.; Frisch, M. J., *Ab Initio* Calculation of Vibrational Absorption and Circular Dichroism Spectra Using Density Functional Force Fields. *J. Phys. Chem.* **1994**, *98*, 11623–11627.

224. Becke, A. D., Density-Functional Thermochemistry. III. The Role of Exact Exchange. *J. Chem. Phys.* **1993**, *98*, 5648–5652.

225. Lee, C.; Yang, W.; Parr, R. G., Development of the Colle-Salvetti Correlation-Energy Formula into a Functional of the Electron Density. *Phys. Rev. B* **1988**, *37*, 785–789.

226. Vosko, S. H.; Wilk, L.; Nusair, M., Accurate Spin-Dependent Electron Liquid Correlation Energies for Local Spin Density Calculations: A Critical Analysis. *Can. J. Phys.* **1980**, *58*, 1200–1211.

227. Roy, L. E.; Hay, P. J.; Martin, R. L., Revised Basis Sets for the LANL Effective Core Potentials. *J. Chem. Theory Comput.* **2008**, *4*, 1029–1031.

228. Ehlers, A. W.; Böhme, M.; Dapprich, S.; Gobbi, A.; Höllwarth, A.; Jonas, V.; Köhler, K. F.; Stegmann, R.; Veldkamp, A.; Frenking, G., A Set of f-Polarization Functions for Pseudo-Potential Basis Sets of the Transition Metals Sc–Cu, Y–Ag and La–Au. *Chem. Phys. Lett.* **1993**, *208*, 111–114.

229. Hay, P. J.; Wadt, W. R., *Ab Initio* Effective Core Potentials for Molecular Calculations. Potentials for K to Au Including the Outermost Core Orbitals. *J. Chem. Phys.* **1985**, *82*, 299–310.

230. Powers, D. C.; Ritter, T., Bimetallic Pd(III) Complexes in Palladium-Catalysed Carbon–Heteroatom Bond Formation. *Nat. Chem.* **2009**, *1*, 302–309.

231. Reed, S. A.; White, M. C., Catalytic Intermolecular Linear Allylic C−H Amination via Heterobimetallic Catalysis. *J. Am. Chem. Soc.* **2008**, *130*, 3316–3318.

232. Shiri, A.; Khoramabadi-zad, A., Preparation of Several Active *N*-Chloro Compounds from Trichloroisocyanuric Acid. *Synthesis* **2009**, *16*, 2797–2801.

233. Wentrup, C., Nitrenes, Carbenes, Diradicals, and Ylides. Interconversions of Reactive Intermediates. *Acc. Chem. Res.* **2011**, *44*, 393–404.

234. Gephart, R. T., III; Warren, T. H., Copper-Catalyzed sp^3 C−H Amination. *Organometallics* **2012**, *31*, 7728–7752.

235. Alderson, J. M.; Corbin, J. R.; Schomaker, J. M., Tunable, Chemo- and Site-Selective Nitrene Transfer Reactions through the Rational Design of Silver(I) Catalysts. *Acc. Chem. Res.* **2017**, *50*, 2147–2158.

236. Singh, R.; Mukherjee, A., Metalloporphyrin Catalyzed C−H Amination. *ACS Catal.* **2019**, *9*, 3604–3617.

237. Cho, I.; Jia, Z.-J.; Arnold, F. H., Site-Selective Enzymatic C–H Amidation for Synthesis of Diverse Lactams. *Science* **2019**, *364*, 575–578.

238. Nageli, I.; Baud, C.; Bernardinelli, G.; Jacquier, Y.; Moraon, M.; Mullet, P., Rhodium(II)-Catalyzed CH Insertions with {[(4-Nitrophenyl)sulfonyl]imino}phenyl-λ^3-iodane. *Helv. Chim. Acta* **1997**, *80*, 1087–1105.

239. Nguyen, Q.; Sun, K.; Driver, T. G., Rh_2(II)-Catalyzed Intramolecular Aliphatic C−H Bond Amination Reactions using Aryl Azides as the N-Atom Source. *J. Am. Chem. Soc*. **2012**, *134*, 7262–7265.

240. Chiappini, N. D.; Mack, J. B. C.; Du Bois, J., Intermolecular C (sp^3) -H Amination of Complex Molecules. *Angew. Chem. Int. Ed.* **2018**, *130*, 5050–5053.

241. Das, A.; Maher, A. G.; Telser, J.; Powers, D. C., Observation of a Photogenerated Rh_2 Nitrenoid Intermediate in C–H Amination. *J. Am. Chem. Soc.* **2018**, *140*, 10412–10415.

242. Harrison, J. G.; Gutierrez, O.; Jana, N.; Driver, T. G.; Tantillo, D. J., Mechanism of Rh_2(II)-Catalyzed Indole Formation: The Catalyst does not Control Product Selectivity. *J. Am. Chem. Soc.* **2016**, *138*, 487–490.

243. Wang, J.; Zhao, C.; Weng, Y.; Xu, H., Insight into the Mechanism and Site-Selectivity of $Rh_2^{II,II}(esp)_2$-Catalyzed Intermolecular C–H Amination. *Catal. Sci. Technol.* **2016**, *6*, 5292–5303.

244. Shay, D. T.; Yap, G. P. A.; Zakharov, L. N.; Rheingold, A. L.; Theopold, K. H., Intramolecular C−H Activation by an Open-Shell Cobalt(III) Imido Complex. *Angew. Chem. Int. Ed.* **2005**, *44*, 1508–1510.

245. Laskowski, C. A.; Miller, A. J. M.; Hillhouse, G. L.; Cundari, T. R., A Two-Coordinate Nickel Imido Complex that Effects C−H Amination. *J. Am. Chem. Soc.* **2011**, *133*, 771–773.

246. Bakhoda, A.; Jiang, Q.; Bertke, J. A.; Cundari, T. R.; Warren, T. H., Elusive Terminal Copper Arylnitrene Intermediates. *Angew. Chem. Int. Ed.* **2017**, *56*, 6426–6430.

247. Downs, A. J.; Greene, T. M., Coming to Grips with Reactive Intermediates. *Adv. Inorg. Chem.* **1998**, *46*, 101–171.

248. Ulatowski, F.; Dąbrowa, K.; Bałakier, T.; Jurczak, J., Recognizing the Limited Applicability of Job Plots in Studying Host–Guest Interactions in Supramolecular Chemistry. *J. Org. Chem.* **2016**, *81*, 1746–1756.

249. Brynn Hibbert, D.; Thordarson, P., The Death of the Job Plot, Transparency, Open Science and Online Tools, Uncertainty Estimation Methods and Other Developments in Supramolecular Chemistry Data Analysis. *Chem. Commun.* **2016**, *52*, 12792–12805.

250. Dash, C.; Yousufuddin, M.; Cundari, T. R.; Dias, H. V. R., Gold-Mediated Expulsion of Dinitrogen from Organic Azides. *J. Am. Chem. Soc*. **2013**, *135*, 15479–15488.

251. Dias, H. V. R.; Polach, S. A.; Goh, S.-K.; Archibong, E. F.; Marynick, D. S., Copper and Silver Complexes Containing Organic Azide Ligands: Syntheses, Structures, and Theoretical Investigation of $[HB(3,5\text{-}(CF_3)_2Pz)_3]CuNNN(1\text{-}Ad)$ and $[HB(3,5\text{-}(CF_3)_2Pz)_3]AgN(1\text{-}Ad)NN$ (Where Pz) Pyrazolyl and 1-Ad) 1-Adamantyl). *Inorg. Chem.* **2000**, *39*, 3894–3901.

252. Seok, W. K.; Klapötke, T. M., Inorganic and Transition Metal Azides. *Bull. Korean Chem. Soc.* **2010**, *31*, 781–788.

253. Dunkin, I. R.; Shields, C. J.; Quast, H.; Seiferling, B., The Photolysis of 1-Azido-4-methylbicyclo[2.2.2]octane and 1-Azidoadamantane in Low-Temperature Matrices. *Tetrahedron Lett.* **1983**, *24*, 3887–3890.

254. Dunkin, I. R.; Thomson, P. C. P., Photolysis of *t*-Butyl Azide in N_2 at 12 K, and Matrix IR Spectra of Three Isomeric C_4H_9N Imines. *Tetrahedron Lett.* **1980**, *21*, 3813–3816.

255. Dunkin, I. R.; Thomson, P. C. P., Pentafluorophenyl Nitrene: A Matrix Isolated Aryl Nitrene that does not Undergo Ring Expansion. *J. Chem. Soc., Chem. Commun.* **1982**, 1192–1193.

256. Radziszewski, J. G.; Downing, J. W.; Jawdosiuk, M.; Kovacic, P.; Michl, J., 4-Azahomoadamant-3-ene: Spectroscopic Characterization and Photoresolution of a Highly Reactive Strained Bridgehead Imine. *J. Am. Chem. Soc.* **1985**, *107*, 594–603.

257. Wayne, G. S.; Snyder, G. J.; Rogers, D. W., Measurement of the Strain Energy of a Transient Bridgehead Imine, 4-Azahomoadamant-3-ene, by Photoacoustic Calorimetry. *J. Am. Chem. Soc.* **1993**, *115*, 9860–9861.

258. Brinker, U. H.; Walla, P.; Krois, D.; Arion, V. B., Study of the Structure and Photochemical Decomposition of Azidoadamantanes Entrapped in α- and β-Cyclodextrin. *Eur. J. Org. Chem.* **2011**, *2011*, 1249–1255.

259. Garman, E. F., Radiation Damage in Macromolecular Crystallography: What is it and why should we care? *Acta Crystallogr. D* **2010**, *66*, 339–351.

260. The formation of **IV-3b**·N_2 results in the structure evolution from $P2_1/c$ to $P2_1/n$, with only minor changes in the unit cell parameters [**IV-2b**: a = 10.8913(10) Å, b = 14.274(1) Å, c = 18.732(2) Å, β = 105.847(1)°, V = 2801.7(4) Å^3; **IV-3b**·N_2: a = 11.030(2) Å, b = 14.251(2) Å, c = 18.763(3) Å, β = 107.025(2)°, V = 2820.2(8) Å^3]. This is not a transformation of the monoclinic standard space group $P2_1/c$ to the

nonstandard space group $P2_1/n$ [matrix (1 0 1/0 1 0/−1 0 0), new cell: 18.924, 14.275, 10.891, 107.77].

261. Wang, J.; Zheng, K.; Lin, B.; Weng, Y., A Comparative Study of Inter- and Intramolecular C–H Aminations: Mechanism and Site Selectivity. *RSC Adv.* **2017**, *7*, 34783–34794.

262. Azek, E.; Khalifa, M.; Bartholoméüs, J.; Ernzerhof, M.; Lebel, H., Rhodium(II)-Catalyzed C–H Aminations using *N*-mesyloxycarbamates: Reaction Pathway and By-product Formation. *Chem. Sci.* **2019**, *10*, 718–729.

263. Kono, M.; Harada, S.; Nemoto, T., Chemoselective Intramolecular Formal Insertion Reaction of Rh–Nitrenes into an Amide Bond Over C−H Insertion. *Chem. Eur. J.* **2019**, *25*, 3119–3124.

264. Pan, D.; Wei, Y.; Shi, M., Mechanistic Studies for Dirhodium-Catalyzed Chemoselective Oxidative Amination of Alkynyl-Tethered Sulfamates. *Org. Chem. Front.* **2019**, *6*, 1123–1132.

265. Lin, X.; Zhao, C.; Che, C.-M.; Ke, Z.; Phillips, D. L., A DFT Study on the Mechanism of $Rh_2^{II,II}$-Catalyzed Intramolecular Amidation of Carbamates. *Chem. Asian J.* **2007**, *2*, 1101–1108.

266. Arai, K.; Ueda, Y.; Morisaki, K.; Furuta, T.; Sasamori, T.; Tokitoh, N.; Kawabata, T., Intermolecular Chemo- and Regioselective Aromatic C–H Amination of Alkoxyarenes Promoted by Rhodium Nitrenoids. *Chem. Commun.* **2018**, *54*, 2264–2267.

267. Gao, D.; Bao, X., Mechanistic Insights into the Different Chemoselectivities of Rh_2(II)-Catalyzed Ring Expansion of Cyclobutanol-Substituted Aryl Azides and C–H Bond Amination of Cyclopentanol-Substituted Aryl azides: A DFT Study. *Org. Chem. Front.* **2018**, *5*, 1471–1482.

268. Zhao, Y.; Truhlar, D. G., The M06 Suite of Density Functionals for Main Group Thermochemistry, Thermochemical Kinetics, Noncovalent Interactions, Excited States, and Transition Elements: Two New Functionals and Systematic Testing of Four M06-Class Functionals and 12 Other Functionals. *Theor. Chem. Acc.* **2008**, *120*, 215–241.

269. Becke, A. D., Density-Functional Exchange-Energy Approximation with Correct Asymptotic Behavior. *Phys. Rev. A* **1988**, *38*, 3098–3100.

270. Wadt, W. R.; Hay, P. J., *Ab Initio* Effective Core Potentials for Molecular Calculations. Potentials for Main Group Elements Na to Bi. *J. Chem. Phys.* **1985**, *82*, 284–298.

271. Weigend, F.; Ahlrichs, R., Balanced Basis Sets of Split Valence, Triple Zeta Valence and Quadruple Zeta Valence Quality for H to Rn: Design and Assessment of Accuracy. *Phys. Chem. Chem. Phys.* **2005**, *7*, 3297–3305.

272. Swart, M., Accurate Spin-State Energies for Iron Complexes. *J. Chem. Theory Comput.* **2008**, *4*, 2057–2066.

273. Salomon, O.; Reiher, M.; Hess, B. A., Assertion and Validation of the Performance of the B3LYP* Functional for the First Transition Metal Row and the G2 Test Set. *J. Chem. Phys.* **2002**, *117*, 4729–4737.

274. Grimme, S.; Ehrlich, S.; Goerigk, L., Effect of the Damping Function in Dispersion Corrected Density Functional Theory. *J. Comput. Chem.* **2011**, *32*, 1456–1465.

275. Glendening, E. D.; Badenhoop, J. K.; Reed, A. E.; Carpenter, J. E.; Bohmann, J. A.; Morales, C. M.; Landis, C. R.; Weinhold, F., Theoretical Institute, University of Wisconsin, Madison, WI. **2013**; http://nbo6.chem.wisc.edu.

276. Kornecki, K. P.; Berry, J. F., Dirhodium Catalysts that Bear Redox Noninnocent Chelating Dicarboxylate Ligands and their Performance in Intra- and Intermolecular C–H Amination. *Eur. J. Inorg. Chem.* **2012**, *2012*, 562–568.

277. Radziszewski, J. G.; Downing, J. W.; Jawdosiuk, M.; Kovacic, P.; Michl, J., 4-Azahomoadamant-3-ene: Spectroscopic Characterization and Photoresolution of a Highly Reactive Strained Bridgehead Imine. *J. Am. Chem. Soc.* **1985**, *107*, 594-603.

278. Jones, C. G.; Asay, M.; Kim, L. J.; Kleinsasser, J. F.; Saha, A.; Fulton, T. J.; Berkley, K. R.; Cascio, D.; Malyutin, A. G.; Conley, M. P.; Stoltz, B. M.; Lavallo, V.; Rodríguez, J. A.; Nelson, H. M., Characterization of Reactive Organometallic Species via MicroED. *ACS Cent. Sci.* **2019**, *5*, 1507–1513.

279. Ohashi, Y.; Sasada, Y., X-Ray Analysis of Co–C Bond Cleavage in the Crystalline State. *Nature* **1977**, *267*, 142–144.

280. Das, A.; Van Trieste III, G. P.; Powers, D. C., Crystallography of Reactive Intermediates. *Comment. Inorg. Chem.* **2020**, *40*, 116–158.

281. Hennessy, E. T.; Betley, T. A., Complex *N*-Heterocycle Synthesis via Iron-Catalyzed, Direct C–H Bond Amination. *Science* **2013**, *340*, 591–595.

282. Ochiai, M.; Miyamoto, K.; Kaneaki, T.; Hayashi, S.; Nakanishi, W., Highly Regioselective Amination of Unactivated Alkanes by Hypervalent Sulfonylimino-λ^3-Bromane. *Science* **2011**, *332*, 448–451.

283. Hong, S. Y.; Park, Y.; Hwang, Y.; Kim, Y. B.; Baik, M.-H.; Chang, S., Selective Formation of γ-Lactams via C–H Amidation Enabled by Tailored Iridium Catalysts. *Science* **2018**, *359*, 1016–1021.

284. Lei, H.; Rovis, T., A Site-Selective Amination Catalyst Discriminates between nearly Identical C–H Bonds of Unsymmetrical Disubstituted Alkenes. *Nat. Chem.* **2020**, *12*, 725–731.

285. Yang, Y.; Cho, I.; Qi, X.; Liu, P.; Arnold, F. H., An Enzymatic Platform for the Asymmetric Amination of Primary, Secondary and Tertiary C(sp^3)–H Bonds. *Nat. Chem.* **2019**, *11*, 987–993.

286. Jiang, H.; Lang, K.; Lu, H.; Wojtas, L.; Zhang, X. P., Asymmetric Radical Bicyclization of Allyl Azidoformates via Cobalt(II)-Based Metalloradical Catalysis. *J. Am. Chem. Soc.* **2017**, *139*, 9164–9167.

287. Das, A.; Chen, Y.-S.; Reibenspies, J. H.; Powers, D. C., Characterization of a Reactive Rh_2 Nitrenoid by Crystalline Matrix Isolation. *J. Am. Chem. Soc.* **2019**, *141*, 16232–16236.

288. Shen, M.; Leslie, B. E.; Driver, T. G., Dirhodium(II)-Catalyzed Intramolecular C–H Amination of Aryl Azides. *Angew. Chem. Int. Ed.* **2008**, *47*, 5056–5059.

289. Takayama, T.; Mitsumori, T.; Kawano, M.; Sekine, A.; Uekusa, H.; Ohashi, Y.; Sugawara, T., Direct Observation of Arylnitrene Formation in the Photoreaction of Arylazide Crystals. *Acta Crystallogr. B* **2010**, *66*, 639–646.

290. The photolysis of **V-3a** could not be monitored in the solution phase by either UV-vis or NMR due to the fact that: (1) o-biphenylazide is a weakly bound ligand and (2) o-biphenylazide by itself has a background photochemistry to generate the carbazole

291. **V-3a**: $P2_1/n$, a = 10.712(2) Å, b = 12.937(2) Å, c = 32.667(4) Å, β = 96.259(3)°; **V-5a**·N_2: $P2_1/c$, a = 10.9316(8) Å, b = 12.9312(9) Å, c = 32.433(2) Å, β = 99.310(1)°.

292. Baek, Y.; Das, A.; Zheng, S.-L.; Reibenspies, J. H.; Powers, D. C.; Betley, T. A., C–H Amination Mediated by Cobalt Organoazide Adducts and the Corresponding Cobalt Nitrenoid Intermediates. *J. Am. Chem. Soc.* **2020**, *142*, 11232–11243.

293. Chai, J.-D.; Head-Gordon, M., Long-Range Corrected Hybrid Density Functionals with Damped Atom–Atom Dispersion Corrections. *Phys. Chem. Chem. Phys.* **2008**, *10*, 6615–6620.

294. Andrae, D.; Häußermann, U.; Dolg, M.; Stoll, H.; Preuß, H., Energy-Adjusted *Ab Initio* Pseudopotentials for the Second and Third Row Transition Elements. *Theor. Chim. Acta* **1990**, *77*, 123–141.

295. Cao, X.; Dolg, M., Valence Basis Sets for Relativistic Energy-Consistent Small-Core Lanthanide Pseudopotentials. *J. Chem. Phys.* **2001**, *115*, 7348–7355.

296. Dolg, M.; Wedig, U.; Stoll, H.; Preuss, H., Energy-Adjusted *Ab Initio* Pseudopotentials for the First Row Transition Elements. *J. Chem. Phys.* **1987**, *86*, 866–872.

297. Petersson, G. A.; Al-Laham, M. A., A Complete Basis Set Model Chemistry. II. Open-Shell Systems and the Total Energies of the First-Row Atoms. *J. Chem. Phys.* **1991**, *94*, 6081–6090.

298. Petersson, G. A.; Bennett, A.; Tensfeldt, T. G.; Al-Laham, M. A.; Shirley, W. A.; Mantzaris, J., A Complete Basis Set Model Chemistry. I. The Total Energies of Closed-Shell Atoms and Hydrides of the First-Row Elements. *J. Chem. Phys.* **1988**, *89*, 2193–2218.

299. Wu, X.; Bao, X., Computational Insights into Different Chemoselectivities in Rh_2(II)-Catalyzed *N*-aryl Nitrene and Analogous Rh_2(II)/Cu(I)-Catalyzed Aryl-Substituted Carbene Involving Reactions. *Catal. Sci. Technol.* **2019**, *9*, 1518–1527.

300. During the *in crystallo* generation of **V-3b**, the unit cell parameters changed from [a = 12.881(2) Å; b = 12.949(2) Å; c = 18.331(3) Å; β = 102.871(2) °; V = 2981.0(7) $Å^3$] to [a = 12.961(2) Å; b = 12.909(2) Å; c = 18.381(3) Å; β = 100.334(2) °; V = 3025.5(8) $Å^3$].

301. Che, C.-M.; Cheng, M.-C.; Wang, Y.; Gray, H. B., Trans-Effect of Dialkyl Sulfide on a Pt(III)–Pt(III) Bond. Synthesis, Spectroscopy and X-Ray Crystal Structure of $[Bu_4N]_2[Pt_2(P_2O_5H_2)_4(SEt_2)_2]$. *Inorg. Chim. Acta* **1992**, *191*, 7–9.

302. Che, C. M.; Lee, W. M.; Mak, T. C. W.; Gray, H. B., Axial-Ligand and Metal-Metal Trans Influences in Binuclear Platinum(III) Complexes. Crystal Structures and Spectroscopic Properties of $K_4[Pt_2(P_2O_5H_2)_4(SCN)_2]\cdot 2H_2O$, $K_4[Pt_2(P_2O_5H_2)_4(NO_2)_2]\cdot 2KNO_2\cdot 2H_2O$, and $K_4[Pt_2(P_2O_5H_2)_4(C_3H_3N_2)_2]\cdot 7H_2O$. *J. Am. Chem. Soc.* **1986**, *108*, 4446–4451.

303. Appleton, T. G.; Clark, H. C.; Manzer, L. E., The Trans-Influence: Its Measurement and Significance. *Coordin. Chem. Rev.* **1973**, *10*, 335–422.

304. Alexander, K. A.; Bryan, S. A.; Fronczek, F. R.; Fultz, W. C.; Rheingold, A. L.; Roundhill, D. M.; Stein, P.; Watkins, S. F., Crystal and Molecular Structures of Dihalotetrakis(pyrophosphito)diplatinum(III) Complexes. Integrative use of Structural and Vibrational Data to Assess Intermetallic Bonding and the Trans Influence of the Platinum(III)-Platinum(III) Bond. *Inorg. Chem.* **1985**, *24*, 2803–2808.

305. Ariafard, A.; Hyland, C. J. T.; Canty, A. J.; Sharma, M.; Brookes, N. J.; Yates, B. F., Ligand Effects in Bimetallic High Oxidation State Palladium Systems. *Inorg. Chem.* **2010**, *49*, 11249–11253.

306. Ravel, B.; Newville, M., ATHENA, ARTEMIS, HEPHAESTUS: Data Analysis for X-Ray Absorption Spectroscopy using IFEFFIT. *J. Synchrotron Radiat.* **2005**, *12*, 537–541.

307. Mustre de Leon, J.; Rehr, J. J.; Zabinsky, S. I.; Albers, R. C., *Ab Initio* Curved-Wave X-Ray-Absorption Fine Structure. *Phys. Rev. B* **1991**, *44*, 4146–4156.

308. Zhao, Y.; Truhlar, D. G., A New Local Density Functional for Main-Group Thermochemistry, Transition Metal Bonding, Thermochemical Kinetics, and Noncovalent Interactions. *J. Chem. Phys.* **2006**, *125*, 194101.

309. Yanai, T.; Tew, D. P.; Handy, N. C., A New Hybrid Exchange–Correlation Functional using the Coulomb-Attenuating Method (CAM-B3LYP). *Chem. Phys. Lett.* **2004**, *393*, 51–57.

310. Weigend, F., Accurate Coulomb-Fitting Basis Sets for H to Rn. *Phys. Chem. Chem. Phys.* **2006**, *8*, 1057–1065.

311. Stokes, B. J.; Jovanović, B.; Dong, H.; Richert, K. J.; Riell, R. D.; Driver, T. G., Rh_2(II)-Catalyzed Synthesis of Carbazoles from Biaryl Azides. *J. Org. Chem.* **2009**, *74*, 3225–3228.

312. Weik, M.; Ravelli, R. B. G.; Kryger, G.; McSweeney, S.; Raves, M. L.; Harel, M.; Gros, P.; Silman, I.; Kroon, J.; Sussman, J. L., Specific Chemical and Structural Damage to Proteins Produced by Synchrotron Radiation. *Proc. Natl. Acad. Sci. U.S.A.* **2000**, *97*, 623–628.

313. Harman, W. H.; Chang, C. J., N_2O Activation and Oxidation Reactivity from a Non-Heme Iron Pyrrole Platform. *J. Am. Chem. Soc*. **2007**, *129*, 15128–15129.

314. Tolman, W. B., Binding and Activation of N_2O at Transition-Metal Centers: Recent Mechanistic Insights. *Angew. Chem. Int. Ed.* **2010**, *49*, 1018–1024.

315. Zhuravlev, V.; Malinowski, P. J., A Stable Crystalline Copper(I)–N_2O Complex Stabilized as the Salt of a Weakly Coordinating Anion. *Angew. Chem. Int. Ed.* **2018**, *57*, 11697–11700.

316. Mokhtarzadeh, C. C.; Chan, C.; Moore, C. E.; Rheingold, A. L.; Figueroa, J. S., Side-On Coordination of Nitrous Oxide to a Mononuclear Cobalt Center. *J. Am. Chem. Soc.* **2019**, *141*, 15003–15007.

317. Gyton, M. R.; Leforestier, B.; Chaplin, A. B., Rhodium(I) Pincer Complexes of Nitrous Oxide. *Angew. Chem. Int. Ed.* **2019**, *58*, 15295–15298.

318. Neu, R. C.; Otten, E.; Stephan, D. W., Bridging Binding Modes of Phosphine-Stabilized Nitrous Oxide to $Zn(C_6F_5)_2$. *Angew. Chem. Int. Ed.* **2009**, *48*, 9709–9712.

319. Piro, N. A.; Lichterman, M. F.; Harman, W. H.; Chang, C. J., A Structurally Characterized Nitrous Oxide Complex of Vanadium. *J. Am. Chem. Soc*. **2011**, *133*, 2108–2111.

320. Andino, J. G.; Caulton, K. G., Mechanism of N/O Bond Scission of N_2O by an Unsaturated Rhodium Transient. *J. Am. Chem. Soc*. **2011**, *133*, 12576–12583.

321. Murahashi, S.-I.; Kitani, Y.; Hosokawa, T.; Miki, K.; Kasai, N., Synthesis and Structure of α-Diazomethyl Palladium σ-Complexes; X-Ray Crystal Structure of Chloro[diazo(ethoxycarbonyl)methyl]bistriphenylphosphinepalladium. *J. Chem. Soc., Chem. Commun.* **1979**, 450–451.

322. Deydier, E.; Menu, M.-J.; Dartiguenave, M.; Dartiguenave, Y., Wolff Rearrangement in a Transition-Metal Diazoalkane Complex. Synthesis of the First η^1-Ketenyl Rhodium Complex $[Rh\{C(CO)SiMe_3\}(CO)(PEt_3)_2]$. *J. Organomet. Chem.* **1993**, *458*, 225–228.

323. Mizobe, Y.; Ishii, Y.; Hidai, M., Synthesis and Reactivities of Diazoalkane Complexes. *Coord. Chem. Rev.* **1995**, *139*, 281–311.

324. Sutton, D., Organometallic Diazo Compounds. *Chem. Rev.* **1993**, *93*, 995–1022.

325. Dartiguenave, M.; Joëlle Menu, M.; Deydier, E.; Yves, D.; Siebald, H., Crystal and Molecular Structures of Transition Metal Complexes with *N*- And C-Bonded Diazoalkane Ligands. *Coord. Chem. Rev.* **1998**, *178–180*, 623–663.

326. Liu, L.; Ruiz, David A.; Munz, D.; Bertrand, G., A Singlet Phosphinidene Stable at Room Temperature. *Chem* **2016**, *1*, 147–153.

327. Hansmann, M. M.; Bertrand, G., Transition-Metal-like Behavior of Main Group Elements: Ligand Exchange at a Phosphinidene. *J. Am. Chem. Soc*. **2016**, *138*, 15885–15888.

328. Hansmann, M. M.; Jazzar, R.; Bertrand, G., Singlet (Phosphino)phosphinidenes are Electrophilic. *J. Am. Chem. Soc*. **2016**, *138*, 8356–8359.

329. Abbenseth, J.; Delony, D.; Neben, M. C.; Würtele, C.; de Bruin, B.; Schneider, S., Interconversion of Phosphinyl Radical and Phosphinidene Complexes by Proton Coupled Electron Transfer. *Angew. Chem. Int. Ed.* **2019**, *58*, 6338–6341.

330. Transue, W. J.; Velian, A.; Nava, M.; García-Iriepa, C.; Temprado, M.; Cummins, C. C., Mechanism and Scope of Phosphinidene Transfer from Dibenzo-7-phosphanorbornadiene Compounds. *J. Am. Chem. Soc.* **2017**, *139*, 10822–10831.

331. Courtemanche, M.-A.; Transue, W. J.; Cummins, C. C., Phosphinidene Reactivity of a Transient Vanadium P≡N Complex. *J. Am. Chem. Soc*. **2016**, *138*, 16220–16223.

332. Yang, W.; Krantz, K. E.; Dickie, D. A.; Molino, A.; Wilson, D. J. D.; Gilliard Jr, R. J., Crystalline BP-Doped Phenanthryne via Photolysis of The Elusive Boraphosphaketene. *Angew. Chem. Int. Ed.* **2020**, *59*, 3971–3975.

333. Geeson, M. B.; Transue, W. J.; Cummins, C. C., Organoiron- and Fluoride-Catalyzed Phosphinidene Transfer to Styrenic Olefins in a Stereoselective Synthesis of Unprotected Phosphiranes. *J. Am. Chem. Soc*. **2019**, *141*, 13336–13340.

334. Menu, M. J.; Desrosiers, P.; Dartiguenave, M.; Dartiguenave, Y.; Bertrand, G., Reaction of the (Trimethylsilyl)diazomethane Anion with Metal Complexes: Synthesis and X-Ray Study of Iodomethyltris(trimethylphosphine)rhodium(III) (trimethylsilyl)diazomethane, $RhICH_3(PMe_3)_3\{C(N_2)SiMe_3\}$. *Organometallics* **1987**, *6*, 1822–1824.

335. Coppens, P.; Benedict, J.; Messerschmidt, M.; Novozhilova, I.; Graber, T.; Chen, Y.-S.; Vorontsov, I.; Scheins, S.; Zheng, S.-L., Time-Resolved Synchrotron Diffraction and Theoretical Studies of Very Short-Lived Photo-Induced Molecular Species. *Acta Crystallogr. A* **2010**, *66*, 179–188.

336. Kim, C. D.; Pillet, S.; Wu, G.; Fullagar, W. K.; Coppens, P., Excited-State Structure by Time-Resolved X-Ray Diffraction. *Acta Crystallogr. A* **2002**, *58*, 133–137.

337. Stein, P.; Dickson, M. K.; Roundhill, D. M., Raman and Infrared Spectra of Binuclear Platinum(II) and Platinum(III) Octaphosphite Complexes. A Characterization of the Intermetallic Bonding. *J. Am. Chem. Soc*. **1983**, *105*, 3489–3494.